Palaeoenvironments and position of the Precambrian–Cambrian boundary within the lower Vanrhynsdorp Group of South Africa: sedimentary facies analysis, U-Pb series zircon geochronology and micropalaeontology

by

Bianca Harrison

HRRBIA001

Supervisor: Dr Emese M. Bordy

Co-supervisor: Dr Wendy L. Taylor

A thesis presented for the degree of Master of Science in Geology

In the Department of Geological Sciences at

February 2018

Declaration

1. I know that plagiarism is wrong. Plagiarism is to use another's work and pretend that it is one's own.

2. I have used the South African Journal of Geology convention for citation and referencing. Each contribution to, and quotation in, this project from the work(s) of other people has been attributed, and has been cited and referenced.

3. This project is my own work.

4. I have not allowed, and will not allow, anyone to copy my work with the intention of passing it off as his or her own work.

Signature: Signed by candidate

Date: 19 February 2018

Acknowledgements

I would like to thank both my supervisors Dr Emese Bordy and Dr Wendy Taylor for their enormous support and dedication to this project. Without their help and commitment this work wouldn't have been possible. I also wish to thank all my friends and family members who were always cheering me on!

I would like to thank Dr. John A. Almond and Dr. Pieter G. Gresse for graciously taking the time to meet with us in the field and share their extensive geological knowledge of the area. Without their assistance, fieldwork would have been nearly impossible. I would also like to further thank Dr. John A. Almond for donating his samples to this project.

To my colleagues at UCT, a huge thank you all your help during field or lab work, especially Miengah Abrahams, Claire Browning, Robert Muir, Akhil Rampersadh, Mhairi Reid, Lorena Tafur and Aaron Vardi. You guys rock!

Last but not least, I acknowledge the following for financial support:

- Centre of Excellence (Palaeosciences) for funding the project and myself, and giving me the opportunity to further my studies.
- The National Research Foundation (NRF) for supporting me during the project.
- University of Cape Town for the conference grant to attend the International Meeting of Sedimentology (IMS), Toulouse, France, October 10-13.
- My supervisor Dr Emese Bordy for the conference grants to attend the PSSA and IMS meetings.
- Dr Anette Hogstrom and the Digermulen Early Life Research Group for giving me the opportunity to further my skills and allowing me to attend their field season.

Abstract

The Vanrhynsdorp Group is a mainly fluvio-marine siliclastic succession that outcrops in the northwestern part of South Africa. The critical Precambrian-Cambrian boundary falls within the group, however the depositional environments across the boundary, its exact stratigraphic position and nature are unresolved. The group was deposited in the Vanrhynsdorp Basin, which has been shown to be the southernmost extension of the Nama Foreland Basin. Consequently, the Vanrhynsdorp Group has been correlated with the world-famous Nama Group, which features diverse Ediacaran-Cambrian fossils. To date, no body fossils have been discovered in the Vanrhynsdorp Group.

Through U-Pb dating of detrital zircons using LA-ICP-MS, radiometric ages for the middle part of the Vanrhynsdorp Group (Besonderheid Formation) were obtained in a preliminary study of this project. The radiometric data, yielding a maximum depositional age of 524 to 528 Ma from the youngest zircon grain population, indicated that the Precambrian-Cambrian boundary is stratigraphically lower in the group than it was thought before. To further constrain the age of the lower Vanrhynsdorp Group, and by extension the position of the Precambrian-Cambrian boundary, several detrital zircon samples were processed for age determination from the succession in this study. In addition, using sedimentary facies analysis, the lateral and vertical facies variation in this lower part of the group were (re)documented in order to refine the palaeoenvironmental setting.

The current results suggest a dominantly shallow marine, partly storm-dominated depositional environment for the lowermost units as opposed to the previous interpretations of dominantly alluvial settings. Because of the global importance of the Ediacaran-Cambrian transition for diversification of marine biota in the Cambrian, addressing these palaeoenvironmental inconsistencies is the vital outcome of this study. By integrating our sedimentological and geochronological results, the project presents an improved understanding of the depositional history of the Vanrhynsdorp Group during the critical Ediacaran-Cambrian transition.

Contents

1. Introduction

The Late Proterozoic to Early Cambrian Vanrhynsdorp Group is a ~3 km thick, fossiliferous and largely undeformed, fluvial to marine and mainly siliciclastic unit exposed in the Northern and Western Cape of South Africa (Figure 1.1; Gresse, 1992). The Vanrhynsdorp Group correlates with the world-famous Nama Group of southern Namibia which features diverse Ediacaran-Cambrian fossils of the earliest complex multicellular organisms. Key evolutionary processes occurred prior to and during the earliest phases of the Cambrian metazoan "explosion" which makes this boundary of global palaeobiological significance (Jensen et al., 2000). To date, there have been no body or microfossil discoveries in the Vanrhynsdorp Group; however, it contains a prolific trace fossil record that has only been preliminarily documented (e.g., Buatois et al., 2007; Almond et al., 2009; Buatois et al., 2013). Microfossils have biostratigraphic potential and thus may assist with regional and age correlations as well as pinpointing the boundary. Precise correlation of the South African successions within the Nama and Vanrhynsdorp Groups remains elusive pending detailed sequence stratigraphic, sedimentological and palaeontological analyses.

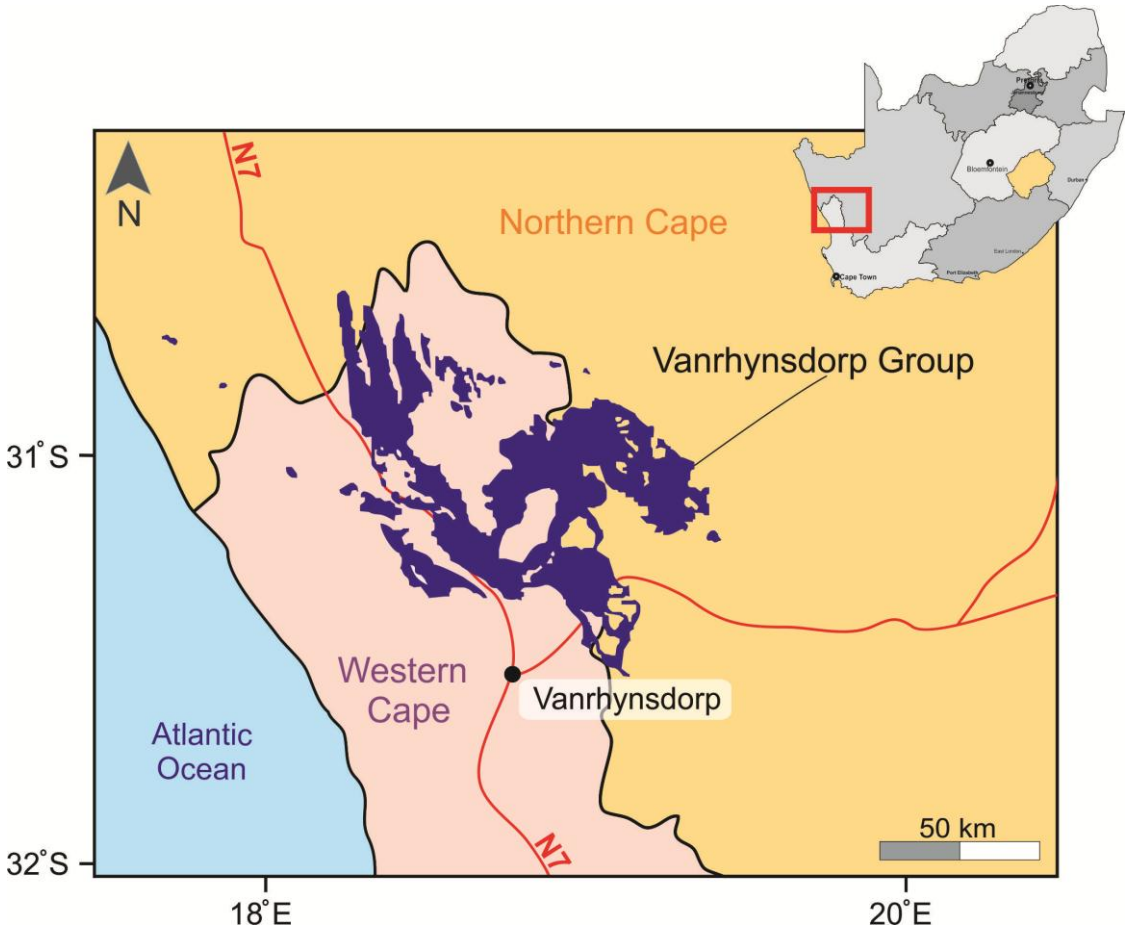

Figure 1.1. Simplified geology of the NW part of South Africa showing the general outcrop of the Vanrhynsdorp Group (purple infill) in parts of the Western and Northern Cape.

The overall lithostratigraphic and ichnologic similarities between the Vanrhynsdorp and Nama Groups provide some equivocal correlation (Gresse and Germs, 1993). However, the geochronological age constraint for the less well-studied Vanrhynsdorp Group and the stratigraphic position of the boundary within it remains unresolved. Detrital zircon dating in one of the middle units (lowermost Besonderheid Formation) within the group yielded a maximum depositional age of 524 to 528 Ma (Harrison, 2014). Additionally, current biostratigraphic studies suggests that the lowermost units in the Vanrhynsdorp Group are Late Ediacaran, while the bulk of the succession is Early Cambrian (Table 1.1). Nevertheless, the precise stratigraphic position and nature of the Precambrian–Cambrian boundary within the Vanrhynsdorp Group remains unresolved (Buatois et al., 2007; Aceñolaza et al., 2009; Almond et al., 2009; Macey et al., 2011).

The trace fossil record suggests that the boundary is located between the Gannabos and Besonderheid Formations (Table 1.1; Herbosch and Verniers, 2011). Detrital zircon dating has tentatively confirmed a Cambrian age for the Besonderheid Formation but no dating has taken place for the Gannabos Formation or the subsequent lower formations (Harrison, 2014). Given that the lower Vanrhynsdorp Group is largely comprised of coarse siliclastic rocks, their potential detrital zircon content was considered promising for U-Pb isotope dating. Additionally, the fine-grained siliciclastic rocks were targeted for microfossil processing in order to aid in locating the position of the boundary.

The Vanrhynsdorp Group has not been extensively studied since the late 1980-90's and lacks a detailed stratigraphic framework. This has caused contradictions in palaeoenvironmental interpretations of some of the formations (Table 1.1). These contradictions could be resolved through the use of systematic sedimentological, palaeontological, taphonomic, and ichnological assessments. Central to this project are the palaeoenvironmental analyses of the lowermost siliciclastic units - i.e., Flaminkberg, Hoedberg and Arondegas Formations. The detrital zircon dating of these formations is vital to locate the Ediacaran-Cambrian boundary, and so are the microfossil investigations.

Although the Vanrhynsdorp and Nama Groups were deposited in the same basin, precise correlation between the successions remains elusive. Potential tuffaceous horizons in the Gannabos and Besonderheid Formations have been identified but have yet to be dated (Germs et al., 2009). The U-Pb detrital zircon dating of this project will add to the geochronological framework and potential correlations.

Table 1.1. Stratigraphic chart of the Late Proterozoic to Early Cambrian (c. 550-540 Ma) Vanrhynsdorp Group. The position of the Precambrian-Cambrian boundary (in red) is not yet resolved, but based on the occurrence of the Cambrian index ichnofossil *Oldhamia* sp. in the Besonderheid Formation, the boundary is assumed to be at the underlying contact (Almond et al., 2009; Herbosch and Verniers, 2011; Buatois et al., 2013). Note that various authors interpret the sedimentology of the succession very differently (sources: Aceñolaza et al., 2009; Germs et al., 2009; Buatois et al., 2013).

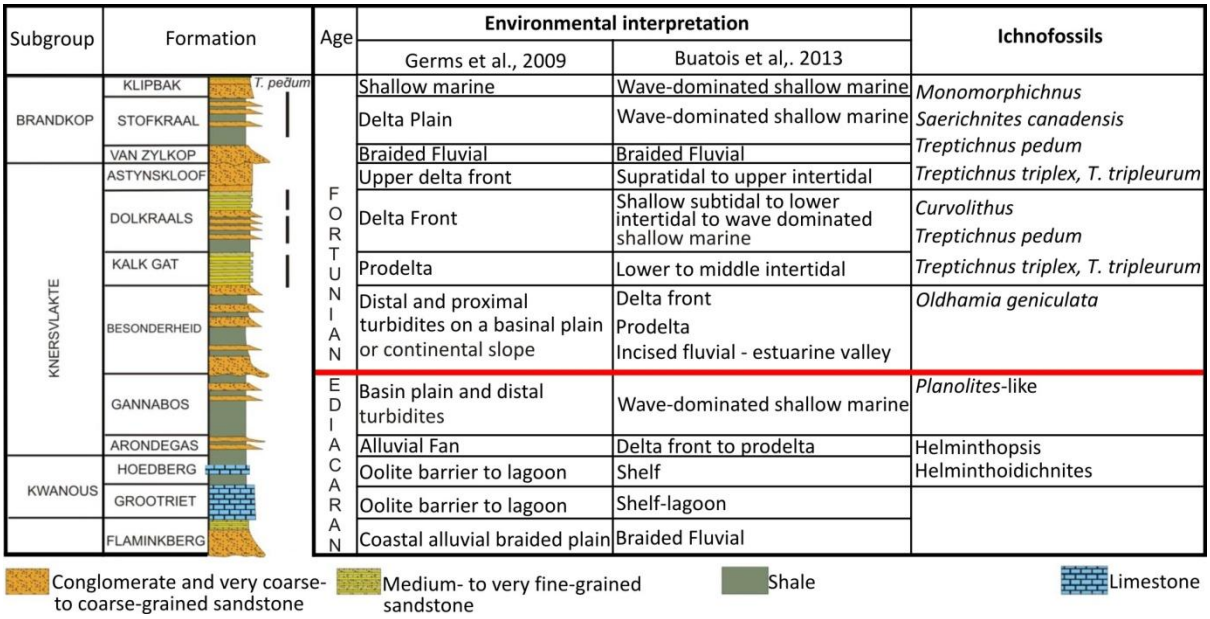

Subgroup	Formation	Age	Environmental interpretation		Ichnofossils
			Germs et al., 2009	Buatois et al,. 2013	
BRANDKOP	KLIPBAK	FORTUNIAN	Shallow marine	Wave-dominated shallow marine	*Monomorphichnus* *Saerichnites canadensis* *Treptichnus pedum* *Treptichnus triplex, T. tripleurum*
	STOFKRAAL		Delta Plain	Wave-dominated shallow marine	
	VAN ZYLKOP		Braided Fluvial	Braided Fluvial	
KNERSVLAKTE	ASTYNSKLOOF		Upper delta front	Supratidal to upper intertidal	
	DOLKRAALS		Delta Front	Shallow subtidal to lower intertidal to wave dominated shallow marine	*Curvolithus* *Treptichnus pedum*
	KALK GAT		Prodelta	Lower to middle intertidal	*Treptichnus triplex, T. tripleurum*
	BESONDERHEID		Distal and proximal turbidites on a basinal plain or continental slope	Delta front Prodelta Incised fluvial - estuarine valley	*Oldhamia geniculata*
	GANNABOS	EDIACARAN	Basin plain and distal turbidites	Wave-dominated shallow marine	*Planolites*-like
	ARONDEGAS		Alluvial Fan	Delta front to prodelta	Helminthopsis Helminthoidichnites
KWANOUS	HOEDBERG		Oolite barrier to lagoon	Shelf	
	GROOTRIET		Oolite barrier to lagoon	Shelf-lagoon	
	FLAMINKBERG		Coastal alluvial braided plain	Braided Fluvial	

1.1 Aims

The aims of this project on the lower Vanrhynsdorp Group are to:

1. Determine the stratigraphic location of the Ediacaran-Cambrian boundary;
2. Refine the sedimentological interpretation of the units via sedimentary facies analysis;
3. Date the detrital zircons from key stratigraphic units using Laser Ablation ICP-MS;
4. Investigate the micropalaeontological content of the lower Vanrhynsdorp Group.

2. Geological background

2.1 Foreland Basin Formation

The Late Proterozoic to early Cambrian Vanrhynsdorp Group in the Northern and Western Cape of South Africa was deposited in the Vanrhynsdorp sub-basin, which is the southernmost subsidiary basin of the Nama Foreland Basin (NFB). The latter was a ~1000 km long basin and developed between the Kalahari Craton in the east and the partly contemporaneous Damara and Gariep Orogenic Belts in the north and west (Figures 2.1-2; Gresse et al., 2006). The Nama and Vanrhynsdorp Groups are found over an area that is more than 350 000 km^2 and overlies the Gifberg Group (Gariep Supergroup) and Little Namaqualand Suite (~ 1.15 Ga) (Germs, 1983; Eglington, 2006; Germs et al., 2009). Division of the Nama Foreland Basin, the Zaris, Witputs and Vanrhynsdorp sub-basins, occurred through the development of east-west striking forebulges (Figure 2.1; Germs and Gresse, 1991). The Osis Ridge in the north separated the Zaris and Witputs sub-basins, and the Kamieskroon Ridge in the south separated the Vanrhynsdorp and Witputs sub-basin (Germs et al., 2009). The deposits of the Zaris and Witputs sub-basins outcrop predominantly in Namibia with minor exposures of the Witputs sub-basin in the Northern Cape. The deposits of the Vanrhynsdorp sub-basin outcrop exclusively in South Africa and have not been as extensively studied as their Namibian counterparts. During late Nama depositional times (upper Fish River Subgroup), the above ridges no longer functioned as dividers between the sub-basins and the sediments were mainly shed into one major foreland basin (Germs and Gresse, 1991).

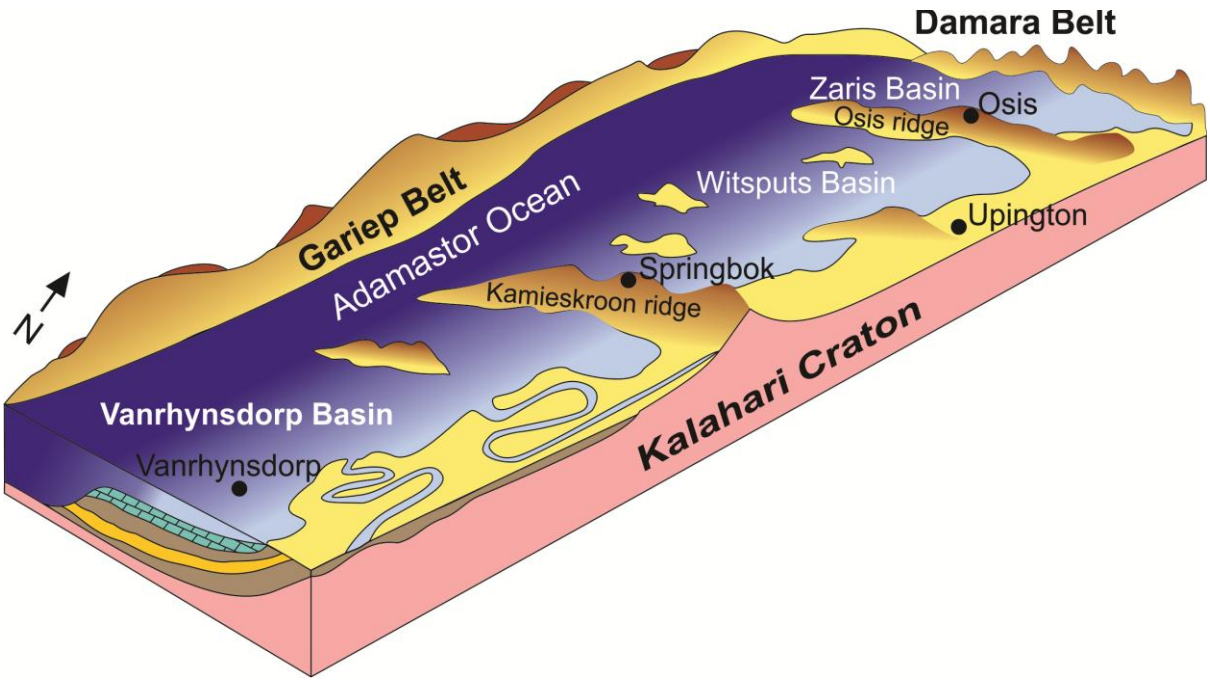

Figure 2.1. Palaeogeographic map of the Nama Foreland Basin showing its sub-basins, the east-west ridges and the orogenic belts responsible for the basin formation to the west and north (modified after MacCrae, 1999).

The NBF formed during the assembly of the Gondwana supercontinent in the Neoproterozoic and early Palaeozoic and has been linked to high angle and oblique convergence of the three orogenic systems, subduction, collision of continental blocks, accretion of exotic terranes, and thrust belt developments within the Pan-African-Brasiliano belts (Miller, 1983; Germs, 1995; MacCrae, 1999; Gaucher and Germs, 2002; Saylor, 2003; Bossi and Gaucher, 2004; Basei et al., 2005). The stacked thrusts within the orogens created tectonic (or supracrustal) loads, which caused isostatic subsidence and facilitated the accumulation of sediments adjacent to the orogenic loads (Gresse, 1992).

The Damara Orogen represents a triple junction point where the Gariep and Damara Belts converged (Frimmel et al., 2002). The latter consists of two smaller belts: the Kaoko and the Khomas belt. These resulted from the collision between the Congo, Kalahari and South American Cratons during the closure of the Khomas Sea and Adamastor Ocean (Figure 2.2). The first tectonic event of the Damara Orogen was the Katangan event (650 Ma – Figure 2.2A), which preceded the deposition of the Nama and Vanrhynsdorp Groups (Gresse, 1992). The closure of the Khomas Sea is represented by syn-tectonic granites that formed ca. 650 – 550 Ma ago and post-tectonic granites that formed ca. 500 Ma in the Damara Belt (Kröner, 1982; Miller, 1983; Jung, 2000; Johnson et al., 2006). Deposition of the lower Nama Group and possibly the Vanrhynsdorp Group began ca. 550 Ma ago (Gresse, 1992; Grotzinger et al., 1995).

Gresse (1992) attributed the style of folding in the region to simple shearing and detachment folding along the basal gneiss. Due to the ongoing subduction, the basin sediments experienced compressional forces during the amalgamation of southwestern Gondwana and the closing of the Adamastor Sea during the Pan-African orogenic cycle (Figure 2.2). This resulted in a northeasterly verging, low grade thrust fold belt with intermediate pressures experienced comparable to the Otago/Sanbagawa zone. After the formation of the NFB (Figures 2.2B-C), deformation of the foreland basin occurred during late transpression of the Gariep Orogeny (Figure 2.2D). The amalgamation of SW Gondwana was only completed by the Late Cambrian and/or Early Ordovician as supported by geochronological studies in the Pan African Belt in southern Africa and Brasiliano Belt in South America (Jung et al., 2000; Goscombe et al., 2007; Gaucher et al., 2008). The style of deformation in the Vanrhynsdorp Group in South Africa is similar to the Kuibis Subgroup of the Nama Group in the Naukluft area in Namibia; however, there is an increasing trend in the metamorphic temperatures experienced over the area (Gresse, 1992). Due to an increasing metamorphic gradient from northwest to southeast, deformation is more intense to the south and east of Vanrhynsdorp. Consequently, the study localities of this project were situated in the

northwest; ~100 km north of Vanrhynsdorp, where the deformation is mild and the stratigraphic contacts are better preserved (Figure 2.3).

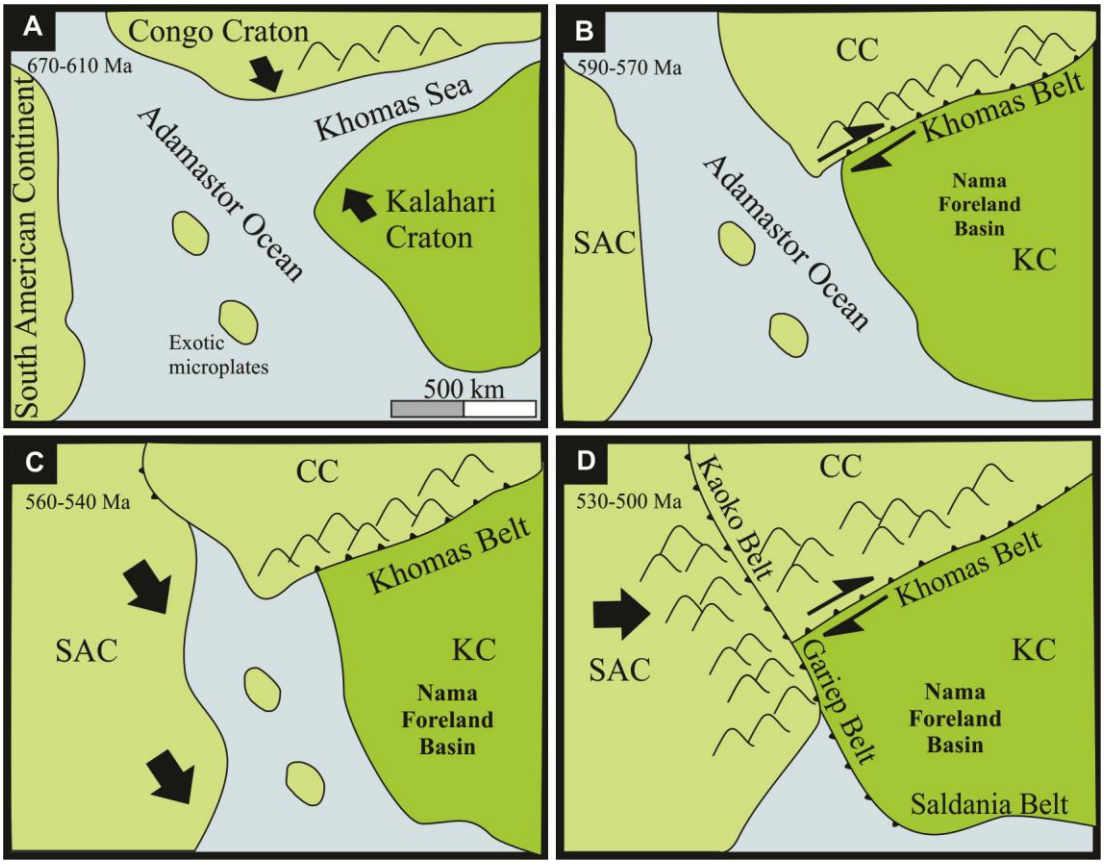

Figure 2.2. Tectonic evolution of northwestern South Africa and southern Namibia during the formation of the Nama Foreland Basin. Note that the Damara Belt is divided into the Khomas and Kaoko Belts. Abbreviations: Congo Craton (CC), Kalahari Craton (KC) and South American Continent (SAC) (modified after Germs, 1995). A) Closure of the Khomas Sea between the converging Congo and Kalahari Cratons between 670-610 Ma and the formation of the Khomas Belt. B-C) Closure of the Adamastor Ocean and the formation of the Nama Foreland Basin between 590-540 Ma. D) Amalgamation of SW Gondwana and the formation of the Gariep Orogeny.

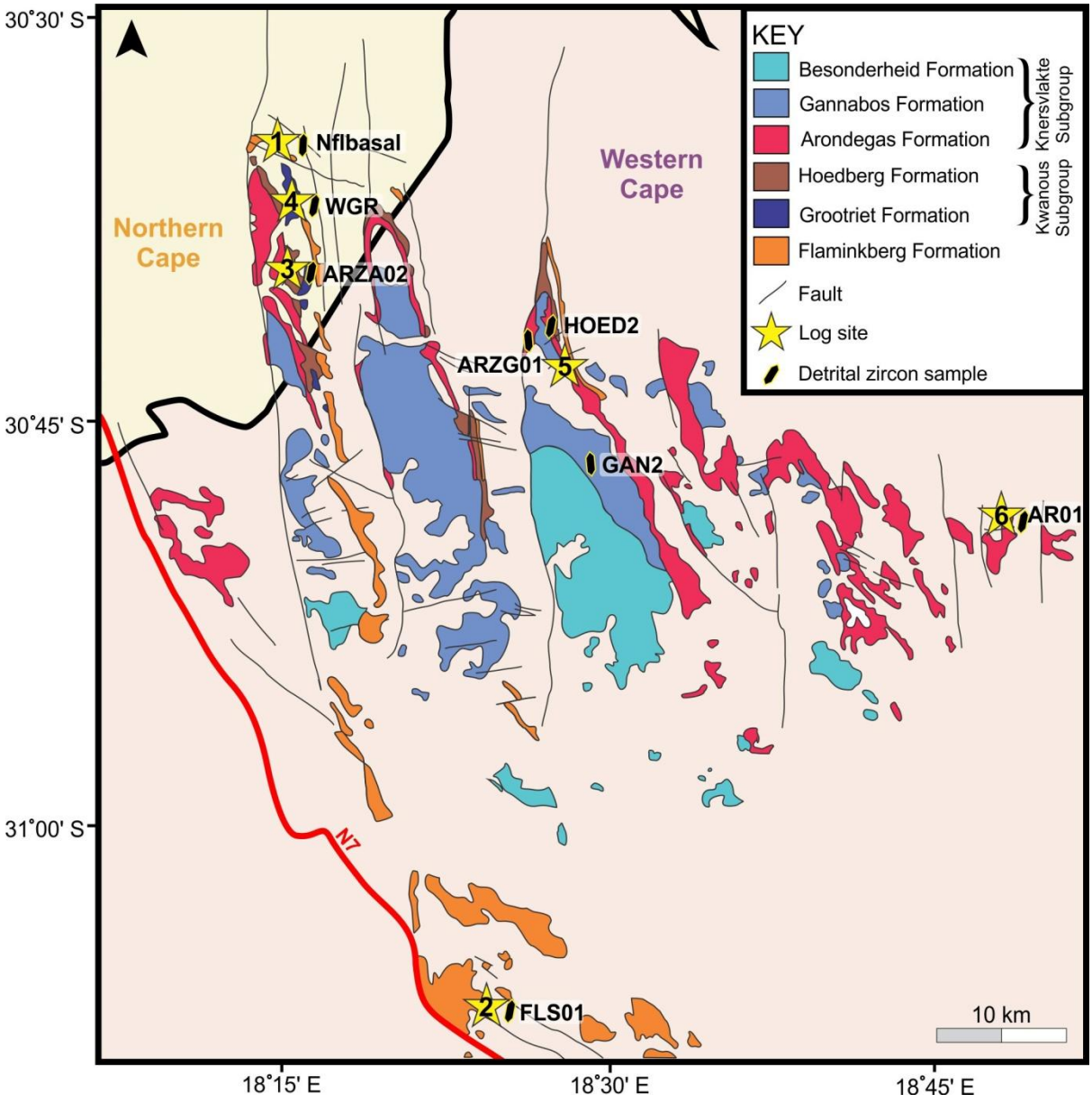

Figure 2.3. Simplified geological map of the study area showing the key structural features in the lower Vanrhynsdorp Group and the location of the six log sites (numbered stars) and detrital zircon samples.

2.2 Lithology

The predominantly siliciclastic Vanrhynsdorp Group comprises shale and mudstone (40%) and sandstone with minor conglomerate units (60%) (Table 1.1; Gresse, 1992). Although the succession is considered to be stratigraphically equivalent to the Nama Group, because of its overall unique lithological character, the succession is classified as a separate group and subdivided into three subgroups of regional extent: the Kwanous, Knersvlakte and Brandkop Subgroups with the basal Flaminkberg Formation separate to the subgroups (Table 1.1; Germs et al., 2009). The Kwanous Subgroup is unconformably overlain by the Knersvlakte Subgroup which is in turn unconformably overlain by the Brandkop Subgroup (Gresse, 1992; Germs et al., 2009). The basal Flaminkberg

Formation to the lower Knersvlakte Subgroup is the focus of the study because it is thought that the Ediacaran-Cambrian boundary occurs within the lower formations. These formations will be investigated in detail and this section serves as a brief introduction to the lower Vanrhynsdorp Group (Table 2.1).

2.2.1 Lithology of the lower Vanrhynsdorp Group

Overall, the succession shows an upward increase in immaturity and a change in colour from greenish-gray rocks in the Kwanous and Knersvlakte Subgroups to reddish rocks in the Brandkop Subgroup (Table 1.1; Germs et al., 2009). Similar to the Nama Group, a change in the depositional slope and overall sediment source areas is also shown by the regional palaeocurrent patterns throughout the succession which suggest that the sediments were supplied initially from the east (i.e., Kalahari Craton) and then from the west (i.e., Gariep Belt) with broad oscillations throughout the formations (Figure 2.4; Gresse, 1992).

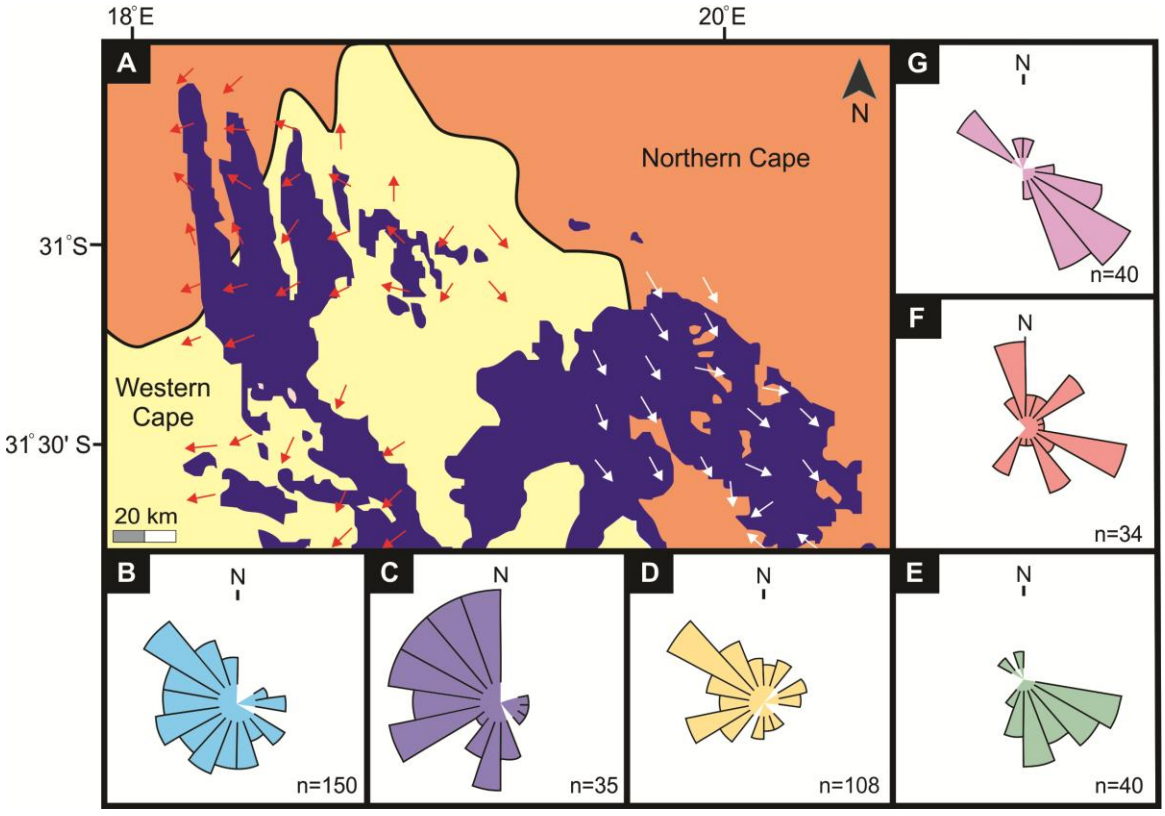

Figure 2.4. Palaeocurrent directions of the Vanrhynsdorp Group. A) Average cross-bedding current direction throughout the Vanrhynsdorp Group. Orange arrows summarise the Flaminkberg and Arondegas Formations data. White arrows summarise the Dolkraals, Astynskloof and Klipbak Formations. B – G: Rose diagrams of palaeocurrent measurements from cross-bedding unless otherwise stated. B) Flaminkberg Formation. C) Arondegas Formation. D) Current measurements using pebble imbrication in the Besonderheid Formation. E) Dolkraals Formation. F) Astynskloof Formation. G) Klipbak Formation (modified after Gresse, 1992).

Flaminkberg Formation

The Flaminkberg Formation (Figure 2.3; Table 2.1) is the basal, 70 m thick unit of the Vanrhynsdorp Group with outcrops in the Western and Northern Capes from Lutzville in the southeast to Kliprand in the north. It unconformably overlies the basal gneiss of the Namaqua Belt and older metasediments of the Gariep Supergroup (Germs et al., 2009). As the overlying Kwanous Subgroup has limited regional extent and pinches out compared to the Flaminkberg Formation, the Flaminkberg Formation is considered separate from the overlying subgroups. The Formation comprises medium to thick beds (av. 20–40 cm), graded, coarse- to very coarse-grained sandstone beds, which are occasionally interbedded with shales, thin conglomerate layers and medium-grained sandstones. Due to regional metamorphism, the sandstones were largely recrystallised into a quartzite, and lost most of their primary sedimentary structures, especially in the south. Furthermore, the interbedded shale is crenulated and sheared into a sericite schist. Palaeocurrent data, especially from cross-bedding, which is common in the north and increases in abundance upward within the unit, indicate south-easterly and westerly current directions with a minor south-easterly component in the northeast (Figure 2.4; Gresse, 1992). The Formation was deposited on a coastal alluvial braided plain that progrades into a shallow marine environment in the south (Gresse, 1992; Gresse and Germs, 1993; Germs et al., 2009).

Kwanous Subgroup

The Kwanous Subgroup is ~620 m thick and restricted to the trough areas of the synclines in the northwest outcrops of the Vanrhynsdorp Group, north of Bitterfontein (Figure 2.3; Gresse, 1992). The subgroup consists of the Grootriet and Hoedberg Formations (Table 2.1), which thin to the south and wedge out between the basal Flaminkberg Formation and the overlying Arondegas Formation.

Grootriet Formation

The Grootriet Formation (Figure 2.3; Table 2.1) is 460 m thick limestone that is interbedded with subordinate siliciclastic layers. The unit is very poorly exposed in outcrops to the east of Garies in a ~10-15 km wide strip along the northern margin of the Vanrhynsdorp Basin (Gresse and Germs, 1993). The cross-bedding, brecciation, horizontal layering, oncolites in the limestone suggest that the formation was probably deposited in an oolite barrier to shallow lagoonal environment (Gresse, 1992).

Hoedberg Formation

The Hoedberg Formation (Figure 2.3; Table 2.1) is 160 m thick and comprises dark, bluish grey green shale that has intercalated limestone layers, lenses and nodules with calcareous seams from 1 cm to 10 cm (Gresse, 1992). Limestone layers are more common in the lower part. Nodules and lenses occur in the middle of the unit with the lenses being more prevalent towards its upper part. Rare

trace fossils and pyrite pseudomorphs are also present locally (Gresse, 1992; Almond et al., 2009). Sedimentary structures (e.g., asymmetrical ripples, soft sediment deformation) are rare and coupled with the laminated bedding indicate a quiet, low energy palaeoenvironment (Gresse, 1992; Almond et al., 2009). It was subsequently deposited in a near-shore environment but occurrence of wavy lamination and lenticular carbonate clasts in the upper part, suggests an upward gradation into a transitional environment (Gresse, 1992; Buatois et al., 2009).

Lower Knersvlakte Subgroup

Arondegas Formation

The Arondegas Formation (Figure 2.3; Table 2.1) thins rapidly from 90 m in the northwest to 50 m in the south, and thus shows a lateral thickness trends that is similar to the southward pinching out of the underlying Kwanous Subgroup (Gresse, 1992). The Arondegas Formation is dominated by white, grey to pinkish coarse- to very coarse-grained sandstones that are immature and feldspathic (feldspar content 6–34%; Gresse, 1992). Palaeocurrent data, predominantly from cross-bedding, indicate a range of westerly current directions with a minor south-easterly component (Figure 2.4; Gresse, 1992). Overall, the formation rarely preserves any sedimentary structures; however it has been interpreted as an alluvial fan environment by Gresse (1992).

Gannabos Formation

The Gannabos Formation (Figure 2.3; Table 2.1) is 400 m thick and is characterised by rhythmically bedded green shale and siltstone with sheet-like bed geometries. Sedimentary structures are very rare and reinforce the low energy environment suggested by the grain sizes (Gresse, 1992). There are very few erosive features (e.g., flute casts) indicative of occasional high energy events in the prevailing calm palaeoenvironment. However, an upward-thickening and coarsening trend is present in its upper part, where soft sediment deformation structures indicative of rapid sedimentation rates, become abundant. Various marine settings have been suggested for the formation, from wave dominated shallow marine, off-shore marine storm influenced settings to distal turbiditic deposits (Gresse, 1992; Almond et al., 2009).

Besonderheid Formation

The Besonderheid Formation (Figure 2.3; Table 2.1) is 450 m thick and is dominated by brown to green medium to fine-grained, massive sandstones (Gresse, 1992; Germs et al., 2009). The sandstone beds are dominantly tabular. Channel-fill shaped units are especially prevalent in the subordinate conglomerates in its basal part. Palaeocurrent data, from pebble imbrication, indicate strong northwesterly and southwesterly current directions (Figure 2.4; Gresse, 1992). In comparison to the underlying formations, the Besonderheid Formation has a variety of sedimentary structures including ripple marks, ripple cross-lamination, overturned ripples, micro-ripples, repetitive

mudstone-sandstones couplets, and soft sediment deformation structures (i.e., dewatering structures). Overall, the formation shows an upward-fining grain size trend into the above formations (Gresse, 1992; Germs et al., 2009). The Besonderheid Formation accumulated on a continental slope/basin plain with turbidite events (Gresse, 1992; Gresse and Germs, 1993). Buatois et al., (2009) contradicts this depositional environment by suggesting it was deposited in a delta front to prodelta environment.

Table 2.1. Key lithological characters of the lower Vanrhynsdorp Group (source: Gresse, 1992; Almond et al., 2009; Buatois et al., 2013).

Properties	Flaminkberg Formation	Grootriet Formation	Hoedberg Formation	Arondegas Formation	Gannabos Formation	Besonderheid Formation
Thickness (m)	70	460	160	90 - 100	400	450
Lithology	Blue, white and red sandstone or quartzite with intermittently interbedded shale and gritstones to small pebble conglomerates Sharp, planar bedding surfaces with channel beds.	Black limestone and interbedded shale.	Dark, bluish-greenish shale with carbonate nodules and lenses (~5 cm thick). Lenses become more prevalent in the upper section.	White, grey to pink beds of conglomerate, arkose, subarkose, sandstone and quartzite beds. Beds between 20 cm to 3 m thick, vary from coarse- to very coarse-grained.	Rhythmically bedded green shale and siltstone with minor chert and sandstone (~10-30 cm thick). White limestone horizons, 10–100 cm thick, only above the contact with the Arondegas Formation.	Basal polymictic conglomerate channel lags grade into sandstone and green shales Sharp and planar bedding surfaces. Conglomerate beds 20 cm – 3 m thick, with poorly sorted, rounded to well rounded, predominantly metamorphic clasts that range in size from granule to boulder. Sandstone beds ~10 cm – 1 m thick, vary in grain size from very fine to very coarse.
Sedimentary structures	Massive, planar and minor trough cross-bedding in sandstones. Lamination in interbedded shales.	Oolitic limestone, cross-laminated limestone, pisolithic limestone, brecciation.	Lamination, asymmetrical ripples, flaser bedding, soft sediment deformation.	Massive, planar and trough cross-bedding, ripple cross-lamination, flute casts.	Ripple cross-lamination, ripple marks, cross-bedding, flute casts, soft sediment deformation including slump structures.	Massive beds, cross-bedding, ripple cross-lamination, ripple marks, sole marks (flute casts, grooves) .
Palaeocurrent	Southwesterly - westerly direction, however in the Nuwerus region and extreme northwest, it changes to south – southeasterly.	NA	NA	Southwesterly to southeasterly direction, with a northwesterly component in the Tafelberg region (north).	Broad southerly direction. Results derived from asymmetrical ripples.	North-easterly direction with some south-easterly and north-westerly components in the northwest and southeast region, respectively. Results derived from pebble imbrication and foreset orientation measurements.
Main fossil types	NA	Microbial binding of fine-grained carbonates (oncolites).	Horizontal burrows of *Helminthopsis* ichnoguild, microbial mat textures.	Horizontal burrows of *Helminthopsis* ichnoguild.	Large 1–2.3 cm wide *Planolites*–like burrows.	*Oldhamia geniculata*
Boundaries	Upper – conformable. Lower – erosional, nonconformity.	Upper – gradational, conformable. Lower – conformable.	Upper – varies from gradational and erosional. Lower – gradational, conformable.	Upper – gradational, conformable. Lower – gradational, conformable to erosional. Kwanous Subgroup pinches out and Arondegas Group in contact with basement.	Upper – regionally conformable but abrupt, erosional contacts where in contact with channel lags of the overlying unit. Lower – gradational, conformable	Upper – gradational. Lower – regionally conformable but abrupt, erosional contacts where it commences with channel lags.
Genesis	Coastal braided fluvial plain.	Oolite barrier to shallow lagoonal environment.	Oolite barrier to near shore lagoon or shelf.	Alluvial fan or delta front to prodelta.	Basin plain and distal turbidites or wave-dominated shallow marine.	Turbidites on basinal plain or delta front to prodelta.

2.2.2 Correlation of the Vanrhynsdorp with the Nama Group

The Nama Group is subdivided into the Kuibis, Schwarzrand and Fish River Subgroup (Table 2.2; Germs, 1983). The siliciclastic rocks of the Kuibis Subgroup are generally white and quartz-rich whereas the overlying Schwarzrand Subgroup have a lower quartz content and greenish in colour. The Fish River Subgroup are reddish and have a high feldspar content which indicates that the maturity of the sediments increases with age (Germs et al., 2009; Blanco et al., 2011). There are major unconformities at the base of the Nama Group as well as within the succession, namely below the Nomtsas Formation and below the Fish River Subgroup (Saylor et al., 1995; Blanco et al., 2011). Volcanic ash beds occur within the Schwarzrand Subgroup and U-Pb dating has constrained the deposition of the Kuibis and Schwarzrand Subgroups between 539–550 Ma (Table 2.2; Grotzinger et al., 1995). Additionally, $^{40}K/^{40}Ar$ and $^{40}Ar/^{39}Ar$ cooling dates of detrital muscovite in the sandstones correspond to the Damara and Gariep metamorphic ages (Horstmann et al., 1992; Gresse, 1992). The prolific fossil record within the Nama Group further aids its age constraints. The lower Nama Group contains Ediacaran fossils, organic-walled microfossils and shelly fossils (section 2.3; Germs et al., 2009; Blanco et al., 2011). The upper Nama Group (from the Nomtsas Formation) is Cambrian in age as indicated by the trace fossils *Treptichnus pedum* and *Dipltichnites* (Germs et al., 2009).

The general lack of absolute dates, distinct lithostratigraphic markers and paucity of fossils in the Vanrhynsdorp Group hinder direct correlation with the Nama Group, which contains not only fossils, but also several dated tuffaceous horizons as mentioned above. Differences in diagnostic lithological characters which suggest that the Vanrhynsdorp Group was deposited in a slightly deeper-water setting than the Nama Group, further sets the two units apart (Germs and Gresse, 1991; Gresse, 1992; Gresse and Germs, 1993; Germs et al., 2009). Although the two groups are lithologically dissimilar, broad trends that aid correlation have been recognized. For example, the lower Flaminkberg Formation vaguely resembles the Dabis Formation of the Kuibis Subgroup in the Nama Group at Vioolsdrif, Steinkop and Springbok (Table 2.2). Germs and Gresse (1991) suggested that the units between the upper Flaminkberg Formation and Klipbak Formation correlate to the Schwarzrand Subgroup of the Nama Group. The Grootriet Formation contains the only limestones in the Vanrhynsdorp Group that resemble limestones of the Nama Group in the Mooifontein and Huns Members. Furthermore, the conglomerates in the Van Zylkop Formation of the upper Vanrhynsdorp Group resemble the conglomerates of Nomtsas and possibly Vergesig Formations. Finally, the typical fluvial strata in the Fish River Subgroup of the Nama Group have no equivalent in the Vanrhynsdorp Group, and it is assumed that the Fish River equivalent in the Vanrhynsdorp Group may have been eroded away.

Table 2.2. Tentative lithostratigraphic correlation of the Vanrhynsdorp and Nama Groups based on lithological similarities, which are more distinct for the units marked with coloured blocks (modified after Germs and Gresse, 1991, Gresse, 1992; Grotzinger et al., 1995; Grotzinger, 2000; Harrison, 2014; Germs et al., 2009). The dotted line represents the tentative correlation suggested by Germs and Gresse (1991) between the majority of the Vanrhynsdorp Group and Schwarzrand Subgroup.

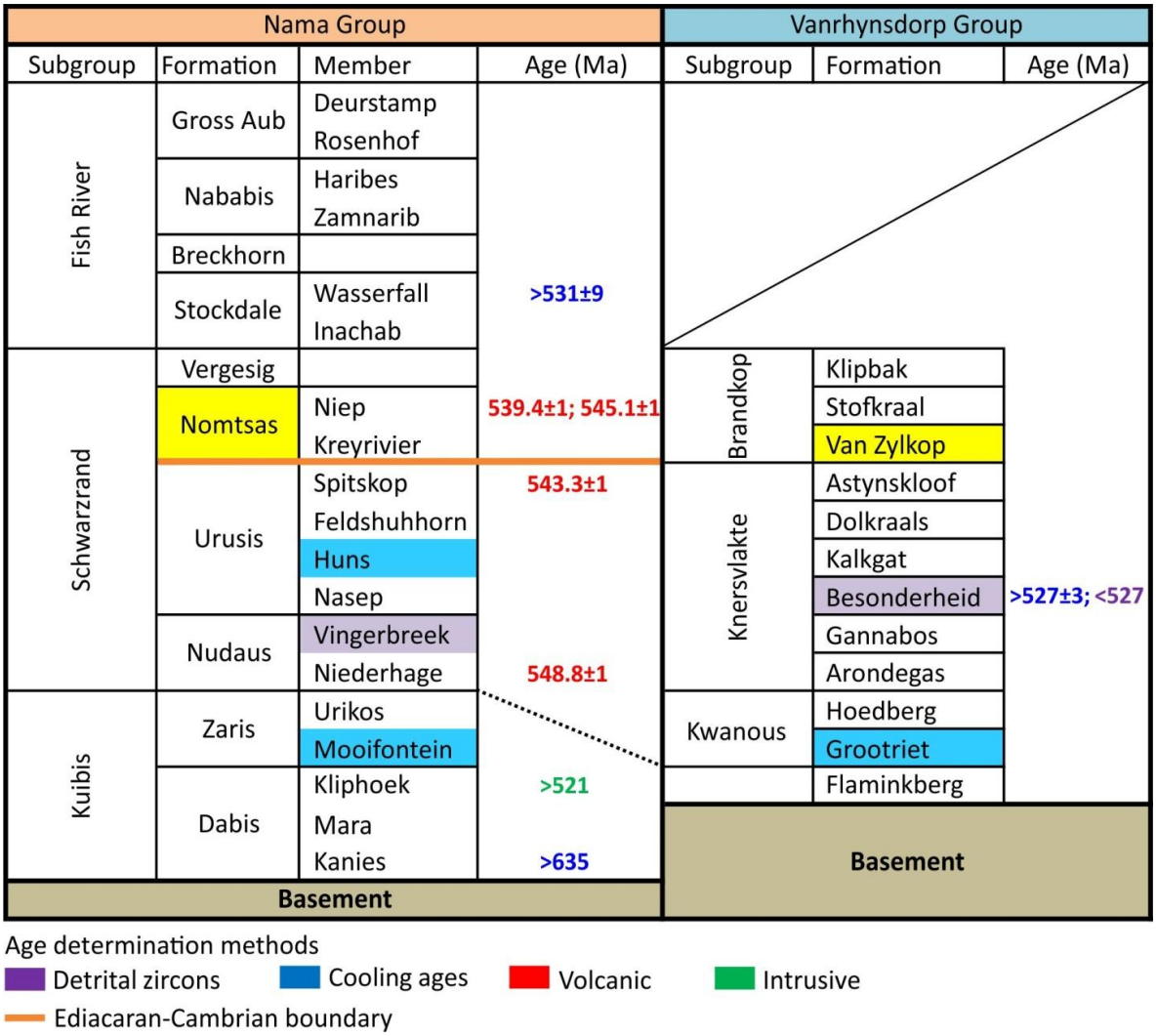

2.3 Palaeontology

2.3.1 Trace fossils of the Vanrhynsdorp Group

Precambrian trace fossils are very important, because they are rare windows into the ancient biosphere when the dominant organisms were soft-bodied and had low preservation potential. The earliest convincing evidence of animal activity is from the White Sea Assemblage (~ 560 Ma) (Buatois and Mángano, 2016). These bilaterally symmetrical trace fossils indicate that there were organisms in the environment that had the ability to penetrate and rework the sediment. These traces serve as proxies for infaunal metazoans indicating that the organisms had an advanced nervous and muscular system to allow for the locomotion and behaviour recorded (Almond et al., 2009). Trace fossils from the Ediacaran have a low ichnodiversity with only seven categories of architectural designs: 1) simple horizontal trails, 2) passively filled horizontal burrows, 3) actively filled (massive) horizontal burrows, 4) plug-shaped burrows, 5) oval-shaped impressions, 6) rasping traces, and 7) horizontal burrows with horizontal to vertical branches (Buatois and Mángano, 2016). It is important to note that microbial mats were vital in shaping Ediacaran ecosystems (Aceñolaza et al., 2009; Schiffbauer et al., 2016). Benthic communities (bottom dwellers) developed in direct association with microbial mats either as a source of food or tunnels mined underneath them. Throughout the Vanrhynsdorp Group, there is evidence of trace fossils and microbial mats co-occurring, especially within the fine-grained units (e.g., Hoedberg and Gannabos Formations).

The Vanrhynsdorp Group is emerging as a key study area for observing the development of ichnodiversity and ichnostratigraphy of infaunal metazoans across the Precambrian-Cambrian boundary through the high abundance and good preservation of the traces (Seilacher et al., 2005; Buatois et al., 2007; Almond et al., 2009). Generally, the infaunal traces are simple horizontal burrows that range in size from 0.5-2.3 cm in width (Figure 2.5). Their simple shape indicates that they were created by unspecialised organisms that produced indistinct horizontal patterns as they moved through the sediment (Seilacher et al., 2005; Aceñolaza et al., 2009). The high abundance of traces has also been used as an indication of favourable preservational conditions (e.g., lack of predators; Aceñolaza et al., 2009). Consequently, refining the age of the Vanrhynsdorp Group and locating the Ediacaran-Cambrian boundary has the potential to develop better age constraints on the tempo (i.e., sudden vs. protracted) of metazoan evolution in the Cambrian (Aceñolaza et al., 2009). The coarse basal Flaminkberg Formation has not yielded any convincing fossils; however, there is an increasing trend in the abundance of traces in the Vanrhynsdorp Group (Tables 1.1 and 2.1).

Kwanous Subgroup

The Grootriet Formation does not yield any definitive trace fossils however there is evidence for microbial binding of fine-grained carbonates (e.g., oncolites). The Hoedberg Formation contains the first occurrence of trace fossils within the Vanrhynsdorp Group in the form of narrow, straight to curved horizontal, unbranched burrows. These belong to the *Helminthopsis* ichnoguild and, as previously mentioned, they are associated with microbial mat textures (Figure 2.5A). The occurrence of these traces with microbial mat textures suggests that the organisms were exploiting the matgrounds. These unspecialised traces are typical of near shore and deeper water settings within the Ediacaran, although the age and more precise depositional setting of the Hoedberg Formation are still unclear.

Lower Knersvlakte Subgroup: Arondegas, Gannabos and Besonderheid Formations

Interestingly, the heterolithic Arondegas Formation may also contain well-preserved horizontal burrows of the *Helminthopsis* ichnoguild, although their exact stratigraphic position is unclear and these traces may occur within the upper Hoedberg Formation (Almond et al., 2009). The upper Gannabos Formation contains abundant horizontal burrows that are 1–2.3 cm wide. They are considered *Planolites*-like but have not been assigned a taxonomic group (Figure 2.5B) (Aceñolaza et al., 2009). The burrows have a distinctive sub-rectangular cross-section and preserve occasional meniscate back-fills. The burrows are gentle to tightly curving structures that frequently overlap, creating a meandering and foraging pattern, although they could potentially represent avoidance patterns. The Besonderheid Formation contains one of the most important traces in the succession, the Cambrian ichnogenus *Oldhamia* (Figure 2.5C). The specimens have been assigned to *O. geniculata* and they also co-occur with microbial textures. *O. geniculata* specimens exhibit complete, asymmetrical hair-pin loops which connect to curved, radiating burrows. This structure clearly shows the foraging behaviour of the organism through the repetitive forwards and backwards motion preserved in the burrow (Almond et al., 2009).

Upper Knersvlakte (Kalk Gat, Dolkraals and Astynskloof Formations) and Brandkop Subgroups

The upper Vanrhynsdorp Group is dominated by probe burrows of *Treptichnus* isp. and microbial textures (Figures 2.5D-E) (Almond et al., 2009). Priapulid worms, or an organism with a similar locomotion style, have been tentatively suggested as the trace makers for this feeding strategy (Jensen et al., 2006; Vannier et al., 2010). The structure of the subhorizontal burrows is variable throughout the formations due to preservational and morphological differences. The burrows range from linear to curved and from smooth, bilobed or trilobed. Thus, it is common for *Treptichnus pedum* to change between other *Treptichnus* species e.g., *T. triplex, T. tripleurum* within the same burrow systems (Seilacher, 2007; Almond et al., 2009; Wilson et al., 2012; Buatois

et al., 2013). *Curvolithus-, Saerichnites-, Arthrophycus*- and *Cruziana*-like morphotypes also occur in the upper Vanrhynsdorp Group (Almond et al., 2009).

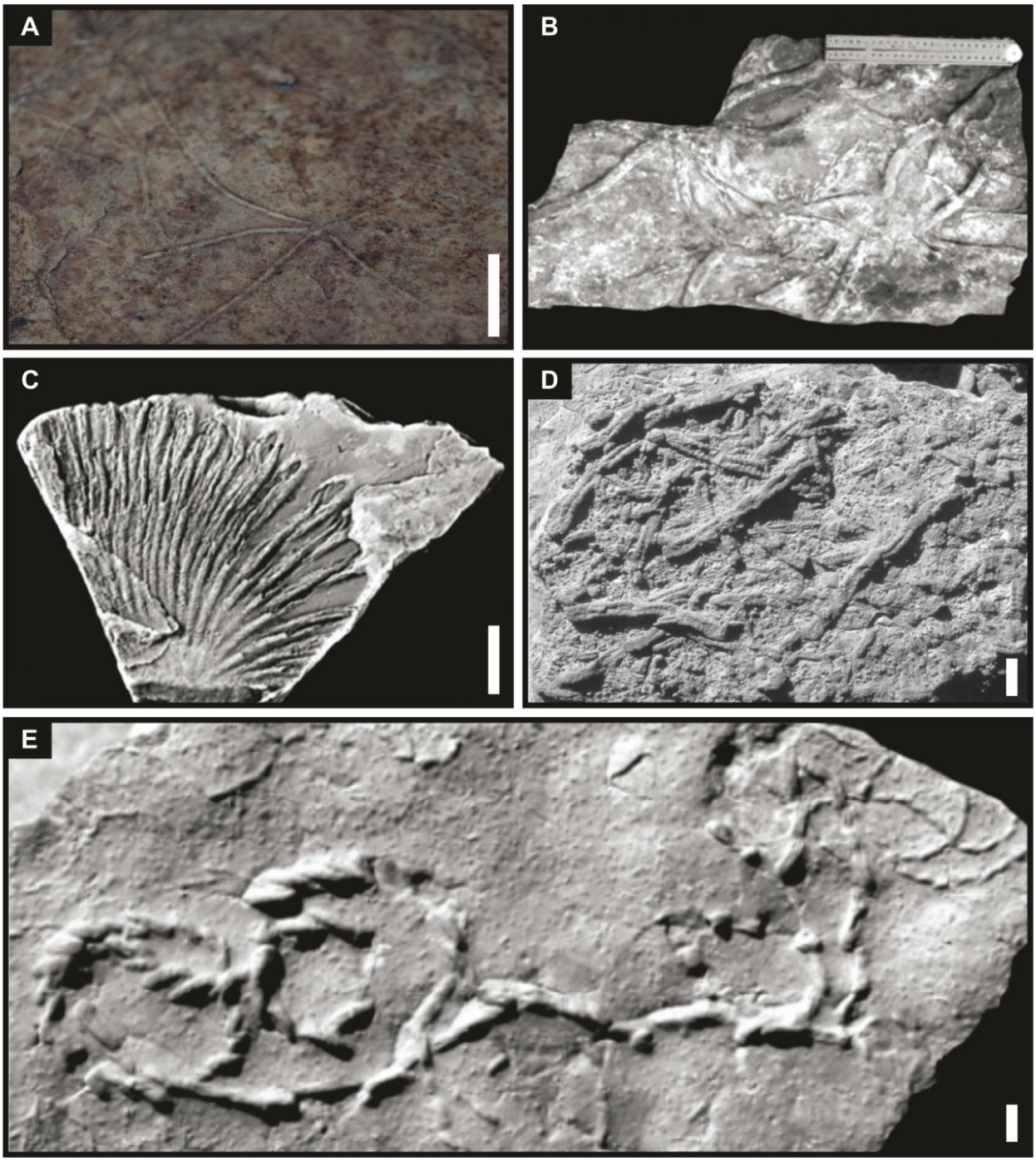

Figure 2.5. Trace fossils in the Vanrhynsdorp Group. A) *Helminthopsis* ichnoguild, Hoedberg Formation. B) *Planolites* isp., Gannabos Formation. C) *Oldhamia geuiculata,* Besonderheid Formation. D) Treptichnids, Knersvlakte Subgroup. E) *Treptichnus pedum,* Kalkgat Formation. White scale bar = 1 cm. Image sources: B, C and E from Aceñolaza et al., 2010; D from Almond et al., 2009.

Position of the Ediacaran-Cambrian boundary

Trace fossils are of utmost importance within the Vanrhynsdorp Group, because to date, they are the only age indicators within the succession. There are several lines of evidence used to suggest that the Ediacaran-Cambrian boundary occurs at the contact between the Gannabos and Besonderheid Formations (Gresse et al., 2006; Almond et al., 2009). In addition to being useful in locating the lower boundary of the Cambrian within the Vanrhynsdorp Group, these traces can reveal the evolution of complex behavioural patterns of invertebrates across the Ediacaran-Cambrian boundary (Almond and Pether, 2009).

The occurrence of the index ichnofossil *Oldhamia geniculata* in the Besonderheid Formation suggests an early Cambrian age for this unit (Tables 1, 2; Figure 2.5B) (Seilacher et al., 2005; Herbosh and Verniers, 2011). *O. geniculata* is also found in the early Cambrian formations of Argentina which were deposited in palaeogeographical proximity during the closure of the NFB (Figure 2.3) (Seilacher et al., 2003). While *O. geniculata* was exclusively found in the southern outcrops of the Besonderheid Formation, the Cambrian ichnofossil *T. pedum* is more common and reoccurs throughout the overlying formations.

The first appearance of *T. pedum* was chosen as the location of the base of the Cambrian at the Ediacaran-Cambrian Global Stratotype Section and Point (GSSP) at Fortune Head, Newfoundland, Canada (Narbonne et al., 1987; Landing, 1994; Mcilroy and Brasier, 2016). This ichnofossil is regarded not only as an index fossil for the Ediacaran-Cambrian boundary, but also as the earliest widespread complex trace fossil in the global palaeontological record (Seilacher et al., 2005). Recently, *T. pedum* has fallen under scrutiny as a reliable biostratigraphic marker because it has been discovered in association with Ediacaran fossil assemblages, below the GSSP at Fortune Head (Gehling et al., 2001; Buatois et al., 2013). Other treptichnids (subhorizontal burrows) co-occur with the upper Ediacaran body fossil *Cloudina* in Namibia and Iberia, which further reduces its reliability in the Vanrhynsdorp Group, where *T. pedum* co-occurs with other treptichnids (Jensen et al., 2000; Jensen, 2003). Fortunately, the position of the boundary is not based solely on the appearance *T. pedum* but is supported by the occurrence of *O. geniculata* in the Besonderheid Formation. The upper successions may further be constrained by the conspicuous absence of definitive arthropod burrows (e.g., *Rusophycus* and *Cruziana*). Despite the limited value of negative evidence, the absence of such fossils has been used to imply that arthropods had not yet evolved in the environment and may signify an earliest Cambrian age for the upper Vanrhynsdorp Group (Buatois et al., 2007; Almond et al., 2009). Additionally, the Gannabos Formation is considered Ediacaran in age due to the absence of *T. pedum* probe burrows that characterised early Cambrian shelfs and is prolific in the upper formations. To date, no further evidence has been found in the Gannabos Formation to confirm its Ediacaran age, so

it is possible that the formation was deposited during the Cambrian. It is important to resolve the age of the Gannabos Formation, because if it is indeed Ediacaran, its burrows would be evidence of large infaunal organisms (<2 cm in diameter) that lived in the substrate before the end of the Precambrian which has global biological significance.

2.3.2 Organic-walled microfossils: Acritarchs

Microfossils are very small remains of organisms that range from less than one micron (<1 µm) to one millimetre (1mm) in size and require magnification for study. Consequently, micropalaeontology comprises a heterogeneous array of taxonomic groups unlike the disciplines of plant, invertebrate and vertebrate palaeontology. Organic-walled microfossils have a non-mineralised, carbonaceous vesicle wall which is comprised of recalcitrant, sporopollenin-like biopolymers which render the fossils acid-resistant. They are generally fossils of either prokaryotes or eukaryotes, or their biosedimentary signatures (e.g., stromatolites) (Mendelson and Schopf, 1992; Brasier, 2012; Ward and Kirschvink, 2015). Acritarchs are an enigmatic, diverse group of primarily marine microfossils which are thought to represent the resting cysts of phytoplanktonic eukaryotic algae of an unknown biological affinity. The word 'Acritarcha' was invented by the US palaeontologist William Evitt in 1963 and it is derived from the Greek words *achritos* and *arché,* meaning 'uncertain' and 'origin'. The taxon served as a collective group for fossils and modern organisms that although they looked similar to existing taxon, were still difficult to classify and were placed into the group including phytoplankton, early protists and animal egg cases (Agić, 2016). The name Acritarcha is slowly becoming obsolete as the taxa are being re-classified into known groups of microorganisms.

Although their origin is uncertain, acritarchs are long ranging and are useful in biostratigraphic studies. The oldest definitive acritarchs have been found in Palaeoproterozoic shales from North China (Lamb et al., 2009; Peng et al., 2009) however, Javaux et al., (2010) reported potential acritarchs from the 3.2-billion-year-old Moodies Group of South Africa. This suggests that acritarchs are almost twice as old as previously thought (Buick, 2010). Acritarchs are especially useful in the Neoproterozoic through to the Permian, with an increase in abundance and diversity occurring at the base of the Cambrian (Huntley et al., 2006; Moczydlowska, 2011). However, their abundance decreases from the Devonian thus limiting their stratigraphic utility in post-Devonian successions.

The discovery of acritarchs within the Vanrhynsdorp Group has the potential to further constrain the location of the Ediacaran-Cambrian using the subsequent Ediacaran and Cambrian assemblage zones. Additionally, the discovery of microfossils could further aid the correlation of the Vanrhynsdorp Group across the basin and into SW Gondwana.

2.3.2.1 Acritarch taxonomy

Acritarchs are classified based on their defining morphological characteristics (Lister, 1970; Fensome et al., 1990). They are composed of a round or elongate organic vesicle that is between 20–150 µm in diameter. Some species may have ornamentation (spines) or sculptures (patterns on the vesicle wall) that further aid classification (Palacios, 2015). Furthermore, possible biological uses for ornamentation have been suggested that may also provide insight into the palaeoenvironment such as spines for buoyancy throughout the water column (Willman, 2009). However, due to the limited understanding of their taxonomy, biological affinity and rarity in modern environments, this reduces their usefulness in palaeoecological interpretations. Most acritarchs are marine, however the lagoonal facies are characterised by a low diversity and monospecific assemblage of sphaeromorph (unornamented) acritarchs and prasinophytes, which may complicate the palaeoenvironmental interpretation in old rocks if there are no other palaeoenvironmental indicators (Palacios, 2015; Agić, 2016).

There are three main acritarchs morphotypes from the Proterozoic to early Cambrian (Javaux, 2011; Agić, 2016): 1) sphaeromorphs (unornamented); 2) acanthomorphs (possessing processes or spines); and 3) dispharomorphs (sphere-in-sphere) (Figure 2.6). The most common morphotypes encountered in the Precambrian fossil record are sphaeromorphs and acanthomorphs (Agić, 2016). Sphaeromorphs are the oldest acritarchs group (1.8 billion years old) and they may be smooth (Leiosphaerids group) or have sculptures such as meshwork, pores, corrugation. Acanthomorphs first appeared 1.6 billion years ago and they have spiny protrusions (processes) on their surface, which may vary in size, shape and distribution across the surface. As previously mentioned, there is some ambiguity regarding the purpose of the processes. Three functions have been suggested: 1) the hair-like spines may have increased buoyancy and helped the organism remain in the photic zone; 2) during the reproduction phase of living unicellular algae (dinoflagellates, chlorophytes), the cell contracts and produces a thick outer layer which creates spiny protrusions from the surface; and, 3) spiny ornamentation occurs on resting-egg cases of living arthropods, which suggests that acritarchs may be the resting-egg stages of early animals (Fensome et al., 1990; Willman, 2009; Agić, 2016). Acanthomorphs remained rare until the Ediacaran Period where there was a diversification of large spine-bearing acanthomorphs. Disphaeromorphs have an outer membrane and appear as a sphere-in-sphere. There has been very little change in disphaeromorphs since the Mesoproterozoic and they have been linked to prasinophyte algae because of their morphological similarity to a phycoma (prasinophyte reproductive cyst). Prasinophytes are a related to green algae and are single-celled organisms with a single chloroplast and mitochondrion (Fensome et al., 1990; Willman, 2009). They are the smallest eukaryote as they can be <0.2 µm.

Excystments (opening/lid) or small internal bodies may be observed in some specimens but this is thought to relate to the reproductive phase when the gametes were released and has been seen to occur in both sphaeromorphs and acanthomorphs. Consequently, excystments are not species specific and do not aid in identification.

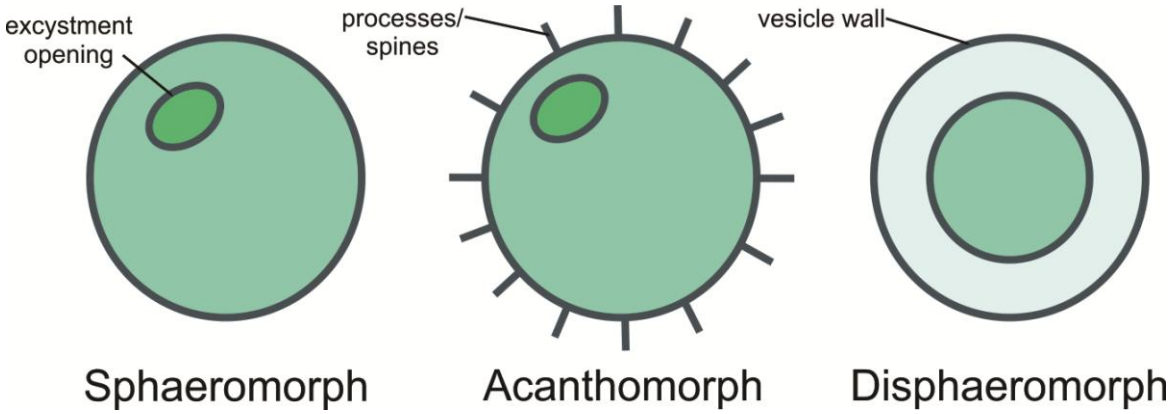

Figure 2.6. The three main morphotaxa of Precambrian acritarch microfossils.

2.3.2.2 Ediacaran – Early Cambrian acritarch assemblages

The Ediacaran Period can be divided into three acritarch assemblages linked to three major evolutionary phases: 1) early Ediacaran recovery; 2) middle Ediacaran expansion; and 3) the late Ediacaran crisis. This is then followed by the Cambrian acritarch radiation (Figure 2.7).

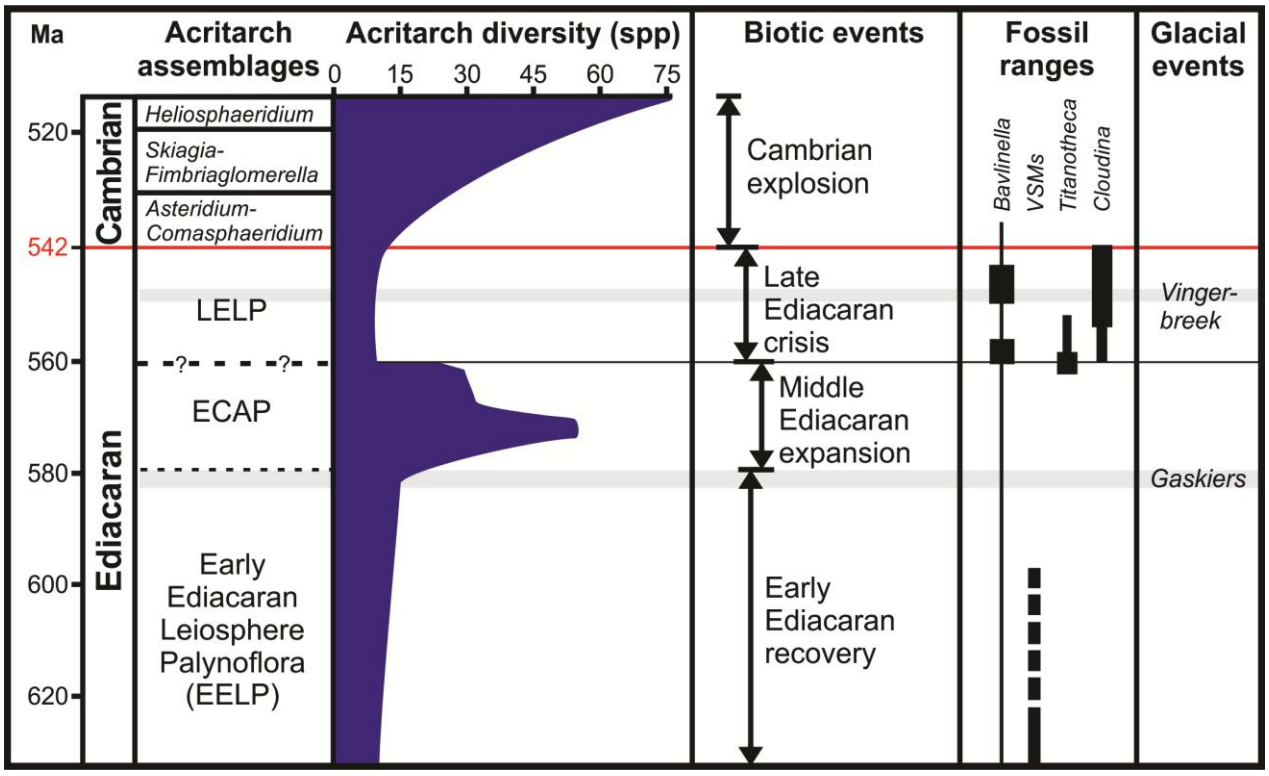

Figure 2.7. Ediacaran-Cambrian acritarch assemblages, global acritarch diversity and temporal ranges of potential index fossils (width of the bars indicate relative abundance and/or diversity). Biotic and glacial events are indicated as proposed driving forces for diversification. Acronyms - LELP: Late Ediacaran Leiosphere Palynoflora; ECAP: Ediacaran Complex Acanthomorph Palynoflora; VSMs: Vase-shaped microfossils (modified after Gaucher and Sprechmann, 2009).

Early Ediacaran recovery (635–580 Ma)

This assemblage is characterized by a low diversity of acritarch species. One of the sphaeromorph taxons, *Leiosphaeridia*, occurs with large leiosphaerids (>200 µm), which signifies the recovery of eukaryotic plankton from the late Cryogenian crisis from the pre-glacial eutrophication of the oceans. Consequently, the early Ediacaran assemblage is termed the Ediacaran Leiosphere Palynoflora (ELP) (Grey et al., 2005). This assemblage was first studied and named by Grey et al., (2003) and Grey (2005) from studies at the Ediacaran GSSP site in Australia. Gaucher and Sprechmann (2009) proposed a further subdivision of the ELP into early and late assemblages. The early ELP (EELP) contains various species of *Leiosphaeridia, Chuaria* and *Octoedryxium* with an absence of large acantomorphs (Grey, 2005; Gaucher and Sprechmann, 2009). In SW Gondwana, this assemblage zone has been reported in the Las Ventanas Formation of Uruguay and the Maieberg Formation of the Otavi Group, Namibia. A problem with the proposed subdivision of the ELP into early and late assemblages is that they are not taxonomically distinct and subsequently rely on the co-occurrence of skeletonised fossils to temporally constrain the assemblages (Gaucher and Sprechmann, 2009). The late ELP has been linked to the occurrence of *Cloudina, Namacalathus* and *Titanotheca.*

Middle Ediacaran expansion (580 – 560 Ma)

The middle Ediacaran expansion is characterized by an abundance and diversification of large acanthomorph acritarchs (200-500 µm). This assemblage is known as the Ediacaran Complex Acanthomorph Palynoflora (ECAP) and was first named after the Australian Ediacaran assemblages (Grey, 2005). The acanthomorphs are complex, diverse and larger than Cambrian species. Four different biozones within the ECAP have been proposed owing to over 70 species occurring in Australia: 1) *Appendisphaera barbata-Alicesphaeridium medusoidum-Gyalosphaeridium pulchrum* Assemblage Zone; 2) *Tanarium conoideum-Schizofusa risoria-Variomargosphaeridium litoschum* Assemblage Zone; 3) *Tanarium irregulare-Ceratosphaeridium glaberosum-Multifronspltaeridium peloriurn* Assemblage Zone; and 4) *Ceratosphaeridium mirabile-Distosphaera australica-Apodastoides verobturatus* Assemblage Zone (Grey et al., 2005; Gaucher and Sprechamnn, 2009). This assemblage is relatively short-lived (<20 my) compared to the EELP (>20 my) and to date, and has not been found in SW Gondwana successions.

Late Ediacaran crisis (560–542 Ma)

This is the youngest assemblage of the proposed subdivision of the ELP that co-occurs with skeletonised fossils termed the Late Ediacaran Leiosphere Palynoflora (LELP). Curiously, after the large diversity seen in the ECAP, the late Ediacaran is characterised by a loss of diversity and a dominance of sphaeromorph acritarchs. This loss in diversification has not been linked to any global glacial event, unlike the previous diversification events of the Neoproterozoic. Nearly all of

the complex acritarch species of the ECAP disappear, with less than 25% remaining (Vidal and Moczydlowska-Vidal, 1997; Knoll et al., 2006). The LELP is characterised by a low diversity assemblage consisting of: small (<150 µm) *Leiosphaerida* spp., *Chuaria, Bavlinella faveolata*, colonial microfossils of the S*oldadophycus* genus and small (<20 µm) acanthomorphs of the genus *Asteridium.* Importantly for this study, the LELP extensively occurs within SW Gondwana and is found in the lower Nama Group (Namibia; Germs et al., 1986), Holgat Formation of Port Nolloth Group (Namibia; Gaucher et al., 2005), the upper Cango Caves of the Gamtoos Group (South Africa; Gaucher and Germs, 2006) and the Arroyo del Soldado Group (Uruguay; Gaucher, 2000; Gaucher et al., 2004), amongst others.

Cambrian Acritarchs

From 542-470 Ma, there is an explosion and diversification of acritarchs. The rock record shows an increase from <10 to over 100 species from the lower to middle Cambrian (Gaucher and Sprechmann, 2009). This is followed by a second diversity explosion in the late Cambrian-Early Ordovician. The early Cambrian has been subdivided into four biozones based on the radiating taxa: 1) *Asteridium tornatum-Comasphaeridium velvetum* Assemblage Zone; 2) *Skiagia ornata-Fimbriaxlomerella membranacea* Assemblage Zone; 3) *Heliosphaeridium dissimilare-Skiagia ciliosa* Assemblage Zone; and 4) *Volkovia dentifera-Liepaina plana* Assemblage Zone. It is hypothesised that the Ediacaran sphaeromorphs developed processes as a defense mechanism against increasing planktonic predation and this resulted in the evolution of the Cambrian acanthomorphs (Butterfield, 1997).

3. Methodology

This study required both lab and field-based techniques, which combined qualitative and quantitative approaches. This was necessary to obtain a holistic interpretation of the formations and their role in the basin. Seven localities across the northern region of the map were visited (Figure 2.3). They are natural exposures in dry river beds, hillsides and valleys. Detailed sedimentological investigations and sampling occurred at these localities. The study of the outcrops allowed for the external and internal documentation of the formations under investigation and consequently, the reconstruction of their depositional settings.

3.1 Sedimentary facies analysis

Standard sedimentary facies analysis (sensu Miall, 1996) was used for interpreting sedimentary processes and their depositional settings. This method aids in the identification and interpretation of sedimentary rocks in the field and was pioneered in ancient fluvial environments since the 1970s (for a review see Miall, 1996). It hinges on the observation and the identification of physical and/or biological properties in the units (Dalrymple, 2010a). There are different ways to subdivide facies and this is dependent upon the purpose and time available in the project e.g. unit-by-unit facies analysis vs. a regional study where simple 'fluvial facies or marine facies' is adequate. This study involved unit-unit facies analysis at a detailed level. The basic steps in building a facies model are identifying the lithofacies as well as their facies associations, which are called architectural elements. These are genetically linked rock assemblages with distinctive 3D geometry and thus their identification does require a degree of interpretation as well as a reiterative analytical process (Colombera et al., 2013; Wilson et al., 2014). Once these diagnostic facies associations have been described, identified and their relative proportions have been at least estimated, the results can be compared to standardised facies models. This comparison also means accounting for potential differences that emerge between the analysed facies (and the architectural elements they build) and those predicted by the models in the literature. Only when these, again iterative, steps are concluded can the depositional environment be reconstructed for any study area or rock succession (Figure 3.1).

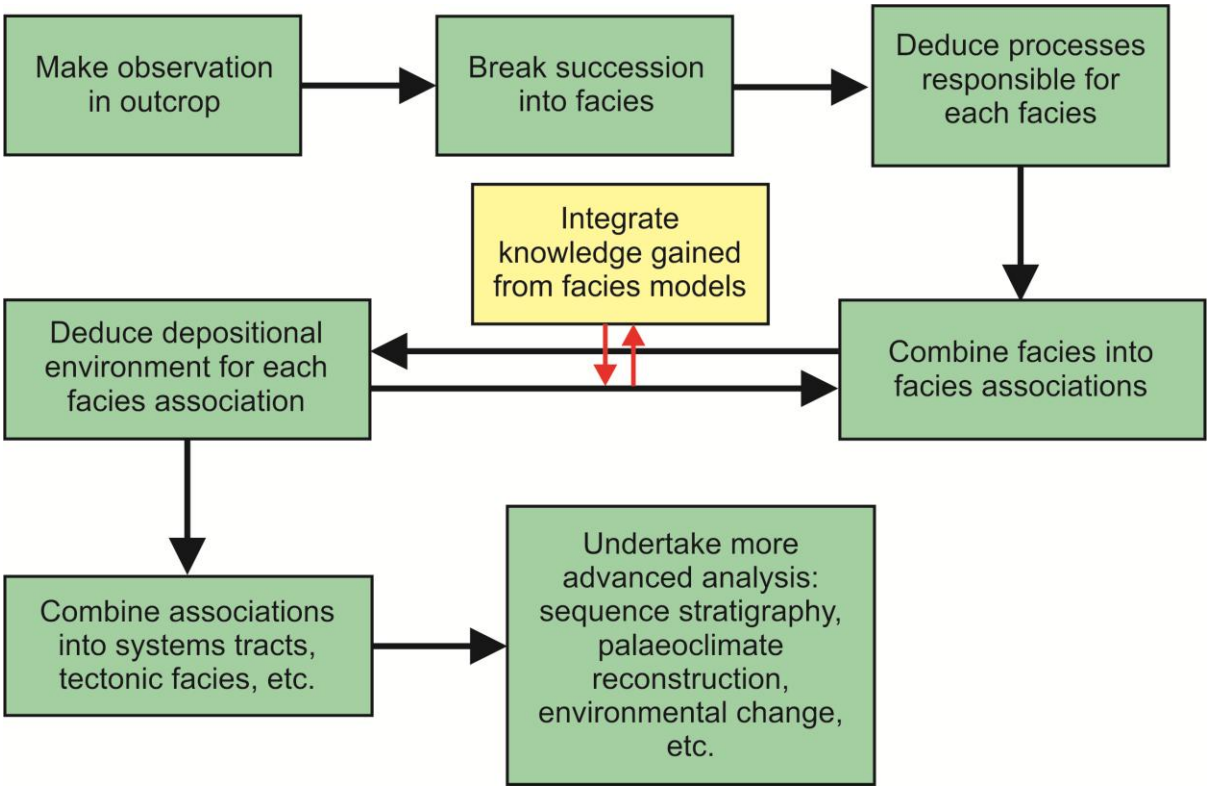

Figure 3.1 Flowchart showing the relationship between facies, facies associations and depositional settings (modified after Dalrymple, 2010a). The chart indicates the logical progression for interpreting depositional environments and the iterative steps involved, which is indicated here by arrows that point in opposing directions.

Facies refers to a distinctive sediment or rock unit that formed under certain conditions of sedimentation and reflects a particular depositional process that may or may not be characteristic of a single environment (Reading, 1978). Identification of the facies is a purely descriptive process that accounts for the diagnostic sedimentary properties of the bed e.g. rock lithologies, grain size, sedimentary structures, colours, bounding surfaces and shape of the units, etc. Miall (1977) suggested a simple classification scheme that uses a two-letter code system when recording observations and documentation. In this scheme, which is now a standard approach in clastic sedimentology, a multi letter facies code is assigned. In the code, the first letter stands for the dominant grain size of the sedimentary bed (G= gravel, S= sand, F= fines including very fine sand, silt and mud); the second letter characterises the fabric of the bed (e.g. m = massive; c = clast supported) and the last letter is for the sedimentary structures in the lithofacies (e.g. l = low angle cross-bedding; h = horizontal lamination; r = ripple cross-lamination). Sixteen unique lithofacies were identified in this study and shown in Table 3.1. The bed shape, colour, grain size, thickness, nature of the contacts and sedimentary structures were recorded together with facies codes for each bed. To aid the facies analysis, detailed sedimentary logs were generated at centimetre scale resolution for each formation. The logs were generated using the free multi-platform software, SedLog (available at: www.sedlog.com) and redrafted using CorelDRAW (available at: www.coreldraw.com). Lateral and

vertical distributions of the sedimentary strata were observed to analyse the sedimentary facies and enable comparison to the literature. Additionally, to record the field observations, photomosaics were generated and annotated using CorelDRAW X7. The photomosaics serves as the facies maps of the outcrops and allow for capturing the 3D facies relationships, which includes the bed geometries.

Individual lithofacies are not useful in determining the palaeoenvironment as each lithofacies can occur in multiple depositional settings. The key to interpreting the depositional environment is to analyse all the facies that occur together i.e. the facies association with distinctive 3D geometry or architectural elements (Miall, 1985; Dalrymple, 2010a). Architectural elements (AEs) were first defined and are mostly used in studies of fluvial sediments, and while the AE approach can be applied to other deposits, they are most useful in channelized environments (e.g., deltas, submarine fans) as this is where the most complicated bed geometries tend to occur (Dalrymple, 2010a).

The classification of facies associations (or AEs) is based on their lateral extent, bounding surfaces, internal geometry, scale, as well as organisation, abundance and combination of the sedimentary facies (Table 3.2). These aspects are studied through careful analysis of large outcrops and captured in photomosaics (outcrop facies maps). Because AEs are 3D depositional units, they exhibit a large degree of variability in adjacent outcrops, and this can make their identification difficult in outcrops that are not extensive and at right angle to one another. The recognition of AEs is aided by identifying and ranking their bounding surfaces, which is based on their lateral extent, erosional or accretionary features (Table 3.3). Following the identification of facies and AEs (i.e., the building blocks of facies models), the data is then compared to facies models and finally synthesised into a palaeoenvironmental interpretation of the formation during the time of deposition.

Table 3.1. Lithofacies codes and classifications used in this study. Modified after Miall (1978 and 2010).

Facies code	Facies description	Interpretation	Formation
Gmm1	Gravel, matrix-supported, massive gritstone. Poorly-sorted clasts (av. 0.2 cm) are quartz, quartzite, sandstone fragments and feldspar clasts.	Plastic debris flow (high strength, viscous) Mostly found at the base of new channel deposit cycles (i.e. basal gravel). Lack of internal structure indicates rapid flow speed reduction.	Flaminkberg (Figure 4.1)
Gmm2	Gravel, matrix-supported, massive conglomerate. Very poorly-sorted, pebble sized clasts (av. 1 cm) are quartz, quartzite, sandstone fragments, feldspar clasts and mud flakes.	Plastic debris flow (high strength, viscous). Higher energy than Gmm1. Mostly found at the base of new channel deposit cycles (i.e. basal gravel). Lack of internal structure indicates rapid flow speed reduction.	Flaminkberg (Figure 4.1)
Gmm3	Gravel, matrix-supported, massive conglomerate. Very poorly-sorted clasts (av. 2.4 cm) range from 0.2 to 33.4 cm in size and are carbonate, quartz, feldspar and quartzites. Weak to normal grading.	Plastic debris flow (high strength, viscous). Higher energy than Gmm1 and Gmm2. Mostly found at the base of new channel deposit cycles (i.e. basal gravel). Lack of internal structure indicates rapid flow speed reduction. Grading may indicate a consistent decrease in channel flow strength.	Arondegas (Figure 4.8)
Gmh1	Gravel, matrix-supported, horizontally bedded conglomerate. Moderately-sorted quartz clasts (av. 0.4 cm).	Longitudinal bedforms, lag deposits.	Flaminkberg (Figure 4.2)
Gmh2	Gravel, matrix-supported, horizontally bedded conglomerate. Moderately-sorted quartz clasts (av. 3 cm).	Longitudinal bedforms, lag deposits.	Flaminkberg (Figure 4.2)
Gml	Gravel, matrix-supported, low-angle cross-bedded conglomerate. Moderately-sorted quartz clasts (av. 0.4 cm).	Transverse bedforms, channel fills.	Flaminkberg (Figure 4.2)
Gcm	Gravel, clast-supported, massive conglomerate. Very poorly-sorted, clasts range in size from 0.25 to 26 cm. Clasts (av. 3 cm) are composed of carbonate, quartz, feldspar and quartzite. Weak grading.	Pseudoplastic debris flow (inertial bedload, turbulent flow)	Arondegas (Figure 4.8)
Sh	Sand, medium- to coarse-grained, poorly- to moderately-sorted. Horizontally laminated. Occur as tabular, laterally continuous bodies.	Upper flow regime, plane bed (critical flow) destroys dunes and ripples	Flaminkberg (Figures 4.1-2) and Arondegas (Figures 4.7-8)
Sl	Sand, medium- to very coarse-grained. Low-angle cross-beds (<15^{o}). May locally contain coarser clasts.	Scour fills; humpback or washed out dunes. Flood deposits or offshore deposits	Flaminkberg (Figures 4.1-2) and Arondegas (Figures 4.8-9)
Sl2	Sand, medium- to very coarse-grained. Low-angle cross-beds (<15^{o}). Cross-bedding defined by sorting of coarser clasts.	Scour fills; humpback or washed out dunes. Flood deposits or offshore deposits	Flaminkberg site 1
Sm	Sand, mostly coarse-, occasionally medium-grained, poorly- to moderately-sorted, massive. Mud flakes may be present.	Sediment gravity flows with very high deposition rates.	Flaminkberg (Figure 4.1-2) and Arondegas (Figure 4.8-9)
Sr	Sand, fine- to medium-grained, ripple laminated or ripple marked surface.	Lower flow regime, lower shoreface deposit or flood deposit	Flaminkberg (Figure 4.1) and Hoedberg (Figure 4.5)
Srm	Sand, medium- to coarse-grained. Mega ripple marks with ~ 30 cm crest to crest associated with silt-facies.	Lower flow regime with high energy event, lower shoreface deposit or flood deposit	Hoedberg (Figure 4.5)
St	Sand, medium- to coarse-grained, poorly-sorted. Very large- to large-scale trough cross-bedded.	Forms from the migration of 3D sinous-crested and languid dunes.	Arondegas (Figure 4.9)
HCS	Sand, medium- to coarse-grained, hummocky cross-bedded, poorly- to moderately-sorted.	Oscillatory wave-generated and unidirectional storm-induced currents, lower shoreface, shelf or offshore transition zone in marine settings	Flaminkberg (Figure 4.1)
Fl	Mud/silt size, fine laminations, olive green/grey to purple colour. Sandstone bodies occur as lenses and have wavy bedding. Mud content low and often contain carbonate nodules and lenses.	Waning low energy environment. Abandoned channel fills or shelf environment	Hoedberg (Figure 4.5-6)
Fm	Silt/mud size, massive	Low deposition rates	Hoedberg (Figure 4.5-6)

Table 3.2. Typical architectural elements found within channels in fluvial settings. After Miall (2010).

Element	Symbol	Principal facies assemblage	Geometry and relationship
Channels	CH	Any combination	Finger, lens or sheet; concave-up erosional base; scale and shape highly variable; internal concave-up 3rd order erosion surfaces common.
Gravel bars and bedforms	GB	Gm, Gp, Gt	Lens, blanket; usually tabular bodies; commonly interbedded with SB.
Sandy bedforms	SB	St, Sp, Sh, St, Sr, Se, Ss	Lens, sheet, blanket, wedge, occurs as channel-fills, crevasse splays, minor bars.
Upstream accretion macroform	UA	St, Sp, Sh, St, Sr, Se, Ss	Lens, resting on bar remnant or LA/DA deposit. Accretion surfaces dipping gently upstream.
Downstream accretion macroform	DA	St, Sp, Sh, St, Sr, Se, Ss	Lens resting on flat or channelled base, with convex-up 3rd order internal erosion surfaces and upper 4th order bounding surface. Accretion surfaces orientated downstream.
Lateral accretion macroform	LA	St, Sp, Sh, St, Sr, Se, Ss, less common Gm, Gt, Gp	Wedge, sheet, lobe; characterised by internal lateral-accretion 3rd surfaces. Accretion surfaces orientated across channel. Typically downlaps onto flat basal erosion surface.
Scour hollows	HO	Gh, Gt, St, Sl	Scoop-shaped hollow with asymmetric fill.
Sediment gravity flows	SG	Gmm, Gmg, Gci, Gcm	Lobe, sheet, typically interbedded with GB.
Laminated sand sheet	LS	Sh, St, minor Sp, Sr	Sheet, blanket.

Table 3.3. Hierarchical bounding surfaces of primarily fluvial lithofacies units. After Miall (1988) and Collinson (1996).

Order	Nature of the surface	Significance and process
1st	Separates individual cross-bedded sets.	Migration of dune bedform under steady flow conditions.
2nd	Separates cossets of contrasting set type.	Change in hydrodynamic conditions through time, related to short-term unsteady flow or local non-uniformity.
3rd	Inclined erosion surfaces within coset or group of cosets.	Medium-term change in hydrodynamic conditions related to stage fluctuation or major shifting of flow across/around a bar form.
4th	Separates units with discrete accretionary integrity.	Shift of bar/sub-channel pattern related to inherent channel flow stability or to reorganization during a major flood.
5th	Surfaces with a marked shift in grain size, bedform scale, etc. Laterally extensive with relief.	Shifting and erosion of a channel floor. Isolated channels with relief reflect channel switching. Extensive surfaces within larger sandbodies record channel migration.
6th	Separates major channel sand bodies from contrasting facies (i.e., from fine-grained sediment or from different channel facies.	Major change in fluvial regime. May record shifts or base level or climatic or tectonic changes.

3.2 Clast count

Clast counts of conglomerate beds were assessed in the field in order to investigate the provenance of the beds as clast counts can determine the proximity, sediment source type and energy levels of the depositional processes. The clast size measurements also consisted of photographing a defined area or traverse across an exposure and then identifying the long axes of the first 100 pebbles (as recommended in Howard 1994). The length measurements were performed using the freeware *ImageJ* and the results were sorted according to clast size and the compositions recorded (available at: https://imagej.net/Downloads) (Table 3.4; Lindsay et al., 2005; Lindsay et al., 2007). Three dimensional assessments of the clast morphologies were difficult to determine and biased towards the larger clasts. This is because the large carbonate clasts tended to preferentially weather out and facilitated better 3D assessments whereas the strong cementation of the matrix prevented the extraction and analysis of the small pebble populations (<1 cm). Consequently, the small pebble populations are considered under-represented in the counts and statistical analysis is not viable on the dataset. Thus, some of the observations are not fully quantifiable.

Table 3.4. Gravel size classes of the standard Udden–Wentworth grain size scale used in this study.

Granules	Small pebbles	Medium pebbles	Large pebbles	Very large pebbles	Small cobbles	Large cobbles	Boulders
0.2 - 0.4 cm	0.4 - 0.8 cm	0.8 - 1.6 cm	1.6 - 3.2 cm	3.2 - 6.4 cm	6.4 - 12.8 cm	12.8 - 25.6 cm	>25.6 cm

3.3 U-Pb geochronology using detrital zircons

Detrital zircon dating was undertaken to assist in dating and characterising the dominant sandstone lithologies under investigation. Zircon ($ZrSiO_4$) is a resistant mineral which records information regarding its growth and thermal history. It occurs in a variety of rock types e.g., intermediate igneous, volcanic, metamorphic rocks as well as clastic sedimentary rocks (usually as accessory mineral grains) (Bowring et al., 2006). In the zircon crystal structure, uranium (U) is often substituted into the site of zirconium (Zr^{4+}) due to the similarity in their size, however lead (Pb) is excluded from the structure due to its difference in size (Roberts and Spencer, 2015). Thus, it is assumed that any Pb (^{206}Pb, ^{207}Pb) present in the zircon grain is due to the radioactive decay of U (^{238}U, ^{235}U) in the U-Th-Pb decay scheme. Zircons are resilient to weathering, transport, erosion and diagenesis and consequently are considered closed systems (Bowring et al., 2006; Gehrels, 2012). Thus, U-Th-Pb ages can be reliably extracted and provide a robust age of crystallisation and cooling of the source rock. Furthermore, the youngest detrital zircon grain population can be used to indicate the maximum depositional age of the sedimentary unit, or it can infer the timing of metamorphism that alters the sedimentary rocks after deposition, depending on the degree of

metamorphism. Detrital zircon ages can also be used to reveal the provenance of a sedimentary unit and not only yield information concerning the maximum depositional age. The youngest detrital zircon population may also be of limited use as they may only reveal the age of the youngest source area available at the time, and not necessarily reflect the maximum age of deposition.

The U-Th-Pb system is especially useful in age dating as there are three different decay schemes and they serve as a self checkers in age determination: $^{238}U \rightarrow ^{206}Pb$ (half-life of 4.47 Ga), $^{235}U \rightarrow ^{207}Pb$ (half-life of 0.70 Ga), and $^{232}Th \rightarrow ^{208}Pb$ (half-life of 14.01 Ga) (Jaffey et al., 1971; Gehrels, 2014). Three ages can be calculated from the measured decay schemes: $^{206}Pb/^{238}U$, $^{207}Pb/^{235}U$, and $^{208}Pb/^{232}U$ age. An intermediate thorium decay scheme ($^{208}Pb/^{232}Th$) can be used to calculate an age however; this is seldom used in zircon geochronology. The U-Pb system can also yield an age from measuring the $^{206}Pb/^{207}Pb$ ratio as well as the ^{238}U content because it has been shown that $^{238}U/^{235}U$ has a constant ratio of 137.82 (Hiess et al., 2012). Due to the abundance of decay schemes, not all decay schemes need to be measured and given the relative imprecision of ^{235}U and ^{207}Pb measurements, they are not measured by the mass spectrometer but rather calculated. The isotopes measured in zircon studies include $^{206}Pb/^{238}U$, $^{206}Pb/^{207}Pb$, and $^{206}Pb/^{204}Pb$ (Gehrels, 2014; Spencer et al., 2016). U-Pb ages are considered concordant when the $^{206}Pb/^{238}U$ and $^{207}Pb/^{235}U$ ratios produce the same age. The discrepancy in the ratios is represented either by the percentage concordance or discordance of each grain. The percentage of concordance has implications on how robust the zircon age is and whether the system has been tampered with. Typically, studies only use zircon ages that are >90% concordant (<10% discordant) to make further interpretations.

3.3.1 Sample collection and preparation

Samples were mainly collected from the base of each sandstone unit, based on the assumption that the largest and densest particles accumulate first from traction currents as dictated by their hydrodynamic properties. Potential lithified tuffs were sampled as well. Samples of at least two kg were collected from each layer to ensure the extraction of a representative population of the detrital zircon grains.

The least weathered samples were chosen in the field for analysis, and once collected, they were thoroughly washed before crushing to remove surface contamination. A Sturtevant Model 4 rock crusher was used and it underwent intensive cleaning in-between samples to prevent cross-contamination. Each sample was further crushed using a disc mill at the Central Analytical Facility at Stellenbosch University (CAF SU) and sieved for grains below <350 µm. This interval was chosen in order to enhance the possibility of sampling potential distal volcanic ash derived zircons (Tucker et

al., 2013). The sieved grains were thoroughly washed in order to remove the clay-sized fraction. The material was placed onto a panning machine in order to separate the heavy and light minerals, and a pipette was used to extract the heavy minerals. Magnetic separation of the sample was achieved using two methods: firstly, combing of the grains with a hand-held magnet, followed by further separation using a Frantz magnetic separator. Then non-magnetic minerals were further refined in the heavy liquid separation phase using tetrabromomethane. The sample was then washed and dried. A transmitted light microscope was used to manually pick 150 random zircon grains, which were then mounted on a 25 mm diameter epoxy resin puck. Finally, the mount was polished in order to expose the zircon grain mid-sections, which were then imaged (Figure 3.2) using the Carl Zeiss: MERLIN–Field Emission Scanning Electron Microscope (SEM) with an attached cathodoluminescence (CL) detector at the CAF SU. This yielded information on the cores, microstructures, cracks, inclusions and other complexities within the zircon grains. This is important as it yields information regarding the grain history and has implications on the viability of the grain for dating (Connelly, 2001; Bowring et al., 2006). Zoning and structure of the core reveals whether the grain is magmatic, metamorphic or has complex age zoning (Cawood and Nemchin, 2000). The zoning serves as a proxy for the grain history and complex age zoning should be avoided unless each component can be analysed individually (Corfu et al., 2003; Nasdala et al., 2003). Inclusions are unknown domains within the grains and are avoided as they produce a junk signal (Gehrels, 2012). Microstructures and cracks are important to identify as they can indicate whether a grain has been compromised and the U or Pb zones may have been recalibrated or undergone Pb loss (Gehrels, 2012)

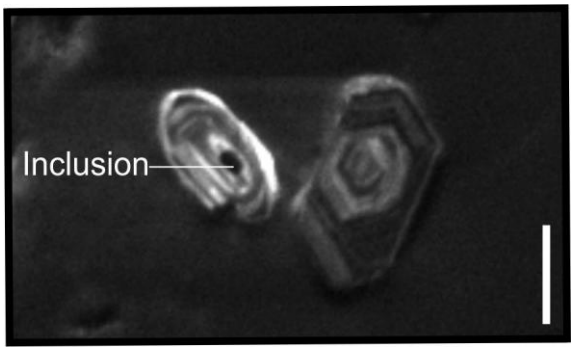

Figure 3.2. CL-image of rounded and semi-rounded detrital zircon grains from GAN2 sample displaying well-developed oscillatory zoning, typical of magmatic zircons. Dark areas in the CL-imaging indicate U-rich zones and white/bright areas indicate Pb-rich zones. Scale bar is 50 µm long.

3.3.2. Laser ablation ICPMS

Using the CL images of the zircon grains, certain grains were selected for analysis using the ASI Resolution M-50-SE Excimer laser coupled to a Thermo Element 2 Laser Ablation-Magnetic Sectorfield-inductively Coupled Plasma - Mass Spectrometry (LA-SF-ICP-MS) instrument at CAF SU.

This method is both time and cost effective and is considered to yield reliable results where high precision accuracy is not required (Jackson et al., 2004; Gehrels, 2012). There is no consensus in the literature concerning how many zircon grains need to be ablated to accurately represent a zircon population however, it is widely accepted that at least 60 concordant grains are used in the dataset to represent the grain population and reduce picking bias (Vermeesh, 2004; Andersen, 2005; Gehrels, 2012; Košler, 2012). This study follows the suggestions outlined by Vermeesh (2004) whereby at least 114 grains were picked and ablated. Two runs of 500 laser ablations were conducted using the LA ICP-MS. Each run consisted of analysing four samples and the standards with a spot size of 30 µm. Consequently, only 100-115 ablations per sample were analysed due to the limiting 500 ablations per run. Each individual sample analysis consists of 5 to 15 seconds of the gas baseline measurement, which is immediately followed by 17 seconds of ablation. Particular grains may have been ablated twice in two different regions of interest if the grain exhibited different zoning at the rim and core. Grains that were largely black with no zoning, had irregular zoning or were compromised by cracks were avoided (Bowring et al., 2006).

3.3.3 Data reduction and age determination

Data reductions were performed using the software programs *IgorPro, Iolite* and *VisualAge* under licence of the Stellenbosch University. The raw analyses were imported into *IgorPro* and *Iolite*. The gas background baselines were set and the standards identified (i.e., GJ-1, PLES and M127). The reported ID-TIMS age for GJ-1 is 608.5 ± 0.4 Ma (Jackson et al., 2004), 524 Ma for M127 (Nasdala et al., 2016) and 337.13 ± 0.37 Ma for the Plešovice zircon standard (Sláma et al., 2008). Each ablation signal was individually processed and an integration period selected over the ^{235}U, ^{238}U, ^{204}Pb, ^{206}Pb, and ^{207}Pb signals. The signals were evaluated using the live concordia plot in *iolite* and a section of the signal was selected using the following criteria: 1) keep the data clustered; 2) use the concordant part of the signal; 3) the start or the middle of the signal may be integrated if the signal is flat; 4) select the integration period over the same domain i.e., ensure that the ^{235}U and ^{206}Pb signals mimic each other and do not intersect over the selected integration period; and 5) monitor the ^{204}Pb signal to evaluate lead contamination. The whole signal cannot be used due to the fast drop in the signal over the whole ablation and due to down-pit fractionation of the signal (Gehrels, 2008; Kosler et al., 2013; Ibanez-Mejia et al., 2015). Once all the integration periods were set, the data was verified by Dr. Jeanne Taylor, the part-time geochronologist at Stellenbosch University. The data was then imported into *Microsoft Excel* and prepared for presentation using the add-in program, *Isoplot 4v15* and *jAgeDisplay*.

In order to determine meaningful depositional ages, the data is screened and a concordance filter is applied. This can be visually estimated using a concordia plot or the percentage may be calculated as:

$$Concordance = \frac{206Pb/238U}{207Pb/206Pb} * 100$$

There is no set concordance interval in the literature and although it is widely accepted to disregard data with discordance higher than 10%, 30% discordance is occasionally used in studies of zircons associated with sedimentary rocks due to the multiple sources and complex history of the detrital zircons (Gehrels et al., 2006). Thus, a 10% discordance interval was selected (i.e., 90–110% concordance accepted) to represent the data. The concordance filter can greatly influence the age as it can incorporate data that is not truly representative of the sample and may result in the incorporation of compromised data. Although a common lead correction was performed in *Iolite* and the data is available in Appendix C, the corrected data was not used as it had a tendency to overcorrect and shift the entire dataset into discordance. Detrital zircons often have highly complex provenance histories and by correcting for common Pb when it does not affect every grain, it could potentially compound unknowns. Additionally, not all mass spectrometers are able to measure ^{204}Pb reliably, which has repercussions on the data corrections (Gehrels et al., 2006).

Dependent upon the zircon ages, it is normal to use the ^{206}Pb/^{238}U ages for zircons younger than 1.2 Ga and ^{207}Pb/^{206}Pb for zircons older than 1.2 Ga. The exact cut off varies in the literature but ranges between 1–1.5 Ga (Gehrels, 2008; Voice et al., 2011; Roberts and Spencer, 2014: Spencer et al., 2016). The cut off must not occur in the middle of a zircon population as isotropic consistency is vital in a study, thus the range allows for datasets to be evaluated and a suitable gap in the zircon population to be chosen as the cut off value.

There are multiple ways to determine the maximum depositional age of the sample and they are listed in order of increasing statistical reliability: 1) youngest single grain age; 2) youngest graphical age peak controlled by more than one grain; 3) mean of the youngest two or more grains that overlap at 1σ and, 4) mean age of the youngest three or more grains that overlap at 2σ (Dickinson and Gehrels, 2009). The youngest single grain is the least conservative age as it lacks reproducibility (single data point) and it may be affected by Pb loss, however it may be the closest to the actual depositional age. If it is used in a basin where there are no other age constraints, it must be rigorously scrutinised as it may have significant ramifications for the geological history of the basin (Sircombe et al., 2001). The mean age of the youngest three or more grains is the most conservative method but is also the least likely to be close to the true depositional age. Dickinson

and Gehrels (2009) found that all the methods overlapped with the depositional age and were reasonable age indicators. Consequently, it was suggested that multiple methods could be used to find agreement within the dataset and that if there are no other age constraints available for a given rock unit, it is wiser to use the most statistically robust methods (Dickinson and Gehrels, 2009; Tucker et al., 2013; Spencer et al., 2016). AgePick was used to identify populations of similar ages and characteristics and the mean age of the youngest three or more grains that overlap at 2σ were calculated using an algorithm in *Isoplot v4.15*.

3.4 Microfossil investigation

This method was applied in order to further aid in constraining the location of the Ediacaran-Cambrian boundary within the Vanrhynsdorp Group using acritarch assemblages as well as to aid with the regional correlation of the Vanrhynsdorp and Nama Groups.

Microfossil sample preparation followed a standard palynological method as described by Vidal (1988) for the extraction of organic-walled microfossils. Samples were broken down into <1 cm^3 pieces using either a geological hammer or a mechanical rock crusher, depending on how lithified the sample was. Approximately ~50 g of the freshest material was immersed in hydrofluoric acid (40% HF) for several days. The samples dissolved over 5–6 days and were stirred at intervals and the acid was changed on the third day (Figure 3.3A). After the process was complete, the excess HF acid was decanted and the residue was repeatedly rinsed in deionised water. The sample was brought to a boil and then simmered in hydrochloric acid (37% HCl) for 10 to 20 min to remove fluorides (Figure 3.3B). The boiling time is dependent on the organic content of the sample. Organic-rich samples require less boiling time, while clay-rich samples require longer boiling periods. Once the boiled residue had sufficiently cooled, it was filtered through <30 µm sieves. The sample was filtered with a steady flow of water and the container was tapped to facilitate the flow (Figure 3.3C). The filtered sample was transferred into a labelled test tube and then rinsed in ethanol (90%) and acetone and centrifuged between rinsing for 1 min at 3000 rpm (Figures 3.3D-E). A small volume of acetone was left in the test tube to submerge the sample and prevent algal growth. Permanent mounts on microscope slides were produced using synthetic resin. The resin was sourced from Advanced Materials Composites (AMT) and was made up of two components: part A (EP resin LR 20) and part B (LH 281 hardener). They were mixed in a weight ratio of 1:0.33. The resin was placed on a slide and a pipette was used to transfer the residue onto the slide (Figures 3.3F-G). The cover slip was then lowered carefully on top of the resin (Figure 3.3H). Care was taken to ensure no epoxy was on top of the cover slip. The slides were cured in an oven for 1 hour at 50^{o} C. Alternatively; the slide could have been left over night to dry. Clean laboratory conditions and procedures were implemented to prevent possible contamination.

The slides were imaged using an Axiocam 105 colour camera attached to a Nikon AX10 microscope with 5x, 10x, 20x and 50x Zeiss lens objectives.

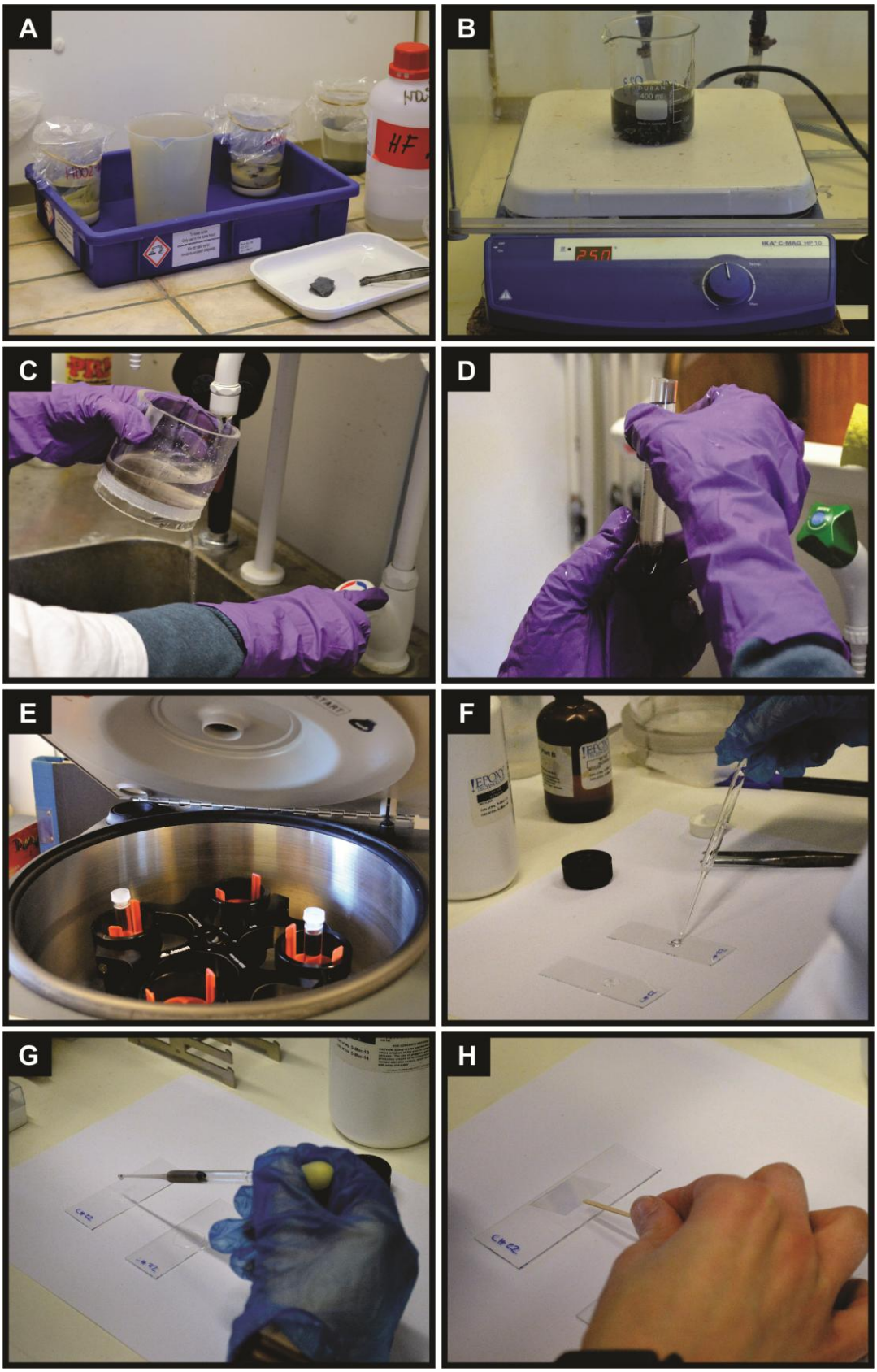

Figure 3.3. Various stages of microfossil processing. A) Maceration of samples in 40% HF acid in the fume hood. B) Residue boiled in 37% HCl acid to dissolve fluorides. C) Residue filtered through <30 µm mesh. The running tap ensures a steady flow and suction through the mesh. D) Filtered residue transferred into a test tube. E) Test tube centrifuged for one minute at 3000 rpm in 90% ethanol and then repeated in acetone. F) Mixed resin placed onto the microscope slide. G) Residue pipetted on to the slide. H) Cover slip lowered carefully onto the sample and epoxy.

4. Results

4.1 Facies analysis of the lower Vanrhynsdorp Group

The lower Vanrhynsdorp Group outcrops in a 120 km x 102 km area across the border of the Northern and Western Cape Provinces (Figure 2.3). Generally, the coarse-grained lithologies form better exposures as steep hills whereas the finer-grained facies occupy low lying areas or regions characterized by recessive weathering. Although the area contains the most extensive exposures of the lower units, structural deformation limits the number of outcrops suitable for sedimentary facies analysis.

Study sites and measured sections were selected based on the availably of the highest quality outcrops (e.g., largest lateral and vertical continuity; preferably outcrops perpendicular to one another to afford a 3D control of the facies architecture; Figure 2.3). Most of the outcrops are exposed on privately owned farms and access to them is often difficult without the local contacts. Outcrop exposure and accessibility in the area mostly allowed for high resolution 2D field analysis and to some extent 3D analysis. Most accessible outcrops span laterally for a few-to-tens of metres only. Lateral and vertical continuity in access of this is rare with many key stratigraphic contacts being obscured either by vegetation or scree. These limitations prevented a fully quantitative assessment of the sedimentary facies architecture, and resulted in the qualitative approach. Vertical lithofacies changes were documented using sedimentary logs (Figures 4.1-2; 4.5-6; 4.8-9; the log key can be found in Appendix A), whereas changes in facies associations were mapped on photomosaics, which are shown in Figures 4.3, 4.4, 4.7, 4.10, 4.11 and 4.12. Each panel is shown in its own and then with an interpretative overlay in order to facilitate the reader's independent assessment of the outcrop photos, which are essentially vertical facies maps. For architectural element descriptions refer to Tables 3.2.

4.1.1 Flaminkberg Formation

The average dimensions of the Flaminkberg outcrops are 20 m to 1 km in height and span several kilometres in width. Due to faulting and folding, bed-by-bed or even unit-by-unit correlation of adjacent outcrops is not possible (Figure 2.3). The formation is dominated by coarse-grained sandstone-dominated units, although recessive weathering implies the presence of fine-grained units as well. No outcrop of the mudstone facies was observed in the study area preventing the in-depth facies analysis of these fine-grained rocks. The sandstone beds are predominantly laterally continuous for ~80 m, and form several, well-defined upward-coarsening cycles (Figure. 4.1). The beds thicken upwards from 10 cm on average in the lower part to 30 cm on average in the upper part, and few architectural elements are observed. The sandstone beds are sheet-like and occasionally form laterally accreted units that are confined to channel-like features. The most

common sedimentary structures in the sandstones include horizontal and low-angle cross-bedding; hummocky cross-stratification is present but rarely observed. Massive gritstone and pebble conglomerate layers occur throughout the formation (Figure 4.1).

4.1.1.1 Lithofacies

Gravel facies

Gritstones (Gmm1; Table 3.1) and pebble conglomerates (Gmm2, Gmh1-2, Gml; Table 3.1) constitute a small percentage of the measured sections in the Flaminkberg Formation (4-25%; Figures 4.1-2). They occur throughout the formation and their matrix is predominantly coarse-grained sandstone (grain size equal to or less than 2mm). The clasts are compositionally similar to the overlying and underlying sandstone units and the majority of clasts are quartz with feldspar and sandstone clasts also present. Mud rip up clasts are rarely observed (Figure 4.1H). Subdivisions within this facies are possible based on average clast size and internal structures. Gritstones are matrix-supported, massive and poorly-sorted with clasts averaging 0.2 cm in size (Figure 4.1C). The beds are tabular and have subparallel erosional surfaces. Occasionally, a gritstone layer may be welded on to the top of a sandstone bed (Figure 4.1F). Pebble conglomerates can be divided into small pebble conglomerates (Gmh1; clasts av. diameter: 0.4 cm, Gml; clasts av. diameter: 0.4 cm), medium pebble conglomerates (Gmm2; clasts av. diameter: 1 cm) and large pebble conglomerates (Gmh2; clasts av. diameter: 3 cm) (Figures 4.1-2). The conglomerates are all matrix-supported, moderately- to very poorly-sorted and have weakly developed internal structures ranging from horizontal bedding to low-angle cross-bedding (Figures 4.1-2; Table 3.1). The beds are laterally continuous for ~600 m, ~20 cm thick and marked by predominantly sub-parallel erosional surfaces (Figures 4.3-4).

Sandstone facies

Sandstone beds are the most commonly observed lithology in Flaminkberg Formation. They vary from white to red-purple in colour, range from 0.5 to 60 cm in thickness (i.e., mostly thickly bedded) and span 300 m to 1 km in width (Figure 4.3). The coarse- to very coarse-grained sandstones occur as lenses, ribbons and sheets, which locally pinch out laterally and are interbedded with medium-grained sandstones (Figures 4.3-4). Tabular beds are bounded by planar to gently undulatory erosional surfaces; the lenticular beds may form channel fills (Figure 4.4A-A'). Approximately 73-76% of the Flaminkberg Formation sandstones display low-angle cross-bedding, horizontal lamination or no internal features at all (massive, structureless sandstones) (Figures 4.1-2). Thin horizontally bedded sandstones (4-5 cm thick) are commonly interbedded with massive sandstones and laterally pinch out. The sandstones associated with the gravel facies tend to be clast-rich, especially in low-angle cross-beds where grain size variations occur across the foresets (Sl2; Figure 4.2), a feature

which is more prevalent in the upper part of the formation. Other sedimentary structures include hummocky cross-stratification and ripple cross-lamination (Figures 4.1D-E). The beds generally have sharp bounding surfaces although they locally may have wavy lower boundaries where thin beds tend to laterally thicken as well. A few fine-grained micaceous sandstone beds occur in the upper part of the formation (Figure 4.1I).

4.1.1.2 Facies associations

The most common architectural elements in the Flaminkberg Formation are the sheet-like sandstone beds (Figures 4.3-4), however the local development of small-scale channel shaped deposits and laterally accreted beds also occur. On large-scale, these tabular coarse-grained units, which are made up of beds with lateral continuity of ~10's of m's, have erosive lower boundaries that are flat and lack evidence for major channel scours or incisions. The small-scale channel-shaped beds and small-scale, lenticular beds pinching out laterally. Downward accretion bars could not be confirmed in the formation due to the lack of suitable 3D exposure of the facies associations. For the interpretations of the architectural element sub-environments, refer to Table 5.1 in section 5.1.

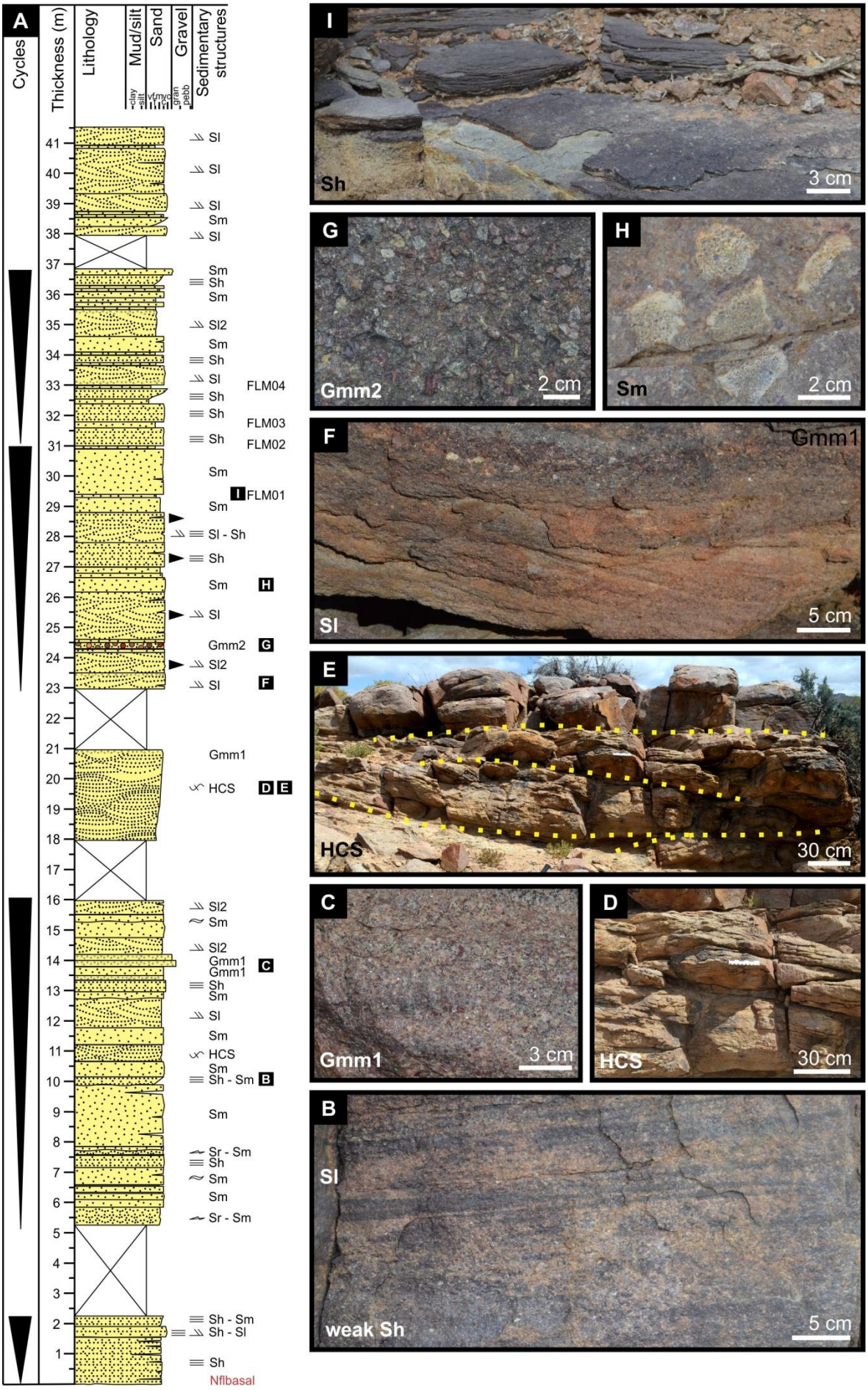

Figure 4.1. Lithofacies of the Flaminkberg Formation at log site 1 (Figure 2.3; 30°40'50.3"S, 18°16'40.6"E). A) Sedimentary log. B) Sandstone bed showing changes from weak horizontal lamination (Sh) to low-angle cross-bedding (Sl). C) Poorly-sorted gritstone (Gmm1). D-E) Hummocky cross-stratification (HCS). F) Low-angle cross-bedding (Sl) capped by a gritsto layer (Gmm1). G) Massive, matrix-supported pebble conglomerate (Gmm2). H) Mudstone rip up clasts. I) Fine-grained micaceous sandstone sampled for microfossils (FLM01-04).

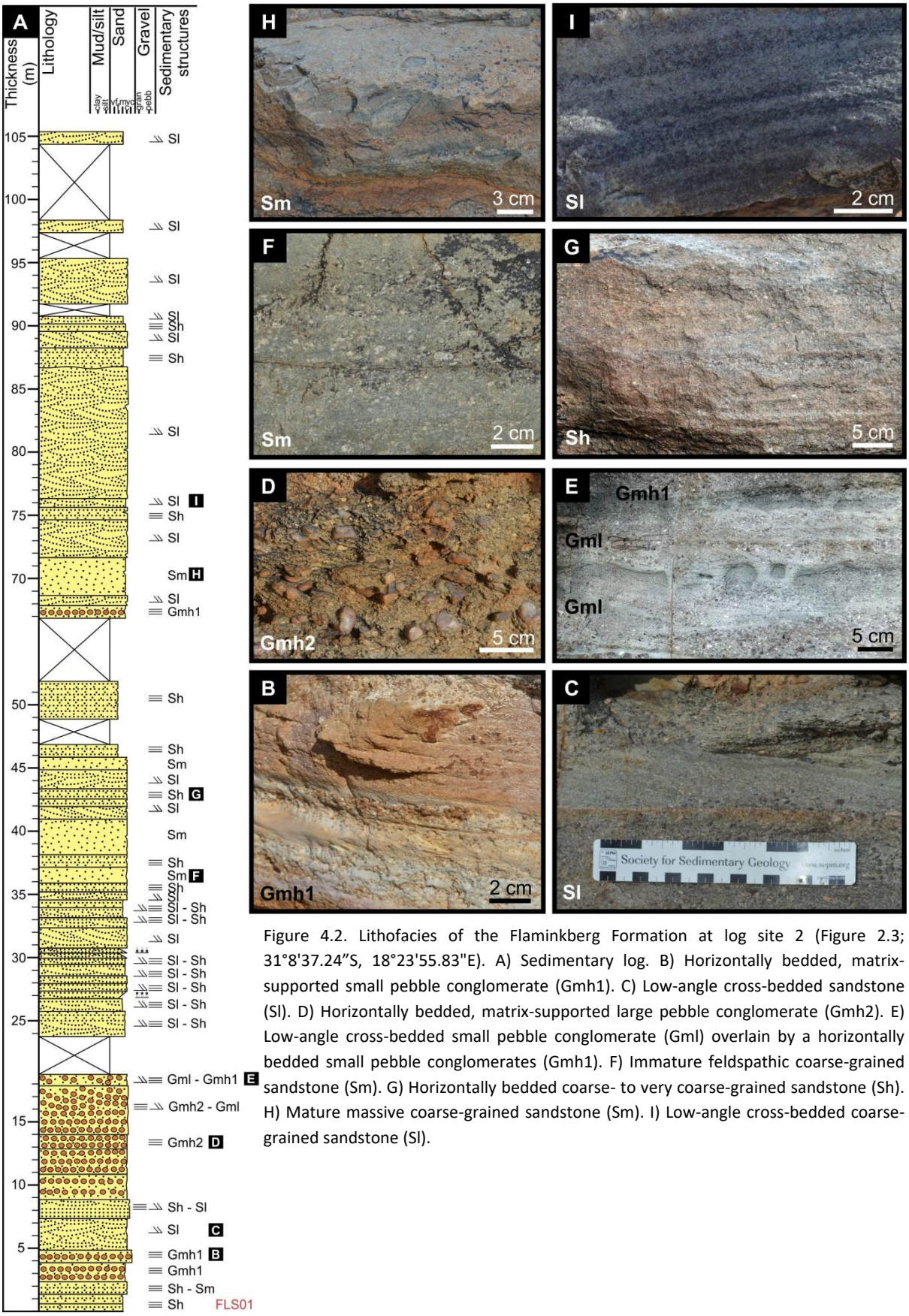

Figure 4.2. Lithofacies of the Flaminkberg Formation at log site 2 (Figure 2.3; 31°8'37.24”S, 18°23'55.83"E). A) Sedimentary log. B) Horizontally bedded, matrix-supported small pebble conglomerate (Gmh1). C) Low-angle cross-bedded sandstone (Sl). D) Horizontally bedded, matrix-supported large pebble conglomerate (Gmh2). E) Low-angle cross-bedded small pebble conglomerate (Gml) overlain by a horizontally bedded small pebble conglomerates (Gmh1). F) Immature feldspathic coarse-grained sandstone (Sm). G) Horizontally bedded coarse- to very coarse-grained sandstone (Sh). H) Mature massive coarse-grained sandstone (Sm). I) Low-angle cross-bedded coarse-grained sandstone (Sl).

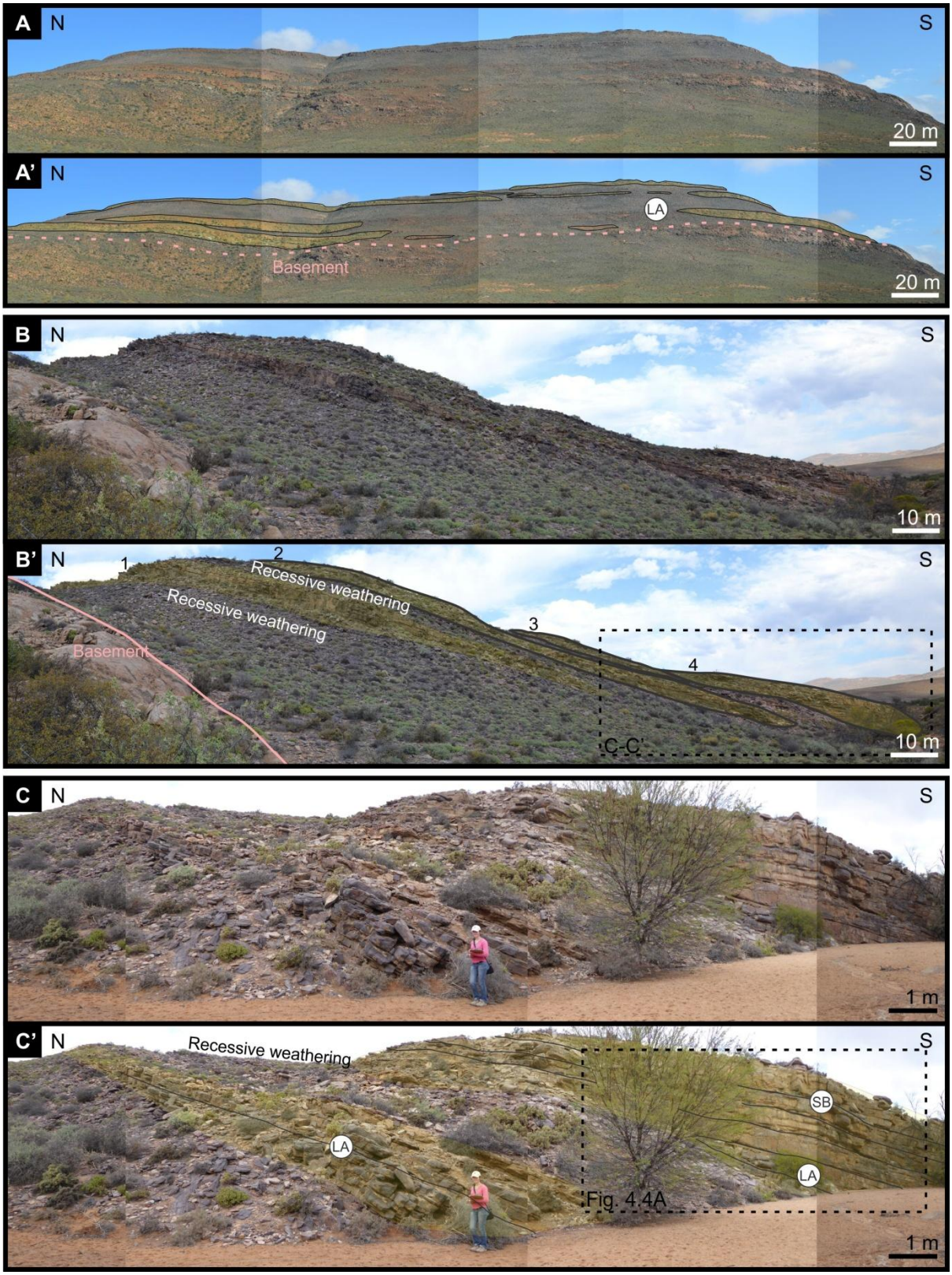

Figure 4.3. Facies mapping of the architectural elements of the Flaminkberg Formation outcrops using photomosaics. Paired images show the original outcrop and the interpretive overlays (AEs in white circles). A-A') Large-scale laterally accreting (LA) beds at log site 2. B-B') Four coarsening-upwards packages with recessive weathering profiles in between ridges at log site 1. Inset shows location of C. C-C') Laterally accreting (LA) beds within the sandstone packages and sheet-like sandstone beds (SB). Inset shows the location of Figure 4.4A panel.

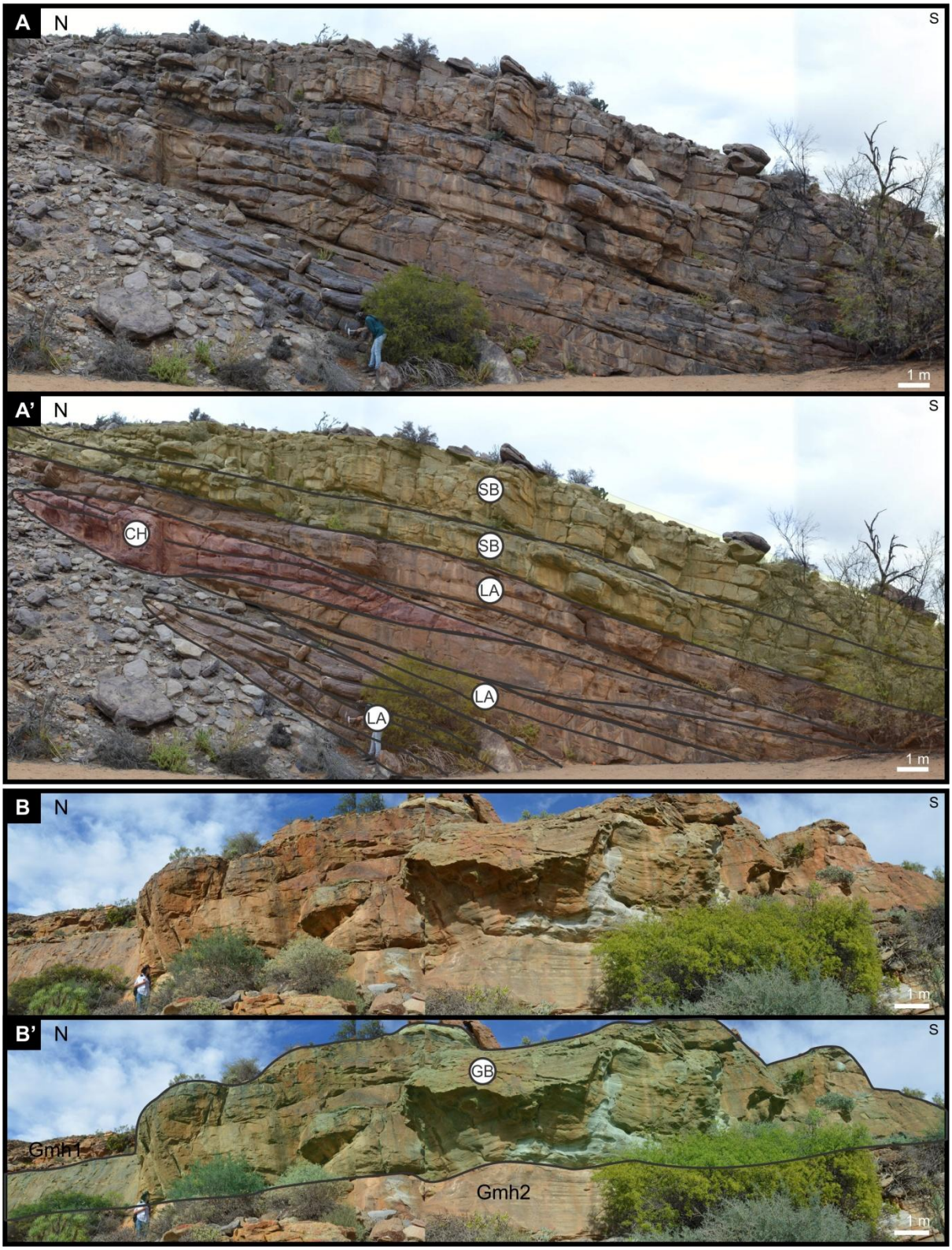

Figure 4.4. Facies mapping of the architectural elements of the Flaminkberg Formation using photomosaics. Paired images show the original outcrop and the interpretive overlays (AEs in white circles). A-A') Channel deposits in the outcrop depicting lateral accretion (LA), channel fills (CH) and sheet-like sandstone beds (SB) at log site 1. Main internal architecture shows vertically stacked sand bodies. B-B') Thick gravel beds (GB) with an uncommon down cutting lower boundary indicating local incision at log site 2.

4.1.2 Hoedberg Formation

The Hoedberg Formation is dominated by intercalating, greyish-green, very fine- and fine-grained sandstone and siltstone. The outcrops of the formation are extensively weathered and commonly covered in scree, except for a few hill sides and dry river beds. The outcrops are generally 10-50 m in height and 50-100 m wide, and show an increase in sandstone content and grain-size towards the upper part of the formation (Figures 4.5 and 4.7). This upward-coarsening grain size trend from fine-grained sandstone at the base to medium-grained sandstones at the top also changes the overall morphology of the distribution area of the formation. More specifically, the landscape underlain by the lower Hoedberg Formation is characterized by low relief (and exposures in dry river beds), whereas the upper Hoedberg Formation is cliff forming on the hillsides, which exposes laterally continuous beds (Figures 4.5-6). Brown carbonate nodules and lenses also constitute a small proportion of the formation (<1%). Due to the dominant fine-grained lithologies, especially in the lower part of the unit, mapping out the facies associations is very difficult. The formation contains no gravel facies. The upper contact with the Arondegas Formation may be gradational or erosive (Figures 4.7 and 4.10). In the former case, medium- to coarse-grained sandstone beds that are prominent in the upper Hoedberg Formation are frequently interbedded with siltstones (Figure 4.7).

4.1.2.1 Lithofacies

Sandstone facies

There are a variety of sandstone beds ranging from 5 cm to 60 cm in thickness (Figure 4.5). Horizontally-laminated, very fine-grained sandstone beds are commonly interbedded with siltstones throughout the Hoedberg Formation (Figure 4.5). Ripple cross-lamination, flaser bedding and soft sediment deformation structures are rare but present (Figures 4.5-6). Within the coarsening-upward formation, the sandstone beds first appear as thin lenticular beds with large ripple marks on the upper bedding surface (~30 cm crest to crest; Figure 4.7). These beds have erosional bases, and pinch out laterally. The beds gradually thicken upwards, becoming more laterally extensive and internally structureless (Figures 4.5I and 4.7C).

Mudstone facies

Olive green/grey siltstones are the dominant lithology of the Hoedberg Formation. They are finely-laminated or massive siltstones with soft sediment deformation structures and diagenetic carbonate nodules (Fl, Fm; Figures 4.5-6). The beds are laterally continuous, sheet-like units with flat, semi-parallel lower and upper bedding planes (Figure 4.5B).

4.1.2.2 Facies Associations

There are very few architectural elements observed in the Hoedberg Formation, which is largely composed of fine-grained, laterally continuous siltstone and sandstones beds that are tabular. Lateral accretion is rarely observed within the sandstone bodies (Figure 4.7). The mudstone-dominated units are vertically stacked and bounded by planar surfaces (Figure 4.7B).

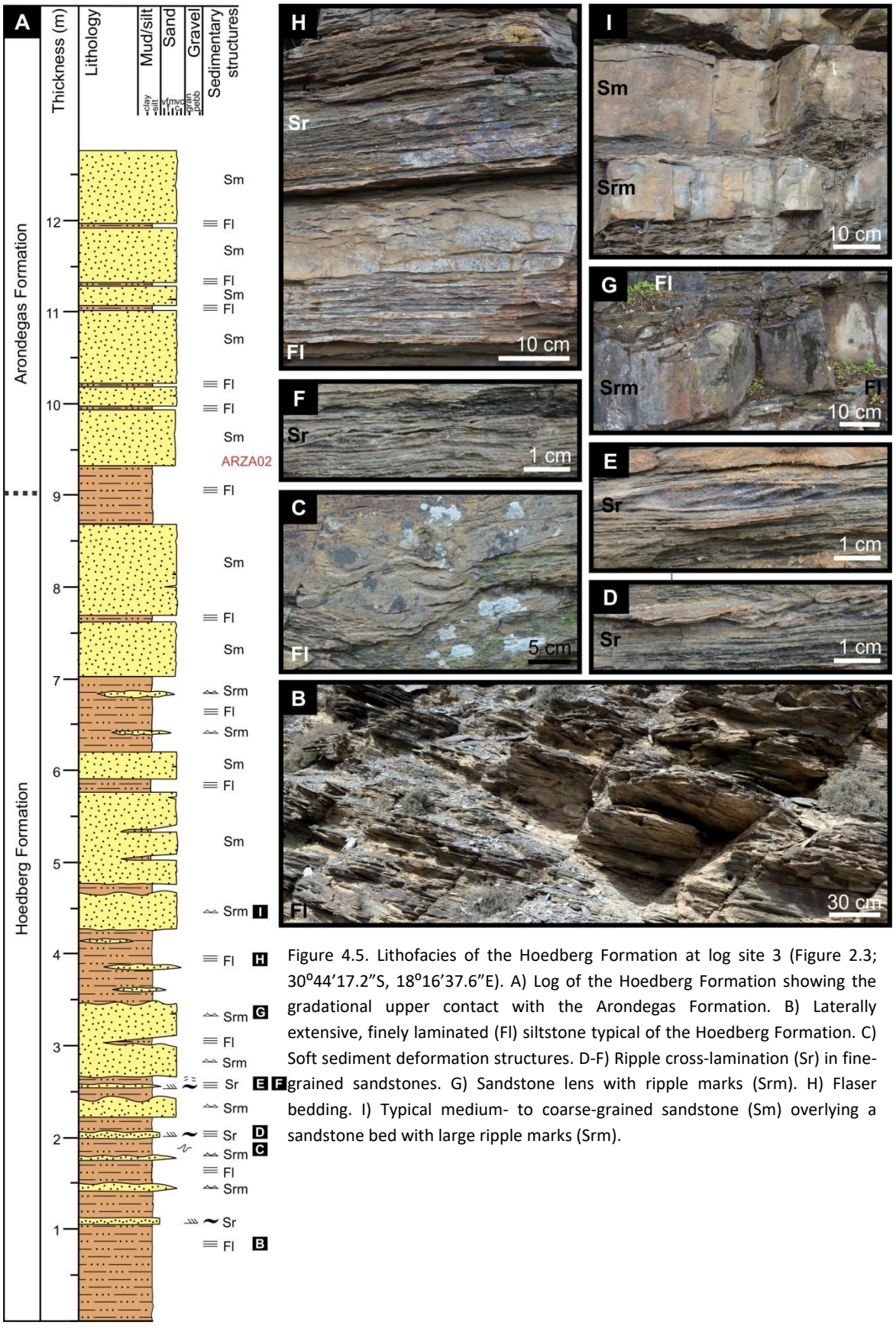

Figure 4.5. Lithofacies of the Hoedberg Formation at log site 3 (Figure 2.3; 30°44'17.2"S, 18°16'37.6"E). A) Log of the Hoedberg Formation showing the gradational upper contact with the Arondegas Formation. B) Laterally extensive, finely laminated (Fl) siltstone typical of the Hoedberg Formation. C) Soft sediment deformation structures. D-F) Ripple cross-lamination (Sr) in fine-grained sandstones. G) Sandstone lens with ripple marks (Srm). H) Flaser bedding. I) Typical medium- to coarse-grained sandstone (Sm) overlying a sandstone bed with large ripple marks (Srm).

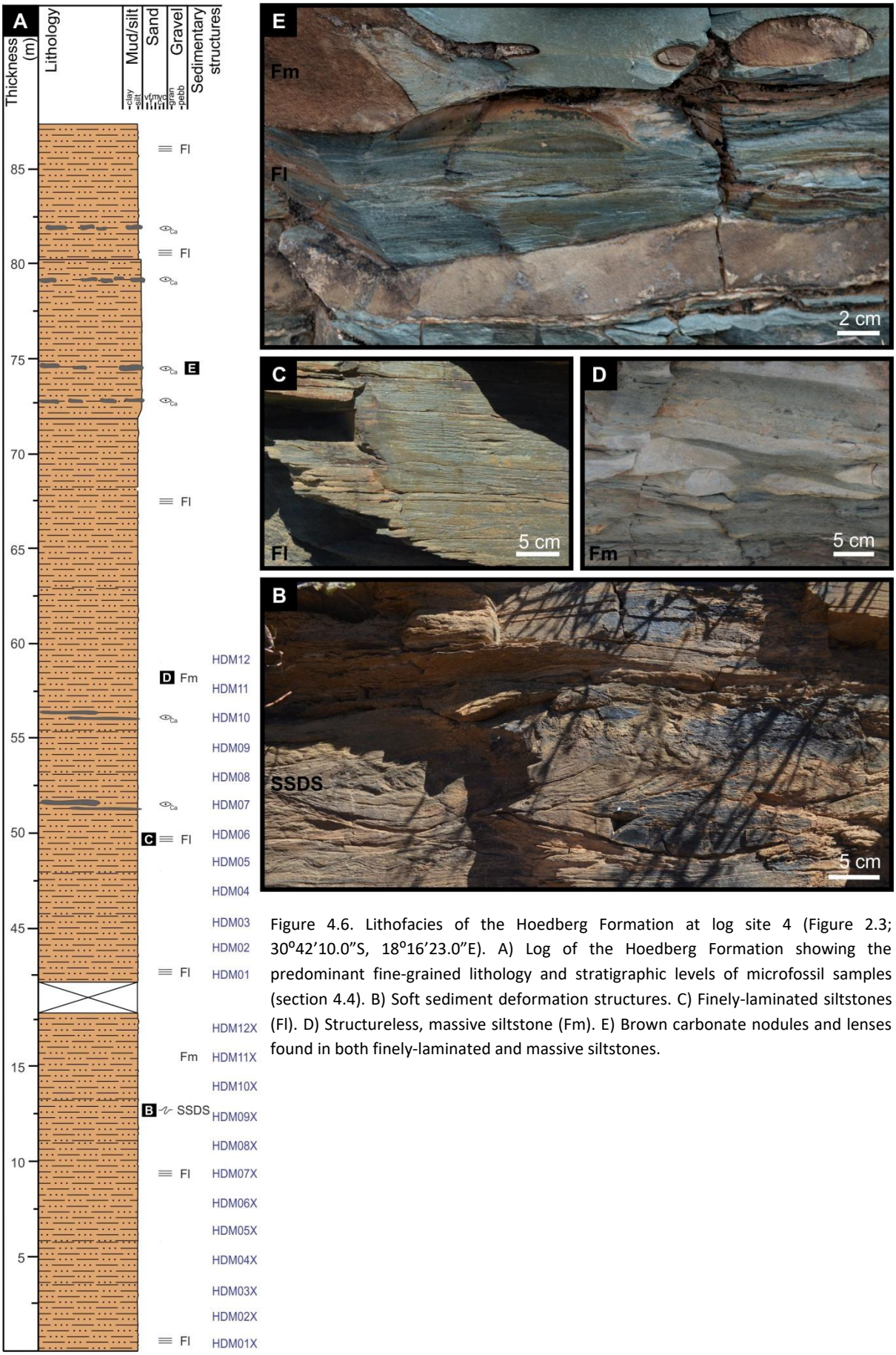

Figure 4.6. Lithofacies of the Hoedberg Formation at log site 4 (Figure 2.3; 30°42'10.0"S, 18°16'23.0"E). A) Log of the Hoedberg Formation showing the predominant fine-grained lithology and stratigraphic levels of microfossil samples (section 4.4). B) Soft sediment deformation structures. C) Finely-laminated siltstones (Fl). D) Structureless, massive siltstone (Fm). E) Brown carbonate nodules and lenses found in both finely-laminated and massive siltstones.

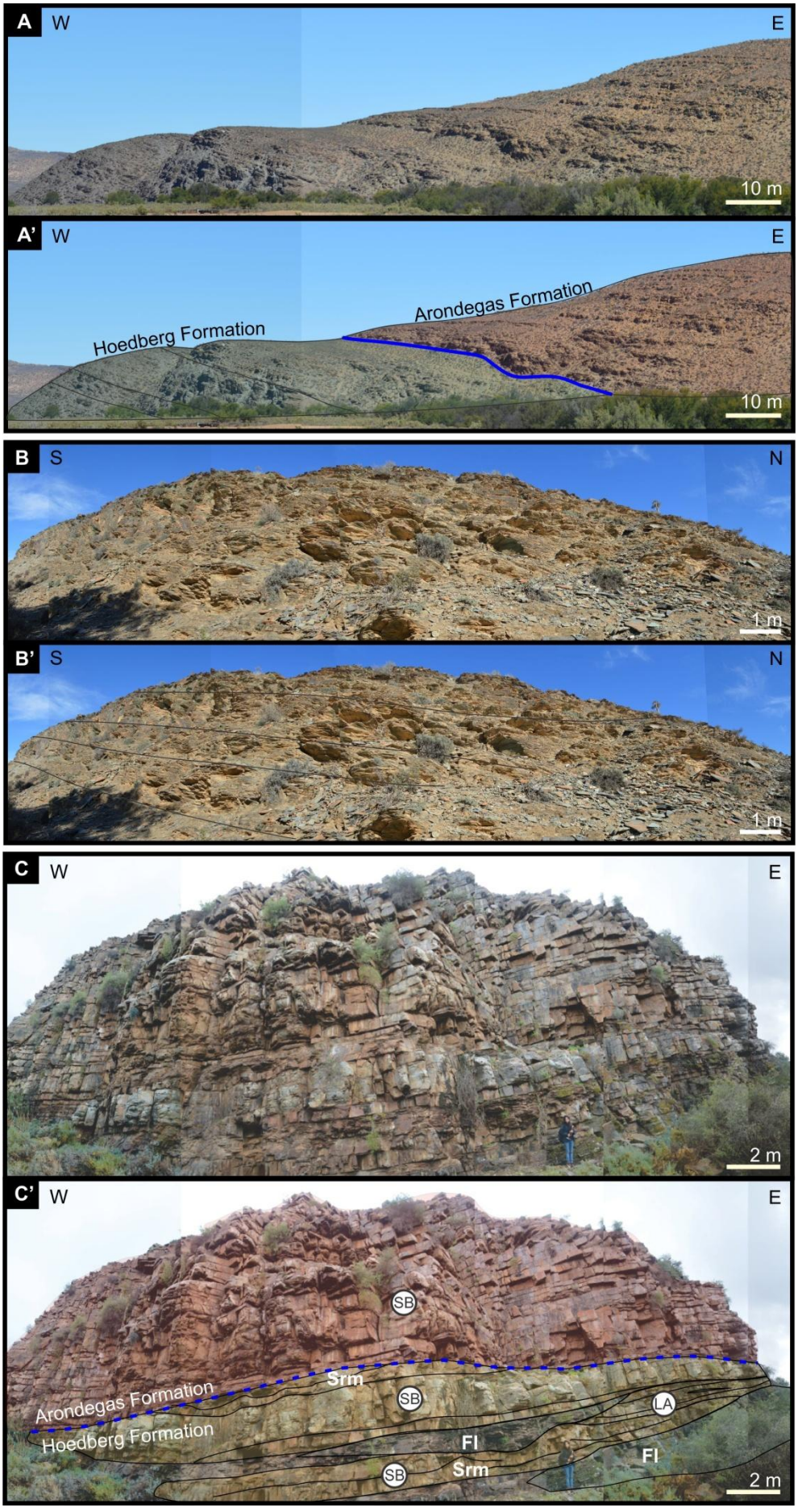

Figure 4.7. Facies mapping of the architectural elements of the Hoedberg Formation using photomosaics. Paired images show the original outcrop and the interpretive overlays (AEs in white circles). A-A') Photomosaic showing the variable nature of the upper contact (blue line) between the Hoedberg and Arondegas Formations. The Arondegas Formation is downcutting into the laterally continuous Hoedberg Formation at log site 4. B-B') Typical Hoedberg Formation outcrop with laterally continuous fine-grained sandstone and siltstone beds at log site 4. C-C') Lenticular sandstone bodies (SB) and interbedded siltstones in the upper Hoedberg Formation at log site 3. Lateral accretion (LA) is rare in these sandstone units. Overlying Arondegas Formation exhibits vertically stacked tabular sandstone beds (SB).

4.1.3 Arondegas Formation

The outcrops in the Arondegas Formation are about 40 m in height and ~1 km in width. The outcropping rock units can be tracked for 10's of m's and are dominated by thick, laterally accreted sandstone beds. Gravel and sandstone facies are mostly massive, especially in the lower part of the formation (Figures 4.8-9). The formation is characterized by multiple fining-upward successions in which the beds thicken upwards. The fining-upwards packages are also thicker in the upper part of the formation. Unique, locally developed carbonate-clast conglomerate beds are observed at one locality within the Arondegas Formation (see section on Clast Counts). These beds are normally graded and transition from clast-supported to matrix-supported conglomerates and massive sandstones, which together form fining-upward packages that are 10 m thick on average (Figure 4.8-9). As mentioned in the section on the Hoedberg Formation (section 4.1.2; Table 2.1; Figures 4.7A, C), the boundary between the Arondegas and Hoedberg Formations varies from gradational to erosional. In the latter case, the Arondegas Formation downcuts into the underlying Hoedberg Formation (Figure 4.7A) as well as into the basement rocks (Figure 4.12).

4.1.3.1 Lithofacies

Gravel beds

Gravel beds (GB) are only observed on the Draaihoek farm (log site 5: 30°45'44.0"S, 18°25'55.0"E). The matrix is predominantly coarse-grained sandstone (grain size equal to or less than 2 mm). The majority of the clasts are carbonate fragments, although quartz, feldspar and sandstone clasts are also common (see section 4.2 on clast counts). The gravel beds are very poorly-sorted and have erosive, down-cutting lower boundaries (Figures 4.8 and 4.11). Subdivisions within these gravelly facies (Table 3.1) are based on fabric and clast-content (i.e., whether the beds are matrix- or clast-supported), because the beds have no other distinguishing features. Consequently, clast-supported (Gcm) and matrix-supported conglomerates (Gmm3) were identified, ranging in thickness from 0.25 to 26 cm and from 0.2 to 33.4 cm, respectively (Figures 4.8-9 and 4.11). Matrix-supported conglomerate beds are more common. Although, *in situ* gravel beds are restricted to one locality (Figure 2.3; Figure 4.8), a dislodged block of rock at an Arondegas locality ~29 km from Draaihoek farm (Figure 4.9) showed similar features to the gravel facies described here (Figure 4.9I).

Sandstone facies

Sandstones are the most commonly facies of the Arondegas Formation. These white, grey to pinkish coarse- to very coarse-grained sandstones are typically immature and feldspathic (Figures 4.8-9). The sandstone beds form narrow sheets ranging from 5 cm to 60 cm in thickness and 40 m to 500 m in width (Figure 4.12). Typically, within the sandstone sheets, the individual beds are 10 cm to 20 cm in

thickness. Lenticular sandstone layers that pinch out laterally are often offset relative to each other. The coarse- to very coarse-grained and poorly-sorted sandstone beds show a thickening-upward trend but this is coupled with a decrease in grain size i.e., very coarse-grained sandstones at the base of the formation transition upward into medium-grained sandstones (Figure 4.9). Occasionally, the beds show normal or reverse grading (Figure 4.9). The massive sandstones are frequently interbedded with horizontally laminated sandstones, and together they constitute approximately 50-82% of the vertical sections measured in the study area (Figure 4.9). Other sedimentary structures observed include rare trough cross-bedding and ripple marks (Figure 4.9).

4.1.3.2 Facies associations

Gravel beds (GB) are well-developed at one locality at Draaihoek farm and occur as lens shaped beds or tabular bodies in association with sandy bedforms (SB). The gravel beds have erosive bases (Figure 4.11). Sandy bedforms (SB) occur frequently throughout the formation and are laterally extensive, sheet-like bodies (Figures 4.10 and 4.12). These SBs generally rest on sharp, planar surfaces but erosive bases are also observed (Figures 4.10B and 4.12B-C). Lateral accretion macroforms are common in the Arondegas Formation, and their identification is possible due to the off-set of lenticular sandstone beds that pinch out (Figures 4.10-12). It is difficult to determine the presence of downstream accretion macroforms due to the lack of 3D outcrop control, weathering, folding and tilting, which collectively mask the original depositional architecture in the outcrops. For the interpretations of the architectural element sub-environments, refer to Table 5.3 in section 5.1.

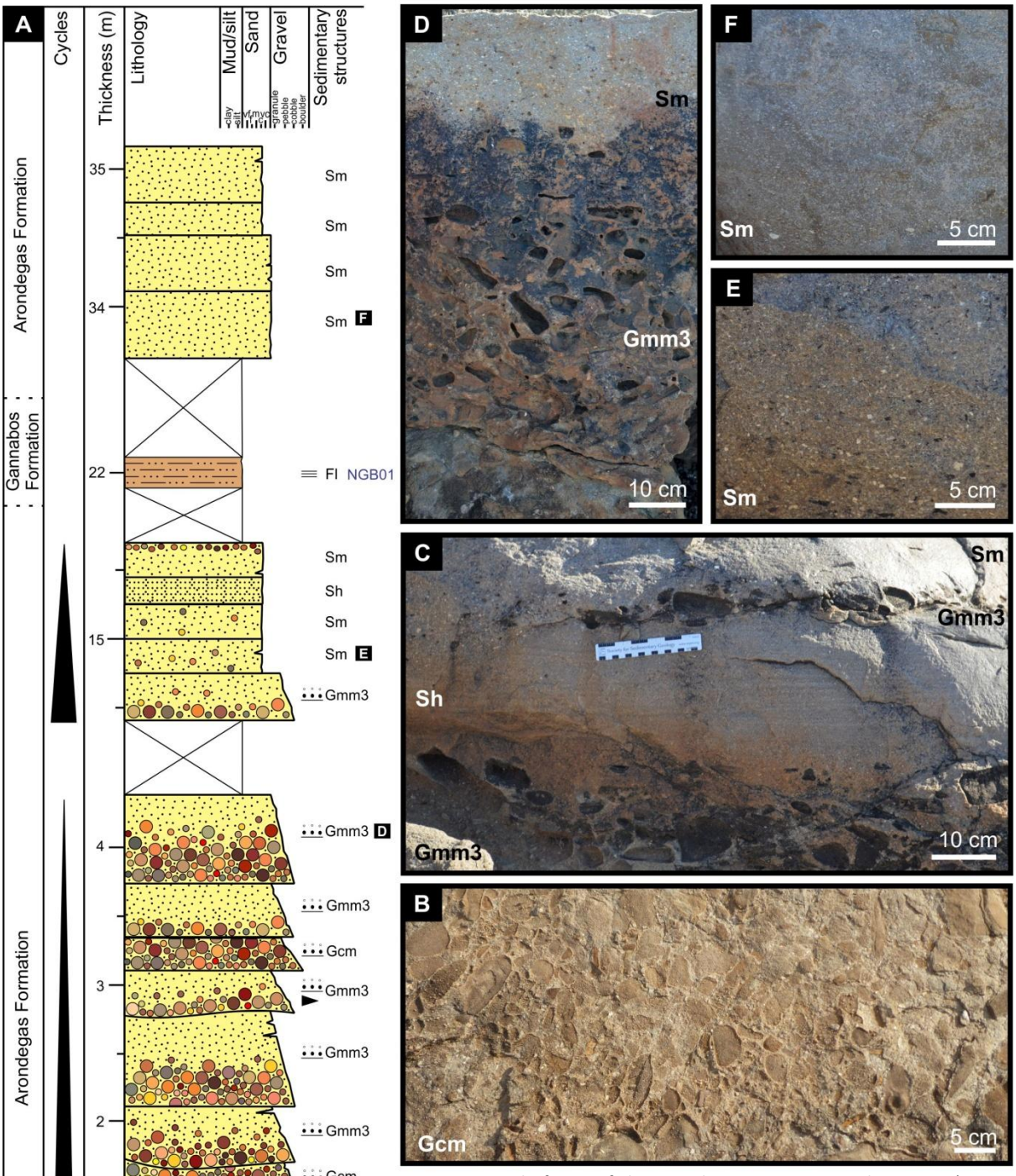

Figure 4.8. Lithofacies of the Arondegas Formation at log site 5 (Figure 2.3; 30°45'44.0"S, 18°25'55.0"E). A) Sedimentological log showing the interfingering nature between the Arondegas and Gannabos Formations. B) Clast-supported, massive conglomerate beds (Gcm). C) Succession of weakly graded, matrix-supported conglomerate beds (Gmm3) interbedded with a horizontally laminated sandstone (Sh). D) Normal graded matrix-supported, massive conglomerate bed (Gmm3) with weathered carbonate clasts. E) Immature, poorly-sorted massive sandstone with feldspar clasts (Sm). F) Mature, well-sorted massive sandstone (Sm).

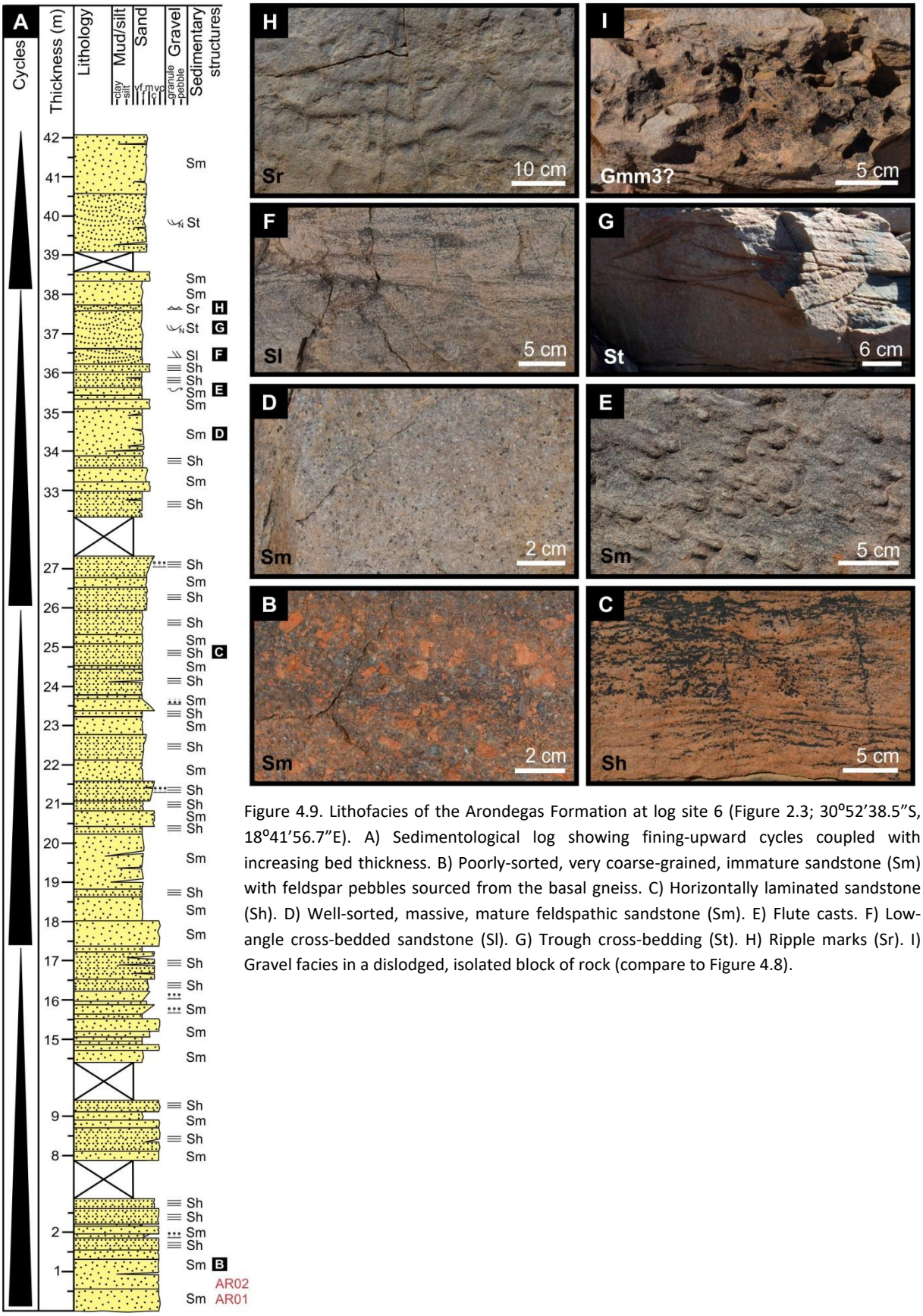

Figure 4.9. Lithofacies of the Arondegas Formation at log site 6 (Figure 2.3; 30°52'38.5"S, 18°41'56.7"E). A) Sedimentological log showing fining-upward cycles coupled with increasing bed thickness. B) Poorly-sorted, very coarse-grained, immature sandstone (Sm) with feldspar pebbles sourced from the basal gneiss. C) Horizontally laminated sandstone (Sh). D) Well-sorted, massive, mature feldspathic sandstone (Sm). E) Flute casts. F) Low-angle cross-bedded sandstone (Sl). G) Trough cross-bedding (St). H) Ripple marks (Sr). I) Gravel facies in a dislodged, isolated block of rock (compare to Figure 4.8).

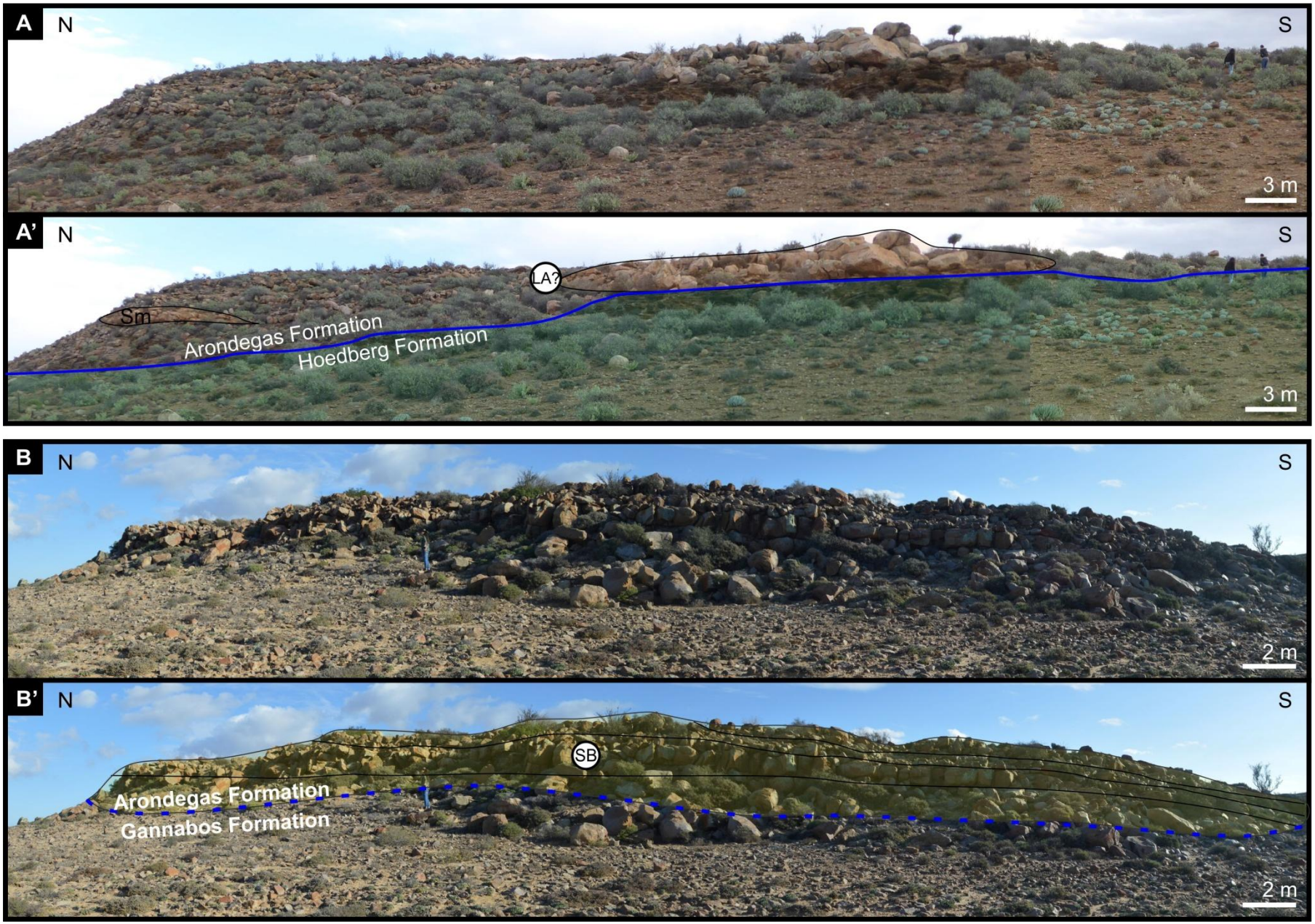

Figure 4.10. Facies mapping of the architectural elements of the Arondegas Formation using photomosaics at log site 5. Paired images show the original outcrop and the interpretive overlays (AEs in white circles). A-A') Contact (blue line) between the Hoedberg and Arondegas Formations exposed at Draaihoek farm. B-B') Laterally extensive, sheet-like sandstone beds (SB) form the second coarse-grained unit at Draaihoek farm with the Gannabos Formation interfingered between the two coarse-grained units (refer to Figure 4.8).

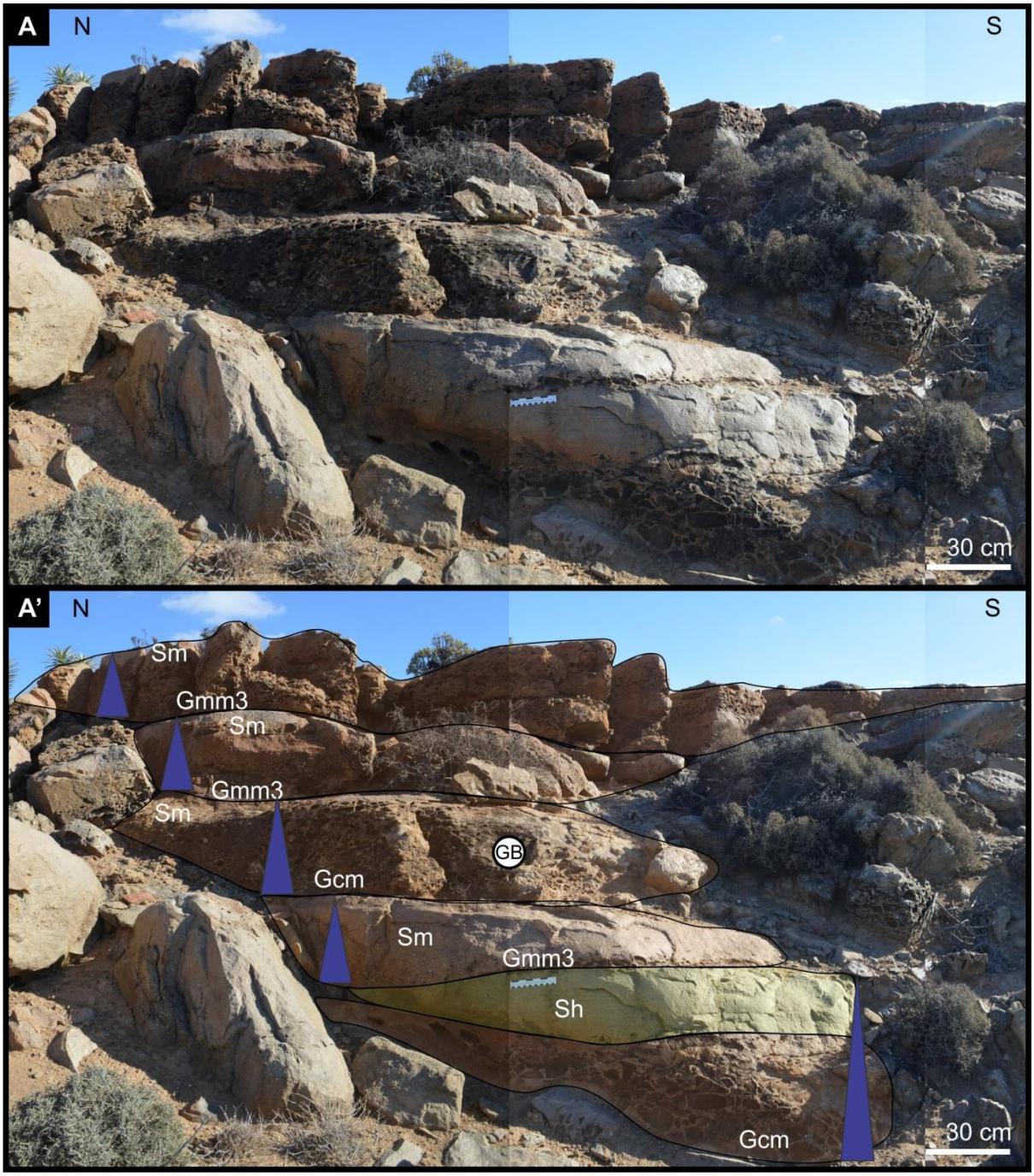

Figure 4.11. Facies mapping of the architectural elements of the Arondegas Formation using photomosaics at log site 5. Paired images show the original outcrop and the interpretive overlays (AEs in white circles). A-A') Lens shaped, normally graded gravel beds (GB) with erosional bases.

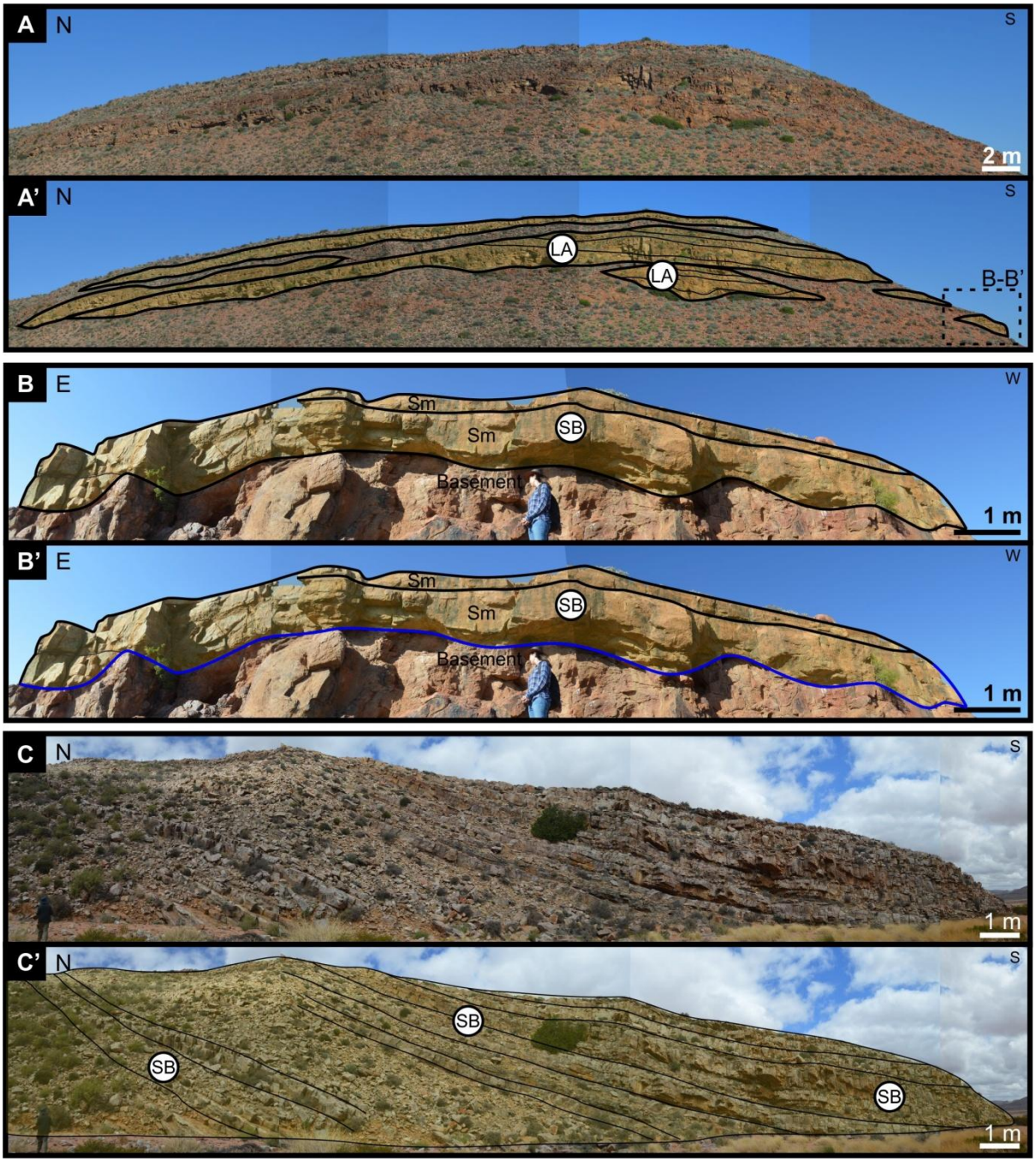

Figure 4.12. Facies mapping of the architectural elements of the Arondegas Formation using photomosaics. Paired images show the original outcrop and the interpretive overlays (AEs in white circles). A-A') Laterally accreted (LA) sandstone beds at log site 6. Inset shows location of panel B. B-B') Erosive contact (blue line) between the basement rocks and vertically stacked sand bodies (SB). C-C') Laterally extensive, vertically stacked sandstone beds (SB).

4.2 Clast counts

Clast counts, aimed at better understanding the ancient depositional conditions, were conducted in a total of 12 beds at two successive units of the Arondegas Formation at log site 5 on the Draaihoek farm (30°45'44.0"S, 18°25'55.0"E; Figures 2.4, 4.8, 4.10 and 4.11). The two units represent a total vertical stratigraphic thickness of 35 m, with average bed thickness of 30 cm with bed 4 yielding no clast fraction and subsequently omitted from the figures (Figure 4.8A). The lower unit contains predominantly matrix-supported carbonate-clast conglomerate beds, whereas the upper unit only contains sandstones with scattered clasts that comprise 5% of the total rock, making these beds conglomeratic sandstones (Figure 4.8).

The carbonate-clast conglomerate beds are unique, because they have not been documented elsewhere in the Arondegas Formation. Measurements were made on *in situ* clasts as well as moulds of clasts. The latter resulted from the dissolution of the carbonate clasts due to recent, surficial chemical weathering of the outcrops. All counted clasts were subangular to subrounded.

Approximately 88% of the 1100 counted clasts are pebble-sized ranging from 0.4 to 6.4 cm in diameter. About 50% of the clasts are large and very large pebbles with diameters between 1.6-6.4 cm (Figure 4.13). Cobbles (6.4-25.6 cm) account for ~9% of the counted clasts, and boulders (>25.6 cm in diameter) are very rare (see inset in Figure 4.13; Appendix B). Feldspar clasts are generally ~0.4 cm in size with the largest feldspar clast being ~1 cm in diameter. No correlation exists between the average clast size and bed thickness (Appendix B: Table B2). Systematic clast size changes across the sampled layers are also lacking as the clast size classes are similarly represented in each of the beds (Figure 4.14).

Carbonate clasts are the most abundant as they are present in all beds and account for 42% of the measured clasts (460 clasts out of 1100; Figure 4.15; Appendix B). Feldspar clasts increase in frequency from bed 5 and account for 23% of the measured clasts (256 clasts out of 1100) whereas vein quartz clasts account for 20% (223 clasts out of 1100; Figure 4.15). Quartzite clasts constitute 8% of the measured clasts (66 clasts out of the 1100) and sandstone, igneous and chert fragments make up the remaining 7% of the clasts. Igneous rock fragments are only present in the basal two beds and chert fragments in bed 1, 2, 3 and 10 (Figure 4.15).

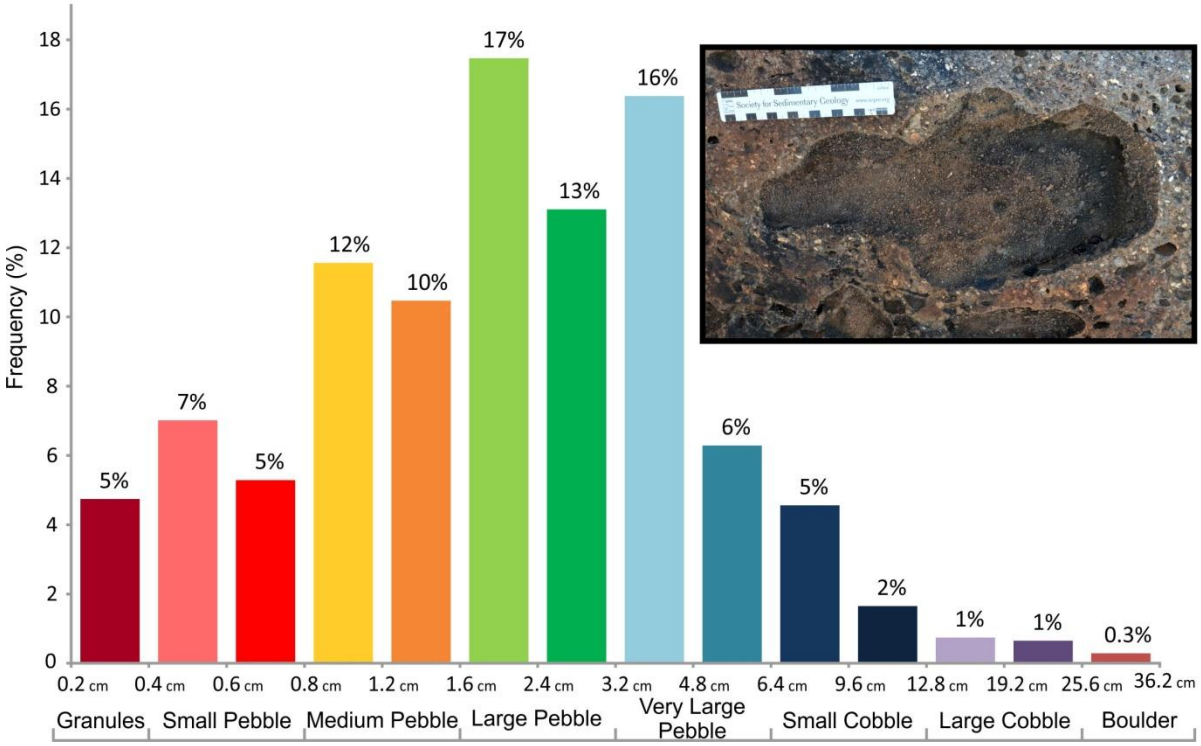

Figure 4.13. Clast size histogram of the 1100 clasts in the conglomerates of the Arondegas Formation. The majority of the clasts are medium to very large pebbles with ~ 70% of the clasts ranging in size from 0.8 to 4.8 cm. Inset shows the largest clast, which is a ~33.4 cm diameter boulder (mould of a subangular carbonate clast) observed in bed 9 on the Draaihoek farm.

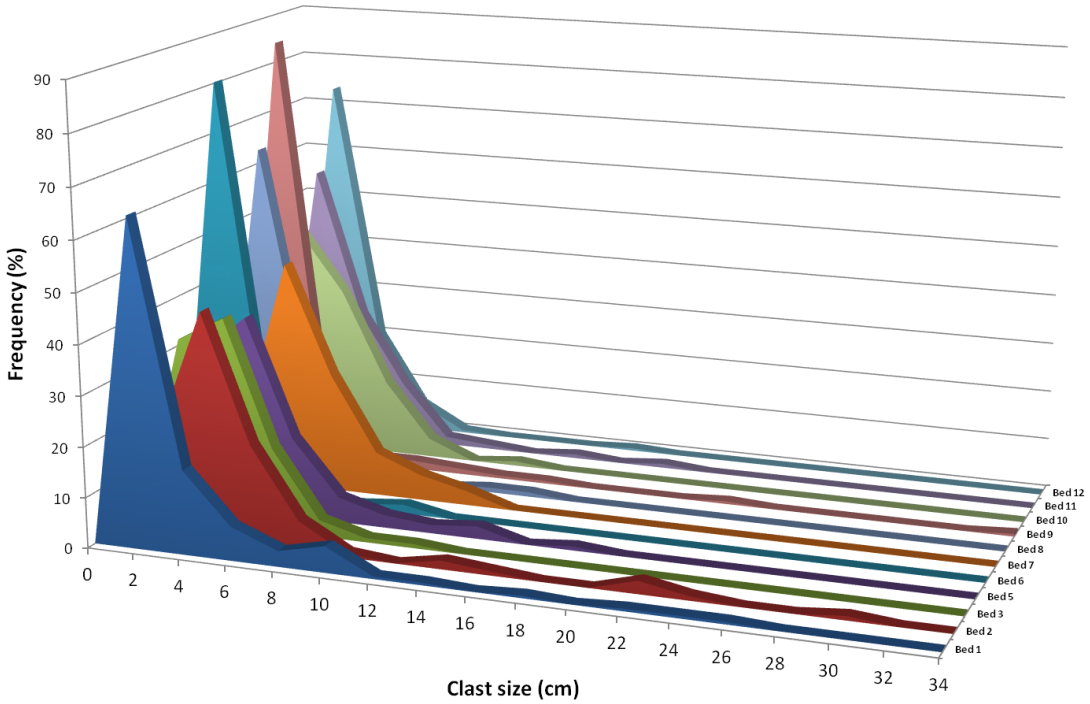

Figure 4.14. Comparative histograms of the clast size distribution in 11 conglomerate beds in the Arondegas Formation. The beds, listed in stratigraphic order from oldest to youngest, have relatively similar distribution of clast sizes and no systematic clast size change. See Figures 2.3 and 4.8, for clast count locality.

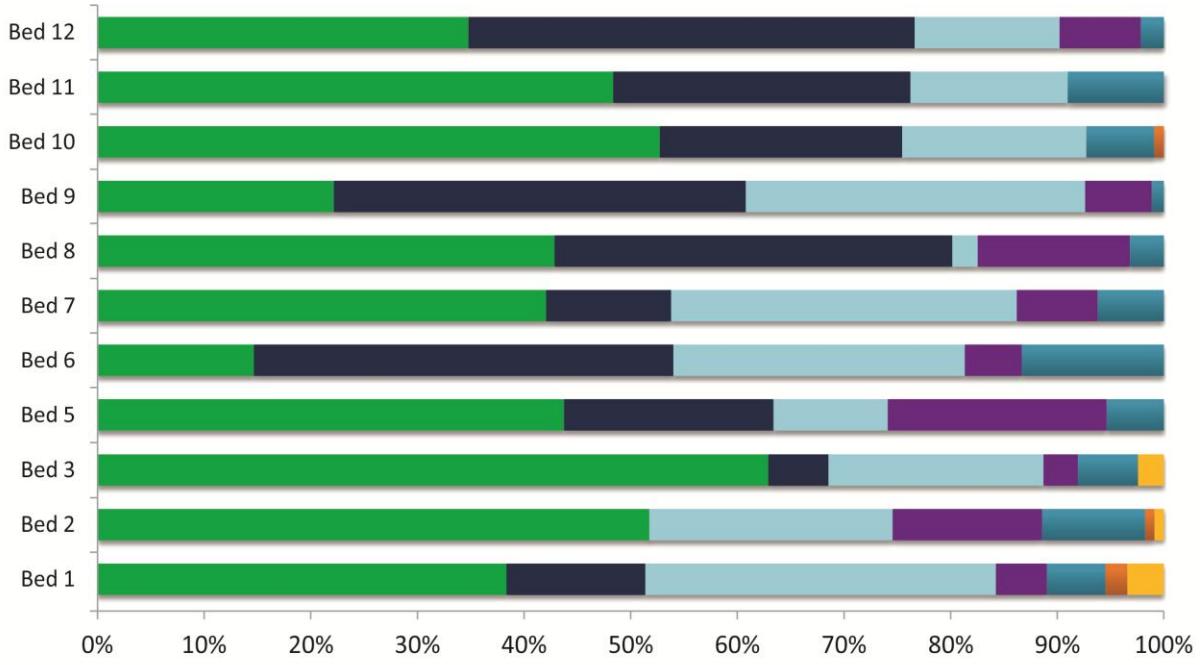

	Bed 1	Bed 2	Bed 3	Bed 5	Bed 6	Bed 7	Bed 8	Bed 9	Bed 10	Bed 11	Bed 12
Carbonate clasts	37	52	63	44	15	42	43	29	53	48	35
Feldspar clasts	13	0	6	20	39	12	37	37	23	28	42
Vein quartz	33	23	20	11	27	32	2	29	17	15	14
Quartzite	6	14	3	21	5	8	14	5	0	0	8
Sandstone RF	5	10	6	5	13	6	3	0	6	9	2
Chert	2	1	0	0	0	0	0	0	1	0	0
Igneous RF	3	1	2	0	0	0	0	0	0	0	0

Figure 4.15. Clast composition chart and table for comparing 11 conglomerate beds in the Arondegas Formation. Fragments of chert and igneous rocks are rare (10 clasts out of the 1100 clasts counted) and mainly present in the lower beds. Note the higher abundance of feldspar clasts in the upper five relative to the lower six beds (average 33% vs 15%, respectively).

4.3 U-Pb detrital zircon geochronology results

U-Pb dating was undertaken on six sandstone samples collected from the study area and two potential tuffaceous samples donated by Dr. John Almond. These eight samples span the lowermost formations i.e., Flaminkberg, Grootriet, Hoedberg, Arondegas and Gannabos Formations. U-Pb detrital zircon dating was performed in order to determine the maximum depositional ages of these formations in order to produce a geochronological framework for the lower group. The analyses of ~115 detrital zircon grains from each sample run are represented in concordia plots, which graphically illustrate the spread of the data. All the concordant U-Pb analytical zircon data is available in Table C1-C8 in Appendix C.

4.3.1 Zircon standards

The Central Analytical Facilities at the University of Stellenbosch (SU) uses three zircon standards that are ablated during the sample runs to monitor the accuracy of the measurements. The first standard, GJ1 is used to calibrate the analyses using Iolite Software (iolite-software.com) and has a

reported ID TIMS age of 608.5 ± 0.4 Ma (Jackson et al., 2004). The ages of GJ1 analyses are not an indicator of the accuracy of the study as they are calibrated to the known age. However, the remaining two standards, namely M127 and Plešovice, have been dated using high precision LA-TIMS and are used as quality controls for each run. The reported ID-TIMS age for M127 is 524 Ma (Nasdala et al., 2016) and the reported ID-TIMS age for the Plešovice zircon standard is 337.13 ± 0.37 Ma (Sláma et al., 2008). The analysed ages for M127 and Plešovice zircon standards are within error of the published ID-TIMS ages (Table 4.1). Due to the set up of the LA-ICPMS at SU, these standards were sampled amongst each detrital sample. Each run of the LA-ICPMS was able to process 500 analyses, thus FLS01, Nflbasal, ARZA02 and ARZG01 were analysed with standards $M127_a$ and $PLES_a$, whereas WGR and AR01 were analysed with the standards $M127_b$ and $PLES_b$ (Appendix C: Figure C1).

Table 4.1. Calculated ages of the standards and the corresponding sample runs.

Standard	206Pb/ 238 U age with error (Ma)	MSWD	Sample analyses linked to standard
$M127_a$	527.4 ± 1.1	0.73	FLS01, Nflbasal, ARZA02 and ARZG01
$PLES_a$	338.1 ± 1.1	0.82	
$M127_b$	524.9 ± 1.0	0.4	WGR, HOED2, AR01 and GAN2
$PLES_b$	337.0 ± 1.3	3.1	

4.3.2 Flaminkberg Formation

Two samples were collected from the base of the Flaminkberg Formation. Sample 1, FLS01, was collected from a poorly-sorted, medium-grained sandstone above the contact of the Nuwerus Gneiss (31°8'37.24”S; 18°23'55.83"E). Sample 2, Nflbasal, was sampled from a ferruginous dark pink, medium- to coarse-grained sandstone above the contact with the basement rock (30° 40' 50.3"S; 18° 16' 40.6"E). Sample locations are shown in Figure 2.3.

FLS01

The detrital zircons are clear to light brown/pink in colour and range in length from 66 to 302 µm with the majority of the grains measuring between 125 to 175 µm in diameter (Appendix C: Figure C2). The detrital zircon grain morphologies vary from euhedral to rounded as expected from a detrital sample, where the grains have undergone abrasion during transport. The smaller grains tend to be rounded, and there are a few broken grain fragments as well. The cathodoluminescence (CL) images show the majority of the grains have oscillatory zoning or broad, faint zoning indicative of crystallisation from a magma or melt reservoir (Figure 4.16; Cawood and Nemchin, 2000). There are very few bright or low luminosity zones occurring as rims as well as no evidence of overgrowth patterns thus limiting the degree of metamorphic processes observed. Xenocrystic cores are not common and there are a few with complex internal structures and inclusions.

Of the 115 analysed detrital zircon grains, 95 ages with less than 10% discordance were obtained and utilised for further age interpretations (Figure 4.17A; Appendix C: Table C1). There are clustered age peaks between 1005 to 1200 Ma with outliers at 1283 Ma, 1447 Ma and 1568 Ma (Figure 4.17B). The most dominant peak occurs at 1086 Ma and comprises 23 grains (24% of the concordant analyses). The obtained Late Mesoproterozoic age peaks (Figure 4.17) cluster in the Stenian (1000–1200 Ma), with four grains dated from the Calymmian (1400–1600 Ma) of the Early Mesoproterozoic. Detrital zircons are evaluated for metamorphic reworking by investigating their Th/U ration. There is no consensus as to the exact cut-off value but it is either regarded as 0.07 or 0.1 (Hietpas et al., 2011; Hoskin and Schaltegger, 2003; Möller et al., 2003: Rubatto, 2002). A value below 0.1 has been selected as the cut-off value for this study. The Th/U content is variable and ranges from 0.06–2.3 (Figure 4.17C). The concordant detrital zircons are largely derived from a magmatic source as only two grains have a Th/U ratio below 0.1 and two grains are at the cutoff value. The youngest detrital zircon population present in the sample clusters around 1002.7 ± 3.4 Ma with an MSWD of 1.08 at a 95% confidence limit (Figure 4.17D). The youngest grain morphologies are rounded indicative that they had undergone abrasion during transportation before deposition (Figure 4.17E).

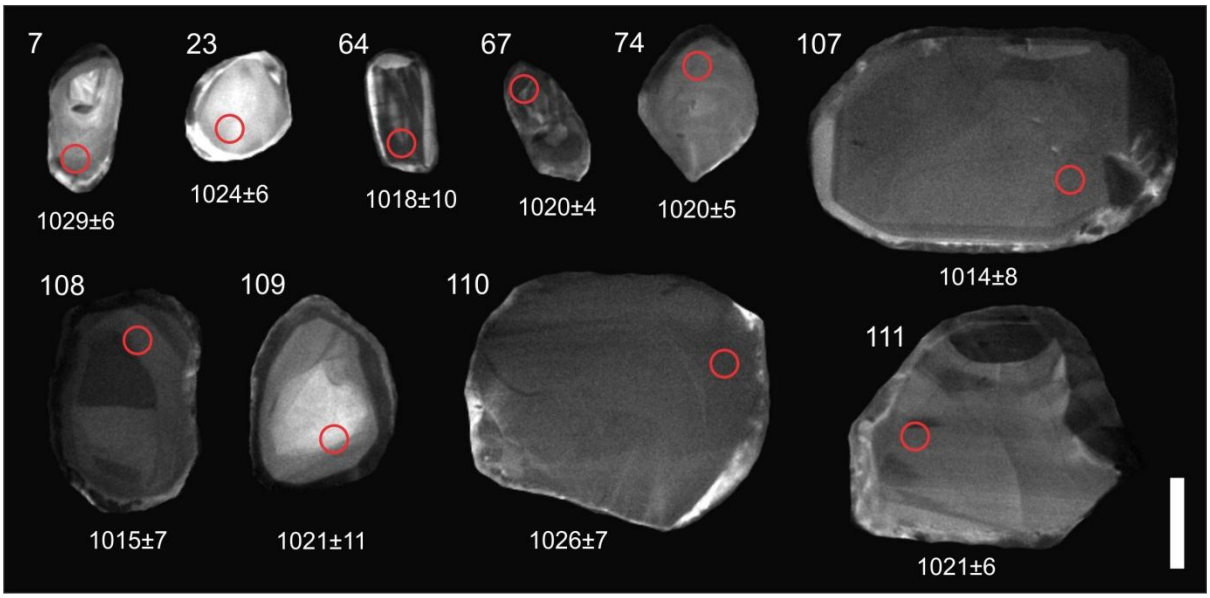

Figure 4.16. Cathodoluminescence (CL) SEM images showing the internal textures of 10 concordant detrital zircon grains from sample FLS01. Red circles indicate the sites of ablation with their corresponding ages. Grain numbers correlate to Table C1 in Appendix C. Scale bar is 100µm long.

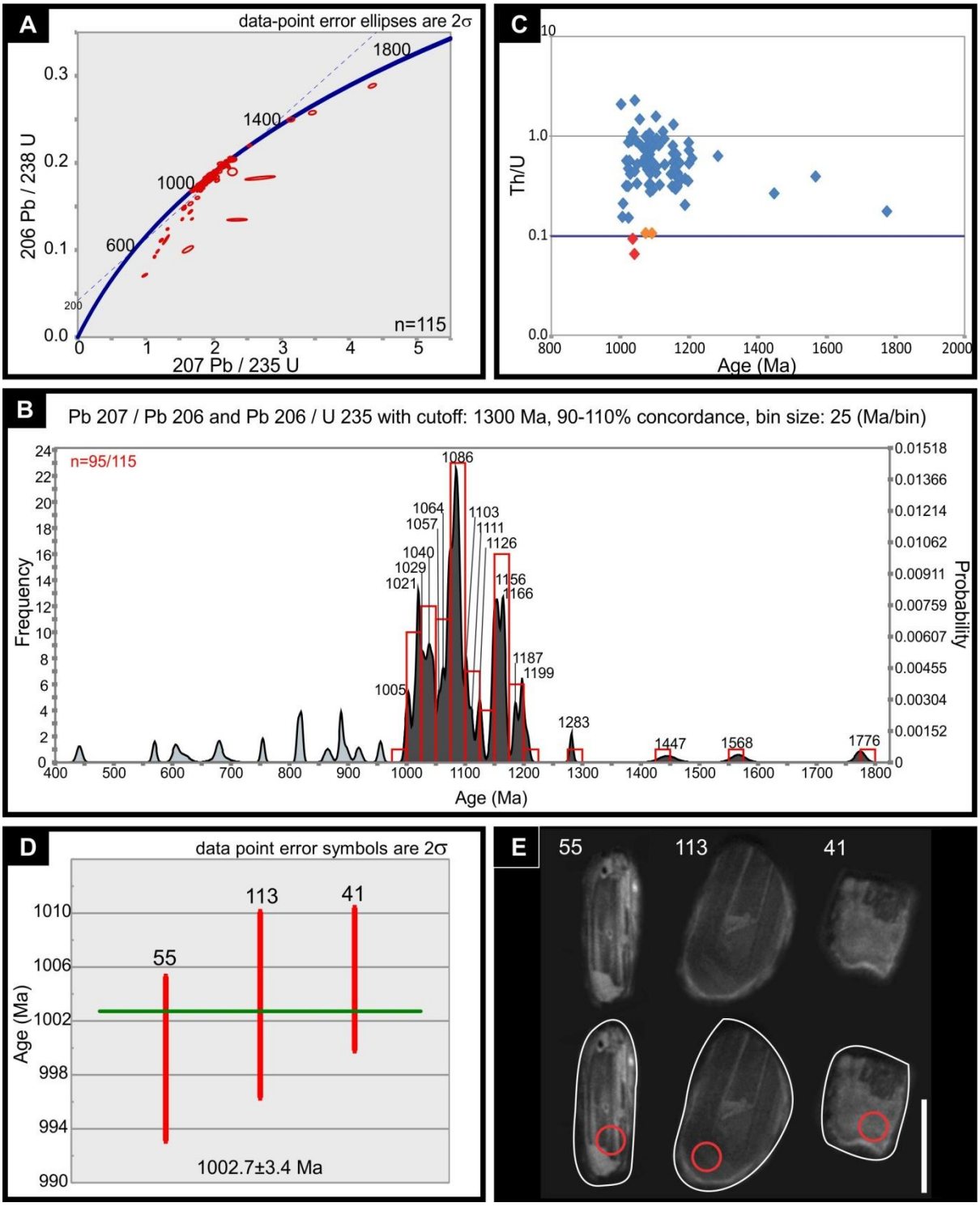

Figure 4.17. Summary of all the detrital zircon results pertaining to the basal Flaminkberg Formation: FLS01, 31°8'37.24”S; 18°23'55.83"E. A) Concordia plot of all the concordant and discordant analyses. B) Probability density plot and frequency diagram of all the analyses. The analyses shaded in dark grey indicate analyses that lie within the 10% concordance filter. C) Th/U ratio obtained for detrital zircon dates with the blue line at 0.1 signifying the dividing value between a magmatic or metamorphic origin. Metamorphic grains are plotted as red and intermediate values as orange. D) Weighted average plot of the youngest detrital zircon population with an MSWD of 1.08 at a 95% confidence interval. E) CL images of the three youngest detrital zircons with a set of outlined images depicting grain morphology. Grain 55, 113 and 41 corresponds to 55, 113 and 41 in figure D and Table C1 in Appendix C. Red circles indicate sites of ablation. Scale bar is 100 µm long.

Nflbasal

The detrital zircons are similar to the zircons from FLS01 and are clear to light brown/pink in colour. The detrital zircons range in length from 32 to 245 µm with the majority of the grains measuring between 100 to 150 µm in diameter (Appendix C: Figure C2). The zircon grain morphologies vary from euhedral to rounded, however there is a large proportion with a needle-like habit. The smaller grains tend to be rounded and there are a few broken grain fragments. The CL images show the majority of the grains have oscillatory zoning or broad, faint zoning (Figure 4.18). There are some metamorphic textures present in the form of bright or low luminosity zones occurring along the rims of the grains. There are also grains with complex internal structures as well as xenocrystic cores. Some grains have a lumpy, corroded surface texture, which indicates partial reabsorption into the melt.

Of the 105 analysed detrital zircon grains, 55 ages with less than 10% discordance were obtained and utilised for further age interpretations (Figure 4.19A; Appendix C: Table C2). There are clustered age peaks between 1037 to 1225 Ma (Figure 4.19B). The dominant peaks occur at 1083 and 1097 Ma and collectively comprises of 15 grains (27% of the concordant analyses). The age peaks span the Mesoproterozoic with the clustered age peaks occurring during the Stenian (1000–1200 Ma). The Th/U content is variable and ranges from 0.09 to 2.3 (Figure 4.19C). The concordant detrital zircons are largely derived from a magmatic source as only one grain has a value below 0.1. The youngest detrital zircon population was determined at 1034.9 ± 4.9 Ma with an MSWD of 0.27 at a 95% confidence interval (Figure 4.19D). The youngest grains were used for the weighted average calculation and there are no younger outliers. The youngest grain morphologies are rounded indicative that they have undergone abrasion during transportation before deposition (Figure 4.19E).

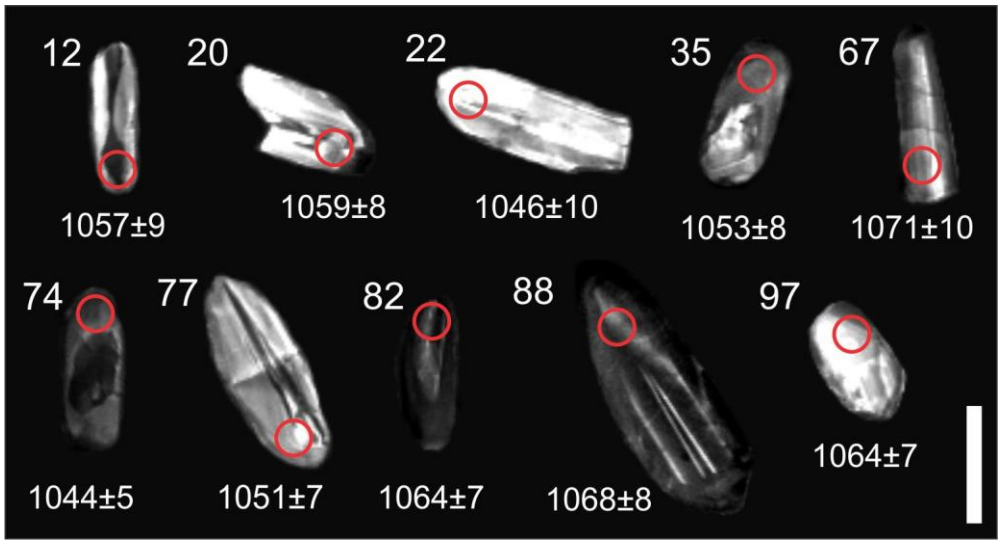

Figure 4.18. Cathodoluminescence (CL) SEM images showing the internal textures of 10 concordant detrital zircon grains from sample Nflbasal. Red circles indicate the sites of ablation with their corresponding ages. Grain numbers correlate to Table C2 in Appendix C. Scale bar is 100µm long.

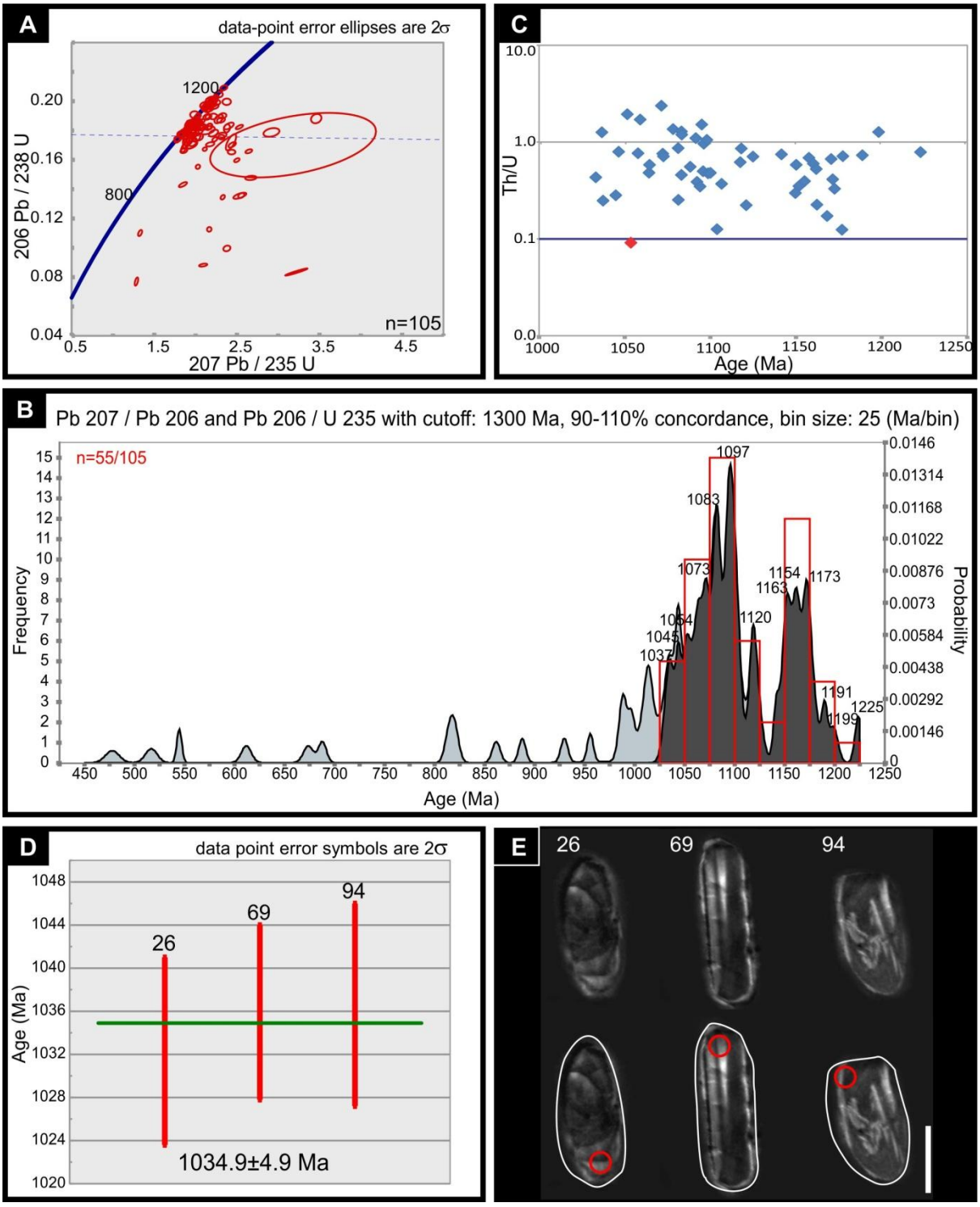

Figure 4.19. Summary of all the detrital zircon results pertaining to the basal Flaminkberg Formation sample: Nflbasal, 30°40'50.3"S; 18°16'40.6"E. A) Concordia plot of all the concordant and discordant analyses. B) Probability density plot and frequency diagram of all the analyses. The analyses shaded in dark grey indicate analyses that lie within the 10% concordance filter. C) Th/U obtained for detrital zircon dates with the blue line at 0.1 signifying the dividing value between a magmatic or metamorphic origin. Metamorphic grains are plotted as red. D) Weighted average plot of the youngest detrital zircon population with an MSWD of 0.27 at a 95% confidence interval. E) CL images of the three youngest detrital zircons with a set of outlined images depicting grain morphology. Grain 26, 69 and 94 corresponds to 26, 69 and 94 in Figure D and Table C2 in Appendix C. Red circles indicate sites of ablation. Scale bar is 100 µm long.

4.3.3 Grootriet Formation

One detrital zircon sample was collected from the interbedded shales in the upper part of the Grootriet Formation (30°42'08.6"; S, 18°16'41.6"E). The detrital zircons are clear in colour and range in length from 39 to 175 µm with the majority of the grains occurring between 75 to 100 µm (Appendix C: Figure C2). This sample had the smallest sized detrital zircons of all the six detrital samples collected. The grains vary from euhedral to rounded with elongated axes. The smaller grains tend to be rounded and there are a few broken grain fragments and cracked grains. The CL images show the majority of the grains have oscillatory zoning. There are inclusions, complex internal structures and very dark grains with faint, unorganised zoning (Figure 4.20).

Of the 112 analysed detrital zircon grains, 46 ages with less than 10% discordance were obtained and utilised for further age interpretations (Figure 4.21A; Appendix C: Table C3). There are clustered age peaks from 991 to 1207 Ma (Figure 4.21B). The most dominant peak occurs at 1069 Ma and comprises 14 grains (30% of the concordant analyses). The age peaks span the Neoproterozoic and Mesoproterozoic Eras with the clustered age peaks largely occurring during the Stenian of the Late Mesoproterozoic. There are two outliers at 1664 Ma and 1781 Ma and these are from the Statherian (1600–1800 Ma; Late Palaeoproterozoic). The Th/U content is variable and ranges from 0.12–1.8 (Figure 4.21C). The concordant detrital zircons are largely derived from a magmatic source as all the grains had a Th/U > 0.1. The youngest detrital zircon population was determined at 1012.0 ± 4.2 Ma with an MSWD of 0.29 at a 95% confidence interval (Figure 4.21D). There are younger grains present in the sample but they did not statistically represent a population. The youngest ages are from two rounded grains: 984 ± 8 Ma and 991 ± 6 Ma, both with 90% concordance (Grains 5 and 7 respectively in Figure 4.21E). The youngest grain morphologies are rounded indicative that they have undergone abrasion during transportation before deposition (Figure 4.21E).

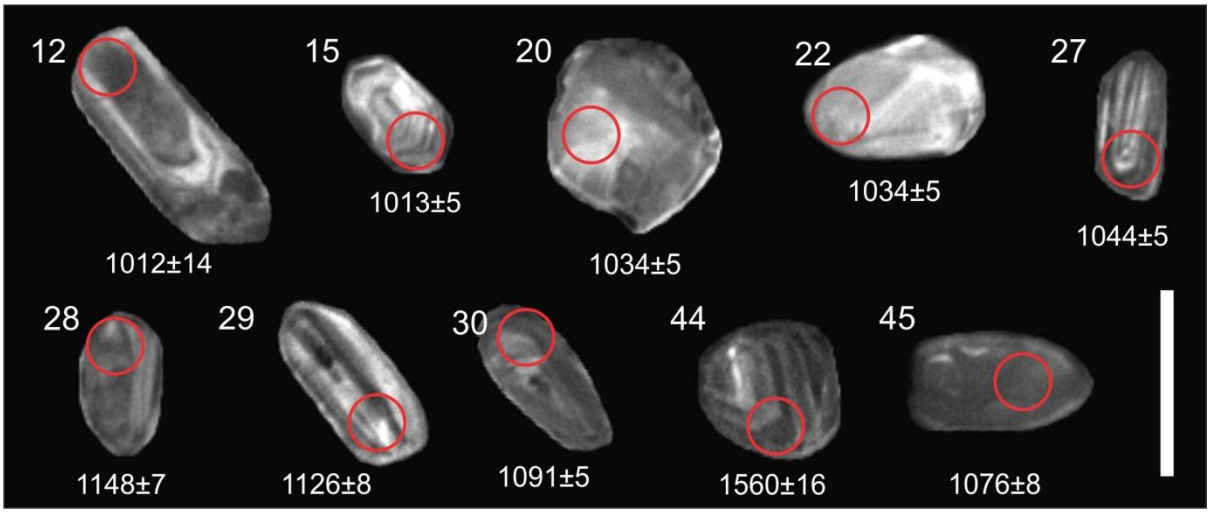

Figure 4.20. Cathodoluminescence (CL) SEM images showing the internal textures of 10 concordant detrital zircon grains from sample WGR. Red circles indicate the sites of ablation with their corresponding ages. Grain numbers correlate to Table C3 in Appendix C. Scale bar is 100µm long.

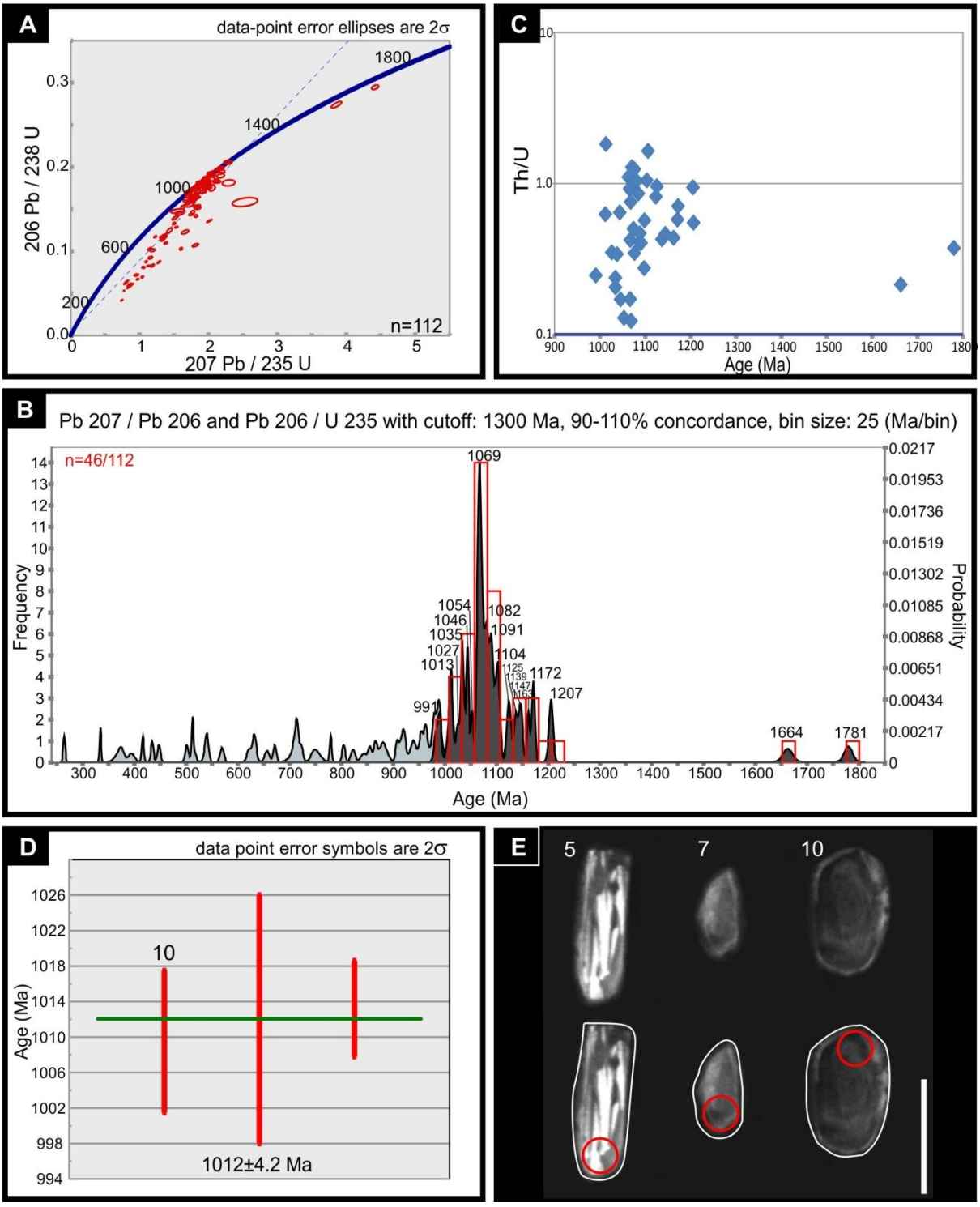

Figure 4.21. Summary of all the detrital zircon results pertaining to the upper Grootriet Formation sample: WGR, 30°42'08.6"S; 18°16'41.6"E. A) Concordia plot of all the concordant and discordant analyses. B) Probability density plot and frequency diagram of all the analyses. The analyses shaded in dark grey indicate analyses that lie within the 10% concordance filter. C) Th/U values obtained for the detrital zircon analyses and all plot above 0.1, indicating a magmatic origin. D) Weighted average plot of the youngest detrital zircon population with an MSWD of 0.29 at a 95% confidence interval. E) CL images of the three youngest detrital zircons with a set of outlined images depicting grain morphology. Grain 5 and 7 are the youngest age outliers and grain 10 corresponds to 10 in Figure D (Appendix C: Table C3). Red circles indicate sites of ablation. Scale bar is 100 µm long.

4.3.4 Hoedberg Formation

One potential tuffaceous zircon sample was collected by Dr John Almond from a thick chert unit in the lower part of the Hoedberg Formation and donated to this study (30°48'20.6"S; 18°27'29.8"E). The zircons are clear in colour and range in length from 31 to 145 µm with the majority of the grains occurring between 60 to 100 µm (Appendix C: Figure C2). The grains vary from euhedral to rounded with elongated axes. The smaller grains tend to be rounded and there are a few broken grain fragments and cracked grains. The CL images show the majority of the grains have oscillatory zoning. There are inclusions, complex internal structures and some very dark grains with faint, unorganised zoning (Figure 4.22).

Of the 114 analysed grains, 67 zircon ages with less than 10% discordance were obtained and utilised for further age interpretations (Figure 4.23A; Appendix C: Table C4). There are clustered age peaks from 970 to 1283 Ma (Figure 4.23B). The most dominant peak occurs at 1065 Ma and comprises 11 grains (10% of the concordant analyses). The age peaks span the Neoproterozoic and Mesoproterozoic Eras with the clustered age peaks largely occurring during the Stenian of the Late Mesoproterozoic. There is one outlier before the clustered peaks at 539 Ma from the Cambrian (488–542 Ma) and two outliers at 1604 Ma and 1781 Ma, from the Statherian (1600–1800 Ma; Late Palaeoproterozoic). The Th/U content is variable and ranges from 0.04–1.6 (Figure 4.23C). The concordant zircons are largely derived from a magmatic source as only four grains had a Th/U < 0.1. The youngest detrital zircon population present in the sample clusters around 987.5 ± 4.4 Ma with an MSWD of 0.34 at a 95% confidence interval (Figure 4.23D). There are younger grains present in the sample but they did not statistically represent a population. The youngest ages are from two rounded grains: 539 ± 4 Ma with 90% concordance and 969 ± 19 Ma with 98% concordance (Grains 25 and 33 respectively in Figure 4.23E). The youngest grain morphologies are rounded indicative that they have undergone abrasion during transportation before deposition however grain A does have a relic euhedral morphology (Figure 4.23E).

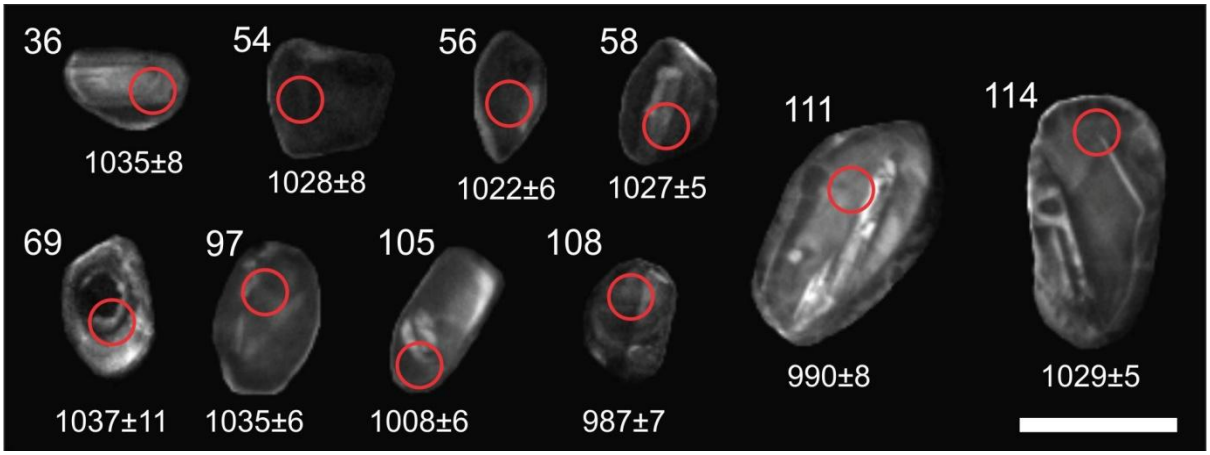

Figure 4.22. Cathodoluminescence (CL) SEM images showing the internal textures of 10 concordant detrital zircon grains from sample HOED2. Red circles indicate the sites of ablation with their corresponding ages. Grain numbers correlate to Table C4 in Appendix C. Scale bar is 100µm long.

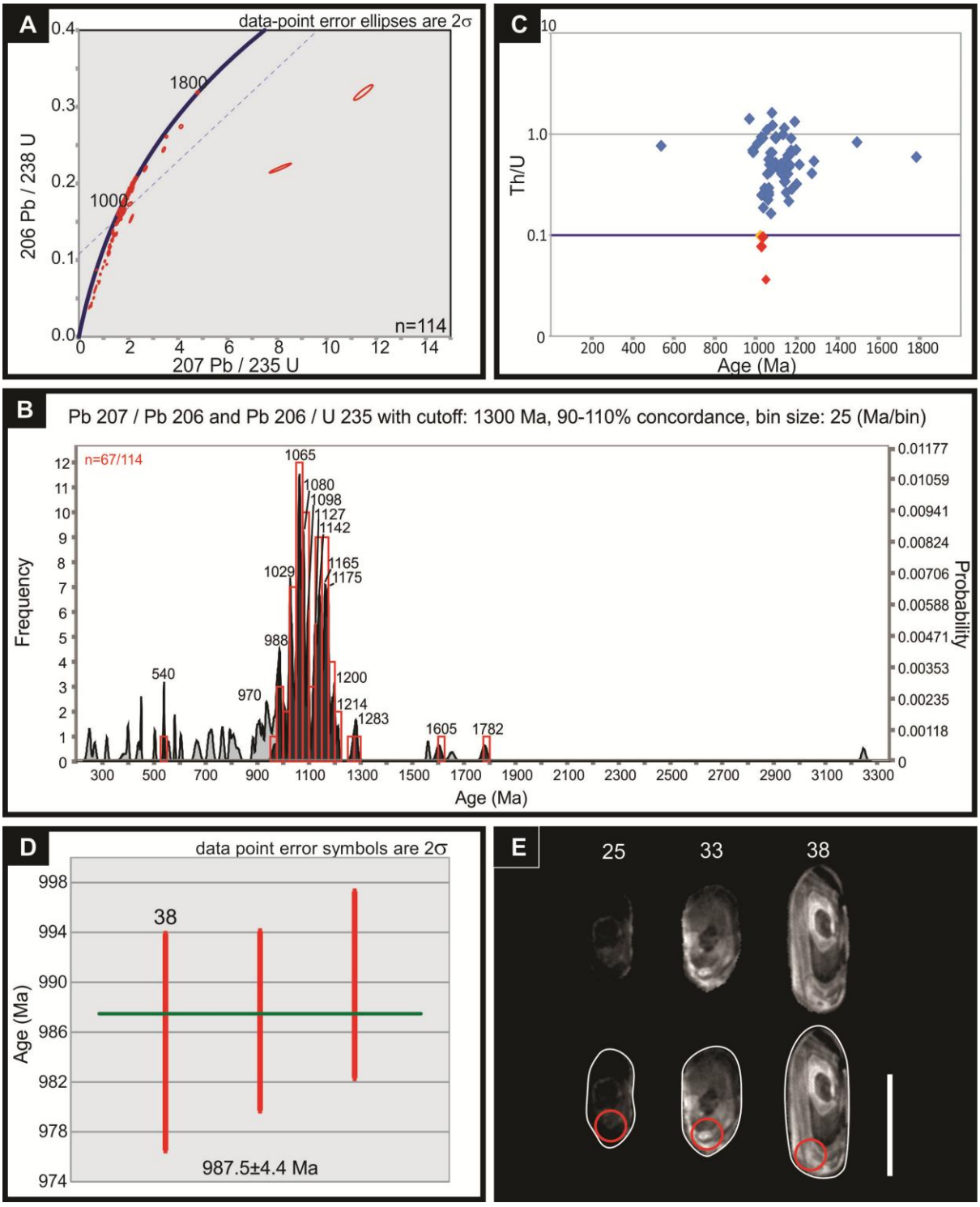

Figure 4.23. Summary of all the zircon results pertaining to the lower Hoedberg Formation sample: HOED2, 30°48'20.6"S; 18°27'29.8"E. A) Concordia plot of all the concordant and discordant analyses. B) Probability density plot and frequency diagram of all the analyses. The analyses shaded in dark grey indicate analyses that lie within the 10% concordance filter. C) Th/U obtained for zircon dates with the blue line at 0.1 signifying the dividing value between a magmatic or metamorphic origin. Metamorphic grains are plotted as red. D) Weighted average plot of the youngest zircon population with an MSWD of 0.34 at a 95% confidence interval. E) CL images of the three youngest zircons with a set of outlined images depicting grain morphology. Grains 25 and 33 are the youngest outliers and grain 38 corresponds to 38 in Figure D (Appendix C: Table C4). Red circles indicate sites of ablation. Scale bar is 100 µm long.

4.3.5 Arondegas Formation

Three samples were collected from the Arondegas Formation. Due to the varying nature of the basal contact, two samples were collected at the base of the formation. One sample, ARZA02, was collected from a moderately-sorted, medium- to coarse-grained sandstone at a section where the Arondegas Formation overlies the Hoedberg Formation. The second sample, AR01, was collected from a poorly sorted, massive coarse-grained sandstone above the contact between the Arondegas Formation and Nuwerus Gneiss (i.e., at this locality, the underlying three formations are not preserved). The third sample, ARZG01, was collected from a poorly-sorted, coarse-grained sandstone at the upper contact of the Arondegas Formation with the Gannabos Formation.

ARZA02

The detrital zircons are clear to light brown/pink in colour and range in length from 39 to 175 µm with the majority of the grains occurring between 75 to 100 µm (Appendix C: Figure C2). The grains vary from euhedral to rounded with elongated axes. There is a large proportion with a needle-like habit. The smaller grains tend to be rounded and there are a few broken grain fragments and cracked grains. The CL images show the majority of the grains have oscillatory zoning or broad, faint zoning, indicative of crystallisation from a magma or melt reservoir (Cawood and Nemchin, 2000). Some grains show complex internal structures, inclusions as well as bright or dull rims indicative of metamorphic alteration (Figure 4.24).

Of the 115 analysed grains, 82 detrital zircon ages with less than 10% discordance were obtained and utilised for further age interpretations (Figure 4. 25A; Appendix C: Table C5). There are clustered age peaks from 999 to 1264 Ma (Figure 4. 25B). The dominant peaks occur at 1054 and 1072 Ma and are collectively comprised of 25 grains (30% of the concordant analyses). The age peaks occur within the Late Mesoproterozoic with clustered age peaks largely occurring during the Stenian (1000–1200 Ma). The Th/U content is variable and ranges from 0.15–1.25 (Figure 4. 25C). The concordant detrital zircons are largely derived from a magmatic source as all the grains have a Th/U value above 0.1. The youngest detrital zircon population present in the sample clusters around 1018.8 ± 2.7 Ma with an MSWD of 0.93 at a 95% confidence interval (Figure 4.25D). There is a young outlier at 998 ± 5 Ma with 90% concordance; however it did not statistically represent a zircon population and was not included in the weighted average calculation (Grain 91 in Figure 4. 25E). The youngest grains are rounded indicating abrasion in transportation before deposition (Figure 4. 25E).

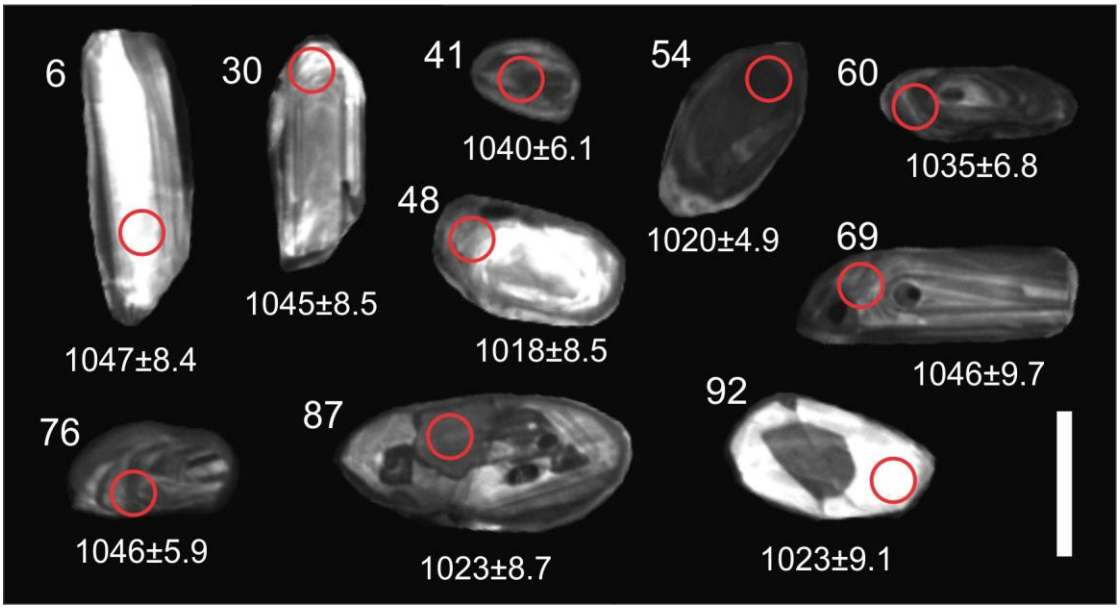

Figure 4.24. Cathodoluminescence (CL) SEM images showing the internal textures of 10 concordant detrital zircon grains from sample ARZA02. Red circles indicate the sites of ablation with their corresponding ages. Grain numbers correlate to Table C5 in Appendix C. Scale bar is 100µm long.

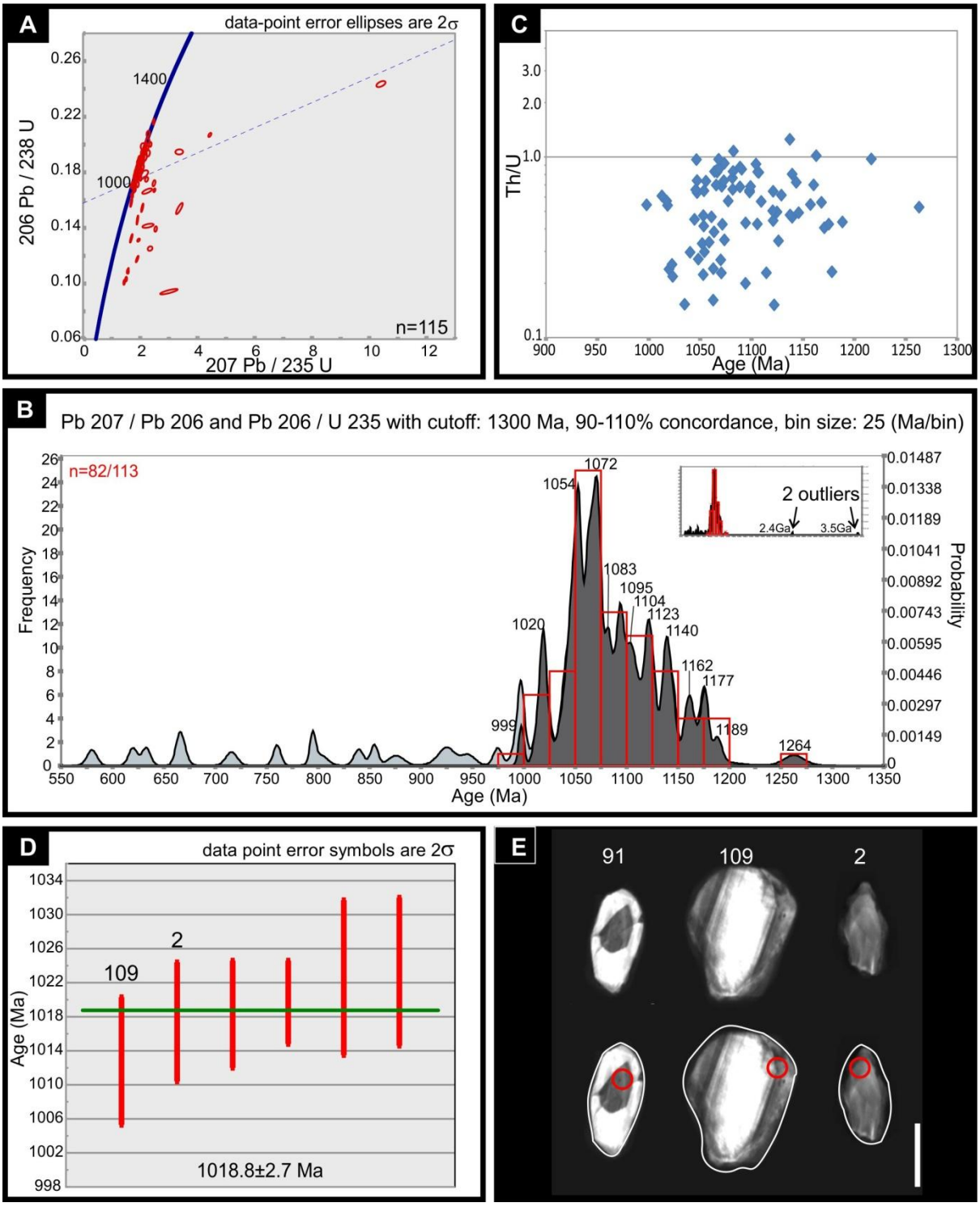

Figure 4.25. Summary of all the detrital zircon results pertaining to the basal Arondegas Formation sample: ARZA02, 30°44'17.2"S; 18°16'37.6"E. A) Concordia plot of all the concordant and discordant analyses. B) Probability density plot and frequency diagram of all the analyses. The analyses shaded in dark grey indicate analyses that lie within the 10% concordance filter. Inset shows that there two discordant outliers between 2.4 Ga and 3.6 Ga. C) Th/U plot showing all the values plotting above the magmatic/metamorphic dividing line between 0.07 - 0.1. D) Weighted average plot of the youngest detrital zircon population with an MSWD of 0.93 at a 95% confidence interval. E) CL images of the three youngest detrital zircons with a set of outlined images depicting grain morphology. Grain 91 is the youngest outlier and grain 109 and 2 correspond to 109 and 2 in Figure D (Appendix C: Table C5). Red circles indicate sites of ablation. Scale bar is 100 µm long.

AR01

The detrital zircons are clear to light brown/pink in colour and ranged in length from 50 to 313 µm with the majority of the grains measuring between 75 to 150 µm in length (Appendix C: Figure C2). The grains vary from euhedral to rounded, with the majority of the grains being sub-rounded. The CL images show that most of the grains have oscillatory zoning or broad, parallel zoning. Some grains show complex internal structures, inclusions and cracks (Figure 4.26).

Of the 114 analysed detrital zircon grains, only 35 concordant ages (less than 10% discordant) were obtained and utilised for further age interpretations (Figure 4.27A; Appendix C: Table C6). This was the least concordant sample. There are clustered age peaks from 976 to 1138 Ma with an old outlier at 1435 Ma (Figure 4.27B). The most dominant peak occurs at 1040 Ma and comprises 16 grains (46% of the concordant analyses). The age peaks occur within the Late Mesoproterozoic with the clustered age peaks occurring during the Stenian (1000–1200 Ma). There is one old outlier from the Calymmian (1400–1600 Ma). The Th/U content is variable and ranges from 0.06–2.1 (Figure 4.27C). The concordant detrital zircons are largely derived from a magmatic source as only one grain has a Th/U below 0.1. The youngest detrital zircon population present in the sample clusters around 1021.6 ± 3.5 Ma with an MSWD of 0.067 at a 95% confidence interval (Figure 4.27D). There are three young outliers at 974 ± 4 Ma with 92% concordance, 977 ± 5 Ma with 92% concordance and 1005 ± 5 Ma with 95% concordance (Grains 46, 39 and 71 in figure 4.27E respectively), however these grains were not included in the weighted average calculation as they did not statistically represent a population. The youngest grains are rounded, which is an indication of abrasion during transportation before deposition occurred (Figure 4.27E).

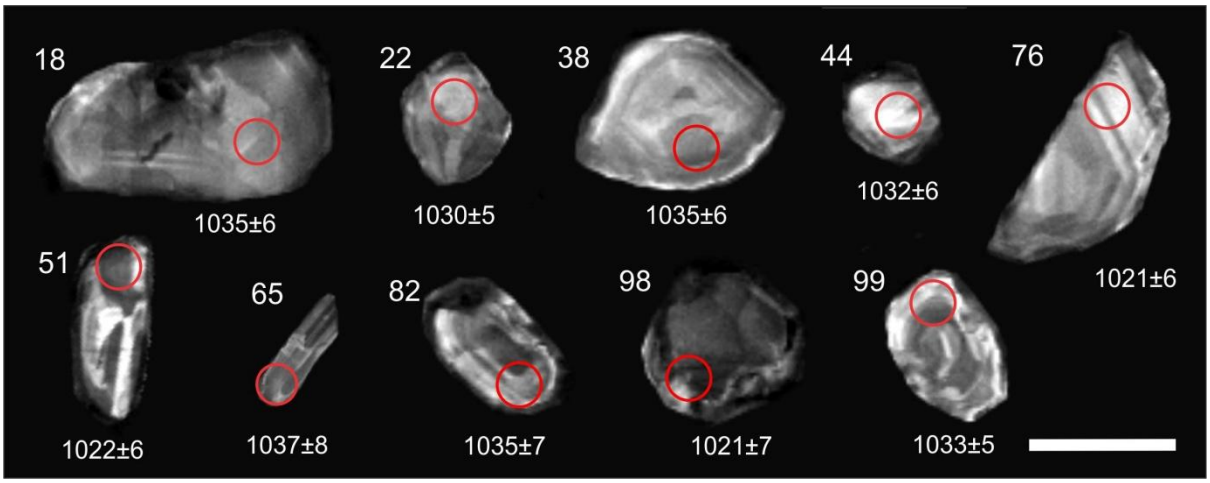

Figure 4.26. Cathodoluminescence (CL) SEM images showing the internal textures of 10 concordant detrital zircon grains from sample AR01. Red circles indicate the sites of ablation with their corresponding ages. Grain numbers correlate to Table C6 in Appendix C. Scale bar is 100µm long.

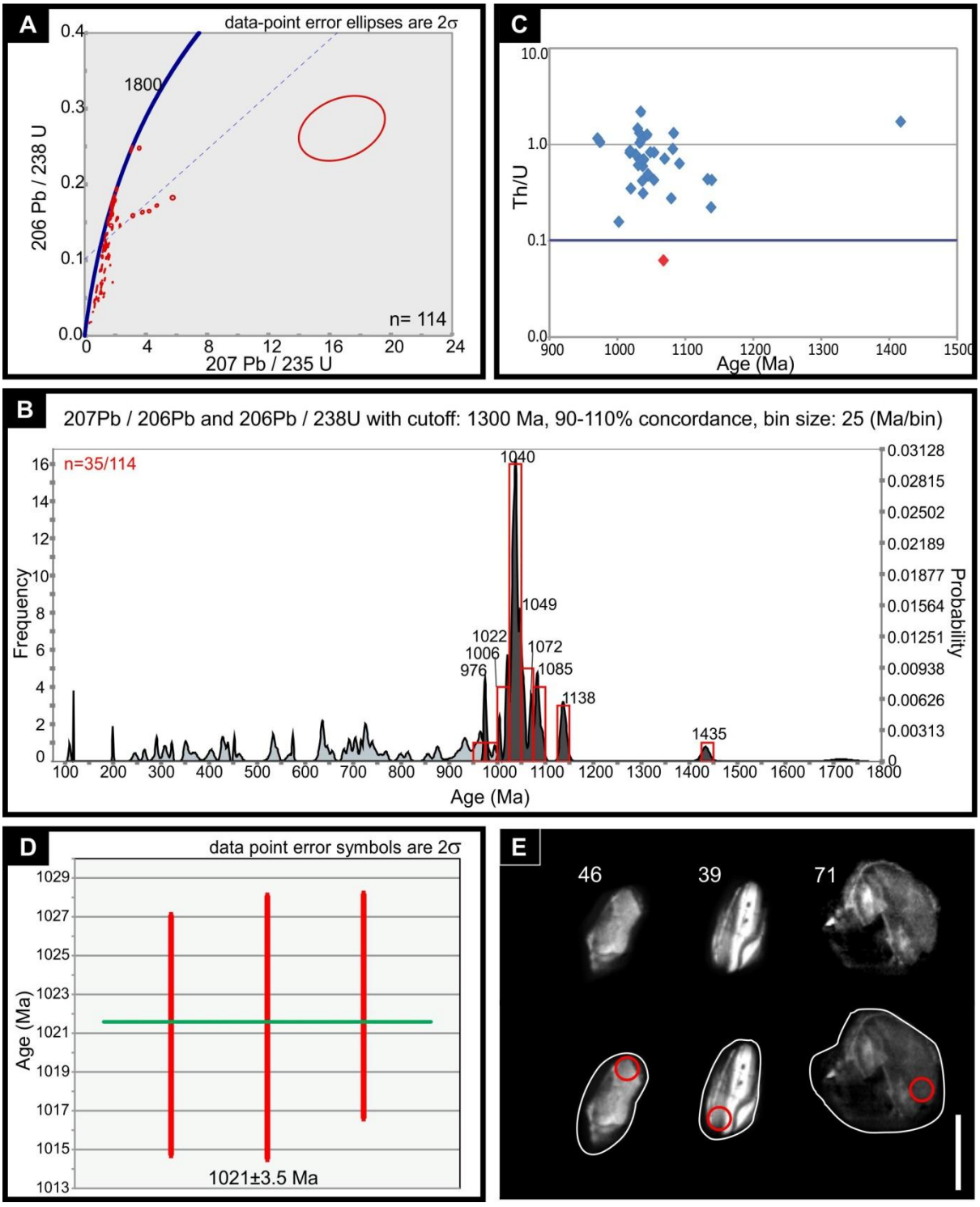

Figure 4.27. Summary of all the detrital zircon results pertaining to the basal Arondegas Formation sample: AR01, 30°52'40.1"S; 18°41'50"E. A) Concordia plot of all the concordant and discordant analyses. B) Probability density plot and frequency diagram of all the analyses. The analyses shaded in dark grey indicate analyses that lie within the 10% concordance filter. C) Th/U obtained for the detrital zircon dates with the blue line at 0.1 signifying the dividing value between a magmatic or metamorphic origin. Metamorphic grains are plotted as red. D) Weighted average plot of the youngest detrital zircon population with an MSWD of 0.067 at a 95% confidence interval. E) CL images of the three youngest detrital zircons with a set of outlined images depicting their grain morphology (Appendix C: Table C6). Red circles indicate sites of ablation. Scale bar is 100 µm long.

ARZG01

The detrital zircons are clear to light brown/pink in colour and ranged in length from 41 to 317 µm with the majority of the grains occurring between 100 to 150 µm (Appendix C: Figure C2). The grains vary from euhedral to rounded. There is a large proportion with a needle-like habit and there are a few broken grain fragments, which tend to be of larger grains. The CL images show the majority of the grains have broad, faint zoning or complex internal structures reminiscent of metamorphic textures. Oscillatory zoning is not common in this sample and the grains have inclusions (Figure 4.28).

Of the 115 analysed detrital zircon grains, 73 concordant ages (less than 10% discordant) were obtained and utilised for further age interpretations (Figure 4.29A; Appendix C: Table C7). There are clustered peaks from 1034 to 1235 Ma (Figure 4.29B). The dominant peaks occur at 1076 and 1085 Ma and are collectively comprised of 15 grains (21% of the concordant analyses). The age peaks occur within the Late Mesoproterozoic and cluster around the Stenian (1000–1200 Ma). There is one old outlier at 1753 Ma from the Statherian (1600–1800 Ma) of the Palaeoproterozoic Era. The Th/U content is variable and ranges from 0.07–1.76 (Figure 4.29C). The concordant detrital zircons are largely derived from a magmatic source as only three grains have a Th/U below 0.1 and one grain has a value at the cutoff. The youngest detrital zircon population present in the sample clusters around 1028.6 ± 5.1 Ma with an MSWD of 2.1 at a 95% confidence interval (Figure 4.29D). There is one young outlier at 1016 ± 11 Ma with 100% concordance but it was not included in the weighted average calculation as it did not statistically represent a population (Grain 37 in Figure 4.29E). The youngest grains are rounded, indicating abrasional transportation processes before deposition occurred (Figure 4.29E).

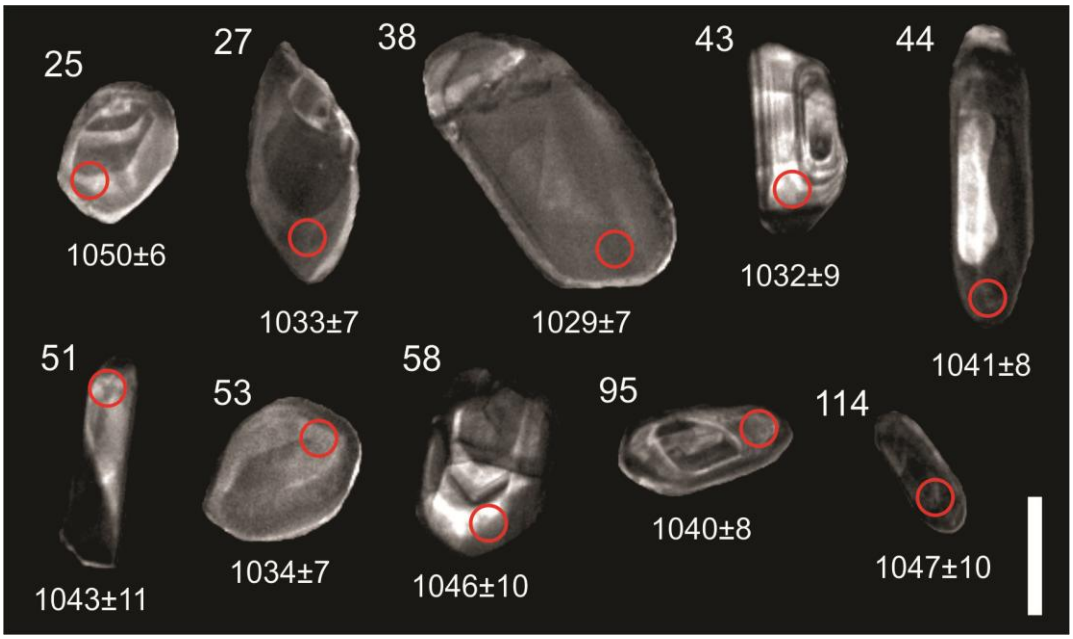

Figure 4.28. Cathodoluminescence (CL) SEM images showing the internal textures of 10 concordant detrital zircon grains from sample ARZG01. Red circles indicate the sites of ablation with their corresponding ages. Grain numbers correlate to Table C7 in Appendix C. Scale bar is 100µm long.

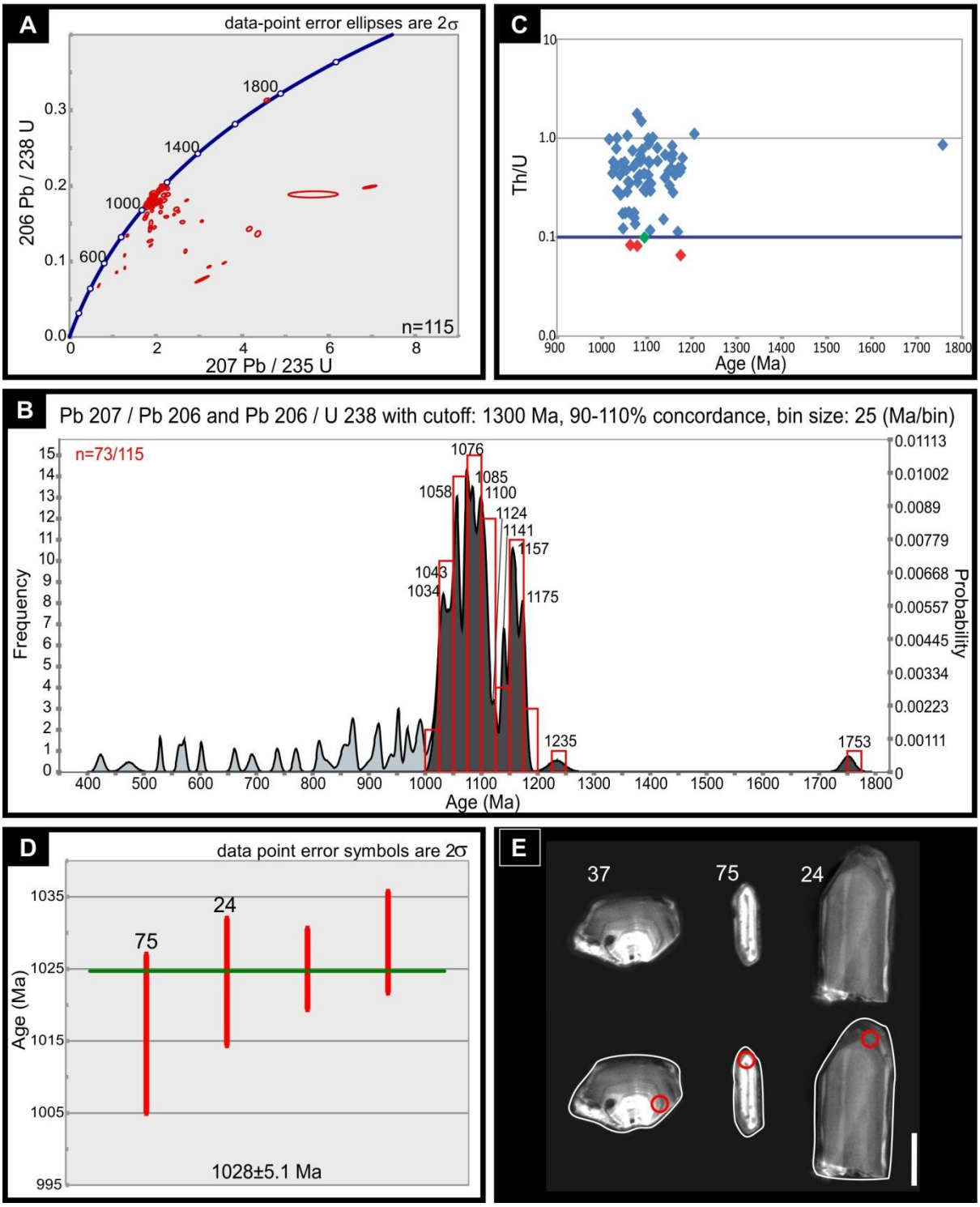

Figure 4.29. Summary of all the detrital zircon results pertaining to the upper Arondegas Formation sample: ARZG01, 30°46'49.7"S; 18°25'07.9"E. A) Concordia plot of all the concordant and discordant analyses. B) Probability density plot and frequency diagram of all the analyses. The analyses shaded in dark grey indicate analyses that lie within the 10% concordance filter. C) Th/U obtained for detrital zircon dates with the blue line at 0.1 signifying the dividing value between a magmatic or metamorphic origin. Metamorphic grains are plotted as red and intermediate values as green. D) Weighted average plot of the youngest detrital zircon population with an MSWD of 2.1 at a 95% confidence interval. E) CL images of the three youngest detrital zircons with a set of outlined images depicting grain morphology. Grain 37 is the youngest age outlier and grain 75 and 24 correspond to 75 and 24 in Figure D (Appendix C: Table C7). Red circles indicate sites of ablation. Scale bar is 100 µm long.

4.3.6 Gannabos Formation

One potential tuffaceous zircon sample was collected by Dr John Almond from a thick chert unit in the upper part of the Gannabos Formation (30°51'25.1"S; 18°27'30.2"E). The zircons are clear in colour and range in length from 38 to 207 µm with the majority of the grains occurring between 60 to 100 µm (Appendix C: Figure C2). The grains vary from euhedral to rounded with elongated axes. The smaller grains tend to be rounded and there are a few broken grain fragments and cracked grains. The CL images show the majority of the grains have oscillatory zoning. There are some inclusions, complex internal structures and some grains are very dark grains with faint, unorganised zoning (Figure 4.30).

Of the 103 analysed grains, only 22 zircon ages with less than 10% discordance were obtained and utilised for further age interpretations (Figure 4.31A; Appendix C: Table C8). Due to the low yield of concordant data, there are numerous small age peaks occurring between 539 to 1031 Ma and each peak is defined by a maximum of 3 grains (Figure 4.31B). There is no dominant age peak however nine grains (41% of the concordant analyses) are dated from 539 to 653 Ma with seven of those grains (32% of the concordant analyses) occurring within the Ediacaran (542–635 Ma). Furthermore, there are small older age peaks in the Neoproterozoic and Mesoproterozoic Eras with peaks from 943 to 1031 Ma. There are five very old ages at: 1555 ± 44 Ma (Statherian; Early Palaeoproterozoic), 1873 ± 20 Ma and 1883 ± 20 Ma (Orosirian: 1800–2050 Ma), 2073 ± 32 Ma (Early Rhyacian: 2050–2300 Ma), and 2774 ± 60 Ma (Late Neoarchaen: 2500–2800 Ma). The Th/U content is variable and ranges from 0.2–1.3 (Figure 4.31C). The concordant zircons are largely derived from a magmatic source as no grains had a Th/U < 0.1. The youngest detrital zircon population present in the sample clusters around 550.4 ± 9.8 Ma with an MSWD of 1.6 at a 95% confidence interval (Figure 4.31D). The youngest age is from a semi-rounded grain: 538 ± 4 Ma with 94% concordance (Grain 98 in Figure 4.31E). It was not used in the MSWD calculation as it did not statistically correlate with the population. The youngest grain morphologies are rounded indicative that they underwent abrasion during transportation before deposition however grain 98 does have a relic euhedral shape (Figure 4.31E).

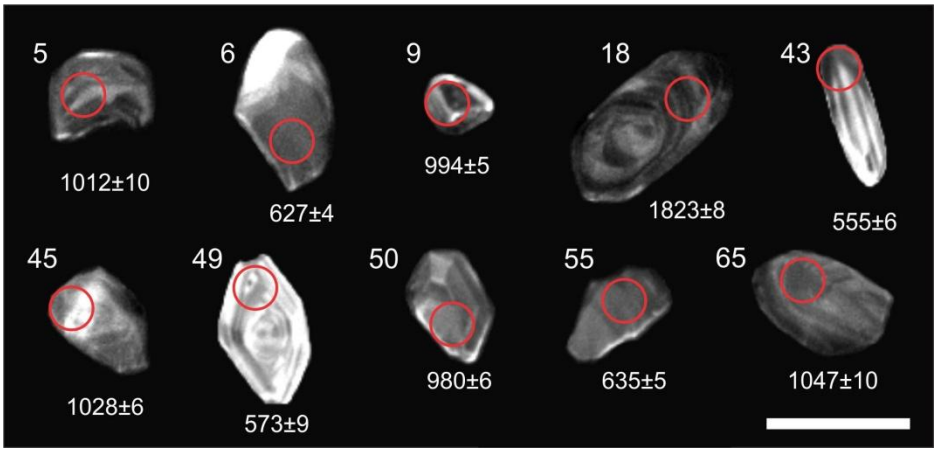

Figure 4.30. Cathodoluminescence (CL) SEM images showing the internal textures of 10 concordant detrital zircon grains from sample GAN2. Red circles indicate the sites of ablation with their corresponding ages. Grain numbers correlate to Table C8 in Appendix C. Scale bar is 100µm.

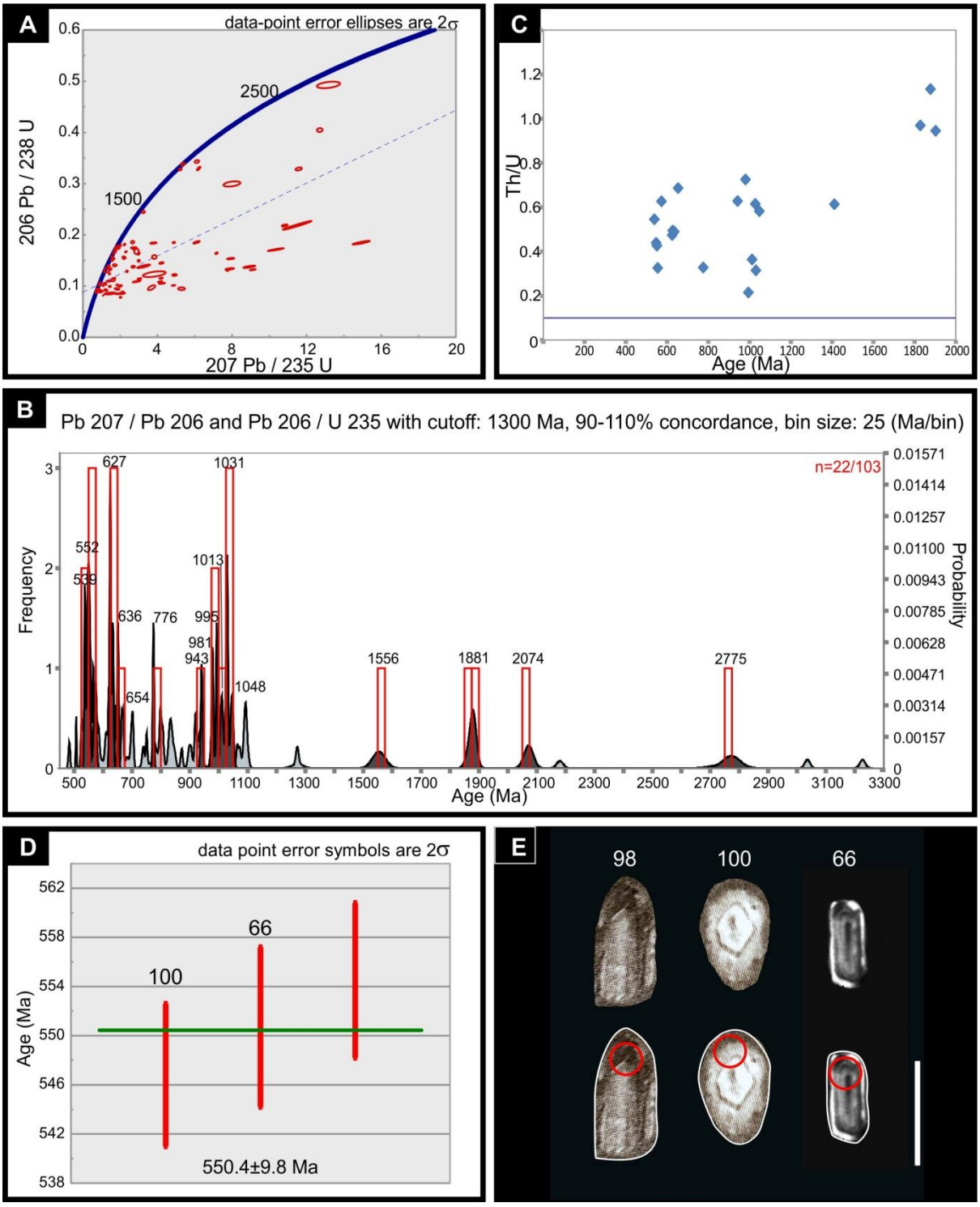

Figure 4.31. Summary of all the zircon results pertaining to the upper Gannabos Formation sample: GAN2, 30°51'25.1"S; 18°27'30.2"E. A) Concordia plot of all the concordant and discordant analyses. B) Probability density plot and frequency diagram of all the analyses. The analyses shaded in dark grey indicate analyses that lie within the 10% concordance filter. C) Th/U values obtained for the zircon analyses and all plot above 0.1, indicating a magmatic origin. D) Weighted average plot of the youngest zircon population with an MSWD of 1.6 at a 95% confidence interval. E) CL images of the three youngest zircons with a set of outlined images depicting grain morphology. Grain 98 is the youngest age outlier and grains 100 and 66 correspond to 100 and 66 in Figure D (Appendix C: Table C8). Red circles indicate sites of ablation. Scale bar is 100 µm long.

4.3.7 Summary of U-Pb detrital zircon geochronology

This section synthesises the key results from the text of each detrital zircon sample (Table 4.2).

Table 4.2. Summary of the youngest zircon populations of each detrital zircon sample and the number of concordant grains used in the age calculation. Two restricting ages are reported using the methods: 1) mean age of the youngest three grains that overlap at 2σ and 2) youngest single detrital zircon age. For more information refer to figures 4.16-31.

Sample	Stratigraphic position	Youngest age from zircon population of 3 or more grains		Youngest single grain (Ma) with concordance	No. of grains within 10% concordance
		Age (Ma)	MSWD		
GAN2 Figure 4.31	Upper Gannabos	550.4 ± 9.8	1.6	538 ± 4 (94%)	22
ARZG01 Figure 4.29	Uppermost Arondegas	1028 ± 5.1	2.1	1016 ± 11 (100%)	73
AR01 Figure 4.27	Lowermost Arondegas	1021 ± 3.5	0.067	974 ± 4 (92%)	35
ARZA02 Figure 4.25	Lowermost Arondegas	1018.8 ± 2.7	0.93	998 ± 5 (90%)	82
HOED2 Figure 4.23	Upper Hoedberg	987.5 ± 4.4	0.34	539 ± 4 (90%)	67
WGR Figure 4.21	Upper Grootriet	1012 ± 4.2	0.29	984 ± 8 (90%)	46
Nflbasal Figure 4.19	Lowermost Flaminkberg	1034.9 ± 4.9	0.27	1032 ± 9 (99%)	55
FLS01 Figure 4.17	Lowermost Flaminkberg	1002.7 ± 3.4	1.08	999 ± 6 (99%)	95

4.4 Micropalaeontology

Twenty one samples from the Flaminkberg, Hoedberg and Arondegas Formations were screened for acritarchs (microfossils). Appendix D contains the specific details for each slide and sample preparation procedures in addition to the general steps described in section 3.4 of the Methods chapter.

4.4.1 Flaminkberg Formation

Four samples were collected from dark purple-grey, black, micaceous siltstone layers that are interbedded with fine-grained sandstones in the upper Flaminkberg Formation (Figures 2.3 and 4.1). Based on their dark colour and fine-grain size, these samples were considered in the field to be suitable for microfossils analysis. In spite of careful sample preparation steps taken, no microfossils or organic residue could be recovered from these samples (Table 4.3; Figure 4.32). The samples resisted maceration with less than half of them dissolving after six days of treatment in 40% hydrofluoric acid.

Table 4.3. Summary of the microscope slide descriptions of the four samples processed from the Flaminkberg Formation.

Sample and location		No. of Slides	Slide description	Microfossil content
Figure 4.1 log	FLM01 Figure 4.32	2	No organic matter. Micas (~100 µm), orange-rimmed quartz (100 –250 µm) and iron oxides (75–200 µm) present.	NA
	FLM02 Figure 4.32	2	No organic matter. Orange-rimmed quartz (80–200 µm) and iron oxides (80–250 µm) present.	NA
	FLM03	2	No organic matter. Orange-rimmed quartz (80– 190 µm) and iron oxides (100–150 µm) present.	NA
	FLM04	1	No organic matter. Orange-rimmed quartz (50–110 µm) and iron oxides (60–180 µm) present.	NA

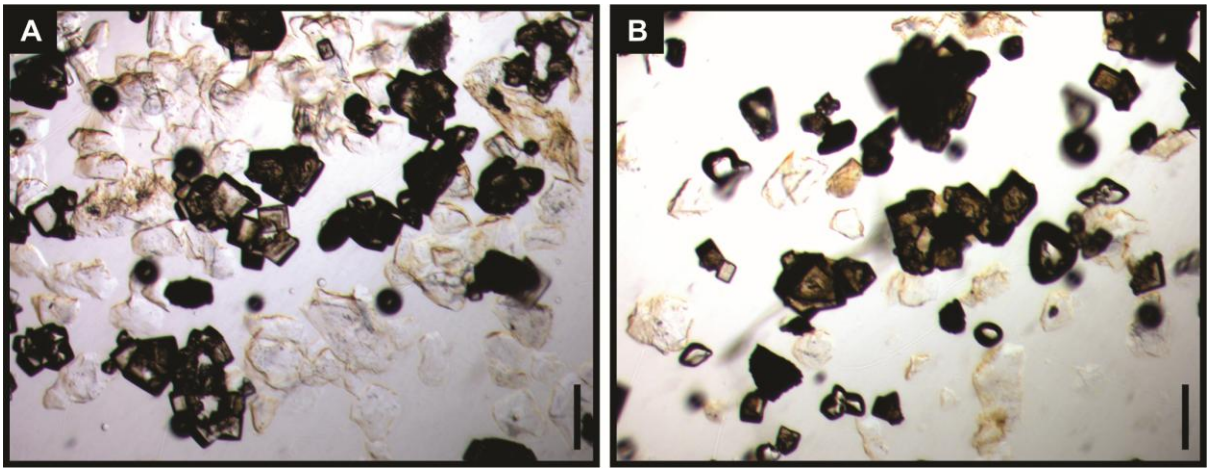

Figure 4.32. Dissolution residue of the fine-grained sandstone sample collected Flaminkberg Formation. No organic matter is present and an abundance of orange-rimmed quartz and iron oxides indicates that dissolution in 40% hydrofluoric acid did not fully occur even after six days. A) Image of sample FLM01. B) Image of sample FLM02. Scale bar is 200 µm long.

4.4.2 Hoedberg Formation

Twenty-four samples were collected at 1.5 m intervals from light green grey to dark purple grey siltstone layers in the Hoedberg Formation (Figure 4.6). Based on their green colour and fine-grain size, 16 samples were processed for microfossils analysis. Only four samples from the lower sample range (HDM-X) were processed, because upon close investigation with binocular microscope, these seemed to be the least weathered samples and thus deemed promising to yield microfossils.

Of the 24 samples, only seven contain fragments of organic matter (Table 4.4). The organic matter is largely amorphous and show no diagnostic biological properties apart from samples HDM02 and HDM03. These samples contain small fragments of cell colonies as well as fragmented organic matter. The latter could potentially be remnants of fragmented sphaeromorphs and possible acanthomorphs (spiny structures present). However, the samples are degraded, contaminated by modern fibres and yield no definitive acritarchs. The colonies of cells observed could be linked to the microbial mats. In particular, the colony arrangements observed in sample HDM06 morphologically

resembles members of the *Sphaerocongregus* genus, of which *Sphaerocongregus variabilis* is the type species as described by Moorman (1974) (Figures 4.33D, F-G). *Sphaerocongregus* (=*Bavlinella* sp.) is a cosmopolitan cyanobacteria/blue-green algae species that dates from late Proterozoic to Early Cambrian (Vidal, 1976; Chiglino et al., 2015). The genus is comprised of three morphological variants: 1) Small single coccoid cells (3–5 µm); 2) Larger coccoid cells (5–16 µm) occurring as individual cells or attached cell rows or long chains and; 3) Globose masses (5–20 µm) composed of coccoid subunits (0.1–2 µm) (Moorman, 1974). The spherical cells in HDM06 range in size from 15 to 25 µm and occur as chains or rows of cells (Figure 4.33), and thus resemble the second morphological subdivision of *Sphaerocongregus,* although some of the cells in HDM06 have a larger diameter. An earlier study by Shepeleva (1962) produced a size range for *Bavlinella* of 16.8 to 24 µm, which fits the sizes observed in this study. Consequently, the spherical cells in HDM06 have been tentatively assigned to the *Sphaerocongregus* genus.

Table 4.4. Summary of the microscope slide descriptions of the 16 samples processed from the Hoedberg Formation.

Sample and location		No. of slides	Slide description	Microfossil content
Figure 4.5 log	HDM01	3	Sediment particles and floccules of organic matter and clay minerals (10–100 µm), individual grains of apatite (~10 µm) with modern contamination present (fibres and plant fragments).	NA
	HDM02 Figure 4.33A-C	3	Amorphous dark organic matter with occasional spherical shapes, fragmentary or relic envelope structures. Sediment particles (70–1130 µm) and clay floccules also present. Modern contamination present.	Colonial cells (cell diameter: 15–25 µm)
	HDM03	6	Amorphous dark organic matter (60–200 µm). Sediment pieces with floccules of clay minerals (40–200 µm), opaque minerals (50–120 µm) and modern contamination.	NA
	HDM04	3	Amorphous, fragmentary organic matter (16–129 µm), opaque minerals (26–252 µm) and modern contamination noted.	NA
	HDM05	3	Minor traces of sediment pieces but not noteworthy. Clear, transparent amorphous fragments (~ 150 µm) and modern contamination present.	NA
	HDM06 Figure 4.33D-H	3	High content of amorphous kerogen (400 µm) with cellular structure on the surface: cells in diameter ~ 3 µm. Fragmentary organic matter with possible relict envelopes (60–400 µm) and cluster of cells (28 µm). Modern contamination present. Sediment particles (60–270 µm). Opaque minerals (60–200 µm).	Possible *Sphaerocongregus variabilis* Colonial cells
	HDM07	2	Very little material present: opaque minerals (130–270 µm) and transparent, cubic mineral (suspected insoluble salt). Sediment fragments (60–700 µm) with clay minerals (<2 µm) and organic matter pieces. Minor contamination present in the form of modern fabric fibres.	NA
	HDM08	2	No organic matter. Predominantly barren slides with small sediment particles and modern contamination.	NA
	HDM09	2	Barren slides. Biotite fragments (80–400 µm) and minor amounts of sediment particles (30–120 µm).	NA
	HDM10	2	Barren slides with minor contamination. Sediment particles (500 µm-15 cm) with traces of organic content (200–330 µm).	NA
	HDM11	2	No organic matter and only sediment particles present (160–430 µm).	NA
	HDM12	2	Only sediment particles (80–306 µm) and clay floccules present with minor modern contamination.	NA
	HDM01X	2	No organic matter observed and only sediment particles present (20–180 µm).	NA
	HDM04X	1	No organic matter and only sediment particles present (20–180 µm).	NA
	HDM08X	2	Only sediment particles (50–400 µm) and minor modern contamination present.	NA
	HDM12X	2	Small amounts of light brown organic matter (~160 µm) and sediment particles (40–310 µm) present.	NA

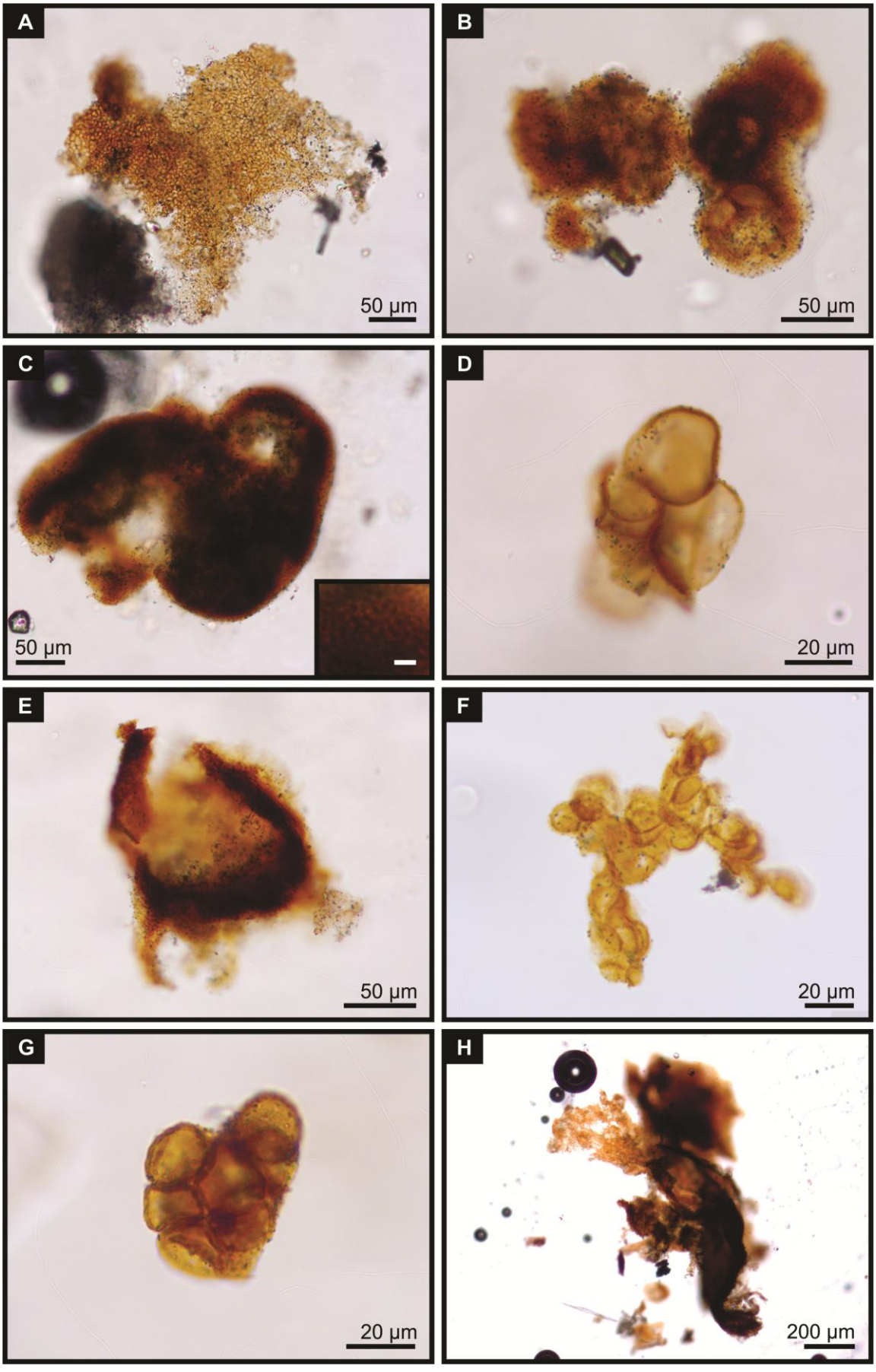

Figure 4.33. Fragmented organic matter and microfossils recovered from the dissolution residue of the Hoedberg Formation samples (A – C: sample HDM02; D – H: sample HDM06). A) Fragments of cell colonies, potentially relics of microbial mats. B) Sphaeromorphic dark organic matter with an internal cellular structure (diameter = 25 µm). C) Two spherical dark organic matter fragments. Insert: cellular surface structure, scale = 5 µm. D) Colony of cells, possible *Sphaerocongregus variabilis* (diameter = 25 µm). E) Sphaeromorphic dark kerogen with structures reminiscent of acritarch processes. F) Chain of cells, possible *Sphaerocongregus variabilis* (diameter = 15-20 µm). G) Rows of spherical cells, possible *Sphaerocongregus variabilis* (diameter = 20 µm). H) Fragments of organic matter with possible envelope structures.

4.4.3 Transition between Arondegas and Gannabos Formation

One fine-grained mudstone sample was collected from the gradational transition between the Arondegas and Gannabos Formations (Figures 2.3 and 4.8). The samples were unproductive with respect to microfossils or organic matter (Table 4.5: Figure 4.34).

Table 4.5. Summary of the microscope slide descriptions of the two samples processed from the transitional beds between the Arondegas and Gannabos Formations.

Sample and location		No. of Slides	Slide description	Microfossil content
Figure 4.8	Ngb Figure 4.34	2	No organic matter only floccules of clay (80–500 µm). Minor contamination noted.	NA

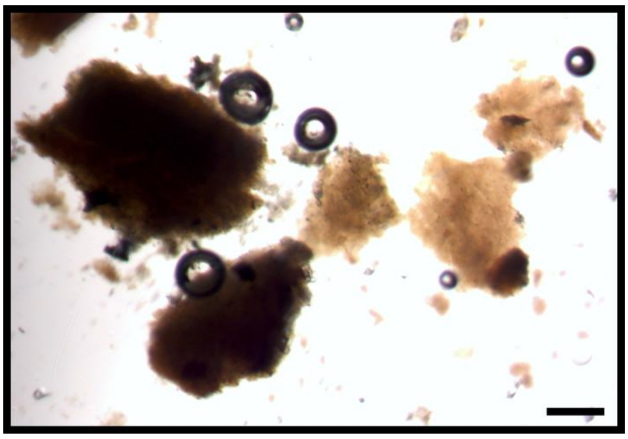

Figure 4.34. Dissolution residue of the mudstone sample collected from the transitional beds between the Arondegas and Gannabos Formations. No organic matter is present. Scale bar is 200 µm long.

5. Discussion

5.1 Interpretation of depositional environments

Facies analysis was undertaken on the three lowermost siliciclastic formations in order to refine their depositional settings and resolve the contradiction in the literature concerning the deposition of the Arondegas Formation (Chapter 1).

5.1.1 Flaminkberg Formation

The formation is dominated by coarse-grained sandstone-dominated units that are predominantly laterally continuous for ~10's of m's, and form several, well-defined coarsening-upward cycles. The interpretation of each lithofacies is presented in Table 3.1. These tabular coarse-grained units have flat, erosive lower boundaries and were deposited in a high energy environment. Four architectural elements (AEs) were documented in the Flaminkberg Formation with sheet-like sandstones (SB) the most common. The depositional energy and sub-environments are explained in Table 5.1 and these associations were used to determine the depositional environment.

The Flaminkberg Formation consists of architectural elements that are not diagnostic of a particular depositional environment. However, there is one sedimentary structure that has not been previously documented in the formation, which firmly diagnoses its depositional setting i.e., hummocky cross-stratification. Hummocky cross-stratification forms below the fair-weather wave-base and above the storm wave-base in large bodies of water e.g., sea or large lake (Walker, 1979; Cheel and Keckie, 1993). They are formed from a combined unidirectional and oscillation flow during storm conditions (Figure 5.1) and predominantly occur in marine environments, in relatively shallow waters of shelf settings (Walker, 1979; Cheel and Keckie, 1993; Dumas and Arnott. 2006). The coarsening-upwards trend in the grain size, the occurrence of sedimentary structures indicative of higher energy events and lack of tidally influenced currents collectively suggest that the Flaminkberg Formation was most likely deposited in a shallowing-upward, wave-dominated marine environment.

The Flaminkberg Formation was initially considered to be a coastal braided fluvial plain deposit (Almond et al., 2009; Buatois et al., 2013). Braided fluvial styles are characterized by high discharge variability and may have several channels separated by temporary bars and islands (Miall, 2010). These temporary structures are created due to the high degree of variability in discharge and high rates of sediment supply in braided systems (Miall, 1996). Vegetation influences the stability and erodibility of the river banks, and consequently, in the pre-Devonian, when little to no vegetation was present, fluvial systems were dominated by 'sheet-braid' style (Miall, 2010; Gibling and Davies, 2012). The Precambrian braided rivers are characterised by high sedimentation rates, wide, shallow channels dominated by a few primary sedimentary structures, rare occurrences of fining-upwards

units and very little evidence for muddy floodplains, similar to modern braided plains in arid environments (Table 5.2; Long, 1978, Bhattacharya, 2006; Gibling and Davies, 2012).

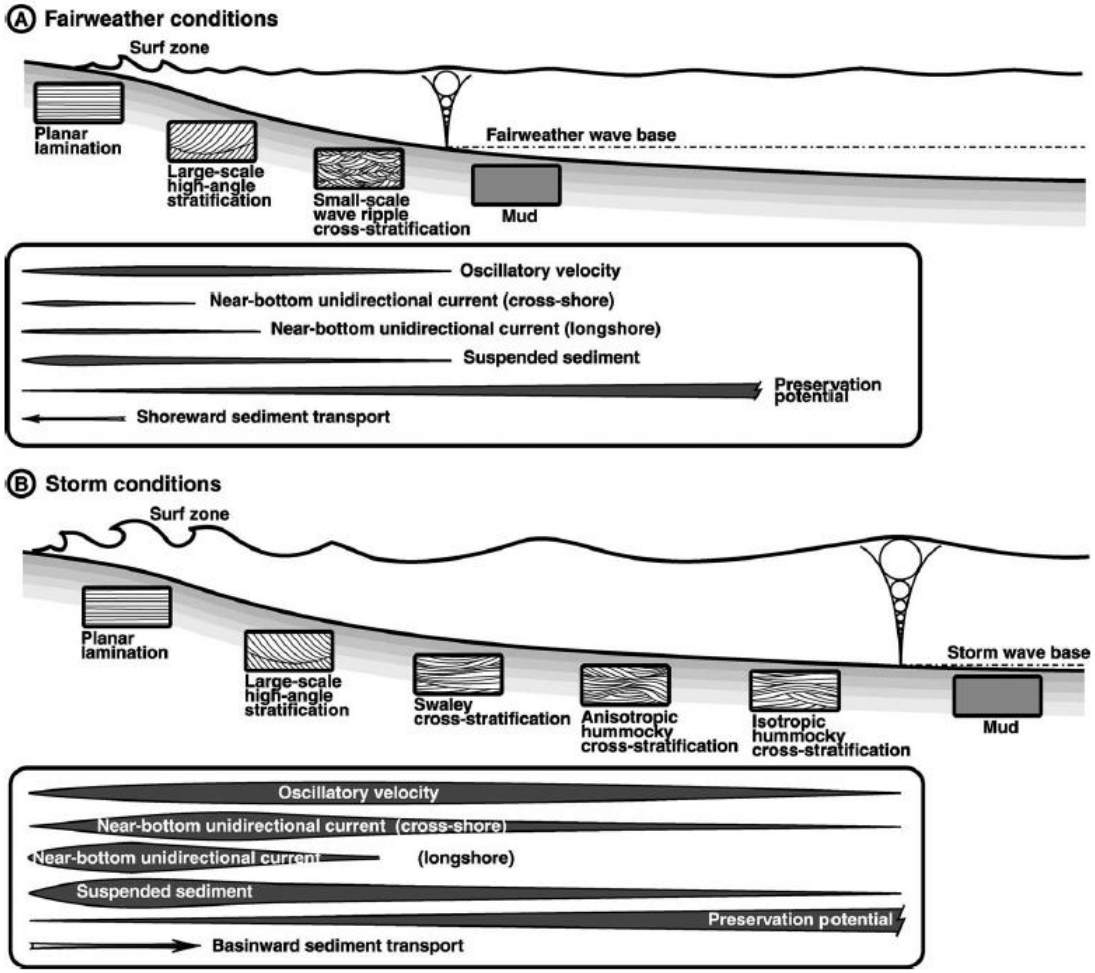

Figure 5.1. Formation of hummocky cross-stratification (source: Dumas and Arnott, 2006).

Table 5.1. Architectural Elements identified in the Flaminkberg Formation and their interpretive sub-environments. Modified after Miall (1985, 1996).

Architectural Element	Geometry	Characteristics, associations and interpreted sub-environment where possible
Gravel bedforms (GB)	Sheet, tabular	Gravel elements (GB: containing facies Gmm1, Gmm2, Gmh1, Gmh2, Gml) are coarse-grained (> granule) elements that constitute up to 25% of the Flaminkberg Formation. Gravel facies are found at the top of coarsening-upwards cycles although not as dominant as the very coarse-grained sandstone facies. The large grain sizes and flat to irregular erosional bases represent deposition during peak flow or traction in high energy environments in strong, turbulent currents with high sediment concentration and large discharge (Miall, 1996). Their formation has also been linked to migrating dunes and gravel bars.
Sandy bedform (SB)	Tabular, lenticular, generally laterally continuous and vertically stacked bodies	Sandstone elements (SB: containing facies Sh, Sl, Sl2, Sm, Sr, HCS) are coarse-grained units with sharp, planar to irregular lower bounding surfaces that range from non-erosive to slightly erosive. The dominance of coarse-grained sandy bedforms demonstrates that high energy traction-current deposition was dominant.
Lateral accretion macrofrom (LA)	Tabular, wedge, lenticular	Lateral accretion macroforms (LA: containing facies Sl, Sm, Sh) are laterally stacked depositional increments with sharp, sub-horizontal to slightly concave-upward lower erosional boundaries. LAs represent the infill of localized channels by laterally migrating bars where the inner bank of the channel has a lower energy condition than the outer bank, and consequently deposition occurs on the inner bank (Miall, 1985).
Channel	Lens	Small channel element (CH: containing facies Sl, Sh) (Figure 4.4) represents the infill of the active channel that was at least 2 m deep and 16 m wide.

Table 5.2: General characteristics of a sandbed braided fluvial plain in arid environments (Long, 1978; Miall, 2010).

Feature	Sandbed-dominated braided plain
General	Shallow (high width to depth ratios), ephemeral, unchannelised
Sedimentary structures	Characterized by 3D dune migration, planar tabular cross-bedding
Bed geometry	Sheet-like, tabular, several m's thick
Architectural elements	Common: upstream, lateral and downstream accretion Minor sandy bedforms (SB) due lobate, planar cross-bedded units to coalesced sand bars
Palaeocurrent direction	Unimodal with variable consistency: low to high

Given that the Flaminkberg Formation is dominated by shallow, unchannelised sandy bedforms, a low consistency of palaeocurrent data (Figure 2.4; Gresse, 1992) with minimal primary sedimentary structures, the previous interpretations of the formation as alluvial deposits are understandable. However, in the light of the newly discovered of hummocky cross-stratification, this depositional setting is considered unlikely and a shallow marine, wave-dominated environment is suggested here.

5.1.2 Hoedberg Formation

The Hoedberg Formation comprises dark, bluish grey green mudstones (facies Fl, Fm) with intercalated limestone layers, lenses and nodules (Table 3.1). The palaeoenvironment of the Hoedberg Formation is well-established as an oolite barrier to nearshore lagoon or shelf environment marine setting (Gresse, 1992; Germs et al., 2009; Buatois et al., 2013).

There are very few architectural elements observed in the Hoedberg Formation, which is largely composed of fine-grained, laterally continuous siltstone and sandstones beds. The mudstone-dominated units are vertically stacked and bounded by planar surfaces. Primary sedimentary structures (e.g., ripples cross-lamination, large ripple marks, soft sediment deformation, flaser bedding) are rare and indicative of occasional high energy depositional events in an otherwise, quiet, low energy palaeoenvironment.

Flaser bedding is a heterolithic deposit of alternating rippled sandstone and mud where the amount of sand exceeds the mud content or the mud units are stripped from the ripple crests by currents (Dalrymple, 2010b). Flaser bedding develops in tidal settings, during episodic flooding of overbank areas on floodplains or in deeper water due to weak storm-wave action. Given the facies associations in both this unit and conformably underlying unit (Grootriet Formation – see section 5.1.4 below) as well as Flaminkberg Formation (which is also interpreted as a shallow marine succession), the latter setting is considered here more likely.

The Hoedberg Formation is characterised by the upward increase in the abundance and thickness of lenses of fine- to medium-grained sandstone beds with ripple marks and erosional bases. These beds are interpreted as storm event beds in a generally low energy setting (Figure 5.2). Event beds form during the rising phase of the storm, when sediment is stripped from the muddy beds and a variety of erosive scour and sole marks are formed (Plint, 2010). As the storm starts to wane, initially planar-laminated sand is deposited under powerful combined flow and this evolves into hummocky cross-stratification (or massive beds) and as the storm settles, ripples develop. The vertical changes in the facies may suggest that the Hoedberg Formation was initially deposited in a distal shelf setting, but with time the shallowing of the environment occurred. This also resulted in the onset of a shallower offshore transition zone below the fair-weather wave-base between the lower shoreface and shelf

environment, where storm-related beds developed (Figure 5.1). This interpretation therefore defines the depositional setting of the Hoedberg Formation as a storm-dominated, lower shoreface to shelf environment below the fair-weather wave-base.

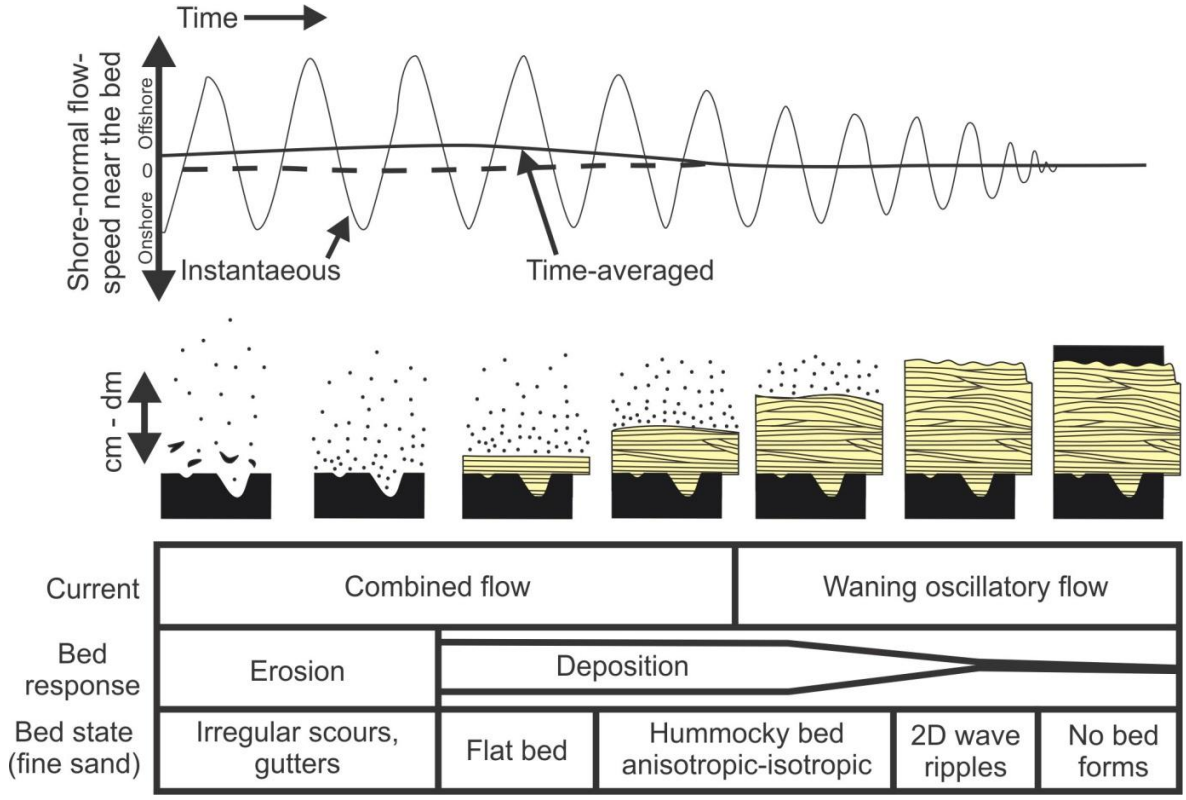

Figure 5.2. The formation of idealized sandstone event beds as a result of storm-generated combined flow (sourced from Plint, 2010 who based it on Cheel, 1991; Cheel and Leckie, 1993).

5.1.3 Arondegas Formation

The Arondegas Formation is dominated by white, grey to pinkish coarse- to very coarse-grained sandstones that are immature and feldspathic. Gravel and sandstone facies are mostly massive, especially in the lower part of the formation. The formation is characterised by multiple fining-upward successions in which the beds thicken upwards. Unique, locally developed carbonate-clast conglomerate beds are observed at one locality within the Arondegas Formation and occur as lens shaped beds or tabular bodies in association with sandy bedforms (SB). Three architectural elements (AEs) were documented in the Arondegas Formation with a high occurrence of sheet-like sandstones (SB) and laterally accreting beds (LA). The depositional energy and sub-environments are explained in Table 5.3 and these associations were used to determine the depositional environment.

Table 5.3: Architectural Elements identified in the Arondegas Formation and their interpretive sub-environments. Modified after Miall (1985, 1996).

Architectural Element	Geometry	Characteristics, associations and interpreted sub-environment where possible
Gravel bedforms (GB)	Sheet, tabular, lens	Gravel elements (GB: containing facies Gmm3, Gcm) are coarse-grained (> granule) elements with flat to irregular erosional bases, very poor sorting, and the largest clasts in the study area. These facies represent deposition during peak flow or traction in high energy environments. The strong, turbulent currents had high sediment concentration and large discharge (Miall, 1996).
Sandy bedform (SB)	Tabular, generally laterally continuous and vertically stacked bodies	Sandy bedform elements (SB: containing facies Sh, Sm) are coarse-grained units with sharp, planar to irregular lower bounding surfaces that range from non-erosive to slightly erosive. The dominance of SBs demonstrates the prevalence of high energy traction-current deposition.
Lateral accretion macrofrom (LA)	Tabular, wedge, lenticular	Lateral accretion macroforms (LA containing facies Sh, Sl, Sm, St) are laterally stacked depositional increments, onto sharp, sub-horizontal to slightly concave-upward lower erosional boundaries. LAs represent the infill of localized channel belts by laterally migrating bars where the inner bank of the channel has a lower energy condition than the outer bank, and consequently deposition occurred on the inner bank (Miall, 1985).

In contrast to the Flaminkberg and Hoedberg Formations, the Arondegas Formation lacks diagnostic properties to accurately determine its depositional environment. Additionally, there is no consensus in the literature regarding the interpretation of its depositional setting, which has been reported both as an alluvial fan (Germs et al., 2009) and a delta front to prodelta setting (Buatois et al., 2013). The large discrepancy between the palaeoenvironmental interpretations of the Arondegas Formation is addressed here by comparing and contrasting the characteristics of the depositional settings proposed in the literature with the characteristics of the sedimentary facies observed in the outcrops of this study (Chapter 4).

Table 5.4. Similarities and differences in the characteristics of the sedimentary facies and palaeoenvironments proposed for the Arondegas Formation (sources Bhattacharya, 2006 and Bridge, 2006 in case of gravelly alluvial systems; Bhattacharya, 2010 for the delta environment).

Characteristic	Alluvial fan	Delta front (intertidal shoreline)	Prodelta
Lithology	Breccias, conglomerates, sandstones.	Sand and/or gravel. Mud may be present.	Fine mud and silt.
Bed geometry	Channel-shape (flat top and down-curving base), sheet-like bodies but laterally restricted, large width-to-depth ratio and, cut-and-fill structures.	Tabular (mouth bars) and channel-shape (distributory channels) in the proximal parts.	Sheet-like.
Sedimentary structures in sandstones	Mostly massive, immature sandstones, poorly- sorted sandstones, graded beds, trough and planar cross-bedding, low angle cross-bedding, unidirectional current ripples, horizontal lamination in very fine-grained sand and, soft sediment deformation structures.	Proximal slope: coarse cross-bedded units Distal slope: finer laminated sediments. Ripple cross-lamination, horizontal lamination (tidal or discharge related), dune scale cross-stratification, soft sediment deformation common, climbing current ripples and, potential tidally influenced strata.	Laminated mudstones (settling from suspension). Rhythmically laminated sediments via tidal or discharge fluctuations in the delta-feeding river (distal event beds).
Vertical succession trends	On metre-scale, multiple fining-upward successions, 3-9 m to 100 m thick. Bounded at the base and top by erosional/sharp contacts. On large-scale, fining-upward successions coarsen-upwards due to alluvial fan progradation.	Upward-coarsening and upward-thickening, cyclic successions due to delta progradation.	Couple to 100's of m's thick, gently upward-coarsening, cyclic successions due to delta progradation.
Lateral trends and distribution of beds	Strong downcurrent and down-fan grain size reduction. Generally, laterally restrictive (narrower compared to marine environments).	Several 10's of km's in width depending on tidal range Overlapping delta lobes result in overlapping lens-shaped beds. Gentle depositional slope. Inter-distributary and interlobe areas are less sandy and thin.	NA
Facies Architecture	Channels at various scales. Rare overbank sediments, crevasse splays and levee deposits.	Foresets common (concave-upward profile with shoreface and mouth bars forming steeply dipping clinoforms), depositional lobes and rare topsets (undulating beds, channel deposits).	Bottomset common: flat-lying deposits.
Palaeocurrent direction	Unimodal Consistency: low to high.	Unimodal (but can be bimodal if wave or tide action strong). Consistency: low to high	Rare, mostly unimodal (depends on marine influence).
Bioturbation	Variable - depends on sedimentation rates and grain size.	Variable – depends on type river-, wave- or tidal-influence	High

The sandstone-dominated Arondegas Formation has a few sedimentary structures and these include horizontally bedded, low-angle cross-bedded and trough cross-bedded sandstones. The sandstone bed shapes are dominantly sheet-like and laterally accreting units. Subsequently, in comparison to the properties listed in Table 5.4, the Arondegas Formation has characteristics that feature in both the alluvial and deltaic environments; however, there are also features in each environment which do not fit the Arondegas Formation. Furthermore, because of Precambrian age of these sediments, they lack diagnostic continental (i.e., non-marine) features of post-Devonian alluvial settings such as palaeosols, desiccation cracks, red beds and terrestrial fossils.

Deltaic systems compromise three main geomorphic depositional environments: 1) delta plain, 2) delta front (coarser grained) and 3) prodelta (finer grained) (Bhattacharya, 2006). These are recognisable by their architecture, sedimentary structures and lithologies. The Arondegas Formation is reminiscent of the coarse-grained, upward-thickening delta front deposits, even though coarsening-upwards packages characteristic of delta front sediments are not present in the study area. The outer edge of delta fronts on the subtidal platforms are typically located at the fair-weather wave-base (Bhattacharya, 2010), resulting in gradational contacts similar to those occasionally observed between the Arondegas and the underlying Hoedberg Formation (the latter of which formed in the offshore transition zone between fair-weather wave-base and storm-wave base). Pertinent to this study is that sediment type and rate of supply is also influenced by the absence of land plants in pre-Devonian rocks. This resulted in higher sedimentation rates and a greater proportion of coarsening- and thickening-upward deltaic packages during periods of regression in sedimentary basins (Bhattacharya, 2006).

Furthermore, alluvial fans are characterised by poorly-sorted, immature and mostly massive deposits, which sufficiently describes the Arondegas Formation as well. The sheet-like sandstones have wide, shallow scours and no significant downcutting, and these could be indicative of unconfined, shallow floodwaters of alluvial fan lobes. The more confined, channeled conglomerates might have acted as incised channels on the fan surface in the proximal part of the fan lobes.

In summary, the Arondegas Formation shows aspects of both alluvial fan and delta front depositional environments. However, despite missing diagnostic criteria of post-Devonian continental environments (e.g., palaeosols, terrestrial fossils), the Arondegas Formation appears to conform slightly more to an alluvial setting, because of: 1) the laterally confined conglomerates; 2) the moderate palaeocurrent consistency (Figure 2.4; Gresse, 1992); and 3) fining-upwards cycles are more diagnostic of high energy alluvial fan than deltaic settings.

Provenance using clast counts

The conglomerate beds on the Draaihoek farm had a high concentration of carbonate clasts, feldspar and quartz as well as very low concentrations of igneous, metamorphic and sedimentary lithic fragments (chert). The lithological heterogeneity of the clasts indicates that source areas were likely dominated by carbonate rocks and rocks with abundant feldspar and vein quartz. Clasts are rounded during transportation due to abrasional forces and the degree of which clasts are rounded during transportation depends mostly on the hardness (lithology) of the clast (Mills, 1979; Lindsey et al., 2007). The most abundant clasts in the beds are subangular to subrounded large carbonate clasts and small pebble sized feldspar clasts. This variation in size further indicates the high energy of the depositional environment. The presence and size of the carbonate and feldspar clasts is unusual as these lithologies are susceptible to chemical and physical weathering. Consequently, their presence in the beds and at such high concentrations indicates that these channels were proximal to the source rocks and that the climate was arid rather than humid. Gresse (1992) suggested that the carbonate clasts were sourced through the erosion and burial of the coastal carbonate facies in the region namely the underlying Gifberg Group and potentially the Grootriet Formation as well. The quartz and feldspar clasts were most likely sourced from the Namaqua-Natal basement rocks which were the primary source rocks of the basin. Correlation of these conglomerate beds across the basin are not possible as these conglomerate beds are only found on the Draaihoek farm.

5.1.4 Palaeoenvironment of the lower Vanrhynsdorp Group

The facies analysis study of the lower Vanrhynsdorp Group resulted in the identification of hummocky cross-stratification in the Flaminkberg Formation, which indicates a shallow marine or shelf depositional setting (Walker, 1979; Cheel and Keckie, 1993). Conformably overlying carbonates and interbedded shales of the Grootriet Formation deposited in an oolite barrier to shallow lagoonal environment (Gresse, 1992). The Grootriet Formation is characterized by black limestones and interbedded shales with an upper gradational contact with the overlying Hoedberg Formation. The latter is a gradual upward-coarsening, laterally continuous unit dominated by siltstones. In this study, the interpretation of its depositional environment has been refined to a storm-dominated, lower shoreface to shelf environment below the fair-weather wave-base. The occurrence of flaser bedding, horizontally laminated siltstones and trace fossils indicate a dominantly low energy environment especially during the deposition of the lower Hoedberg Formation. The combination of frequent ripple trains and large ripple marks signify high energy storm events especially in its upper part. The gradual transition into the higher energy Arondegas Formation indicates a shallowing of the environment into a possible alluvial fan.

These results suggest a shallow marine, partly storm-dominated depositional environment for the lowermost units as opposed to the previous interpretations of dominantly alluvial settings. Furthermore, the results also imply the deepening of the environments from Flaminkberg, Grootriet to Hoedberg Formation and then shallowing of the environments (middle to upper Hoedberg Formation), which culminated in the onset of continental conditions in the Arondegas Formation. This also means that the shoreline in the Vanrhynsdorp Basin moved landward (transgression) until the middle Hoedberg Formation and then seaward (regression) during the deposition of the rest of the Hoedberg and Arondegas Formations.

5.2 Evidence and position of the Ediacaran-Cambrian boundary

During the Ediacaran–Cambrian transition, remarkable global biological, oceanographic and tectonic changes occurred (Knoll and Caroll, 1999; Amthor et al., 2003). Key evolutionary events prior to and during the earliest phases of the Cambrian metazoan "explosion" are the disappearance of the Ediacaran fauna and the subsequent explosive radiation of skeletonized animals from the Early Cambrian. Consequently, the Ediacaran-Cambrian boundary is of global palaeobiological significance and has been described as the most important transition in geological history (Jensen et al., 2000; Buatois, 2018). The Ediacaran-Cambrian boundary is defined by the first appearance datum of the trace fossil Treptichnus pedum at the Fortune Head GSSP section (see section 2.3). The work on the prolific trace fossil record in the Vanrhynsdorp Group has helped elucidate the position of the boundary and consequently provided key stratigraphic framework for this project (e.g., Buatois et al., 2007; Almond et al., 2009; Buatois et al., 2013).

Recent discoveries of new body and trace fossils by Taylor et al. (2017a-b) from the Nudaus Formation, Nama Group and of other Ediacaran body fossils in the Cango Caves Formation (personal communication, Dr. John Almond) illustrate the tremendous need for continued work on Neoproterozic-Cambrian of South Africa. These discoveries may help correlate the Vanrhynsdorp Group with the rocks in the Witsputs and Zaris sub-basins as well as with Late Ediacaran assemblages from Australia, Iran and northern Norway.

The Ediacaran-Cambrian boundary is thought to occur between the Gannabos and Besonderheid Formations or below the Gannabos Formation, based on trace fossils evidence as discussed above and in section 2.3. In this study, detrital zircon dating and microfossil analysis were used to refine the location of the boundary. The detrital zircon dating of the coarse-grained siliciclastics was conducted to provide a framework of radiometric dates and microfossil analysis of the fine-grained units was aimed at establishing biostratigraphic framework for potential regional and global correlations.

5.2.1 U-Pb zircon evidence

Seven of the eight analysed detrital zircon samples yielded concordant ages from the Proterozoic with the majority of the ages clustering in the Stenian (1000-1200 Ma) of the Late Mesoproterozoic. Outliers from the Early Mesoproterozoic and the Late Palaeoproterozoic are also present. The mean ages of the youngest detrital zircon populations yielded ages from 987 to 1034 Ma from the Flaminkberg, Grootriet, Hoedberg and Arondegas Formations (Figures 4.16-31; Table 4.2 in section 4.3). Furthermore, their probability density plots all exhibit similar trends and Mesoproterozoic peaks of 1040-1097 Ma dominate the zircon age spectra (Figures 4.17, 19, 21, 23, 25, 27, 29, 31B). These age spectra imply a zircon source located in the Namaqua-Natal Metamorphic Province, which is associated with a Mesoproterozoic orogenic event (Jacobs et al., 1993; Robb et al., 1999; Hanson, 2003; Basei et al., 2008; Eglington, 2006). At least two samples were dated from the Flaminkberg and Arondegas Formations at different localities and the samples all yielded similar ages, thus verifying the results. It is improbable that four formations were deposited at the same time in such rapid succession. Therefore, the results yielded do not indicate their maximum depositional age but rather, the consistency of the ages suggests a persistent sediment source throughout their deposition.

In contrast, the sample from the upper Gannabos Formation yielded a very different age spectrum (Table 4.2). The detrital zircons in this sample are different to the zircons from the lower seven samples, because they were clear and had more sub-euhedral grain morphologies. This upper Gannabos sample yielded the youngest depositional age of 550.4 ± 9.8 Ma with the widest range in ages from 539 to 2774 Ma (Figure 4.31; Table 4.2). Compared to the youngest populations obtained from the underlying seven samples (Flaminkberg, Grootriet, Hoedberg and Arondegas Formations), the youngest population present in the upper Gannabos sample suggests a new, youngest source area. Supporting this new age determination for the upper Gannabos Formation is the youngest zircon population of 524-528 Ma obtained from the overlying basal Besonderheid Formation, which was dated by Harrison (2014).

Interestingly, although the ages do not provide the desired geochronological framework for the lower Vanrhynsdorp Group nor do they pinpoint the Ediacaran-Cambrian boundary, the age signature clearly shows a change in the sediment source and this is confirmed by the palaeocurrent study by Gresse (1992) (Figure 2.4). All the formations below the Arondegas Formation had source areas from the Namaqua-Natal Metamorphic Province in the east with ages on the order of ~1000 Ma (Eglington, 2006). The sediments from the Gannabos Formation and the overlying units were sourced from the Gariep and Damara orogens in the west and are part of the Pan African orogen, hence a ~550 Ma age (Frimmel and Fölling, 2004; Frimmel et al., 2013). Blanco et al. (2011) reports

detrital zircon dates from siliciclastic units throughout the Nama Group that display the same trends reported in this study. Major age peaks from the Neoproterozoic (Pan-African Orogeny) and Mesoproterozoic (Namaqua-Natal Orogeny) are seen with a change in palaeocurrent direction from the north to west in the upper Nama Group, resulting in a dominance of Neoproterozoic-Cambrian detrital zircons (Blanco et al., 2011).

Of the eight samples, only two youngest zircon population ages have an MSWD values greater than 1.0 i.e., GAN2= 1.6 and ARZG01= 2.1. This suggests that the scatter in the ages is larger than expected based on the precision of the individual measurements and consequently, the three youngest grains from samples GAN2 and ARZG01 are not all of the same true age. This is not a concern for the ARZA02 sample, because there are two other Arondegas samples, which corroborate this result and have a MSWD value <1.0. However, the same cannot be applied to GAN2 and caution is exercised in reporting this age. Another concern is the low percentage of concordant grains within the concordant interval (90-110%) used to try and calculate the maximum depositional age. The number of concordant grains used in each sample ranged from 22 to 95. Some detrital zircon studies e.g., Gehrels et al. (2006) and Dehler et al. (2010) lower the concordance interval to 80-120% in order to incorporate more data in the analyses. This was considered in this study because it would increase the smallest concordant set of 22 grains to 33 grains (see section 4.3; Table 4.3; Appendix C). However, increasing the concordance interval by 10% did not significantly alter the ages of the youngest zircon population and the more statistically robust interval was used. The Gannabos Formation yielded the least reliable result because only 21% of the analyses were concordant (22 zircon grains out of 103). The mean age of the youngest zircon grains in the Gannabos Formation indicates a late Ediacaran source age. However, the youngest single zircon grain is 538 ± 4 Ma is more likely to be closest to the true depositional age of the unit (Dickinson and Gehrels, 2009). An Ediacaran age of the Gannabos Formation would potentially place its large infaunal trace fossils into the Ediacaran, and this would have major biological implications for the evolution of animal life in the Precambrian (Almond et al., 2009). This emphasizes the urgent need for additional geochronological studies of the Gannabos Formation to statistically corroborate this result, because as stated above, only 22 grains are concordant in this critical sample. Furthermore, geochronological studies of reported rutile (Gresse, 1992) and other accessory minerals (e.g., apatite, titanite – cf. Thomsen et al., 2015) in the Vanrhynsdorp Group could provide additional information on the depositional history of the unit and the location of the Ediacaran-Cambrian boundary.

5.2.2 Microfossil evidence

Microfossil analysis of 21 samples from the lower Vanrhynsdorp Group was conducted to provide biostratigraphic control and help determine the position of the Ediacaran-Cambrian boundary. The

majority of the samples were either barren or contained no biostratigraphically significant microfossils. Although fragments of suspected acritarchs were identified, the specimens were not diagnostic. Additionally, the presence of contamination within the samples further reduces their utility. The possible identification of the long-ranging cyanobacteria Sphaerocongregus variabilis in one of the Hoedberg Formation samples (HDM06) does not aid in constraining the depositional age and caution must be used in reporting its occurrence. Even if this taxon was common in the formation, it is of limited biostratigraphic utility due to its long-ranging occurrence in the Precambrian.

The microfossil studies of the lower Vanrhynsdorp Group yielded limited results, partly because of the extensive deep weathering of the rocks, which oxidised and damaged their fossil and organic matter content. Additionally, the organic matter (kerogen) present in the slides is very dark in colour, which could indicate that the samples are thermally altered. Thus, it is possible for the microfossils to have been destroyed or fragmented during metamorphism (Figure 4.33). The fragmentary nature of the organic matter observed in the samples could also have been caused by: 1) recrystallisation and mineral growth of the pyrite cubes into limonite cubes; and 2) the use of centrifuge to separate out the solids in the samples. It should be noted that the use of a centrifuge in microfossil sample preparation is common practice and that extreme care was taken during sample processing. Future attempts to reanalyze the Vanrhynsdorp Group for microfossils should utilize fresh, unaltered material obtained from either core samples or deep excavations.

Gaucher and Germs (2006) reported acritarchs from the Neoproterozoic-Early Palaeozoic of South Africa. In particular, Bavlinella faveolata (=Sphaerocongregus) was reported in both the Gamtoos and Cango Cave Groups. However, the possible S. variabilis specimens in this study are slightly larger than the ones characterized by Moorman (1974) and the South African specimens reported in Gaucher and Germs (2006). Additionally, Gaucher and Germs report on Leiosphaeridia tenuissima in the Groenefontein Formation, Cango Caves Group (Gaucher and Germs, 2006: figure 7, p. 200). A specimen from HDM02 (Figure 4.33A) has a marked similarity to Leiosphaeridia tenuissima, particularly regarding its cellular surface texture. However, the HDM02 specimen is fragmented and no cell envelope is observed/preserved, thus limiting the comparison or further identification.

5.2.3 Location of the Ediacaran-Cambrian boundary

U-Pb dating of the detrital zircons and microfossil analysis of select units in the lower Vanrhynsdorp Group has not resolved the location of the Ediacaran-Cambrian boundary. The youngest single zircon grain from the Gannabos Formation suggests a Cambrian age, although this is a preliminary result based on a small sample set of concordant zircon ages, which can be improved with further analyses

of additional samples. U-Pb dated detrital zircons within other formations of the lower Vanrhynsdorp Group were of limited stratigraphic use due to the strong sediment source signal. At present, the occurrence of large Planolites-like traces in the Gannabos Formation and of the Cambrian traces Treptichnus pedum and Oldhamia geniculata in the Besonderheid Formation remain the only reliable indicators of the probable location of the Ediacaran-Cambrian boundary (Gresse et al., 2006; Almond et al., 2009).

5.3 Correlation with the Nama Group

Although the U-Pb zircon dating did not further constrain the location of the Ediacaran-Cambrian boundary, the youngest zircon populations and single youngest detrital zircon grain from the Gannabos Formation collectively suggest a Cambrian age for the upper Gannabos Formation. This has interesting implications on the hypothesized correlations of the Nama and Vanrhynsdorp Groups (Table 2.2). It was suggested that the Cambrian Nomtsas Formation of the Nama Group correlated with the Van Zylkop Formation in the upper Vanrhynsdorp Group, however the Cambrian age from the Gannabos Formation would shift the correlation lines dramatically. Without high precision absolute dates and age diagnostic fossils within the Vanrhynsdorp Group, the direct correlation with the Nama Group remains limited.

Potential tuffaceous horizons in the Hoedberg, Gannabos and Besonderheid Formations had been identified in previous studies and have yet to be systematically dated (Germs et al. 2009). Two such tuffaceous layers in the Hoedberg and Gannabos Formations were identified and their samples (HOED2 and GAN2) donated to this study by Dr. John Almond. U-Pb ages from tuffaceous deposits are preferred over detrital zircon ages as they yield absolute ages of the deposit, whereas detrital zircon ages only represent the age of the source rocks (Tucker et al., 2013). The detrital zircon ages from the lower Vanrhynsdorp Group reveal a persistent sediment source throughout the deposition and cannot be used for correlations with the much younger dated tuffaceous layers of the Nama Group. Unfortunately, the wide age spectra and rounded nature of the zircon grains within the tuffaceous samples of the Vanrhynsdorp Group (HOED2 and GAN2) reveal that that the samples are reworked and have a complex depositional history (see sections 2.2 and 4.3). These preliminary results imply that rigorous future provenance and geochronological studies of the tuffaceous layers could provide important age controls for the Vanrhynsdorp Group and refine the correlation with the Nama Group.

6. Conclusion

The lowermost five formations of Vanrhynsdorp Group of South Africa straddle the biogeologically important Ediacaran-Cambrian boundary, and therefore the accurate reconstruction of their depositional palaeoenvironments is critical. Outcrop-based sedimentary facies analysis of the Flaminkberg, Hoedberg and Arondegas Formations resulted in the discovery of sedimentary structures diagnostic of a shallow marine, partly storm-dominated depositional setting. The reconstructed marine palaeoenvironments for the lowermost formations are in opposition to the previous interpretations of dominantly alluvial settings for the same units (Gresse, 1992; Germs et al., 2009; Buatois et al., 2013).

Previous studies on trace fossils (Gresse et al., 2006; Almond et al., 2009) suggest that the Ediacaran-Cambrian boundary is located between the Gannabos and Besonderheid Formations. U-Pb detrital zircon geochronology, using LA-ICP-MS, was performed on eight samples spanning the Flaminkberg to Gannabos Formations in order to develop a geochronological framework for the lower Vanrhynsdorp Group. Youngest population ages were calculated using the mean ages of the youngest three zircon grains and ages of 987 to 1034 Ma were obtained from the lowermost four formations (Flaminkberg, Grootriet, Hoedberg and Arondegas Formations). In contrast, the Gannabos Formation had a youngest zircon population at 550.4 ± 9.8 Ma. These ages do not refine the position of the Ediacaran-Cambrian boundary and rather reveal that a Namaqua-Natal sediment source persisted during the deposition of the lower Vanrhynsdorp Group which changed to a younger Gariep Orogen sediment source during the deposition of the Gannabos Formation.

The majority of the samples investigated for the presence of Ediacaran-Cambrian organic-walled microfossil (acritarchs) assemblages were either barren or contained no biostratigraphically diagnostic microfossils, although specimens resembling Sphaerocongregus varibilis and Leiosphaeridia tenuissima were observed. Until larger-scale dating and microfossil analyses can be conducted, the only reliable proxies for the placement of the Ediacaran-Cambrian boundary are still trace fossils, namely: the large Planolites-like traces in the Gannabos Formation, Oldhamia geniculata in the Besonderheid Formation and the abundant occurrence of Treptichnus pedum in the overlying formations. This project emphasizes the need for better age constraints within the Vanrhynsdorp Group and lays the groundwork for the continued study of this critical period in the emergence of early life in South Africa.

7. References

Aceñolaza, G.F., Germs, G.J.B. and Aceñolaza, F.G., 2009. Trace fossils and the Agronomic Revolution at the Neoproterozoic- Cambrian transition in Southwest Gondwana. In: Gaucher, C., Sial, A.N., Halverson, G.P., Frimmel, H.E. (Eds): Neoproterozoic-Cambrian tectonics, global change and evolution: a focus on southwestern Gondwana. Developments in Precambrian Geology, 16, Elsevier, 339-347.

Agić, H., 2016. Fossil Focus: Acritarchs. Palaeontology Online, 6 (11), 1-13.

Almond, J.E., Buatois, L.A., Gresse, P.G. and Germs, G.J.B., 2009. Trends in metazoan body size, burrowing behaviour and ichnodiversity across the Precambrian–Cambrian boundary: ichnoassemblages from the Vanrhynsdorp Group of South Africa. Extended Abstracts of the 15th Biennial Conference of the Palaeontological Society of Southern Africa. September 11-14, Matjiesfontein, South Africa. Palaeontologia Africana, 44, 139-141.

Almond, J. and Pether, J., 2009. Palaeontological Heritage of the Northern Cape. SAHRA Palaeotechnical Report.

Amthor, J.E., Grotzinger, J.P., Schröder, S., Bowring, S.A., Ramezani, J., Martin, M.W. and Matter, A., 2003. Extinction of Cloudina and Namacalathus at the Precambrian-Cambrian boundary in Oman, Geology, 31, 431–434.

Andersen, T., 2002. Correction of common lead in U-Pb analyses that do not report 204Pb. Chemical Geology, 192, 59–79.

Basei, M.A.S., Frimmel, H.E., Nutman, A.P., Preciozzi, F. and Jacob, J., 2005. A connection between the Neoproterozoic Dom Feliciano (Brazil/Uruguay) and Gariep (Namibia/South Africa) orogenic belts - evidence from a reconnaissance provenance study. Precambrian Research, 139, 195-221.

Basei, M.A.S., Frimmel, H.E., Nutman, A.P. and Preciozzi, F., 2008. West Gondwana amalgamation based on detrital zircon ages from Neoproterozoic Riberia and Dom Feliciano belts of South America and comparison with coeval sequences from SW Africa. In: Pankhurst, R. J., Trouw, R. A. J., Brito Neves, B. B. and De Wit, M. J. (Eds) West Gondwana: Pre-Cenozoic Correlations Across the South Atlantic Region. Geological Society, London, Special Publications, 294, 239–256.

Bhattacharya, J. P., 2006. Deltas. In: Posamentier, H.W. and Walker, R.G. (Eds): Facies Models Revisited. Tulsa, Oklahoma: SEPM Special Publication, 84, 237-292.

Bhattacharya, J.P., 2010. Deltas. In: James, N. P. and Dalrymple, R. W. (Eds): Facies Models 4: GEOtext 6, Geological Association of Canada, St. John's, Newfoundland, 233-264.

Blanco, G., Germs, G.J.B., Rajesh, H.M., Chemale, F., Dussin, I.A. and Justino, D., 2011. Provenance and paleogeography of the Nama Group (Ediacaran to early Palaeozoic, Namibia): petrography, geochemistry and U–Pb detrital zircon geochronology. Precambrian Research 187, 15–32.

Bossi, J. and Gaucher, C., 2004. The Cuchilla Dionisio Terrane, Uruguay: an allochtonous block accreted in the Cambrian to SW-Gondwana. Gondwana Research, 7 (3), 661-674.

Bowring, S.A., Schoene, B., Crowley, J.L., Ramezani, J. and Condon, D.J., 2006. High-precision U-Pb zircon geochronology and the stratigraphic record: progress and promise. In Olsewski, T. (Ed): Geochronology: Emerging Opportunities, Paleontological Society Short Course, October 21, 2006, Philadelphia, PA. Paleontological Society Papers, 11.

Brasier, M.D., 2012. Secret chambers: the inside story of cells and complex life. Oxford University Press, 1- 298.

Bridge, J.S., 2006. Fluvial facies models: recent developments. In: Posamentier, H.W. and Walker, R.G. (Eds): Facies Models Revisited. Tulsa, Oklahoma: SEPM Special Publication, 84, 85-170.

Buatois, L.A., Almond, J.A., Gresse, P. and Germs, G., 2007. The elusive Proterozoic-Cambrian boundary: ichnologic data from the Vanrhynsdorp Group of South Africa. Abstracts, 9th International Ichnofabric Workshop, Calgary, 8.

Buatois, L.A., Almond, J.E. and Germs, G.J.B., 2013. Environmental tolerance and range offset of Treptichnus pedum: Implications for the recognition of the Ediacaran-Cambrian boundary. Geology, 41, 519-522.

Buatois L.A. and Mángano M.G., 2016. Ediacaran Ecosystems and the Dawn of Animals. In: Mángano M., Buatois L. (Eds): The Trace-Fossil Record of Major Evolutionary Events. Topics in Geobiology, 39, Springer, Dordrecht.

Buatois, L.A., 2018. Treptichnus pedum and the Ediacaran–Cambrian boundary: significance and caveats. Geological Magazine, 155 (1), 174–180.

Buick, R., 2010. Early life: Ancient acritarchs. Nature, 463, 885-886.

Butterfield, N.J., 1997. Plankton ecology and the Proterozoic–Cambrian transition. Paleobiology, 23, 247–262.

Cawood, P.A. and Nemchin, A.A., 2000. Provenance record of a rift basin: U/Pb ages of detrital zircons from the Perth Basin, Western Australia. Sedimentology Geology, 134, 209-234.

Cheel, R.J., 1991. Grain fabric in hummocky cross-stratified storm beds: genetic implications. Journal of Sedimentary Petrography, 61, 102-110.

Cheel, R.J. and Leckie, D.A., 1993. Hummocky cross-stratification: Sedimentology Review. Blackwell Scientific Publications, 103-122.

Chiglino, L., Gaucher, C., Sial, A.N. and Ferreira, V.P., 2015. Acritarchs of the Ediacaran Frecheirinha Formation, Ubajara Group, Northeastern Brazil. Anais da Academia Brasileira de Ciências, 87, 635-649.

Collinson, J., 1996. Alluvial sediments. Sedimentary Environments: Processes, Facies and Stratigraphy, 3, 37–82.

Colombera, L., Mountney, N.P. and McCaffrey, W.D., 2013. A quantitative approach to fluvial facies models: Methods and example results. Sedimentology, 60, 1526–1558.

Connelly, J.N., 2001. Degree of preservation of igneous zonation in zircon as a signpost for concordancy in U/Pb geochronology. Chemical Geology, 72, 25-39.

Corfu, F., Hanchar, J.M., Hoskin, P.W.O. and Kinny, P.D., 2003. Atlas of zircon textures. Reviews in Mineralogy and Geochemistry, 469-500.

Dalrymple, R. W., 2010a. Interpreting sedimentary successions: facies, facies analysis and facies models. In: James, N. P. and Dalrymple, R. W. (Eds): Facies Models 4: GEOtext 6, Geological Association of Canada, St. John's, Newfoundland, 3-18.

Dalrymple, R.W., 2010b. Tidal depositional systems. In: James, N.P. and Dalrymple, R. W. (Eds): Facies Models 4: GEOtext 6, Geological Association of Canada, St. John's, Newfoundland, 201–231.

Dehler, C.M., Fanning, C.M., Link, P.K., Kingsbury, E.M. and Rybczynski, D., 2010. Maximum depositional age and provenance of the Uinta mountain group and big cottonwood formation, northern Utah. Paleogeography of Rifting Western Laurentia, Geological Society of America Bulletin, 122 (9-10), 1686-1699.

Dickinson, W.R. and Gehrels, G.E., 2009. Use of U-Pb ages of detrital zircons to infer maximum depositional ages of strata: a test against a Colorado Plateau Mesozoic database. Earth and Planetary Science Letters, 288 (1-2), 115-125.

Dumas, S. and Arnott, R.W.C., 2006. Origin of hummocky and swaley cross-stratification—The controlling influence of unidirectional current strength and aggradation rate. Geological Society of America, 34 (12), 1073-1076.

Eglington, B.M., 2006. Evolution of the Namaqua-Natal Belt, southern Africa – A geochronological and isotope geochemical review. Journal of African Earth Sciences, 46, 93-111.

Fensome, R.A., Williams, G.L., Barss, M.S., Freeman, J.M. and Hill, J.M., 1990. Acritarchs and fossil prasinophytes: an index to genera, species and infraspecific taxa. American Association of Stratigraphic Palynologists Contributions, 25, 771.

Frimmel, H.E., Fōlling, P. G. and Eriksson, P. G., 2002. Neoproterozpic tectonic and climatic evolution recorded in the Gariep Belt, Namibia and South Africa. Basin Research, 14, 55-67.

Frimmel, H.E. and Fōlling, P.G., 2004. Late Vendian Closure of the Adamastor Ocean: Timing of Tectonic Inversion and Syn-orogenic Sedimentation in the Gariep Basin. Gondwana Research, 7(3), 685-699.

Frimmel, H. E., Basei, M. A.S., Correa, V. X. and Mbangula, N., 2013. A new lithostratigraphic subdivision and geodynamic model for the Pan-African western Saldania Belt, South Africa. Precambrian Research, 231, 218-235.

Gaucher, C., 2000. Sedimentology, palaeontology and stratigraphy of the Arroyo del Soldado Group (Vendian to Cambrian, Uruguay). Beringeria, 26, 1-120.

Gaucher, C. and Germs, G.J.B., 2002. Stepwise rifting of Rodinia as the prelude to the amalgamation of W-Gondwana. New insights from Uruguay and Brazil. 16th International Sedimentological Congress, 111-112.

Gaucher, C., Chiglino, L. and Pecoits, E., 2004. Southernmost exposures of the Arroyo del Soldado Group (Vendian to Cambrian, Uruguay): palaeogeographic, palaeoclimatic and palaeobiologic implications. Precambrian Research, 120, 241-278.

Gaucher, C., Frimmel, H.E. and Germs, G.J.B., 2005. Organic-walled microfossils and biostratigraphic of the upper Port Nolloth Group (Namibia): implication for the latest Neoproterozoic glaciations. Geological Magazine, 142, 539-559.

Gaucher, C. and Germs, J.G.B., 2006. Recent advances in South African Neoproterozoic-Early Palaeozoic biostratigraphy: correlation of the Cango Caves and Gamtoos Groups and acritarchs of the Sardinia Bay Formation, Saldania Belt. South African Journal of Geology, 109, 193-214.

Gaucher, C., Finney S., Poke, D., Valencia, V., Grove, M., Blanco, G., Paoumukaghlian, L. and Peral, L., 2008. Detrital zircon ages of Neoproterozoic sedimentary successions in Uruguay and Argentina: insights into the geological evolution of the Rio de la Plata Craton. Precambrian Research, 167, 150-170.

Gaucher, C. and Sprechmann, P., 2009. Neoproterozoic Acritarch Evolution, In: Gaucher, C., Sial, A.N., Halverson, G.P., Frimmel, H.E. (Eds): Neoproterozoic-Cambrian tectonics, global change and evolution: a focus on southwestern Gondwana. Developments in Precambrian Geology, 16, Elsevier, 319-326.

Gehling, J. G., Jensen, S., Droser, M. L., Myrow, P. M. and Narbonne, G. M., 2001. Burrowing below the basal Cambrian GSSP, Fortune Head, Newfoundland. Geological Magazine, 138 (2), 213-218.

Gehrels, G.E., Valencia, V.A. and Pullen, A., 2006. Detrital zircon geochronology by laser-ablation multicollector ICOMS at the Arizona laserchron centre. In: Olszewskki, T. (Ed): Geochronology: Emerging Opportunities, Paleontological Society Short Course, Philadelphia, PA. Paleontological Society Papers, 12.

Gehrels, G.E., Valencia, V.A. and Ruiz, J., 2008. Enhanced precision, accuracy, efficiency, and spatial resolution of U-Pb ages by laser ablation-multicollector-inductively coupled plasma-mass spectrometry. Geochemistry, Geophysics, Geosystems, 9, 1-13.

Gehrels, G., 2012. Detrital Zircon U-Pb Geochronology: Current Methods and New Opportunities. In: Busby, C. and Azor, A. (Eds): Tectonics of Sedimentary Basins: Recent Advances, Wiley-Blackwell Publishing, 47-62.

Gehrels, G.E., 2014. Detrital zircon U-Pb geochronology applied to tectonics. Annual Review of Earth and Planetary Sciences, 42, 127-149.

Germs, G.J.B., 1983. Implications of sedimentary facies and depositional environmental analysis of the Nama Group in South West Africa/Namibia. Geological Society of South Africa, Special Publication, 11, 89-114.

Germs, G. J. B. and Gresse, P.G., 1991. The foreland basin of the Damara and Gariep orogens in Namaqualand and southern Namibia: stratigraphic correlations and basin dynamics. South African Journal of Geology, 94, 159-169.

Germs, G.J.B., 1995. The Neoproterozoic of southwestern Africa, with emphasis on platform stratigraphy and paleontology. Precambrian Research, 73, 137-151.

Germs, G.J.B., Miller, R.M., Frimmel, H.E. and Gaucher, C., 2009. Syn- to late-orogenic sedimentary basins of southwestern Africa. Neoproterozoic to Early Palaeozoic evolution of Southwestern Africa. In: Gaucher, C., Sial, A.N., Halverson, G.P., Frimmel, H.E. (Eds): Neoproterozoic-Cambrian tectonics, global change and evolution: a focus on southwestern Gondwana. Developments in Precambrian Geology, 16, Elsevier, 182-203.

Gibling, M.R. and Davies, N.S., 2012. Palaeozoic landscapes shaped by plant evolution. Nature Geoscience, 5, 99-105.

Goscombe, B. and Gray, D.R., 2007. The Coastal Terrane of the Kaoko Belt, Namibia: outboard arc-terrane and tectonic significance. Precambrian Research, 155, 139-158.

Gresse, P.G., 1992. The tectono-sedimentary history of the Vanrhynsdorp Group. Geological Survey of South Africa, Memoir 79, 1-163.

Gresse, P.G. and Germs, G.J.B., 1993. The Nama foreland basin: sedimentation, major unconformity bounded sequences and multisided active margin advance. Precambrian Research, 63, 247-272.

Gresse, P.G., Von Veh, M.W. and Frimmel, H.E., 2006. Namibian (Neoproterozoic) to Early Cambrian successions. In: Johnson, M.R., Anhaeusser, C.R. and Thomas, R.J. (Eds): The geology of South Africa, Geological Society of South Africa, Marshalltown, 395-420.

Grey, K., Walter, M. R. and Calver, C. R., 2003. Neoproterozoic biotic diversification: Snowball Earth or aftermath of the Acraman impact?. Geology, 31 (5): 459–462.

Grey, K., 2005. Ediacaran Palynology of Australia. Memoir of the Association of Australasian Palaeontologists, 31, 1–439.

Grey, K., Laurie, J. and Gehling, J., 2005. The 'New´ Ediacaran Period. Geoscience Australia, 80, 1-2.

Grotzinger, J.P., Bowring, S.A., Saylor, B.Z. and Kauffman, A.J., 1995. Biostratigraphic and geochronologic constraints on early animal evolution. Science, 270, 598–604.

Grotzinger, J.P., 2000. Facies and paleoenvironmental setting of Thrombolite-Stromatolite Reefs, Terminal Proterozoic Nama Group (ca. 550-543 Ma), central and southern Namibia. Communications of the Geological Survey of Namibia, 12, 251-264.

Hanson, H.E., 2003. Proterozoic geochronology and tectonic evolution of southern Africa, In: Yoshida, M., Windley, B.F. and Dasgupta, S. (Eds): Proterozoic East Gondwana: Supercontinent Assembly and Breakup. Geological Society, London, Special Publications, 206, 427-463.

Harrison, B., 2014. Is the South African Precambrian-Cambrian boundary at the contact of the Gannabos to Besonderheid Formations in the Vanrhynsdorp Group?. Unpublished Honours thesis, University of Cape Town.

Herbosch, A. and Verniers, J., 2011. What is the biostratigraphic value of the Ichnofossil Oldhamia for the Cambrian: A Review. Geologica Belgica, 14, 229-248.

Hiess, J., Condon, D.J., McLean, N., and Noble, S.R., 2012. 238U/235U systematics in terrestrial uranium-bearing minerals. Science, 335, 1610-1614.

Hietpas, J., Samson, S., Moecher, D., and Chakraborty, S., 2011. Enhancing tectonic and provenance information from detrital zircon studies: assessing terrane-scale sampling and grain-scale characterization. Journal of the Geological Society, 168, 309–318.

Horstmann, U.E., Ahrendt, H., Clauer, N. and Porada, H., 1992. Damaran metamorphism and its record in the Nama Group. Abstract Geocongress, Geological Society of Southern Africa, 197-199.

Hoskin, P.W.O. and Schaltegger, U., 2003. The composition of zircon and igneous and metamophic petrogenesis. In: Hanchar, J.M. & Hoskin, P.W.O. (eds) Zircon. Mineralogical Society of America and Geochemical Society, Reviews in Mineralogy and Geochemistry, 53, 27–62.

Howard, J.L., 1993. The statistics of counting clasts in rudites: a review, with examples from the upper Palaeogene of southern Califironia, USA. Sedimentology, 40, 157-174.

Howard, J.L., 1994. A note on the use of statistics in reporting detrital clastic compositions. Sedimentology, 41, 747-754.

Huntley, J. W., Xiao, S., and Kowalewski, M., 2006. 1.3 billion years of acritarch history: An empirical morphospace approach. Precambrian Research, 144, 52-68.

Ibanez-Mejia, M., Pullen, A., Arenstein, J., Gehrels, G., Valley, J., Ducea, M., Mora, A., Pecha, M. and Ruiz, J., 2015. Unraveling crustal growth and reworking processes in complex zircons from orogenic lowercrust: The Proterozoic Putumayo Orogen of Amazonia. Precambrian Research, 267, 285-310.

Jackson, S.E., Pearson, N.J., Griffin, W.L. and Belousova, E.A., 2004. The application of laser ablation-inductively coupled plasma-mass spectrometry to in situ U-Pb zircon geochronology. Chemical Geology, 211, 47-69.

Jacobs, J., Thomas, H.J. and Weber, W., 1993. Accretion and indentation tectonics at the southern edge of the Kaapvaal craton during the Kibaran (Grenville) orogeny. Geology, 21, 203-206.

Jaffey, A.H, Flynn, K.F., Glendenin, L.E., Bentley, W.C. and Essling, A.M., 1971. Precision measurement of half-lives and specific activities of 235U and 238U. Physical Review C, 4, 1889–1906.

Javaux, E.J., Marshall, C.P. and Bekker, A., 2010. Organic-walled microfossils in 3.2-billion-year-old shallow-marine siliciclastic deposits. Nature, 463, 934–938.

Javaux E.J., 2011. Acritarch. In: Gargaud M. et al. (Eds) Encyclopedia of Astrobiology. Springer, Berlin, Heidelberg.

Jensen, S., Saylor, B., Gehling, J. and Germs, G., 2000. Complex Trace Fossils from the terminal Proterozoic of Namibia. Geology, 28, 143-146.

Jensen, S., 2003. The Proterozoic and earliest Cambrian trace fossil record; patterns, problems and perspectives. Integrative and Comparative Biology, 43, 219–228.

Jensen S., Droser M.L. and Gehling J.G., 2006. A Critical Look at the Ediacaran Trace Fossil Record. In: Xiao S., Kaufman A.J. (Eds) Neoproterozoic Geobiology and Paleobiology. Topics in Geobiology, 27. Springer, Dordrecht.

Johnson, S.D., Poujol, M. and Kister, A.F.M., 2006. Constraining the timing and migration of collisional tectonics in the Damara Belt, Namibia: U-Pb zircon ages for the syntectonic Salem-type Stinkbank granite. South African Journal of Geology, 109, 611-624.

Jung, S., Hoernes, S., and Mezger, K., 2000. Geochronology and petrogenesis of Pan-African, syn-tectonic, S-type and posttectonic A-type granite (Namibia): products of melting of crustal sources, fractional crystallization and wall rock entrainment. Lithos, 50, 259-287.

Košler, J., 2012. U-Pb Geochronology and Hf isotope geochemistry of detrital zircon in sedimentary systems. In: Sylvester, P., Quantitative Mineralogy and Microanalysis of Sediments and Sedimentary Rocks. Short Course Series 42. Mineralogical Association of Canada, 185-202.

Košler, J., Sláma, J., Belousova, E., Corfu, F., Gehrels, G.E, Gerdes, A., Horstwood, M.S.A, Sircombe, K.N., et al., 2013. U-Pb detrial zircon analysis – results of an inter-laboratory comparison. Geostandards and Geoanalytical Research, 37 (3), 243-259.

Knoll, A. H. and Carroll, S.B., 1999. Early animal evolution: emerging views from comparative biology and geology. Science, 284, 2129-2137.

Knoll, A.H., Javaux, E.J., Hewitt, D. and Cohen, P., 2006. Eukaryotic organisms in Proterozoic oceans. Philosophical Transactions of the Royal Society B, 361, 1023–1038.

Kröner, A., 1982. Rb-Sr geochronology and tectonic evolution of the Pan African belt of Namibia, southwestern Africa. American Journal of Science, 282, 1471-1507.

Lamb, D.M., Awramik, S.M., Chapman, D.J. and Zhu, S., 2009. Evidence for eukaryotic diversification in the ~1800 million-year-old Changzhougou Formation, North China. Precambrian Research, 173, 93-104.

Landing, E., 1994. Precambrian-Cambrian boundary global stratotype ratified and a new perspective of Cambrian time. Geology, 22, 179-182.

Lindsey, D.A., Langer, W.H. and Knepper Jr., D.H., 2005. Stratigraphy, lithology, and sedimentary features of Quaternary alluvial deposits of the South Platte River and some of its tributaries east of the Front Range, Colorado. U.S. Geological Survey Professional Paper, 1705, 1-77.

Lindsey, D.A., Langer, W.H. and van Gosen, B.S., 2007. Using pebble lithology and roundness to interpret gravel provenance in piedmont fluvial systems of the Rocky Mountains, USA. Sedimentary Geology, 199, 223-232.

Lister, T.R., 1970. The acritarchs and chitinozoa from the Wenlock and Ludlow Series of the Ludlow and Millichope areas, Shropshire. Part 1. Palaeontographical Society Monographs, 124(1), 100.

Long, D.G.F., 1978. Proterozoic stream deposits: some problems of recognition and interpretation of ancient sandy fluvial systems. In: Miall, A. D. (ed): Fluvial Sedimentology. Canadian Society of Petroleum Geologists, 5, 313-342.

MacCrae, C., 1999. Life etched in stone – Fossils of South Africa. Linden, South Africa. The Geological Society of South Africa.

Macey, P.H., Siegfried, H.P., Minnaar, H., Almond, J. and Botha, P.M.W., 2011. The geology of the Loeriesfontein Area. Explanation to 1: 250 000 Geology Sheet 3018 Loeriesfontein, Council for Geoscience, Pretoria, 139.

McIlroy, D. and Brasier, M.D., 2016. Ichnological evidence for the Cambrian explosion in the Ediacaran to Cambrian succession of Tanafjord, Finnmark, northern Norway. In: Brasier, A. T., McIlroy, D. and McLoughlin, N. (Eds) Earth System Evolution and Early Life: a Celebration of the Work of Martin Brasier. Geological Society, London, Special Publications, 448, 1-18.

Mendelson, C.V. and Schopf, J.W., 1992. Proterozoic and selected Early Cambrian microfossils and microfossil-like objects. The Proterozoic Biosphere, 865-951.

Miall, A.D., 1977. Lithofacies types and vertical profile models in braided river deposits: a summary.

Miall, A.W., 1978. Lithofacies Types and Vertical Profile Models in Braided River Deposits A Summary. In Miall, A.D. (Ed): Fluvial Sedimentology, Memoir 5, Canadian Society of Petroleum Geologists, Calgary, 597-604.

Miall, A.D., 1985. Architectural-Element Analysis: A New Method of Facies Analysis Applied to Fluvial Deposits. Earth-Science Review, 22, 261–308.

Miall, A.D., 1988. Architectural elements and bounding surfaces in fluvial deposits: anatomy of the Kayenta formation (lower Jurassic), Southwest Colorado. Sedimentary Geology, 55, 233–262.

Miall, A.D., 1996. The Geology of Fluvial Deposits. Sedimentary Facies, Basin Analysis, and Petroleum Geology. Springer-Verlag Berlin Heidelberg, 565.

Miall, A.W., 2010, Alluvial deposits, In: James, N. P. and Dalrymple, R. W. (Eds): Facies Models 4: GEOtext 6, Geological Association of Canada, St. John's, Newfoundland, 105-137.

Miller, R. McG., 1983. The Pan-African Damara Orogen of the South West Africa/Namibia. In: Miller, R McG. (Ed), The evolution of the Damara Orogen of South West Africa/Namibia. Geological Society of South Africa Special Publication, 11, 431-515.

Mills, H.H., 1979. Downstream rounding of pebbles - A quantitative review. Journal of Sedimentary Petrology, 49, 295–302.

Moczydlowska, M., 2011. The early Cambrian phytoplankton radiation: Acritarch evidence from the Lukati Formation of Estonia. Palynology, 35 (1), 43.

Möller, A., O'Brien, P.J., Kennedy, A. and Kroner, A., 2003. Linking growth episodes of zircon and metamorphic textures to zircon chemistry: An example from the ultrahigh temperature granulites of Rogaland (SW Norway) In: Vance, D., Muller, W. and Villa, I. (Eds): Geochronology: Linking the Isotopic Record with Petrology and Textures. Geological Society of London, Special Publication 220, 65-81.

Moorman, M., 1974. Microbiota of the Late Proterozoic Hector Formation, Southwestern Alberta, Canada. Journal of Palaeontology, 48 (3), 524-539.

Narbonne, G. M., Myrow, P. M., Landing, E. and Anderson, M. M., 1987. A candidate stratotype for the Precambrian-Cambrian boundary, Fortune Head, Burin Peninsula, southeastern Newfoundland. Canadian Journal of Earth Sciences, 24, 1277-1293.

Nasdala, L., Zhang, M., Kempe, U., Panczer, G., Gaft, M., Andrut, M. and Plotze, M., 2003, In: Hanchar, J.M., and Hoskin, P.W.O. (Eds): Zircon: Reviews in Mineralogy and Geochemistry, 53, 427-467.

Palacios, T., 2015. Acritarch assemblages from the Oville and Barrios Formations, northern Spain: A pilot proposal of a middle Cambrian (Series 3) acritarch biozonation in northwestern Gondwana. Review of Palaeobotany and Palynology, 219, 71-105.

Peng, Y., Bao, H. and Yuan, X., 2009. New morphological observations for Paleoproterozoic acritarchs from the Chuanlinggou Formation, North China. Precambrian Research, 168, 223-232.

Plint, A. G., 2010. Wave- and storm-dominated shoreline and shallow-marine systems. In: James, N. P. and Dalrymple, R. W. (Eds): Facies Models 4: GEOtext 6, Geological Association of Canada, St. John's, Newfoundland, 167-199.

Reading, H.G., 1978. Sedimentary Environments and Facies: New York, Elsevier Press, 557.

Robb, L.J., Armstrong, R.A. and Waters, D.J., 1999. The history of Granulite-facies metamorphic and crustal growth from single zircon U-Pb geochronology: Namaqualand, South Africa. Journal of Petrography, 40 (12), 1747-1770.

Roberts, N.M.W. and Spencer, C.J., 2014. The Zircon Archive of Continent Formation through Time. Geological Society Special Publications, 389, 197-225.

Roberts, N.M.W. and Spencer, C.J., 2015. The zircon archive of continent formstion through time. From: Roberts, N. M. W., Van Kranendonk, M., Parman, S., Shirey, S. and Clift, P. D. (Eds): Continent Formation Through Time. Geological Society, London, Special Publications, 389, 197–225.

Rubatto, D., 2002. Zircon trace element geochemistry: partitioning with garnet and the link between U-Pb ages and metamorphism, Chemical Geology, 184, 123–138.

Saylor, B.Z., 2003. Sequence Stratigraphy and Carbonate-Siliciclastic Mixing in a Terminal Proterozoic Foreland Basin, Urusis Formation, Nama Group, Namibia. Journal of Sedimentary Research, 73 (2), 264-279.

Schiffbauer, J.D., Huntely, J.W., O'Neil, G.R., Darroch, S.A.F., Laflamme, M. and Cai, Y., 2016. The Latest Ediacaran Wormworld Fauna: Setting the Ecological Stage for the Cambrian Explosion. GSA Today, 26 (11), 4-11.

Seilacher, A., Grazhdankin, D.V. and Legouta, A., 2003. Ediacaran Biota: the dawn of animal life in the shadow of giant protists. Paleontological Research, 7, 43-54.

Seilacher, A., Buatois, L.A. and Mángano, M.G., 2005. Trace fossils in the Ediacaran-Cambrian transition: behavioral diversification, ecological turnover and environmental shift. Palaeogeography, Palaeoclimatology, Palaeoecology, 227, 323-356.

Shepeleva, E.D., 1962. Plant? Fossils of unknown taxonomic position from the deposits of the Bavlinskaya Series in the Volga-Urals oil province. Doklady Akademii Nauk, 142, 170-171.

Sircombe, K.N., Bleeker, W. and Stern, R.A., 2001. Detrital zircon geochronology and grain-size analysis of ~2800 Ma Mesoarchean proto-cratonic cover succession, Slave Province, Canada. Earth and Planetary Science Letters, 189, 207-220.

Sláma, J., Kosler, J., Condon, D.J., Crowley, J.L., Gerdes, A., Hanchar, J.M., Horstwood, M.S.A., Morris, G.A. et al., 2008. Plesovice zircon – A new natural reference material for U-Pb and Hf isotopic microanalysis, Chemical Geology, 249, 1-35.

Spencer, C.J., Kirkland, C.L. and Taylor, R.J.M., 2016. Strategies towards statistically robust interpretations of in situ U-Pb zircon geochronology. Geoscience Frontiers, 7, 581-589.

Palacios, T., Zhiji, O., Agić, H., Högström, A.E.S., Jensen, S., Høyberget, M., Meinhold, G., Taylor, W.L. and Ebbestad, J.O.R., 2017. Organic-walled microfossils and organic fossils across the Ediacaran–Cambrian boundary on the Digermulen Peninsula, Arctic Norway.

Taylor, W.L, Almond, J.E., Jensen, S., Hogstrom, A.E.S., Gresse, P., Harrison, B., Agic, H., Hoyberget, M., Ebbestad, J.O.R., Meinhold, G. and Palacios, T., 2017a. Possible trilobozoans with internal structures from the Late Ediacaran Nama Group, Northern Cape, South Africa, International Symposium on the Ediacaran-Cambrian Transition, St. Johns, Newfoundland.

Taylor, W.L, Almond, J.E., Jensen, S., Hogstrom, A.E.S., Gresse, P., Harrison, B., Agic, H., Hoyberget, M., Ebbestad, J.O.R., Meinhold, G., and Palacios, T., 2017b. A new Ediacaran fossil assemblage from the Vingerbreek Member, (Nama Group), Northern Cape, South Africa, 2nd International

Conference on Continental Ichnology, University of Cape Town, Cape Town, South Africa, 85-86.

Thomsen, T. B., Knudsen, C. and Hinchey, A.M., 2015. Investigations of detrital zircon, rutile and titanite from present-day Labrador drainage basins: fingerprinting the Grenvillean front. Geological Survey of Denmark and Greenland Bulletin, 33, 77–80.

Tucker, R.T., Roberts, E.M., Hu, Y., Kemp, A.I.S. and Salisbury, S.W., 2013. Detrital zircon age constraints for the Winton Formation, Queensland: Contextualizing Australia's Late Cretaceous dinosaur faunas. Gondwana Research, 24, 767-779.

Vannier, J., Calandra, I., Gaillard, C. and Zylińska, A., 2010. Priapulid worms: Pioneer horizontal burrowers at the Precambrian-Cambrian boundary. Geology, 38 (8), 711-714.

Vermeesch, P., 2004. How many grains are needed for a provenance study?, Earth and Planetary Science Letters, 224, 441-451.

Vidal, G., 1976. Late Precambrian microfossils from the Visingso Beds in southern Sweden.Fossils and Strata, 9, 1-57.

Vidal, G., 1988. A palynological preparation method. Palynology, 12, 215-220.

Vidal, G. and Moczydlowska-Vidal, M., 1997. Biodiversity, speciation, and extinction trends of Proterozoic and Cambrian phytoplankton. Paleobiology, 23, 230–246.

Voice, P.J., Kowalewski, M. and Eriksson, K.A., 2011. Quantifying the timing and rate of crustal evolution: global compilation of radiometrically dated detrital zircon grains. The Journal of Geology, 119, 109-126.

Walker, R.G., 1979. Shallow marine sands. In: Walker, R.G. (ed): Facies Models: Geoscience Canada, Reprint series 1, 75-89.

Ward, P. and Kischvink, J., 2015. A New History of Life: The Radical New Discoveries about the Origins and Evolution of Life on Earth. Bloomsbury Publishing USA, 1 -391.

Willman, S., 2009. Morphology and wall ultrastructure of leiosphaeric and acanthomorphic acritarchs from the Ediacaran of Australia. Geobiology, 7, 8-20.

Wilson, J.P., Grotzinger, J.P., Fischer, W.W., Hand, K.P., Jensen, S., Knoll, A.H., Abelson, J., Metz, J.M., McLoughlin, N., Cohen, P.A. and Tice, M.M., 2012. Deep-water incised valley deposits at the Proterozoic-Cambrian boundary in southern Namibia contain abundant Treptichnus pedum. Palaios, 27, 252–273.

Wilson, A., Flint, S. and Payenberg, T., 2014. Architectural Styles and Sedimentology of the Fluvial Lower Beaufort Group, Karoo Basin, South Africa. Journal of Sedimentary Research, 84, 326–348.

8. Appendices

Appendix A: Key for the sedimentary logs (Figures 4.1-2; 4.5-6; 4.8-9)

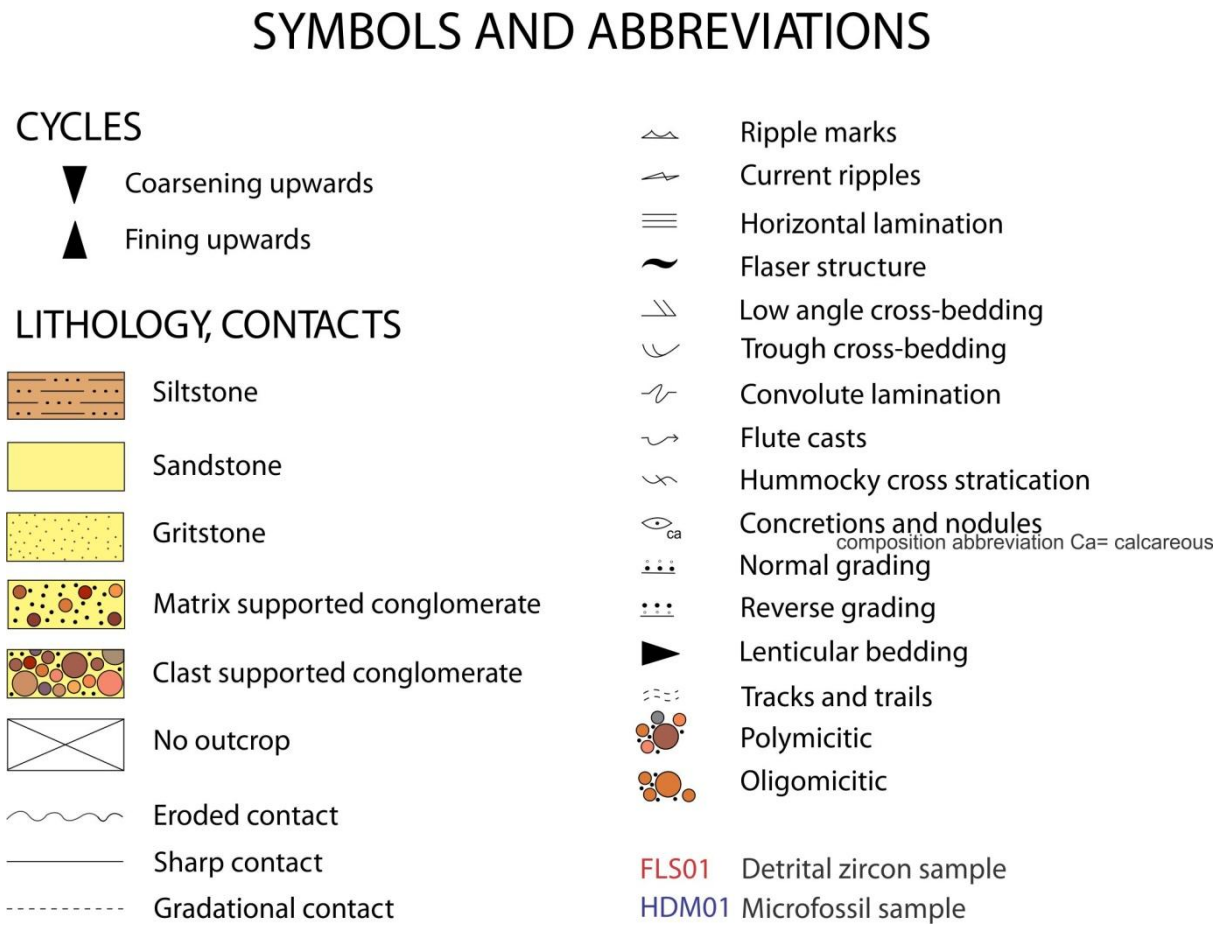

Appendix B: Clast counts

Table B1. Clast size and composition for the 11 measured conglomerate beds on Draaihoek farm.

No.	Bed 1		Bed 2		Bed 3		Bed 5		Bed 6		Bed 7		Bed 8		Bed 9		Bed 10		Bed 11		Bed 12	
	Clast size	Type	Clast size	Type	Clast size	Type	Clast size	Type	Clast size	Type	Clast size	Type	Clast size	Type	Clast size	Type	Clast size	Type	Clast size	Type	Clast size	Type
1	0.26	Quartz	0.67	Shale	0.67	Feldspar	0.76	Shale	0.21	Shale	0.42	Feldspar	0.26	Shale	0.32	Quartz	0.23	Shale	0.32	Shale	0.28	Quartz
2	0.28	Quartz	0.81	Quartz	0.85	Feldspar	0.82	Feldspar	0.21	Quartz	0.47	Shale	0.27	Quartzite	0.32	Quartz	0.32	Feldspar	0.32	Feldspar	0.28	Shale
3	0.28	Shale	0.94	Shale	0.85	Feldspar	0.90	Feldspar	0.21	Quartz	0.84	Feldspar	0.36	Shale	0.33	Quartz	0.47	Feldspar	0.34	Feldspar	0.59	Feldspar
4	0.31	Shale	1.03	Shale	0.95	Feldspar	0.90	Feldspar	0.21	Shale	0.94	Shale	0.36	Quartzite	0.33	Quartz	0.49	Shale	0.46	Feldspar	0.62	Quartz
5	0.31	Quartz	1.13	Shale	0.95	Feldspar	0.95	Feldspar	0.22	Quartz	1.16	Feldspar	0.38	Quartzite	0.33	Quartz	0.61	Feldspar	0.47	Feldspar	0.62	Quartz
6	0.31	Quartz	1.13	Chert	1.06	Feldspar	1.05	Feldspar	0.25	Shale	1.44	Feldspar	0.46	Quartz	0.34	Quartz	0.65	Feldspar	0.47	Feldspar	0.63	Feldspar
7	0.33	Shale	1.14	Shale	1.08	Shale	1.13	Feldspar	0.25	Quartz	1.55	Feldspar	0.46	Quartzite	0.35	Quartz	0.69	Feldspar	0.57	Feldspar	0.65	Shale
8	0.36	Chert	1.14	Quartz	1.20	Shale	1.17	Feldspar	0.25	Shale	1.62	Feldspar	0.46	Feldspar	0.35	Quartz	0.69	Feldspar	0.58	Feldspar	0.65	Feldspar
9	0.39	Quartz	1.38	Shale	1.24	Quartz	1.20	Feldspar	0.28	Quartz	1.82	Feldspar	0.46	Feldspar	0.37	Quartz	0.80	Feldspar	0.64	Feldspar	0.71	Quartz
10	0.40	Quartz	1.44	Quartz	1.29	Shale	1.22	Feldspar	0.28	Shale	1.89	Feldspar	0.49	Feldspar	0.38	Quartz	0.81	Feldspar	0.66	Feldspar	0.74	Feldspar
11	0.42	Quartz	1.46	Shale	1.29	Quartz	1.34	Feldspar	0.28	Quartz	1.91	Feldspar	0.51	Shale	0.39	Quartz	0.81	Feldspar	0.68	Shale	0.78	Quartz
12	0.42	Quartz	1.61	Shale	1.36	Igneous	1.41	Feldspar	0.29	Shale	1.94	Feldspar	0.53	Feldspar	0.40	Quartz	0.82	Feldspar	0.69	Feldspar	0.81	Feldspar
13	0.42	Quartz	1.61	Shale	1.36	Shale	1.41	Feldspar	0.31	Feldspar	1.98	Feldspar	0.55	Feldspar	0.40	Quartz	0.84	Feldspar	0.72	Feldspar	0.89	Quartz
14	0.44	Quartz	1.65	Quartz	1.42	Quartz	1.41	Feldspar	0.35	Feldspar	2.03	Feldspar	0.55	Feldspar	0.41	Quartz	0.89	Feldspar	0.80	Feldspar	0.99	Feldspar
15	0.45	Feldspar	1.80	Shale	1.42	Igneous	1.43	Feldspar	0.35	Quartz	2.16	Quartz	0.58	Feldspar	0.43	Quartz	0.92	Feldspar	0.80	Feldspar	0.99	Feldspar
16	0.45	Feldspar	1.84	Quartz	1.42	Shale	1.49	Feldspar	0.35	Shale	2.27	Quartz	0.58	Feldspar	0.44	Feldspar	0.94	Chert	0.89	Feldspar	1.05	Feldspar
17	0.47	Feldspar	1.84	Quartz	1.49	Quartz	1.59	Feldspar	0.39	Feldspar	2.30	Quartz	0.61	Feldspar	0.44	Quartz	1.07	Feldspar	0.92	Feldspar	1.11	Feldspar
18	0.48	Feldspar	1.84	Igneous	1.50	Shale	1.61	Feldspar	0.40	Shale	2.41	Quartz	0.66	Feldspar	0.46	Feldspar	1.12	Feldspar	0.98	Feldspar	1.15	Feldspar
19	0.48	Igneous	1.89	Quartz	1.50	Quartz	1.68	Feldspar	0.40	Shale	2.42	Quartz	0.69	Feldspar	0.48	Feldspar	1.13	Feldspar	1.02	Feldspar	1.17	Feldspar
20	0.53	Feldspar	1.94	Quartz	1.50	Quartz	1.68	Feldspar	0.40	Shale	2.42	Quartz	0.71	Feldspar	0.48	Feldspar	1.14	Feldspar	1.05	Feldspar	1.17	Quartz
21	0.54	Quartz	1.97	Quartz	1.53	Quartz	1.79	Shale	0.41	Shale	2.47	Quartz	0.71	Feldspar	0.49	Quartz	1.20	Shale	1.05	Feldspar	1.20	Carbonate
22	0.54	Feldspar	2.02	Quartz	1.55	Quartz	1.79	Feldspar	0.44	Feldspar	2.50	Quartz	0.73	Feldspar	0.50	Feldspar	1.33	Feldspar	1.12	Quartz	1.22	Feldspar
23	0.57	Quartz	2.02	Quartz	1.62	Quartz	1.80	Shale	0.44	Feldspar	2.55	Quartz	0.73	Feldspar	0.52	Feldspar	1.33	Feldspar	1.12	Feldspar	1.24	Feldspar
24	0.61	Feldspar	2.02	Quartz	1.66	Quartz	1.86	Shale	0.44	Shale	2.59	Quartz	0.73	Feldspar	0.52	Feldspar	1.37	Feldspar	1.13	Feldspar	1.25	Feldspar
25	0.61	Feldspar	2.07	Quartz	1.70	Quartz	1.93	Shale	0.46	Feldspar	2.63	Quartz	0.73	Feldspar	0.53	Feldspar	1.41	Feldspar	1.14	Feldspar	1.25	Feldspar
26	0.63	Feldspar	2.10	Quartz	1.70	Quartz	1.94	Quartz	0.49	Feldspar	2.65	Quartz	0.75	Feldspar	0.54	Feldspar	1.41	Feldspar	1.21	Feldspar	1.39	Feldspar
27	0.63	Feldspar	2.19	Quartz	1.75	Quartz	1.95	Quartz	0.49	Shale	2.70	Quartz	0.78	Feldspar	0.54	Feldspar	1.48	Feldspar	1.25	Feldspar	1.39	Feldspar
28	0.67	Quartz	2.19	Quartz	1.80	Quartz	2.02	Quartzite	0.49	Feldspar	2.70	Quartz	0.78	Feldspar	0.56	Quartz	1.48	Shale	1.26	Shale	1.45	Feldspar
29	0.68	Igneous	2.24	Quartz	1.81	Quartz	2.07	Quartz	0.50	Feldspar	2.74	Quartz	0.78	Feldspar	0.56	Feldspar	1.59	Quartz	1.27	Feldspar	1.45	Feldspar
30	0.68	Feldspar	2.25	Quartzite	1.90	Quartzite	2.22	Quartz	0.50	Quartz	2.81	Quartz	0.81	Feldspar	0.58	Feldspar	1.59	Shale	1.27	Feldspar	1.47	Feldspar
31	0.69	Chert	2.26	Quartzite	1.92	Quartz	2.23	Quartz	0.50	Feldspar	2.98	Quartz	0.81	Feldspar	0.59	Feldspar	1.59	Shale	1.27	Feldspar	1.48	Feldspar
32	0.74	Feldspar	2.35	Quartz	1.96	Carbonate	2.25	Quartz	0.50	Feldspar	2.99	Quartz	0.84	Feldspar	0.60	Feldspar	1.60	Quartz	1.27	Shale	1.51	Feldspar
33	0.77	Quartz	2.38	Quartz	1.96	Carbonate	2.29	Quartz	0.53	Feldspar	3.00	Quartz	0.91	Feldspar	0.65	Feldspar	1.61	Quartz	1.30	Shale	1.51	Feldspar
34	0.80	Igneous	2.38	Quartzite	1.96	Quartz	2.31	Quartz	0.54	Feldspar	3.07	Quartz	0.93	Feldspar	0.65	Feldspar	1.73	Quartz	1.30	Feldspar	1.57	Feldspar
35	0.81	Quartz	2.42	Quartz	2.00	Quartzite	2.31	Quartz	0.56	Feldspar	3.18	Quartz	0.94	Feldspar	0.66	Feldspar	1.74	Quartz	1.36	Shale	1.57	Feldspar
36	0.83	Quartz	2.46	Quartzite	2.01	Carbonate	2.38	Quartz	0.56	Feldspar	3.18	Quartz	0.95	Feldspar	0.68	Feldspar	1.76	Quartz	1.37	Quartz	1.59	Feldspar
37	0.88	Quartz	2.46	Quartzite	2.01	Carbonate	2.38	Quartzite	0.56	Feldspar	3.30	Quartz	0.98	Feldspar	0.69	Feldspar	1.78	Quartz	1.38	Shale	1.61	Carbonate
38	0.89	Quartz	2.50	Quartzite	2.12	Quartz	2.48	Quartzite	0.56	Feldspar	3.31	Quartz	1.00	Feldspar	0.69	Feldspar	1.83	Quartz	1.39	Shale	1.63	Feldspar
39	0.90	Quartz	2.63	Quartzite	2.13	Carbonate	2.48	Quartzite	0.56	Feldspar	3.34	Quartz	1.00	Feldspar	0.70	Feldspar	1.87	Carbonate	1.41	Quartz	1.67	Feldspar
40	0.93	Quartz	2.63	Quartzite	2.26	Quartz	2.53	Quartzite	0.57	Feldspar	3.40	Quartz	1.00	Feldspar	0.81	Feldspar	1.88	Quartz	1.42	Quartz	1.70	Feldspar
41	0.94	Quartz	2.67	Quartzite	2.29	Carbonate	2.61	Quartzite	0.59	Feldspar	3.46	Quartz	1.00	Feldspar	0.82	Feldspar	1.90	Quartz	1.44	Shale	1.71	Feldspar
42	1.00	Quartz	2.67	Quartzite	2.29	Carbonate	2.65	Quartzite	0.59	Feldspar	3.47	Quartzite	1.04	Feldspar	0.82	Feldspar	1.95	Quartz	1.48	Quartz	1.71	Feldspar
43	1.01	Quartz	2.76	Quartzite	2.30	Carbonate	2.65	Quartzite	0.63	Feldspar	3.49	Quartzite	1.06	Feldspar	0.83	Feldspar	1.96	Carbonate	1.48	Carbonate	1.80	Feldspar
44	1.03	Quartz	2.76	Carbonate	2.30	Quartzite	2.66	Quartzite	0.63	Feldspar	3.54	Quartz	1.06	Feldspar	0.83	Feldspar	2.02	Quartz	1.48	Quartz	1.82	Feldspar
45	1.22	Quartz	2.91	Quartzite	2.30	Carbonate	2.74	Quartzite	0.64	Feldspar	3.59	Quartzite	1.06	Feldspar	0.85	Feldspar	2.02	Carbonate	1.52	Carbonate	1.86	Feldspar
46	1.26	Quartz	2.96	Carbonate	2.30	Carbonate	2.79	Quartzite	0.65	Feldspar	3.60	Quartzite	1.09	Quartzite	0.92	Feldspar	2.03	Quartz	1.53	Carbonate	1.86	Quartzite
47	1.27	Quartz	3.03	Quartzite	2.40	Carbonate	2.83	Quartzite	0.66	Feldspar	3.67	Quartzite	1.12	Quartz	0.93	Feldspar	2.05	Carbonate	1.78	Carbonate	1.86	Feldspar
48	1.31	Quartz	3.04	Carbonate	2.48	Carbonate	2.83	Quartzite	0.66	Quartzite	3.69	Quartz	1.18	Quartzite	0.93	Feldspar	2.12	Quartz	1.80	Quartz	1.90	Feldspar
49	1.36	Quartz	3.06	Quartzite	2.49	Quartz	2.84	Quartzite	0.81	Feldspar	3.71	Quartz	1.21	Quartzite	0.94	Feldspar	2.27	Quartz	1.82	Carbonate	1.91	Feldspar
50	1.37	Quartz	3.08	Carbonate	2.55	Carbonate	2.89	Quartzite	0.84	Feldspar	3.79	Quartzite	1.27	Quartzite	0.95	Feldspar	2.27	Carbonate	1.83	Quartz	1.92	Quartzite
51	1.54	Quartz	3.10	Carbonate	2.56	Carbonate	2.92	Quartzite	0.84	Feldspar	3.81	Quartz	1.29	Quartzite	0.95	Feldspar	2.29	Carbonate	1.87	Carbonate	1.96	Feldspar
52	1.55	Quartz	3.10	Carbonate	2.56	Carbonate	2.96	Carbonate	0.90	Feldspar	3.86	Quartzite	1.30	Quartzite	0.97	Feldspar	2.32	Carbonate	1.94	Quartz	1.98	Quartzite
53	1.61	Quartz	3.17	Carbonate	2.58	Carbonate	2.97	Carbonate	0.94	Feldspar	3.89	Quartzite	1.38	Quartzite	0.99	Quartz	2.33	Carbonate	1.99	Quartz	1.99	Quartz
54	1.69	Quartz	3.18	Carbonate	2.59	Carbonate	3.03	Quartzite	0.96	Feldspar	3.92	Quartz	1.39	Quartzite	0.99	Feldspar	2.34	Carbonate	1.99	Carbonate	2.12	Quartzite

Table B1. continued.

No.	Bed 1		Bed 2		Bed 3		Bed 5		Bed 6		Bed 7		Bed 8		Bed 9		Bed 10		Bed 11		Bed 12	
	Clast size	Type	Clast size	Type	Clast size	Type	Clast size	Type	Clast size	Type	Clast size	Type	Clast size	Type	Clast size	Type	Clast size	Type	Clast size	Type	Clast size	Type
55	1.72	Quartz	3.20	Carbonate	2.63	Carbonate	3.06	Carbonate	0.97	Feldspar	3.96	Quartz	1.55	Carbonate	1.01	Feldspar	2.41	Carbonate	2.01	Carbonate	2.16	Quartzite
56	1.89	Quartz	3.24	Carbonate	2.69	Carbonate	3.15	Quartzite	0.98	Quartz	4.02	Carbonate	1.56	Carbonate	1.02	Quartz	2.41	Carbonate	2.06	Carbonate	2.22	Quartzite
57	1.95	Shale	3.24	Carbonate	2.89	Carbonate	3.16	Carbonate	1.01	Feldspar	4.04	Quartz	1.59	Carbonate	1.06	Feldspar	2.45	Carbonate	2.09	Quartz	2.24	Quartz
58	1.99	Quartzite	3.40	Carbonate	2.89	Carbonate	3.16	Carbonate	1.04	Feldspar	4.05	Carbonate	1.59	Carbonate	1.07	Quartz	2.57	Carbonate	2.19	Carbonate	2.25	Quartzite
59	1.99	Shale	3.42	Carbonate	3.14	Carbonate	3.19	Carbonate	1.05	Feldspar	4.10	Carbonate	1.66	Carbonate	1.08	Quartz	2.67	Carbonate	2.24	Carbonate	2.29	Quartz
60	2.13	Quartzite	3.46	Carbonate	3.14	Carbonate	3.26	Quartzite	1.08	Feldspar	4.11	Quartz	1.70	Carbonate	1.14	Quartz	2.75	Carbonate	2.24	Carbonate	2.31	Quartzite
61	2.17	Quartzite	3.55	Carbonate	3.16	Carbonate	3.32	Carbonate	1.09	Feldspar	4.18	Carbonate	1.75	Carbonate	1.15	Quartz	2.79	Quartz	2.28	Carbonate	2.31	Quartz
62	2.22	Quartzite	3.81	Carbonate	3.19	Carbonate	3.44	Carbonate	1.16	Quartz	4.31	Carbonate	1.79	Carbonate	1.16	Quartz	2.82	Carbonate	2.34	Carbonate	2.32	Carbonate
63	2.25	Quartzite	3.82	Carbonate	3.21	Carbonate	3.70	Quartzite	1.18	Quartz	4.33	Carbonate	1.80	Carbonate	1.21	Quartz	2.86	Quartz	2.43	Carbonate	2.34	Carbonate
64	2.29	Carbonate	3.87	Carbonate	3.23	Carbonate	3.86	Carbonate	1.19	Feldspar	4.34	Carbonate	1.87	Quartzite	1.28	Quartz	2.86	Carbonate	2.54	Quartz	2.35	Carbonate
65	2.45	Carbonate	3.88	Carbonate	3.23	Carbonate	3.94	Quartzite	1.21	Quartzite	4.50	Carbonate	1.91	Quartzite	1.29	Quartzite	3.07	Carbonate	2.54	Quartz	2.37	Quartz
66	2.49	Carbonate	4.03	Carbonate	3.30	Carbonate	3.98	Carbonate	1.23	Quartz	4.55	Carbonate	1.96	Carbonate	1.29	Quartzite	3.14	Carbonate	2.56	Carbonate	2.40	Carbonate
67	2.50	Carbonate	4.03	Carbonate	3.32	Carbonate	4.01	Carbonate	1.24	Feldspar	4.68	Carbonate	2.03	Quartzite	1.29	Quartz	3.17	Carbonate	2.66	Quartz	2.40	Quartz
68	2.55	Carbonate	4.05	Carbonate	3.46	Carbonate	4.08	Carbonate	1.27	Quartz	4.72	Carbonate	2.09	Carbonate	1.30	Quartz	3.22	Carbonate	2.75	Carbonate	2.48	Carbonate
69	2.59	Carbonate	4.11	Carbonate	3.52	Carbonate	4.16	Carbonate	1.27	Quartz	4.90	Carbonate	2.14	Carbonate	1.38	Carbonate	3.24	Carbonate	2.85	Carbonate	2.53	Carbonate
70	2.61	Carbonate	4.13	Carbonate	3.56	Carbonate	4.25	Carbonate	1.27	Quartz	4.91	Carbonate	2.19	Carbonate	1.38	Carbonate	3.24	Carbonate	2.92	Carbonate	2.72	Carbonate
71	2.76	Carbonate	4.22	Carbonate	3.76	Carbonate	4.25	Carbonate	1.29	Quartz	5.31	Carbonate	2.25	Carbonate	1.42	Quartzite	3.32	Carbonate	2.96	Carbonate	2.72	Carbonate
72	2.90	Carbonate	4.33	Carbonate	3.78	Carbonate	4.27	Carbonate	1.29	Quartz	5.46	Carbonate	2.38	Carbonate	1.50	Carbonate	3.36	Carbonate	2.98	Carbonate	2.74	Carbonate
73	2.94	Carbonate	4.34	Carbonate	3.80	Carbonate	4.34	Carbonate	1.30	Quartz	5.50	Carbonate	2.77	Carbonate	1.52	Quartz	3.38	Carbonate	3.10	Quartz	2.82	Carbonate
74	3.12	Carbonate	4.58	Carbonate	3.83	Carbonate	4.35	Carbonate	1.38	Quartz	5.58	Carbonate	2.80	Carbonate	1.67	Carbonate	3.38	Carbonate	3.18	Carbonate	2.89	Carbonate
75	3.14	Carbonate	4.81	Carbonate	3.83	Carbonate	4.40	Carbonate	1.47	Quartz	5.60	Carbonate	2.83	Carbonate	1.69	Quartzite	3.57	Carbonate	3.26	Carbonate	2.97	Quartz
76	3.29	Carbonate	4.91	Carbonate	3.97	Carbonate	4.46	Carbonate	1.60	Quartz	5.62	Carbonate	2.87	Carbonate	1.70	Quartzite	3.66	Carbonate	3.37	Carbonate	3.01	Carbonate
77	3.66	Carbonate	4.98	Carbonate	3.97	Carbonate	4.72	Carbonate	1.64	Quartz	5.63	Carbonate	2.97	Carbonate	1.81	Carbonate	3.78	Carbonate	3.46	Carbonate	3.03	Carbonate
78	3.97	Carbonate	5.09	Carbonate	3.99	Carbonate	4.78	Carbonate	1.75	Quartz	5.64	Carbonate	3.07	Carbonate	1.86	Carbonate	3.79	Carbonate	3.56	Carbonate	3.04	Quartz
79	4.44	Carbonate	5.16	Carbonate	4.03	Carbonate	4.93	Carbonate	1.76	Quartzite	5.67	Carbonate	3.21	Carbonate	1.88	Quartz	3.95	Carbonate	3.64	Carbonate	3.14	Carbonate
80	4.56	Carbonate	5.25	Carbonate	4.04	Carbonate	4.94	Carbonate	1.81	Quartz	5.80	Carbonate	3.36	Carbonate	1.96	Carbonate	4.07	Carbonate	3.86	Carbonate	3.17	Carbonate
81	4.65	Carbonate	5.27	Carbonate	4.06	Carbonate	5.14	Carbonate	1.84	Quartzite	6.42	Carbonate	3.66	Carbonate	1.98	Carbonate	4.20	Carbonate	3.98	Carbonate	3.23	Carbonate
82	4.65	Carbonate	5.32	Carbonate	4.08	Carbonate	5.16	Carbonate	1.92	Quartz	6.87	Carbonate	3.73	Carbonate	2.21	Carbonate	4.22	Carbonate	4.11	Carbonate	3.24	Carbonate
83	4.76	Carbonate	5.49	Carbonate	4.25	Carbonate	5.17	Carbonate	1.94	Quartz	6.89	Carbonate	3.87	Carbonate	2.30	Carbonate	4.33	Carbonate	4.14	Carbonate	3.24	Carbonate
84	4.79	Carbonate	5.87	Carbonate	4.25	Carbonate	5.28	Carbonate	2.00	Quartzite	6.95	Carbonate	3.88	Carbonate	2.46	Carbonate	4.44	Carbonate	4.22	Carbonate	3.29	Carbonate
85	4.87	Carbonate	6.30	Carbonate	4.25	Carbonate	5.44	Carbonate	2.05	Quartzite	7.01	Carbonate	3.95	Carbonate	2.52	Carbonate	4.50	Carbonate	4.23	Carbonate	3.30	Carbonate
86	5.01	Carbonate	6.38	Carbonate	4.27	Carbonate	6.41	Carbonate	2.36	Carbonate	7.41	Carbonate	3.98	Carbonate	2.56	Carbonate	4.51	Carbonate	4.27	Carbonate	3.42	Carbonate
87	5.13	Carbonate	6.38	Carbonate	4.46	Carbonate	6.84	Carbonate	2.47	Carbonate	7.73	Carbonate	4.07	Carbonate	2.73	Carbonate	4.61	Carbonate	4.28	Carbonate	3.75	Carbonate
88	5.46	Carbonate	6.65	Carbonate	4.48	Carbonate	7.00	Carbonate	2.69	Carbonate	7.73	Carbonate	4.16	Carbonate	2.98	Carbonate	5.02	Carbonate	4.43	Carbonate	3.82	Carbonate
89	5.70	Carbonate	7.30	Carbonate	4.54	Carbonate	7.56	Carbonate	2.87	Carbonate	7.96	Carbonate	4.31	Carbonate	3.03	Carbonate	5.02	Carbonate	4.50	Carbonate	4.04	Carbonate
90	5.83	Carbonate	7.36	Carbonate	5.07	Carbonate	7.80	Carbonate	2.88	Carbonate	8.07	Carbonate	4.44	Carbonate	3.62	Carbonate	5.12	Carbonate	4.88	Carbonate	4.05	Carbonate
91	7.23	Carbonate	7.75	Carbonate	5.26	Carbonate	7.90	Carbonate	3.03	Carbonate	8.64	Carbonate	4.45	Carbonate	4.07	Carbonate	5.58	Carbonate	4.94	Carbonate	4.07	Carbonate
92	7.46	Carbonate	8.22	Carbonate	5.36	Carbonate	8.32	Carbonate	3.26	Carbonate	8.74	Carbonate	4.97	Carbonate	4.76	Carbonate	5.63	Carbonate	5.01	Carbonate	4.13	Carbonate
93	8.21	Carbonate	12.34	Carbonate	5.48	Carbonate	8.48	Carbonate	3.31	Carbonate	9.32	Carbonate	5.10	Carbonate	7.40	Carbonate	5.80	Carbonate	5.61	Carbonate	4.19	Carbonate
94	8.42	Carbonate	12.55	Carbonate	5.52	Carbonate	9.21	Carbonate	3.32	Carbonate	9.46	Carbonate	5.30	Carbonate	7.50	Carbonate	5.81	Carbonate	5.68	Carbonate	4.42	Carbonate
95	9.54	Carbonate	15.44	Carbonate	6.17	Carbonate	11.28	Carbonate	3.35	Carbonate	9.70	Carbonate	5.31	Carbonate	8.12	Carbonate	5.94	Carbonate	5.93	Carbonate	4.43	Carbonate
96	12.35	Carbonate	20.84	Carbonate	7.61	Carbonate	11.93	Carbonate	3.38	Carbonate	10.29	Carbonate	5.91	Carbonate	8.41	Carbonate	7.02	Carbonate	6.93	Carbonate	4.56	Carbonate
97	16.37	Carbonate	21.26	Carbonate	7.88	Carbonate	12.01	Carbonate	3.89	Carbonate	11.17	Carbonate	6.00	Carbonate	11.21	Carbonate	7.09	Carbonate	7.80	Carbonate	4.94	Carbonate
98	20.41	Carbonate	21.90	Carbonate	7.89	Carbonate	12.40	Carbonate	5.57	Carbonate	11.64	Carbonate	6.30	Carbonate	12.28	Carbonate	7.47	Carbonate	9.41	Carbonate	5.07	Carbonate
99	23.06	Carbonate	23.55	Carbonate	8.00	Carbonate	12.49	Carbonate	6.92	Carbonate	11.66	Carbonate	10.04	Carbonate	21.94	Carbonate	7.65	Carbonate	13.54	Carbonate	5.83	Carbonate
100	25.97	Carbonate	28.58	Carbonate	11.08	Carbonate	17.95	Carbonate	9.18	Carbonate	13.28	Carbonate	13.10	Carbonate	33.33	Carbonate	10.22	Carbonate	17.13	Carbonate	14.58	Carbonate

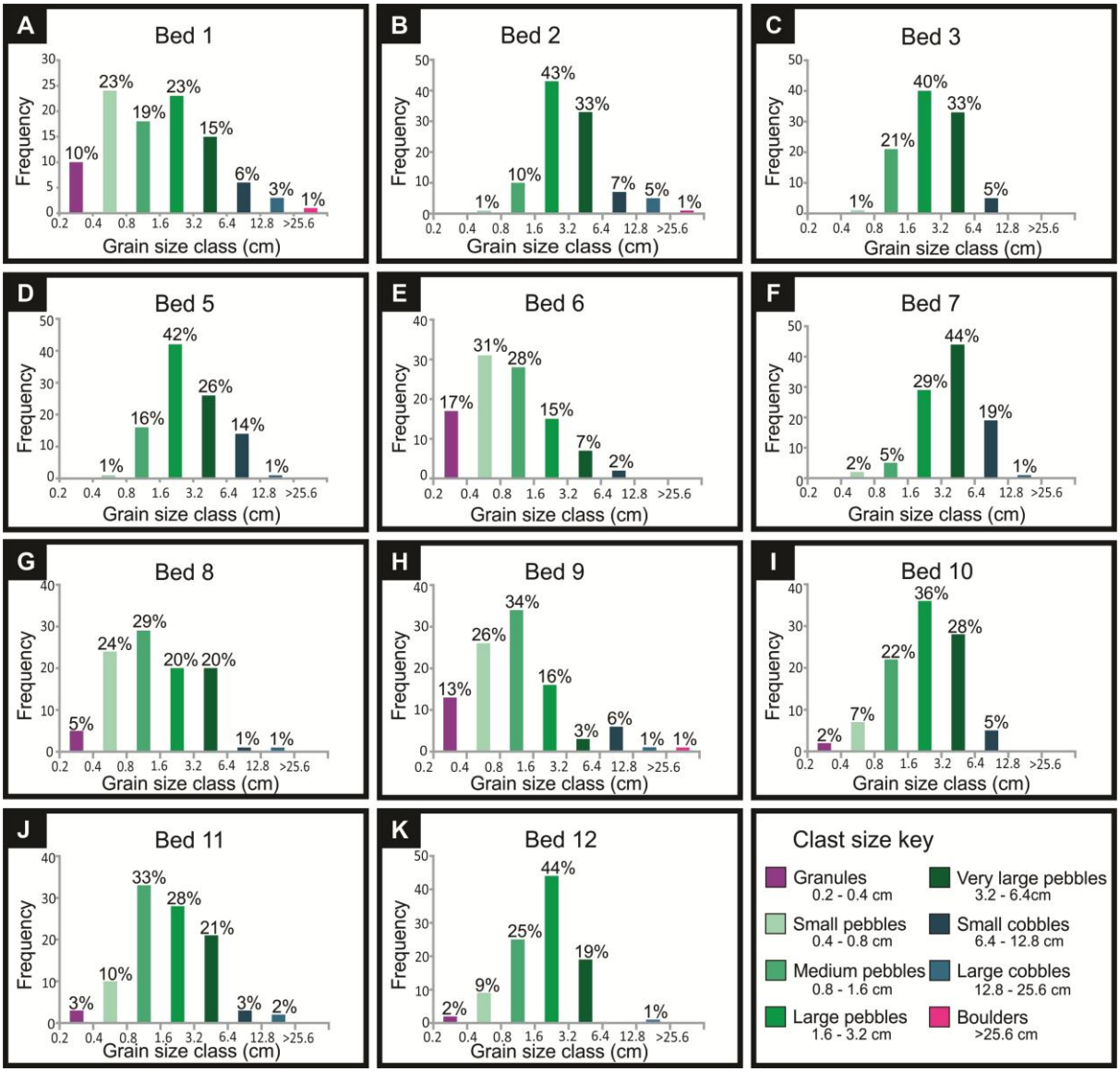

Figure B1. Individual clast size histograms of the 11 conglomerate beds

Table B2. Clast size and bed thickness correlation

	Bed	Average clast size		Smallest clast (cm)	Largest clast (cm)
#	Thickness (cm)	Size (cm)	Group		
1	30	3	Large pebbles	0.3	26
2	80	4.5	Very large pebbles	0.7	28.6
3	25	3	Large pebbles	0.7	11.1
5	20	3.8	Very large pebbles	0.8	18
6	35	1.3	Medium pebbles	0.4	9.2
7	70	4.5	Very large pebbles	0.3	13.3
8	30	2.1	Large pebbles	0.3	13.1
9	30	2.1	Large pebbles	0.3	33.3
10	40	2.7	Large pebbles	0.2	10.2
11	65	2.6	Large pebbles	0.3	17.1
12	35	2.3	Large pebbles	0.3	14.5

Appendix C: U-Pb detrital zircon data

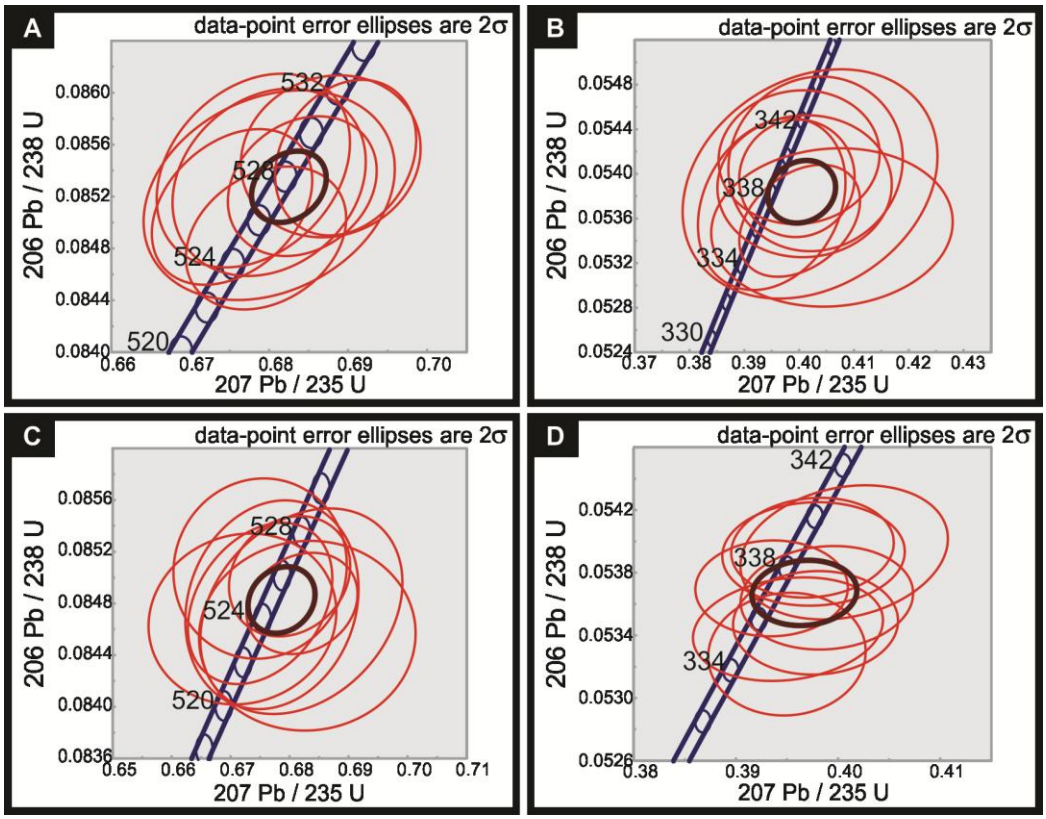

Figure C1. Concordia plots of the two standards from each sample run. A) M217a. B) PLESa. C) M127b. D) PLESb.

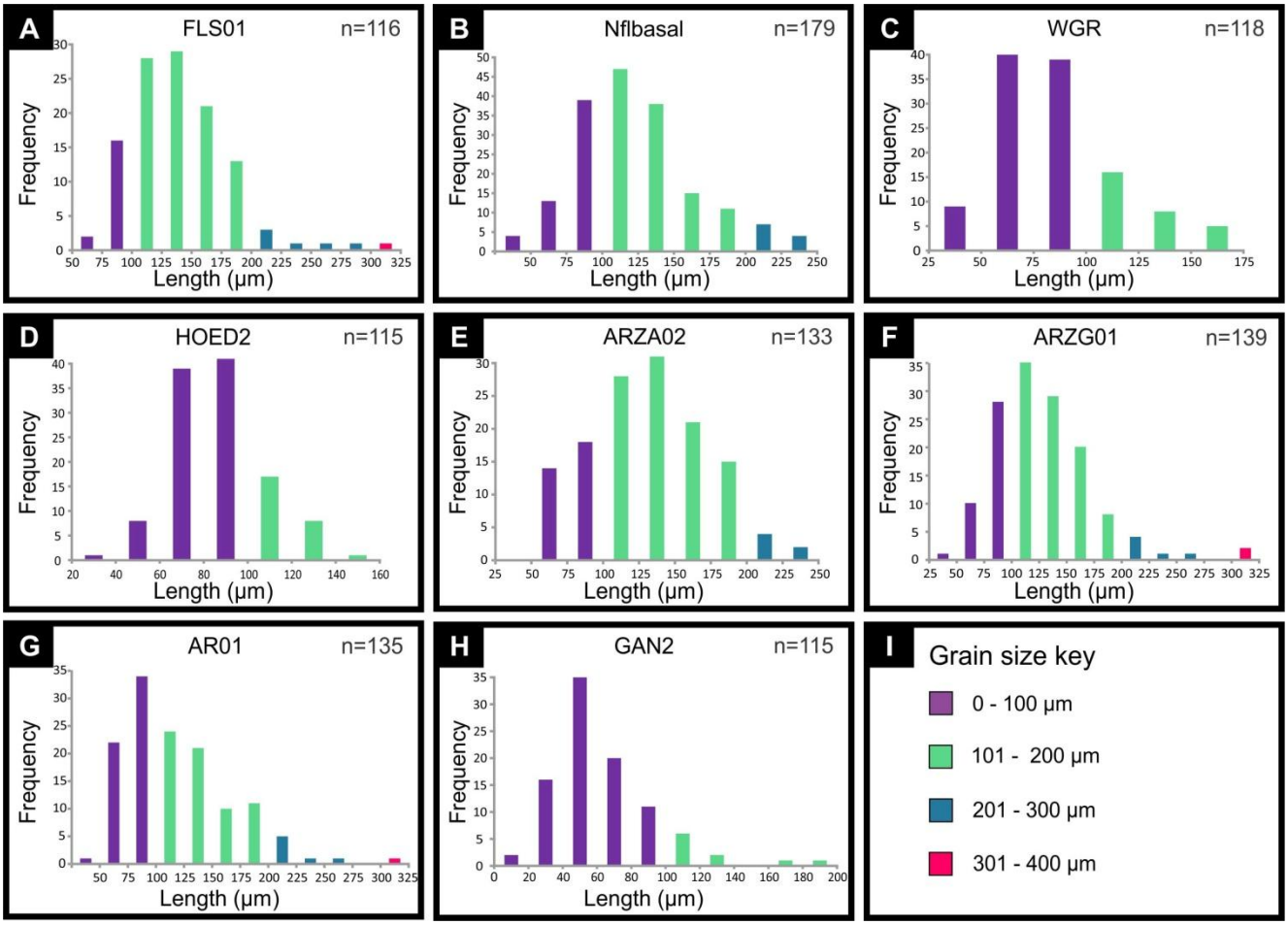

Figure C2. Individual zircon grain size (µm) histograms of the eight detrital zircon

Table C1. Concordant detrital zircon age data obtained from sample FLS01.

Sample FLS01			Isotopic ratios						Ages (Ma)						
Grain #	U [ppm]	Th/U	$^{206}Pb/^{238}U$	±2σ	$^{207}Pb/^{235}U$	±2σ	$^{207}Pb/^{206}Pb$	±2σ	$^{206}Pb/^{238}U$	±2σ	$^{207}Pb/^{235}U$	±2σ	$^{207}Pb/^{206}Pb$	±2σ	% Conc
1	159.5	0.68	0.1816	0.0011	1.8890	0.0260	0.0748	0.0011	1076	6	1076	9	1059	28	102
4	181	0.86	0.204	0.0017	2.2650	0.0370	0.0800	0.0012	1197	9	1201	12	1193	31	100
6	183	0.33	0.183	0.0011	1.9160	0.0280	0.0757	0.0012	1083	6	1085	10	1076	32	101
7	176.3	0.97	0.1731	0.0011	1.7880	0.0330	0.0747	0.0014	1029	6	1039	12	1047	38	98
8	223.7	0.53	0.2042	0.0012	2.2540	0.0240	0.0799	0.0009	1198	6	1197	8	1187	23	101
9	232.4	1.12	0.19	0.0013	2.0870	0.0300	0.0793	0.0012	1122	7	1143	10	1174	30	96
10	197.4	0.99	0.1808	0.001	1.8920	0.0220	0.0756	0.0010	1071	6	1077	8	1079	26	99
11	106.9	0.55	0.1834	0.0013	1.9410	0.0390	0.0765	0.0015	1085	7	1095	13	1101	38	99
12	458	0.76	0.1807	0.0034	1.9670	0.0410	0.0788	0.0008	1070	19	1102	14	1163	20	92
13	295	0.42	0.1832	0.0011	2.0170	0.0230	0.0798	0.0010	1085	6	1121	8	1186	24	91
14	395.3	0.52	0.191	0.0013	2.0580	0.0240	0.0780	0.0009	1127	7	1134	8	1142	24	99
15	182.7	0.31	0.1978	0.0012	2.1370	0.0280	0.0784	0.0011	1163	7	1161	9	1149	27	101
16	192.3	0.38	0.1984	0.0011	2.1640	0.0250	0.0791	0.0010	1166	6	1168	8	1168	25	100
17	93.5	0.94	0.1908	0.0013	2.0320	0.0340	0.0772	0.0014	1126	7	1124	11	1115	36	101
18	859	0.10	0.18073	0.00094	1.8920	0.0160	0.0760	0.0006	1071	5	1079	6	1093	15	98
22	194	0.34	0.1983	0.0013	2.1670	0.0350	0.0793	0.0012	1166	7	1169	11	1172	30	99
23	112.9	0.57	0.1721	0.001	1.7500	0.0270	0.0740	0.0012	1024	6	1028	10	1032	33	99
26	99.9	0.33	0.1762	0.0013	1.8190	0.0370	0.0750	0.0016	1046	7	1050	13	1056	44	99
27	276.2	0.60	0.2059	0.0013	2.2500	0.0270	0.0794	0.0010	1207	7	1196	9	1178	25	102
28	306	0.90	0.1839	0.0011	1.9250	0.0200	0.0760	0.0007	1088	6	1089	7	1094	21	99
29	261.5	0.66	0.183	0.0015	1.9010	0.0280	0.0756	0.0010	1083	8	1080	10	1077	27	101
30	321	0.31	0.195	0.0011	2.0960	0.0200	0.0782	0.0007	1148	6	1147	7	1146	19	100
31	507	0.10	0.18411	0.00087	1.9360	0.0160	0.0765	0.0006	1089	5	1093	6	1104	16	99
32	104.9	0.83	0.1852	0.0012	1.9500	0.0380	0.0768	0.0015	1095	7	1097	13	1097	39	100
33	97.4	0.81	0.1783	0.0013	1.8590	0.0330	0.0760	0.0014	1057	7	1064	12	1078	38	98
34	325.2	0.27	0.1831	0.0016	1.9290	0.0270	0.0761	0.0009	1084	9	1090	9	1095	24	99
35	262.6	0.54	0.1811	0.0013	1.8870	0.0280	0.0758	0.0011	1073	7	1075	10	1082	28	99
37	260	0.29	0.1969	0.0014	2.1770	0.0340	0.0804	0.0012	1159	8	1172	11	1200	29	97
38	549	0.29	0.1844	0.0015	1.9230	0.0250	0.0758	0.0009	1091	8	1088	9	1086	22	100
39	623.3	0.80	0.19535	0.00095	2.2240	0.0200	0.0828	0.0008	1150	5	1188	6	1262	18	91
40	107.7	0.47	0.1821	0.0017	1.8970	0.0410	0.0758	0.0015	1078	9	1076	14	1073	40	101
41	277.8	0.21	0.16874	0.00095	1.6930	0.0220	0.0730	0.0010	1005	5	1005	8	1007	28	100
42	111.4	2.31	0.175	0.0012	1.7830	0.0280	0.0742	0.0013	1039	7	1037	10	1031	35	101
43	237.9	0.54	0.1845	0.0011	1.9120	0.0240	0.0754	0.0010	1092	6	1084	8	1071	26	102
44	104.2	0.84	0.1824	0.0014	1.9090	0.0360	0.0761	0.0014	1080	8	1082	13	1088	36	99
45	86.1	0.54	0.1991	0.0017	2.118	0.045	0.0777	0.0018	1170.2	8.9	1152	15	1121	46	104
46	322.6	0.48	0.19644	0.00097	2.12	0.019	0.07849	0.00069	1156.1	5.2	1154.6	6.3	1155	18	100
47	86.02	0.86	0.183	0.0015	1.903	0.041	0.0756	0.0017	1083.4	8	1079	14	1065	45	102
48	338.1	0.49	0.18648	0.00085	1.956	0.018	0.07617	0.0007	1102.2	4.6	1099.6	6.2	1095	18	101
49	468	0.52	0.17629	0.00098	1.817	0.019	0.07473	0.00071	1046.6	5.3	1050.9	6.8	1060	20	99
50	380	0.3	0.1964	0.0011	2.137	0.019	0.07906	0.00074	1156	5.8	1160.3	6.1	1169	18	99
51	92.7	1.09	0.174	0.0011	1.789	0.036	0.0746	0.0015	1034	6.1	1038	13	1037	42	100
52	104.22	0.41	0.1944	0.0014	2.11	0.036	0.0787	0.0014	1144.8	7.6	1149	12	1163	34	98
53	68.7	1.07	0.1828	0.0015	1.907	0.037	0.0757	0.0015	1082.3	7.9	1080	13	1065	42	102
54	305	0.09	0.1738	0.0012	1.789	0.026	0.0747	0.0011	1033.2	6.4	1042.3	9	1054	31	98
55	134.9	2.11	0.1677	0.0011	1.692	0.026	0.0731	0.0011	999.2	6.1	1005	10	1006	32	99
56	300.5	0.32	0.1826	0.001	1.909	0.019	0.0757	0.00076	1080.9	5.6	1083.5	6.7	1082	20	100
57	160.3	0.52	0.1844	0.001	1.935	0.027	0.0759	0.0011	1091.1	5.5	1091.4	9.5	1082	29	101
58	200.2	0.39	0.1988	0.0013	2.169	0.024	0.07902	0.00093	1168.6	7	1170.1	7.6	1167	23	100
59	330	0.44	0.1749	0.0011	1.882	0.023	0.07791	0.00094	1039.1	6.2	1074.8	8.3	1139	24	91
60	517.3	0.89	0.1757	0.0011	1.847	0.02	0.07597	0.00079	1043.4	6.1	1063.3	6.9	1092	21	96
61	347.4	0.55	0.1957	0.0012	2.131	0.023	0.07853	0.00094	1152.2	6.3	1158.1	7.5	1155	24	100
62	199.8	0.61	0.1806	0.0013	1.904	0.03	0.0763	0.0013	1070.2	7.2	1083	11	1094	35	98
64	413.4	0.63	0.1711	0.0018	1.813	0.03	0.0765	0.0013	1018	10	1049	11	1102	35	92
65	287	0.2	0.2019	0.001	2.231	0.026	0.07971	0.00089	1185.7	5.5	1189.8	8.1	1184	22	100
66	63.88	1.59	0.1863	0.0019	1.994	0.052	0.0774	0.0022	1101	11	1110	18	1103	59	100
67	508	0.47	0.17151	0.0008	1.84	0.016	0.07733	0.00068	1020.4	4.4	1059.2	5.7	1129	18	90
68	247	0.54	0.17945	0.00099	1.873	0.024	0.07509	0.00096	1063.9	5.4	1071.4	8.4	1070	27	99

Table C1. continued.

Sample FLS01			Isotopic ratios						Ages (Ma)						
Grain #	U [ppm]	Th/U	$^{206}Pb/^{238}U$	±2σ	$^{207}Pb/^{235}U$	±2σ	$^{207}Pb/^{206}Pb$	±2σ	$^{206}Pb/^{238}U$	±2σ	$^{207}Pb/^{235}U$	±2σ	$^{207}Pb/^{206}Pb$	±2σ	% Conc
69	432	0.57	0.1833	0.0012	1.923	0.021	0.07555	0.0007	1085.1	6.8	1088.1	7.1	1081	19	100
70	268.5	0.32	0.1882	0.0011	1.993	0.024	0.07642	0.0008	1111.8	6	1111.9	8.1	1101	21	101
73	581.3	0.55	0.1791	0.0011	1.892	0.02	0.07598	0.00082	1062.2	5.8	1077.5	7	1090	22	97
74	248.4	0.31	0.17142	0.00097	1.737	0.024	0.07307	0.00099	1019.8	5.4	1022.1	9.1	1007	28	101
75	803	0.51	0.1834	0.0016	2.053	0.025	0.08079	0.00096	1085.3	9	1132.5	8.5	1212	23	90
79	150.5	1.32	0.1954	0.0017	2.136	0.038	0.0794	0.0014	1152.1	8.4	1161	12	1174	35	98
80	212.3	0.9	0.1732	0.0011	1.816	0.029	0.0757	0.0012	1029.4	6.1	1051	10	1079	33	95
81	182.7	0.78	0.1788	0.0014	1.902	0.035	0.0769	0.0014	1060.3	7.9	1080	12	1108	36	96
82	264.7	0.78	0.1815	0.0011	1.956	0.026	0.07782	0.00099	1074.9	6	1099.5	8.8	1137	25	95
83	173.2	0.72	0.2042	0.0015	2.278	0.036	0.0807	0.0013	1197.5	8	1204	11	1206	32	99
84	219.1	0.37	0.202	0.0014	2.199	0.03	0.0787	0.0012	1186.1	7.3	1179.6	9.6	1158	30	102
85	234.3	1.48	0.17757	0.00087	1.832	0.021	0.07455	0.00083	1053.6	4.7	1055.9	7.5	1056	22	100
86	337.2	0.5	0.1813	0.0012	1.892	0.026	0.0756	0.001	1074	6.6	1077.5	9	1079	27	100
88	193.5	0.39	0.2577	0.0018	3.461	0.043	0.0972	0.0012	1478.2	9.3	1517.3	9.9	1567	24	94
89	172.7	0.3	0.1976	0.0011	2.143	0.028	0.0785	0.0011	1162.5	5.8	1161.3	9	1155	27	101
91	485	0.42	0.1864	0.0011	1.951	0.021	0.07602	0.00081	1101.6	6	1099.1	7.7	1098	21	100
92	277	0.89	0.1758	0.0014	1.866	0.024	0.07689	0.00093	1044.1	7.7	1068	8.4	1113	24	94
93	168.4	0.42	0.198	0.0012	2.136	0.032	0.0782	0.0012	1164.5	6.5	1160	11	1149	31	101
94	138.6	0.67	0.1956	0.0013	2.107	0.031	0.0781	0.0012	1151.4	6.9	1149	10	1140	31	101
96	434	0.63	0.22	0.0011	2.533	0.023	0.08342	0.0007	1282	5.6	1280.9	6.5	1276	16	100
97	134.9	0.26	0.2497	0.0019	3.143	0.044	0.0913	0.0014	1436.6	9.6	1442	11	1446	28	99
98	877	0.06	0.1748	0.0011	1.83	0.015	0.07596	0.0006	1038.3	5.9	1056	5.6	1092	16	95
99	67.64	0.65	0.1973	0.0018	2.156	0.063	0.079	0.0023	1160.5	9.9	1166	21	1157	60	100
100	43.51	0.95	0.1867	0.002	1.985	0.064	0.077	0.0025	1103	11	1105	22	1109	62	99
102	153.6	0.78	0.1846	0.0013	1.931	0.032	0.0757	0.0013	1091.7	6.8	1090	11	1076	34	101
103	316.5	0.74	0.1836	0.0012	1.922	0.025	0.07577	0.00098	1086.5	6.4	1087.5	8.8	1085	25	100
105	168.3	0.41	0.1964	0.0012	2.124	0.029	0.0784	0.0012	1155.8	6.7	1155.1	9.4	1146	31	101
106	138.2	0.35	0.2037	0.0021	2.28	0.052	0.0808	0.0019	1195	11	1204	16	1205	47	99
107	277	0.31	0.1704	0.0014	1.731	0.03	0.0733	0.0013	1014.2	7.6	1019	11	1016	37	100
108	408	0.56	0.1705	0.0013	1.735	0.022	0.0735	0.001	1014.9	7.3	1021	8.1	1024	28	99
109	57.09	0.15	0.1713	0.0019	1.802	0.057	0.076	0.0025	1021	11	1041	21	1056	70	97
110	471.2	0.41	0.1725	0.0012	1.77	0.026	0.074	0.001	1025.9	6.8	1033.7	9.5	1042	27	98
111	121.1	0.87	0.1716	0.0012	1.734	0.028	0.0729	0.0012	1020.6	6.4	1019	10	1010	34	101
112	390.3	0.17	0.2886	0.002	4.345	0.046	0.10867	0.00096	1635	10	1701.1	8.9	1775	16	92
113	1290	0.15	0.1684	0.0013	1.773	0.016	0.07604	0.00055	1003.2	6.9	1035.1	5.9	1096	15	92
114	182.5	0.81	0.1878	0.0016	1.992	0.043	0.0768	0.0019	1109.3	8.8	1111	15	1110	53	100
115	430.2	0.46	0.1816	0.0012	1.992	0.024	0.07906	0.00096	1075.9	6.3	1112.1	8.3	1170	24	92

Table C2. Concordant detrital zircon age data obtained from sample Nflbasal.

Sample Nflbasal			Isotopic ratios						Ages (Ma)						
Grain #	U [ppm]	Th/U	$^{206}Pb/^{238}U$	±2σ	$^{207}Pb/^{235}U$	±2σ	$^{207}Pb/^{206}Pb$	±2σ	$^{206}Pb/^{238}U$	±2σ	$^{207}Pb/^{235}U$	±2σ	$^{207}Pb/^{206}Pb$	±2σ	% Conc
1	204.2	0.59	0.1954	0.0012	2.1150	0.0310	0.0788	0.0012	1151	7	1154	10	1158	31	99
3	181.7	1.27	0.2045	0.0016	2.2790	0.0410	0.0808	0.0016	1199	9	1205	13	1209	38	99
8	132.8	1.10	0.1845	0.0016	1.9320	0.0410	0.0755	0.0016	1091	9	1093	15	1076	45	101
11	132.5	0.36	0.1957	0.0016	2.1230	0.0430	0.0785	0.0016	1152	8	1156	14	1146	41	101
12	176	0.77	0.1782	0.0017	1.8430	0.0530	0.0745	0.0020	1057	9	1059	19	1042	56	101
13	150.6	0.76	0.1809	0.001	1.8950	0.0310	0.0756	0.0012	1072	6	1077	11	1071	32	100
14	516	0.71	0.181	0.0014	1.8890	0.0270	0.0750	0.0010	1072	7	1077	10	1071	30	100
15	345.9	0.23	0.1977	0.0018	2.1720	0.0360	0.0791	0.0013	1163	10	1171	12	1170	32	99
16	428	0.42	0.1994	0.0023	2.1740	0.0390	0.0785	0.0011	1172	12	1171	12	1154	28	102
17	416.7	0.23	0.1899	0.0015	2.0310	0.0270	0.0770	0.0011	1121	8	1125	9	1117	28	100
18	179	0.62	0.1893	0.0016	2.1420	0.0410	0.0813	0.0014	1118	9	1161	13	1227	35	91
20	235.2	1.70	0.1785	0.0014	1.9550	0.0450	0.0785	0.0017	1059	8	1098	15	1150	42	92
22	134.3	0.80	0.1762	0.0018	1.8860	0.0460	0.0771	0.0018	1046	10	1073	16	1108	46	94
24	144.5	0.60	0.1973	0.0016	2.1380	0.0430	0.0786	0.0016	1161	9	1159	14	1156	40	100
25	491	0.37	0.1873	0.0018	1.9870	0.0300	0.0769	0.0010	1107	10	1110	10	1114	25	99
26	592.9	0.44	0.1737	0.0016	1.7750	0.0270	0.0740	0.0011	1032	9	1036	10	1040	31	99
28	409.2	0.53	0.1976	0.0011	2.2240	0.0260	0.0818	0.0010	1162	6	1188	8	1235	23	94
32	257	0.48	0.1858	0.0013	1.9440	0.0270	0.0759	0.0011	1099	7	1095	9	1091	30	101
34	151	1.51	0.1851	0.0015	1.9240	0.0280	0.0757	0.0013	1095	8	1088	10	1077	34	102
35	394	0.09	0.1774	0.0015	1.8450	0.0330	0.0756	0.0015	1053	8	1061	12	1080	40	98
36	199.6	0.87	0.1826	0.0012	1.9120	0.0290	0.0761	0.0012	1081	7	1084	10	1090	31	99
39	69.7	0.69	0.1969	0.0022	2.1320	0.0620	0.0789	0.0024	1158	12	1156	20	1158	59	100
41	639	0.33	0.1996	0.0011	2.1880	0.0200	0.0798	0.0007	1173	6	1177	6	1188	18	99
42	186.5	1.28	0.1829	0.0014	1.9110	0.0310	0.0758	0.0013	1083	7	1084	11	1091	34	99
45	169.6	1.36	0.182	0.0013	1.9910	0.0320	0.0795	0.0013	1078	7	1111	11	1183	32	91
46	81.5	0.72	0.2006	0.0021	2.1950	0.0590	0.0795	0.0021	1178	11	1176	19	1166	54	101
49	205.7	0.73	0.2027	0.0011	2.2460	0.0280	0.0805	0.0011	1190	6	1194	9	1206	25	99
52	638.6	0.86	0.1894	0.0011	2.1460	0.0220	0.0822	0.0008	1118	6	1163	7	1247	19	90
53	151.1	1.05	0.1857	0.0012	1.9640	0.0310	0.0768	0.0012	1098	7	1101	11	1107	33	99
57	255.8	0.79	0.2091	0.0014	2.3420	0.0350	0.0809	0.0012	1224	7	1224	11	1213	28	101
58	305.9	0.40	0.1963	0.0014	2.2270	0.0420	0.0821	0.0015	1155	8	1189	13	1242	35	93
61	201.9	0.71	0.1908	0.0019	1.9870	0.0430	0.0752	0.0018	1125	10	1109	15	1061	49	106
63	413.2	0.49	0.1861	0.0014	2.0700	0.0330	0.0802	0.0011	1100	8	1138	11	1197	27	92
64	158	0.96	0.1853	0.0021	2.0370	0.0380	0.0793	0.0015	1096	11	1126	13	1172	38	94
65	109.3	0.67	0.1992	0.0016	2.2420	0.0470	0.0811	0.0019	1171	9	1192	15	1211	45	97
67	117.2	2.346	0.1807	0.0019	1.962	0.055	0.0781	0.0022	1071	10	1099	19	1132	56	95
69	208.9	1.258	0.1743	0.0015	1.782	0.032	0.0736	0.0015	1035.9	8.1	1038	12	1028	42	101
74	498.3	0.287	0.17583	0.00097	1.915	0.017	0.07833	0.00071	1044.1	5.3	1087	6.3	1153	18	91
77	98.3	1.923	0.1771	0.0012	1.829	0.033	0.0743	0.0013	1050.9	6.7	1054	12	1039	36	101
80	360.5	0.749	0.1938	0.0012	2.148	0.026	0.0796	0.001	1141.8	6.4	1163.6	8.5	1182	25	97
81	125.3	1.192	0.1829	0.0011	1.92	0.028	0.0754	0.0012	1083	6	1086.6	9.7	1073	30	101
82	357.7	0.486	0.1794	0.0012	1.981	0.027	0.07898	0.00098	1063.7	6.8	1108.3	9.2	1177	24	90
84	167	0.393	0.1847	0.002	1.926	0.044	0.0748	0.0015	1092	11	1088	15	1053	39	104
87	122.4	0.56	0.1838	0.002	1.997	0.049	0.078	0.0018	1088	11	1112	17	1135	48	96
88	819	1.526	0.1802	0.0014	1.98	0.026	0.07879	0.00096	1068.3	7.5	1108.3	8.9	1164	24	92
91	386	0.176	0.1988	0.0016	2.186	0.034	0.079	0.0013	1168.7	8.4	1175	11	1165	32	100
94	1362	0.253	0.1745	0.0017	1.881	0.026	0.07768	0.0009	1036.6	9.4	1073.8	9.2	1136	23	91
95	350.3	0.302	0.1952	0.002	2.142	0.058	0.079	0.0022	1150	11	1160	19	1159	57	99
97	192	0.586	0.1795	0.0012	1.859	0.031	0.0747	0.0012	1064	6.8	1064	11	1052	35	101
98	234.8	0.504	0.1853	0.0017	2.013	0.045	0.0784	0.002	1095.6	9.4	1118	15	1145	50	96
99	522	0.257	0.1826	0.002	1.942	0.047	0.0767	0.0018	1081	11	1094	16	1106	48	98
101	733	0.352	0.1849	0.0011	2.029	0.02	0.0792	0.0008	1093.8	5.8	1124.6	6.5	1174	20	93
103	642	0.129	0.1868	0.001	2.02	0.021	0.07825	0.00079	1103.8	5.5	1121.6	7.2	1152	21	96
104	387.7	0.128	0.2004	0.0017	2.199	0.036	0.0796	0.0014	1177.5	9.2	1180	12	1183	35	100
105	342.8	0.462	0.1829	0.0017	2.021	0.036	0.0799	0.0013	1082.8	9.1	1122	12	1195	34	91

Table C3. Concordant detrital zircon age data obtained from sample WGR.

Sample WGR			Isotopic ratios						Ages (Ma)						
Grain #	U [ppm]	Th/U	$^{206}Pb/^{238}U$	±2σ	$^{207}Pb/^{235}U$	±2σ	$^{207}Pb/^{206}Pb$	±2σ	$^{206}Pb/^{238}U$	±2σ	$^{207}Pb/^{235}U$	±2σ	$^{207}Pb/^{206}Pb$	±2σ	% Conc
5	340.7	1.04	0.1825	0.00099	1.9550	0.0260	0.0775	0.0009	1081	5	1099	9	1134	23	95
7	485.5	0.28	0.1856	0.0017	2.0470	0.0400	0.0806	0.0015	1097	9	1131	13	1207	37	91
10	201.2	1.05	0.18665	0.00094	1.9580	0.0300	0.0760	0.0011	1103	5	1100	10	1087	30	101
12	140.36	0.94	0.2056	0.0018	2.2840	0.0470	0.0807	0.0018	1205	9	1205	15	1202	44	100
15	468	0.47	0.1838	0.0014	1.9300	0.0230	0.0764	0.0008	1088	8	1092	8	1100	22	99
18	638.8	0.37	0.2947	0.0022	4.4180	0.0420	0.1089	0.0010	1665	11	1715	8	1780	16	94
20	280.8	0.57	0.1857	0.0012	1.9460	0.0250	0.0760	0.0009	1098	7	1096	9	1087	24	101
22	430	0.58	0.1992	0.0011	2.1810	0.0210	0.0791	0.0008	1171	6	1174	7	1175	21	100
26	305.2	0.86	0.1832	0.0012	1.9860	0.0280	0.0787	0.0011	1085	7	1110	10	1158	28	94
27	408.6	0.76	0.1801	0.0014	1.9060	0.0410	0.0769	0.0014	1068	8	1082	14	1112	37	96
28	406.6	0.38	0.1949	0.0013	2.2000	0.0310	0.0820	0.0013	1148	7	1180	10	1240	31	93
29	128.12	0.96	0.1908	0.0015	2.0350	0.0440	0.0771	0.0017	1126	8	1128	16	1111	44	101
30	338.9	0.40	0.18433	0.00088	1.9930	0.0230	0.0784	0.0010	1091	5	1114	8	1152	26	95
39	481	0.12	0.1803	0.001	1.9460	0.0190	0.0782	0.0007	1069	6	1097	7	1149	18	93
44	425.5	0.21	0.274	0.0032	3.8570	0.0620	0.1023	0.0011	1560	16	1603	13	1663	19	94
45	396.6	0.35	0.1817	0.0014	1.8930	0.0310	0.0761	0.0014	1076	8	1078	11	1092	37	99
48	152.4	0.44	0.19761	0.00092	2.1490	0.0300	0.0790	0.0011	1162	5	1163	10	1162	29	100
50	423	0.41	0.1838	0.0018	1.9410	0.0330	0.0771	0.0013	1088	10	1094	11	1120	33	97
55	277.5	0.13	0.17746	0.00082	1.8210	0.0200	0.0746	0.0008	1053	5	1052	7	1054	22	100
56	149.5	1.28	0.18065	0.00096	1.8690	0.0300	0.0753	0.0012	1070	5	1068	11	1070	30	100
57	197.6	0.21	0.17403	0.00089	1.7680	0.0250	0.0741	0.0010	1034	5	1033	9	1033	28	100
59	322	0.63	0.17	0.0025	1.7010	0.0340	0.0729	0.0012	1012	14	1008	13	1012	36	100
60	316.4	0.39	0.1828	0.0021	1.9850	0.0430	0.0794	0.0018	1082	11	1110	15	1177	45	92
61	156.1	1.83	0.17022	0.00098	1.7180	0.0320	0.0734	0.0014	1013	5	1013	12	1014	38	100
62	343.8	0.47	0.1649	0.0014	1.7160	0.0370	0.0761	0.0018	984	8	1014	14	1091	46	90
64	281.7	0.43	0.1928	0.0011	2.0180	0.0290	0.0761	0.0011	1137	6	1120	10	1092	28	104
67	316	0.50	0.1813	0.0012	1.9040	0.0270	0.0766	0.0011	1074	7	1082	9	1104	28	97
71	154.7	0.55	0.2058	0.0013	2.2720	0.0400	0.0801	0.0014	1206	7	1202	12	1190	34	101
76	396.8	0.92	0.1798	0.0012	1.9510	0.0270	0.0789	0.0010	1066	7	1098	9	1166	25	91
77	227.5	1.64	0.1872	0.0012	1.9580	0.0280	0.0762	0.0012	1106	7	1102	10	1092	33	101
78	465	0.17	0.17607	0.00078	1.8420	0.0190	0.0759	0.0008	1045	4	1060	7	1088	22	96
80	321.2	0.42	0.18001	0.00097	1.9200	0.0270	0.0774	0.0011	1067	5	1087	9	1125	28	95
81	394.2	1.10	0.17922	0.00096	1.8950	0.0230	0.0767	0.0010	1063	5	1079	8	1109	25	96
82	172.5	0.24	0.174	0.00094	1.7580	0.0270	0.0733	0.0012	1034	5	1030	10	1015	34	102
83	870.4	0.08	0.1695	0.0014	1.7810	0.0290	0.0765	0.0015	1010	8	1038	11	1105	37	91
87	343	0.643	0.17577	0.00097	1.794	0.018	0.07436	0.00077	1043.7	5.3	1043.3	6.6	1046	21	100
89	391	0.246	0.1662	0.0011	1.745	0.02	0.07612	0.00082	990.9	5.9	1024.4	7.3	1102	22	90
90	232.6	0.708	0.1994	0.0012	2.184	0.036	0.0799	0.0014	1172.2	6.4	1175	11	1187	34	99
97	235.6	0.35	0.1726	0.0013	1.807	0.035	0.0766	0.0014	1026.1	7.2	1046	13	1099	38	93
99	255	1.156	0.1801	0.0019	1.96	0.052	0.0799	0.0022	1067	10	1100	18	1185	53	90
102	163.8	1.243	0.1816	0.0013	1.877	0.043	0.0758	0.0017	1075.9	7.1	1071	15	1078	47	100
103	344.4	0.819	0.1903	0.0012	2.058	0.037	0.0791	0.0017	1123.2	6.5	1134	12	1165	42	96
104	338.2	0.171	0.1799	0.0012	1.863	0.03	0.0759	0.0013	1066.5	6.7	1067	11	1085	33	98
107	268.2	0.463	0.1942	0.0014	2.092	0.049	0.079	0.0018	1143.9	7.6	1145	16	1165	44	98
109	708.5	0.341	0.1746	0.0013	1.84	0.022	0.07755	0.0008	1037.5	7.3	1059.3	7.7	1133	21	92
111	180.1	0.934	0.1799	0.0011	1.857	0.029	0.0755	0.0012	1066.4	6	1064	10	1070	33	100

Table C4. Concordant detrital zircon age data obtained from sample HOED2.

Sample HOED2			Isotopic ratios								Ages (Ma)				
Grain #	U [ppm]	Th/U	$^{206}Pb/^{238}U$	±2σ	$^{207}Pb/^{235}U$	±2σ	$^{207}Pb/^{206}Pb$	±2σ	$^{206}Pb/^{238}U$	±2σ	$^{207}Pb/^{235}U$	±2σ	$^{207}Pb/^{206}Pb$	±2σ	% Conc
1	169.9	0.34	0.1934	0.0017	2.0710	0.0380	0.0775	0.0014	1140	9	1138	13	1126	37	101
6	110.6	0.63	0.1988	0.0019	2.1670	0.0490	0.0791	0.0017	1169	10	1168	16	1160	44	101
7	121.5	0.50	0.2071	0.0016	2.3080	0.0540	0.0807	0.0019	1213	9	1212	17	1200	47	101
9	270	0.16	0.1813	0.0013	1.9040	0.0380	0.0759	0.0014	1074	7	1081	14	1088	38	99
11	115.4	0.47	0.1829	0.0016	1.9050	0.0390	0.0755	0.0015	1083	9	1081	14	1070	42	101
14	82.4	1.15	0.1934	0.0016	2.0680	0.0610	0.0774	0.0022	1140	8	1137	21	1109	58	103
15	275.7	0.44	0.1903	0.0017	2.0960	0.0460	0.0798	0.0020	1123	9	1147	15	1184	51	95
16	92.6	0.99	0.1922	0.0015	2.0790	0.0650	0.0783	0.0022	1133	8	1136	22	1142	57	99
17	318.8	0.54	0.2204	0.002	2.6910	0.0480	0.0885	0.0012	1284	10	1325	13	1389	27	92
21	150.6	0.34	0.1942	0.0029	2.1440	0.0620	0.0799	0.0022	1144	15	1161	20	1184	53	97
22	372.2	0.29	0.2001	0.0015	2.1950	0.0380	0.0797	0.0014	1176	8	1179	12	1185	36	99
23	115.9	0.59	0.3188	0.0016	4.7910	0.0500	0.1091	0.0012	1784	8	1783	9	1781	20	100
25	774.9	0.77	0.08713	0.00066	0.7210	0.0220	0.0601	0.0018	539	4	551	13	598	64	90
26	152.6	0.65	0.1809	0.0015	1.8800	0.0400	0.0755	0.0017	1072	8	1072	14	1069	46	100
27	315.5	0.22	0.1974	0.0011	2.1430	0.0270	0.0787	0.0009	1161	6	1162	9	1160	24	100
28	211.1	0.62	0.1965	0.0048	2.1290	0.0460	0.0791	0.0018	1156	26	1157	15	1169	45	99
29	136.3	0.44	0.1891	0.0014	2.0110	0.0470	0.0772	0.0018	1116	8	1117	16	1114	47	100
31	89.2	0.91	0.1856	0.0015	1.9630	0.0500	0.0770	0.0021	1099	8	1100	17	1108	52	99
33	317.2	1.42	0.1622	0.0035	1.6070	0.0590	0.0723	0.0019	969	19	971	24	988	55	98
36	140.1	0.92	0.1742	0.0015	1.8330	0.0400	0.0766	0.0017	1035	8	1055	14	1107	42	94
38	197.8	0.69	0.1651	0.0016	1.7370	0.0340	0.0765	0.0016	985	9	1021	13	1098	43	90
40	549.1	0.40	0.1782	0.0011	1.8370	0.0320	0.0752	0.0012	1057	6	1058	11	1070	32	99
41	271.8	0.66	0.1824	0.0023	1.9470	0.0480	0.0780	0.0018	1080	12	1096	17	1143	45	94
44	117.2	0.92	0.1851	0.0013	1.9500	0.0360	0.0767	0.0015	1095	7	1097	12	1095	40	100
45	303.1	0.52	0.1855	0.0013	2.0130	0.0380	0.0790	0.0014	1097	7	1119	13	1165	36	94
47	215.7	0.55	0.1943	0.0014	2.1180	0.0440	0.0795	0.0018	1145	8	1153	14	1177	45	97
48	287.3	1.62	0.1822	0.0012	1.9070	0.0370	0.0764	0.0014	1079	6	1082	13	1099	38	98
50	98.1	0.94	0.1858	0.0018	1.9630	0.0480	0.0776	0.0018	1098	10	1102	17	1126	46	98
51	166	0.70	0.2039	0.0018	2.2440	0.0450	0.0803	0.0018	1196	10	1194	14	1207	42	99
53	226.1	0.55	0.1816	0.0015	1.8940	0.0330	0.0762	0.0014	1076	8	1078	12	1099	39	98
54	913	0.08	0.173	0.0014	1.7670	0.0180	0.0744	0.0006	1028	8	1033	7	1051	15	98
55	208.7	0.83	0.2609	0.0013	3.5360	0.0370	0.0989	0.0011	1494	7	1536	8	1604	20	93
56	349.5	0.10	0.1719	0.001	1.7480	0.0240	0.0741	0.0010	1022	6	1026	9	1039	28	98
57	79.2	0.66	0.2001	0.0014	2.1920	0.0440	0.0799	0.0017	1176	8	1175	14	1189	40	99
58	311.7	0.94	0.17278	0.00093	1.7950	0.0230	0.0759	0.0010	1027	5	1043	9	1089	27	94
59	347.6	0.32	0.2045	0.0012	2.263	0.03	0.0809	0.0011	1199.5	6.4	1200	9.3	1215	27	99
60	309	0.26	0.195	0.0012	2.126	0.029	0.0794	0.0011	1148.6	6.6	1156.4	9.4	1179	28	97
61	272.7	0.29	0.1794	0.0011	1.864	0.033	0.076	0.0014	1063.9	5.8	1067	12	1088	37	98
62	153.7	0.47	0.1977	0.0011	2.132	0.031	0.0788	0.0012	1162.9	6	1159	10	1157	30	101
65	142.9	1.23	0.1829	0.0013	1.907	0.031	0.0762	0.0014	1082.4	7.1	1082	11	1090	36	99
68	318	0.46	0.1913	0.0015	2.054	0.025	0.07825	0.00087	1128.2	8.1	1132.1	8.3	1147	22	98
69	106.19	0.19	0.1746	0.0021	1.78	0.069	0.0741	0.0028	1037	11	1035	25	1023	74	101
70	530.3	0.25	0.1796	0.001	1.892	0.021	0.07678	0.00083	1064.6	5.6	1077.7	7.3	1113	22	96
71	149.7	0.45	0.1824	0.0015	1.89	0.042	0.0756	0.0017	1080	8.1	1076	15	1071	45	101
72	145.4	1.33	0.2028	0.0013	2.241	0.038	0.0802	0.0014	1190.3	7	1193	12	1195	33	100
77	196.63	0.41	0.1967	0.0017	2.143	0.039	0.0794	0.0014	1157.4	9.3	1161	13	1174	35	99
78	170.9	0.45	0.1955	0.0011	2.116	0.034	0.0786	0.0013	1150.9	6.1	1152	11	1156	33	100
81	164.1	0.51	0.1904	0.0019	2.125	0.047	0.081	0.0016	1123	10	1155	15	1217	37	92
82	326	0.42	0.1805	0.0014	1.95	0.027	0.0785	0.0011	1069.6	7.5	1097.6	9.3	1155	27	93
83	847	0.04	0.17685	0.00066	1.817	0.012	0.07446	0.0005	1049.7	3.6	1051.3	4.4	1051	14	100
84	270.6	0.27	0.1794	0.0011	1.866	0.028	0.0757	0.0011	1063.4	6.2	1068	9.8	1082	30	98
85	95.1	0.91	0.1996	0.0017	2.182	0.055	0.0793	0.002	1172.9	9	1173	18	1165	50	101
88	413	0.5	0.18002	0.00094	1.967	0.021	0.07924	0.00079	1067	5.1	1104.6	7	1174	20	91
94	302.1	0.29	0.1757	0.001	1.834	0.022	0.0755	0.00083	1043.5	5.7	1056.7	8	1078	22	97
95	304.6	0.41	0.2187	0.0026	2.684	0.056	0.0884	0.0011	1274	14	1320	15	1386	24	92
96	220.1	0.5	0.19831	0.00089	2.159	0.023	0.07861	0.00084	1166.2	4.8	1167.9	7.1	1156	22	101
97	661.5	0.1	0.1742	0.0012	1.779	0.023	0.07406	0.00095	1035.1	6.4	1037.4	8.5	1040	26	100
100	128.8	0.69	0.1995	0.0013	2.187	0.042	0.0792	0.0016	1172.6	7	1174	13	1161	41	101

Table C4. continued.

Sample HOED2			Isotopic ratios								Ages (Ma)				
Grain #	U [ppm]	Th/U	$^{206}Pb/^{238}U$	±2σ	$^{207}Pb/^{235}U$	±2σ	$^{207}Pb/^{206}Pb$	±2σ	$^{206}Pb/^{238}U$	±2σ	$^{207}Pb/^{235}U$	±2σ	$^{207}Pb/^{206}Pb$	±2σ	% Conc
101	374	0.22	0.17873	0.00083	1.885	0.019	0.07609	0.0008	1060	4.5	1075	6.6	1093	21	97
102	288.6	0.56	0.1793	0.00089	1.851	0.022	0.07454	0.00094	1063.1	4.9	1062.7	7.9	1050	25	101
105	235.8	0.8	0.1693	0.001	1.746	0.033	0.0746	0.0015	1008.3	5.7	1027	11	1056	39	95
107	71.7	1.1	0.1778	0.0015	1.848	0.044	0.0748	0.0017	1054.8	8.1	1059	16	1044	48	101
108	107.4	0.66	0.1654	0.0013	1.713	0.047	0.0749	0.0021	986.9	7.2	1016	16	1073	50	92
111	229.3	0.67	0.166	0.0014	1.662	0.043	0.0726	0.0019	989.8	7.5	993	16	992	54	100
113	445.5	0.49	0.1933	0.0015	2.109	0.028	0.0791	0.0012	1139.2	7.9	1151.3	9.1	1171	30	97
114	443.3	0.25	0.17301	0.00095	1.806	0.02	0.07554	0.00087	1028.6	5.2	1047	7.1	1078	23	95
115	385	0.41	0.1909	0.0016	2.106	0.033	0.0801	0.0012	1126	8.5	1150	11	1196	30	94

Table C5. Concordant detrital zircon age data obtained from sample ARZA02.

Sample ARZA02			Isotopic ratios						Ages (Ma)						
Grain #	U [ppm]	Th/U	$^{206}Pb/^{238}U$	±2σ	$^{207}Pb/^{235}U$	±2σ	$^{207}Pb/^{206}Pb$	±2σ	$^{206}Pb/^{238}U$	±2σ	$^{207}Pb/^{235}U$	±2σ	$^{207}Pb/^{206}Pb$	±2σ	% Conc
1	185.5	1.08	0.18285	0.00092	1.9120	0.0240	0.0758	0.0010	1082	5	1084	8	1079	27	100
2	201.7	0.57	0.171	0.0013	1.7900	0.0320	0.0758	0.0014	1017	7	1042	11	1081	37	94
3	64.9	0.44	0.2025	0.0016	2.2580	0.0530	0.0810	0.0020	1188	9	1197	16	1203	49	99
4	500.8	0.15	0.1902	0.0021	2.0920	0.0360	0.0791	0.0014	1122	11	1146	12	1180	39	95
5	148.4	0.41	0.1775	0.0013	1.8640	0.0390	0.0760	0.0016	1054	7	1067	14	1084	43	97
6	102.7	0.74	0.1764	0.0015	1.8430	0.0370	0.0759	0.0016	1047	8	1059	13	1077	41	97
7	246.5	0.23	0.2006	0.0011	2.1840	0.0250	0.0789	0.0009	1178	6	1175	8	1162	22	101
8	343	0.27	0.18045	0.00097	1.8840	0.0210	0.0755	0.0008	1070	5	1074	7	1075	22	100
9	134.3	0.80	0.1934	0.0012	2.0820	0.0340	0.0780	0.0013	1140	7	1141	11	1137	33	100
12	42.1	0.47	0.179	0.0021	1.9620	0.0640	0.0791	0.0026	1061	12	1099	21	1153	68	92
14	69.6	0.57	0.1878	0.0017	1.9640	0.0480	0.0760	0.0020	1109	9	1099	17	1074	54	103
15	217.5	0.44	0.19	0.001	2.0040	0.0230	0.0764	0.0009	1121	6	1117	8	1104	24	102
16	551.4	0.34	0.1909	0.001	2.1180	0.0210	0.0801	0.0008	1126	6	1154	7	1199	20	94
17	369.6	0.23	0.1807	0.0013	1.8840	0.0220	0.0755	0.0008	1071	7	1074	8	1081	22	99
19	520	0.23	0.1887	0.0013	2.0710	0.0190	0.0797	0.0009	1114	7	1139	6	1188	20	94
20	89	0.57	0.1819	0.0013	1.8980	0.0390	0.0758	0.0015	1077	7	1077	13	1068	40	101
22	93.4	0.68	0.184	0.0013	1.9280	0.0390	0.0762	0.0016	1089	7	1091	13	1088	40	100
24	29.1	0.77	0.1827	0.0018	1.9220	0.0640	0.0767	0.0027	1081	10	1079	22	1047	72	103
25	345.9	0.30	0.17765	0.00085	1.8290	0.0190	0.0748	0.0009	1054	5	1056	7	1058	23	100
27	94.6	0.91	0.1869	0.0015	1.9850	0.0340	0.0771	0.0013	1104	8	1108	12	1117	34	99
29	29.62	0.65	0.1858	0.002	1.9720	0.0630	0.0766	0.0023	1098	11	1096	22	1079	65	102
30	103.9	0.45	0.1759	0.0015	1.8350	0.0400	0.0758	0.0019	1045	9	1056	14	1072	51	97
31	158.2	0.50	0.1906	0.0018	2.0300	0.0380	0.0776	0.0012	1125	10	1123	13	1129	32	100
33	239.1	0.33	0.17727	0.00093	1.8210	0.0240	0.0748	0.0010	1052	5	1052	9	1059	26	99
34	206.7	0.86	0.1803	0.0012	1.8640	0.0250	0.0752	0.0010	1068	6	1067	9	1068	26	100
35	37.3	0.83	0.18	0.0018	1.8820	0.0550	0.0763	0.0022	1067	10	1068	20	1070	60	100
38	224.1	0.88	0.184	0.0017	1.9340	0.0350	0.0765	0.0014	1089	9	1092	12	1102	37	99
41	393.2	0.30	0.1751	0.0011	1.8510	0.0220	0.0770	0.0009	1040	6	1063	8	1117	24	93
43	185.2	0.38	0.1794	0.0015	1.8510	0.0380	0.0748	0.0016	1064	8	1062	14	1063	45	100
45	155.1	0.16	0.1792	0.0011	1.8530	0.0290	0.0751	0.0012	1063	6	1062	10	1060	31	100
46	148.3	0.65	0.1776	0.0012	1.8380	0.0260	0.0754	0.0010	1054	7	1058	9	1070	28	98
47	359.2	0.70	0.1972	0.0016	2.2310	0.0440	0.0822	0.0015	1160	9	1190	14	1245	34	93
48	118.4	0.54	0.1711	0.0012	1.7300	0.0290	0.0735	0.0012	1018	6	1017	11	1013	34	101
49	94.8	0.55	0.1967	0.0017	2.1610	0.0500	0.0799	0.0018	1157	9	1166	16	1179	46	98
50	127.5	0.97	0.2077	0.0018	2.2760	0.0460	0.0798	0.0016	1217	10	1203	14	1182	40	103
52	162.5	1.252308	0.1929	0.0016	2.076	0.041	0.0784	0.0017	1137.2	8.8	1139	14	1145	43	99
53	224.1	0.503347	0.1899	0.0013	2.029	0.031	0.0777	0.0011	1120.6	6.9	1125	11	1136	30	99
54	532.3	0.239151	0.17138	0.0009	1.735	0.017	0.07363	0.0007	1019.7	4.9	1021.2	6.2	1030	20	99
55	259	0.40556	0.1992	0.0016	2.188	0.029	0.0799	0.0012	1170.8	8.7	1176.1	9.2	1188	28	99
56	234.7	0.92288	0.18121	0.00097	1.886	0.026	0.07584	0.001	1073.5	5.3	1076.1	8.8	1083	26	99
58	152.3	0.431385	0.185	0.0011	1.939	0.026	0.0762	0.001	1094.2	5.8	1093	9	1089	28	100
59	264	0.463636	0.1934	0.0013	2.141	0.025	0.0806	0.001	1139.5	7.2	1161.2	8.2	1213	23	94
60	421	0.152969	0.1742	0.0012	1.798	0.026	0.075	0.0011	1034.9	6.8	1043.9	9.4	1064	29	97
62	86.5	0.723699	0.1941	0.0016	2.069	0.039	0.0772	0.0015	1143.5	8.7	1137	13	1115	39	103
63	75.1	0.645806	0.19	0.0017	1.982	0.049	0.0756	0.0018	1121	9.2	1105	17	1065	48	105
64	28.27	0.634949	0.1765	0.002	1.834	0.059	0.0752	0.0024	1047	11	1052	22	1032	70	101
65	227.4	0.337291	0.1785	0.0014	1.917	0.034	0.078	0.0015	1058.7	7.7	1086	12	1138	38	93
66	34.3	0.830904	0.1829	0.0029	1.92	0.066	0.0758	0.0025	1082	16	1084	22	1063	68	102
67	275	0.738182	0.1812	0.0024	1.971	0.033	0.079	0.001	1073	13	1104	11	1166	26	92
69	136.5	0.967033	0.1763	0.0018	1.87	0.037	0.0766	0.0017	1046.4	9.7	1072	14	1117	43	94
70	278.8	0.424677	0.2	0.0011	2.17	0.022	0.0786	0.0007	1175.1	6	1170.5	7.2	1160	19	101
71	336	0.223214	0.1775	0.0014	1.937	0.025	0.07918	0.0009	1053	7.6	1092.9	8.6	1172	23	90
72	355.5	0.272011	0.1766	0.001	1.919	0.021	0.07886	0.0009	1048.2	5.5	1086.8	7.3	1163	22	90
73	86.8	1.016129	0.1977	0.0013	2.136	0.032	0.0783	0.0011	1162.9	7.1	1158	10	1143	28	102
74	37.22	0.970715	0.1802	0.002	1.887	0.06	0.0762	0.0026	1068	11	1071	21	1071	66	100
76	169.7	0.65881	0.1761	0.0011	1.798	0.023	0.0743	0.001	1045.7	5.9	1043.5	8.3	1040	28	101
77	87.2	0.855505	0.1843	0.0015	1.915	0.04	0.0755	0.0017	1090.4	8.3	1086	14	1072	45	102
79	49.7	0.82173	0.1873	0.002	1.965	0.067	0.0762	0.0026	1107	11	1098	23	1078	67	103

Table C5. continued.

Sample ARZA02			Isotopic ratios						Ages (Ma)						
Grain #	U [ppm]	Th/U	$^{206}Pb/^{238}U$	±2σ	$^{207}Pb/^{235}U$	±2σ	$^{207}Pb/^{206}Pb$	±2σ	$^{206}Pb/^{238}U$	±2σ	$^{207}Pb/^{235}U$	±2σ	$^{207}Pb/^{206}Pb$	±2σ	% Conc
80	375.3	0.347455	0.18122	0.00095	1.876	0.018	0.07517	0.0007	1073.6	5.2	1072	6.4	1070	20	100
81	49.84	0.842496	0.1798	0.0016	1.867	0.044	0.0758	0.0019	1065.9	8.8	1066	16	1065	52	100
83	220.1	0.527488	0.2165	0.0017	2.468	0.025	0.08281	0.0008	1263	8.8	1261.8	7.2	1263	20	100
84	83	0.64	0.1857	0.0013	1.979	0.036	0.0774	0.0014	1098.1	7.1	1105	12	1116	37	98
85	40.5	0.826667	0.1871	0.002	2.039	0.072	0.0788	0.0027	1106	11	1122	24	1140	71	97
87	282	0.218085	0.172	0.0016	1.778	0.034	0.0749	0.0016	1023.3	8.7	1037	13	1060	43	97
90	59.4	0.687037	0.1859	0.0017	1.951	0.05	0.0761	0.002	1099	9.2	1094	17	1066	54	103
91	259.5	0.543353	0.16744	0.00094	1.781	0.024	0.077	0.001	997.9	5.2	1037.2	8.7	1113	27	90
92	71.8	0.254318	0.1719	0.0017	1.758	0.045	0.074	0.002	1022.6	9.1	1026	17	1016	57	101
93	87.05	0.699138	0.1798	0.0016	1.854	0.046	0.0745	0.002	1065.6	8.7	1062	16	1033	54	103
95	471.2	0.240874	0.1793	0.001	1.868	0.018	0.07529	0.0008	1062.8	5.7	1069.4	6.3	1073	20	99
96	37	0.83027	0.1796	0.0031	1.951	0.082	0.0784	0.0032	1064	17	1099	30	1145	89	93
97	98	0.42551	0.1871	0.0017	2.006	0.039	0.0777	0.0015	1105.6	9	1115	13	1123	38	98
98	155.9	0.42399	0.1809	0.0012	1.88	0.031	0.0754	0.0013	1071.6	6.7	1075	11	1064	35	101
100	230.3	0.491533	0.1945	0.0011	2.151	0.029	0.0797	0.0011	1145.8	6.1	1164	9.4	1181	29	97
102	368.7	0.662056	0.1827	0.0015	1.928	0.033	0.076	0.0013	1081.7	8	1090	12	1096	32	99
107	72.3	0.73444	0.178	0.0016	1.824	0.043	0.0741	0.0018	1055.6	8.8	1052	15	1020	49	103
108	33.41	0.614786	0.1915	0.0029	2.142	0.074	0.0807	0.0028	1129	16	1156	24	1176	71	96
109	72.6	0.608815	0.1702	0.0014	1.707	0.041	0.0721	0.0018	1012.8	7.5	1010	15	968	51	105
110	73.8	0.560976	0.1986	0.002	2.097	0.068	0.076	0.0026	1168	11	1143	22	1066	72	110
111	42.96	0.68878	0.1808	0.0017	1.872	0.052	0.0747	0.0022	1071	9.3	1067	18	1023	60	105
112	251.1	0.473517	0.1775	0.0011	1.879	0.03	0.0762	0.0012	1053.1	6.3	1074	10	1098	31	96
113	139.3	0.477243	0.193	0.0014	2.107	0.036	0.0786	0.0015	1137.5	7.6	1151	12	1161	37	98
114	283.9	0.199718	0.185	0.001	2.008	0.025	0.0782	0.0011	1094.1	5.6	1118.2	8.2	1144	29	96

Table C6. Concordant detrital zircon age data obtained from sample AR01.

Sample AR01			Isotopic ratios							Ages (Ma)					
Grain #	U [ppm]	Th/U	$^{206}Pb/^{238}U$	±2σ	$^{207}Pb/^{235}U$	±2σ	$^{207}Pb/^{206}Pb$	±2σ	$^{206}Pb/^{238}U$	±2σ	$^{207}Pb/^{235}U$	±2σ	$^{207}Pb/^{206}Pb$	±2σ	% Conc
2	132	0.62	0.1849	0.0014	1.9520	0.0360	0.0771	0.0014	1094	8	1097	12	1112	36	98
4	402	0.80	0.1771	0.0010	1.8230	0.0190	0.0754	0.0009	1051	5	1054	7	1075	23	98
18	301	0.68	0.1741	0.0011	1.7680	0.0230	0.0742	0.0010	1035	6	1033	8	1043	29	99
22	332	0.76	0.1732	0.0010	1.7580	0.0210	0.0740	0.0009	1030	5	1029	8	1041	24	99
30	220	1.22	0.1762	0.0015	1.8170	0.0450	0.0748	0.0017	1046	8	1050	16	1067	51	98
32	234	1.26	0.1833	0.0013	1.9240	0.0360	0.0767	0.0015	1085	7	1088	13	1105	39	98
36	2627	0.06	0.1806	0.0013	1.8770	0.0170	0.0758	0.0004	1070	7	1072	6	1089	10	98
38	367	1.00	0.1742	0.0011	1.7770	0.0250	0.0744	0.0011	1035	6	1036	9	1053	32	98
39	272	1.03	0.1637	0.0010	1.6800	0.0270	0.0746	0.0011	977	5	1000	10	1058	31	92
41	791	1.66	0.2462	0.0040	3.0570	0.0550	0.0905	0.0008	1418	21	1420	14	1434	16	99
43	291	0.67	0.1750	0.0011	1.7970	0.0250	0.0748	0.0010	1040	6	1043	9	1058	27	98
44	153	1.41	0.1737	0.0011	1.7650	0.0270	0.0738	0.0012	1032	6	1031	10	1022	31	101
46	314	1.12	0.1630	0.0008	1.6730	0.0170	0.0747	0.0007	974	4	998	6	1058	20	92
50	162	0.43	0.1925	0.0015	2.0540	0.0420	0.0777	0.0016	1135	8	1132	14	1128	42	101
51	767	0.34	0.1717	0.0011	1.8240	0.0180	0.0774	0.0008	1022	6	1054	6	1128	19	91
52	493	0.27	0.1827	0.0013	1.9400	0.0230	0.0768	0.0009	1082	7	1095	8	1113	24	97
56	283	0.22	0.1934	0.0019	2.0890	0.0390	0.0786	0.0015	1140	10	1144	13	1156	39	99
61	459	0.31	0.1751	0.0010	1.7970	0.0240	0.0747	0.0010	1040	5	1044	9	1057	28	98
62	215	0.87	0.1831	0.0015	1.9280	0.0370	0.0765	0.0013	1084	8	1089	13	1113	35	97
65	145	2.10	0.1745	0.0014	1.7620	0.0320	0.0740	0.0015	1037	8	1034	13	1037	40	100
70	453	0.48	0.1765	0.0010	1.8410	0.0230	0.0758	0.0009	1048	5	1060	8	1090	25	96
71	763	0.16	0.1687	0.0010	1.7230	0.0180	0.0744	0.0007	1005	5	1017	7	1054	21	95
73	263	0.42	0.1937	0.0023	2.1110	0.0410	0.0801	0.0017	1141	12	1151	13	1193	42	96
75	695	0.69	0.1809	0.0011	1.9190	0.0230	0.0774	0.0010	1072	6	1087	8	1130	25	95
76	148	0.79	0.1716	0.0011	1.7300	0.0300	0.0734	0.0013	1021	6	1018	11	1015	35	101
77	313	0.58	0.1750	0.0009	1.7860	0.0210	0.0744	0.0009	1040	5	1040	7	1046	23	99
82	313	1.27	0.1742	0.0013	1.8700	0.0350	0.0781	0.0014	1035	7	1069	12	1148	36	90
84	157	0.80	0.1781	0.0016	1.8250	0.0400	0.0742	0.0018	1056	9	1053	14	1032	49	102
86	157	0.68	0.1753	0.0011	1.7940	0.0300	0.0743	0.0013	1041	6	1042	11	1044	35	100
90	353	0.41	0.1749	0.0016	1.8930	0.0320	0.0787	0.0013	1039	9	1078	11	1159	32	90
91	507	0.46	0.1765	0.0009	1.8410	0.0200	0.0756	0.0008	1048	5	1060	7	1084	23	97
94	362	1.09	0.1747	0.0008	1.7800	0.0180	0.0739	0.0008	1038	5	1038	7	1037	21	100
96	525	0.42	0.1780	0.0009	1.8380	0.0190	0.0748	0.0008	1056	5	1059	7	1065	21	99
98	429	0.84	0.1717	0.0012	1.7420	0.0190	0.0736	0.0009	1021	7	1024	7	1027	26	99
99	312	0.59	0.1738	0.0008	1.7760	0.0200	0.0740	0.0009	1033	5	1036	7	1035	24	100

Table C7. Concordant detrital zircon age data obtained from sampleARZG01.

Sample ARZG01			Isotopic ratios						Ages (Ma)						
Grain #	U [ppm]	Th/U	$^{206}Pb/^{238}U$	±2σ	$^{207}Pb/^{235}U$	±2σ	$^{207}Pb/^{206}Pb$	±2σ	$^{206}Pb/^{238}U$	±2σ	$^{207}Pb/^{235}U$	±2σ	$^{207}Pb/^{206}Pb$	±2σ	% Conc
1	62.8	0.75	0.1802	0.0019	1.9060	0.0540	0.0762	0.0022	1068	11	1079	19	1074	59	99
2	54.8	0.58	0.1835	0.0022	1.9230	0.0610	0.0754	0.0023	1086	12	1082	21	1046	64	104
5	423.4	0.47	0.1973	0.0012	2.1660	0.0260	0.0792	0.0010	1161	7	1169	8	1172	25	99
6	254.9	0.29	0.1856	0.0012	1.9620	0.0230	0.0764	0.0010	1097	6	1102	8	1098	27	100
13	603	0.18	0.1808	0.0011	1.9050	0.0190	0.0760	0.0008	1072	6	1082	7	1093	20	98
15	763.9	0.16	0.1809	0.0012	1.9870	0.0230	0.0793	0.0008	1072	7	1110	8	1177	19	91
17	181.6	0.43	0.1976	0.0012	2.1580	0.0290	0.0786	0.0010	1163	6	1167	9	1164	27	100
18	461	0.36	0.1784	0.0012	1.9380	0.0260	0.0783	0.0010	1058	6	1094	9	1151	26	92
19	162	0.62	0.1962	0.0015	2.1250	0.0400	0.0780	0.0014	1155	8	1155	13	1137	34	102
20	337	0.35	0.1791	0.0019	1.8630	0.0280	0.0753	0.0011	1062	11	1071	11	1072	29	99
21	397	0.18	0.1773	0.0018	1.9470	0.0310	0.0791	0.0012	1052	10	1096	11	1170	30	90
24	142.1	0.58	0.1724	0.001	1.7580	0.0260	0.0732	0.0010	1025	6	1028	10	1014	29	101
25	219.2	0.57	0.1769	0.0011	1.8540	0.0270	0.0755	0.0010	1050	6	1066	9	1078	27	97
27	248.5	1.00	0.1739	0.0013	1.8170	0.0250	0.0747	0.0011	1033	7	1051	9	1059	31	98
29	302.8	0.48	0.1776	0.0011	1.9130	0.0180	0.0772	0.0007	1054	6	1086	6	1126	19	94
37	42.62	0.97	0.1707	0.002	1.7630	0.0560	0.0735	0.0023	1016	11	1028	20	1012	66	100
38	153.7	0.51	0.173	0.0013	1.7660	0.0330	0.0727	0.0013	1029	7	1032	12	998	37	103
39	317	0.84	0.1964	0.0019	2.2760	0.0270	0.0832	0.0012	1156	10	1206	9	1274	27	91
40	314	0.18	0.1787	0.0012	1.9650	0.0220	0.0788	0.0009	1060	7	1103	8	1167	24	91
41	126.2	0.68	0.1936	0.0012	2.0910	0.0270	0.0771	0.0011	1141	6	1144	9	1119	27	102
43	86.1	0.79	0.1736	0.0016	1.8970	0.0470	0.0777	0.0019	1032	9	1078	17	1134	51	91
44	182.9	0.27	0.1753	0.0015	1.8470	0.0290	0.0753	0.0012	1041	8	1061	10	1068	32	98
45	86.9	0.59	0.1904	0.0015	2.0400	0.0410	0.0765	0.0015	1124	8	1128	14	1101	41	102
46	406	0.63	0.2007	0.0017	2.2000	0.0390	0.0783	0.0014	1179	9	1180	12	1148	36	103
48	130.8	0.44	0.1849	0.0015	1.9720	0.0440	0.0762	0.0018	1094	8	1103	15	1090	45	100
50	96.4	0.47	0.195	0.0025	2.0850	0.0490	0.0768	0.0018	1148	14	1143	16	1087	50	106
51	105.8	0.55	0.1756	0.002	1.8540	0.0510	0.0756	0.0022	1043	11	1061	18	1062	58	98
53	511	0.29	0.174	0.0014	1.7790	0.0320	0.0733	0.0013	1034	7	1037	12	1014	37	102
54	532.2	0.35	0.1877	0.0016	1.9900	0.0310	0.0760	0.0012	1109	9	1111	11	1091	30	102
57	1232	0.08	0.1821	0.0013	1.9050	0.0250	0.0752	0.0010	1078	7	1082	9	1070	27	101
58	265.5	0.17	0.1762	0.0019	1.8410	0.0400	0.0750	0.0017	1046	10	1058	14	1064	47	98
59	612.1	0.11	0.1988	0.0015	2.2410	0.0350	0.0812	0.0012	1169	8	1193	11	1220	28	96
61	453	0.07	0.1999	0.0018	2.1310	0.0350	0.0773	0.0014	1175	10	1158	11	1120	37	105
63	741	0.10	0.185	0.0014	1.9340	0.0320	0.0756	0.0012	1094	8	1092	11	1077	33	102
64	207.1	0.33	0.1954	0.0022	2.1250	0.0620	0.0789	0.0022	1150	12	1153	20	1151	55	100
66	114.7	0.42	0.1865	0.002	1.928	0.053	0.0753	0.002	1103	11	1085	18	1036	59	106
68	933.3	0.28	0.1968	0.0015	2.21	0.033	0.0817	0.001	1157.9	8	1184	10	1235	27	94
69	645	0.15	0.1926	0.0013	2.057	0.024	0.0777	0.001	1136.7	7.5	1134.1	8.1	1135	27	100
70	830	0.08	0.1793	0.0012	1.855	0.023	0.0754	0.001	1063	6.5	1064.5	8.2	1074	27	99
71	398.6	0.29	0.178	0.0011	1.781	0.025	0.07294	1E-03	1056.1	6.1	1037.6	9.1	1006	28	105
72	95	0.56	0.1816	0.0019	1.889	0.047	0.0758	0.002	1076	10	1073	16	1071	49	100
73	152	0.36	0.1822	0.0019	1.862	0.047	0.0743	0.002	1079	10	1065	16	1046	49	103
74	588	0.12	0.1873	0.0019	1.991	0.035	0.0777	0.001	1107	10	1112	12	1135	35	98
75	235.3	0.44	0.172	0.0016	1.746	0.037	0.0746	0.002	1023.2	8.8	1024	14	1050	40	97
76	63.6	0.58	0.1869	0.0027	1.965	0.063	0.0773	0.003	1104	15	1100	22	1103	73	100
77	140.6	1.06	0.1781	0.0014	1.847	0.033	0.0762	0.002	1056.6	7.5	1060	12	1089	38	97
78	115.7	0.67	0.1833	0.0014	1.921	0.036	0.0776	0.002	1084.9	7.4	1086	13	1122	41	97
79	98.7	0.86	0.3133	0.0021	4.568	0.05	0.1074	0.001	1757	10	1742.3	9.2	1752	21	100
81	128.1	0.87	0.1868	0.0015	1.98	0.031	0.0784	0.001	1103.7	8.3	1108	11	1151	32	96
82	72.66	0.69	0.1967	0.0016	2.125	0.048	0.0797	0.002	1157.5	8.9	1157	16	1175	48	99
83	64.78	0.76	0.1841	0.0016	1.926	0.051	0.0769	0.002	1089.4	8.9	1088	17	1112	55	98
85	64.61	0.99	0.1866	0.0018	1.967	0.047	0.0784	0.002	1102.9	9.6	1102	16	1148	48	96
87	404	0.52	0.1807	0.0014	1.942	0.02	0.07969	7E-04	1070.7	7.7	1094.8	6.9	1186	16	90
89	164	1.76	0.182	0.0011	1.834	0.026	0.0746	0.001	1077.9	5.7	1056.4	9.2	1048	28	103
90	91.6	1.48	0.1838	0.0012	1.916	0.028	0.0772	0.001	1087.7	6.4	1084.6	9.9	1113	31	98
91	52.1	1.01	0.1885	0.0015	1.919	0.046	0.0752	0.002	1113	8.3	1084	16	1052	47	106
93	161	1.1	0.2056	0.0017	2.278	0.036	0.0818	0.001	1205.3	9	1204	11	1234	29	98
95	218.9	0.43	0.1751	0.0015	1.77	0.031	0.0747	0.001	1039.9	8.1	1034	11	1053	38	99

Table C7. continued.

Sample ARZG01			Isotopic ratios							Ages (Ma)				
Grain #	U [ppm]	Th/U	$^{206}Pb/^{238}U$	±2σ	$^{207}Pb/^{235}U$	±2σ	$^{207}Pb/^{206}Pb$	±2σ	$^{206}Pb/^{238}U$	±2σ	$^{207}Pb/^{235}U$	±2σ	$^{207}Pb/^{206}Pb$	±2σ	% Conc
96	83.6	0.64	0.1836	0.0017	1.891	0.047	0.0761	0.002	1086.5	9.5	1075	16	1081	50	101
98	195.6	0.3	0.1848	0.0015	1.901	0.029	0.0761	0.001	1093.2	8	1080	10	1089	35	100
99	196.8	0.5	0.2002	0.0013	2.153	0.028	0.0793	0.001	1176.3	6.8	1165	9	1177	28	100
100	41.5	0.8	0.1904	0.0024	1.932	0.059	0.0747	0.002	1123	13	1088	21	1041	61	108
101	208.7	0.43	0.18311	0.00098	1.904	0.021	0.07651	9E-04	1083.9	5.3	1081.5	7.5	1105	23	98
102	349	0.14	0.1812	0.0012	1.924	0.025	0.07795	1E-03	1073.7	6.3	1088.7	8.8	1141	25	94
103	225.8	0.5	0.1959	0.0012	2.112	0.026	0.0792	0.001	1152.9	6.3	1151.7	8.5	1170	27	99
104	202.5	0.41	0.1824	0.0013	1.907	0.039	0.0766	0.002	1080	7.2	1082	14	1101	42	98
106	910	0.29	0.1875	0.0028	1.993	0.034	0.07783	7E-04	1108	15	1112	12	1143	16	97
107	119.4	0.56	0.187	0.0018	1.942	0.045	0.076	0.002	1105.1	9.7	1094	16	1082	49	102
108	344	0.33	0.186	0.0011	1.966	0.02	0.07735	8E-04	1099.7	6.2	1103.3	6.8	1125	21	98
110	569.8	0.46	0.1997	0.0016	2.188	0.022	0.07992	9E-04	1173.6	8.7	1176.6	7.1	1192	22	98
113	501.9	0.4	0.1935	0.0014	2.101	0.024	0.079	0.001	1140	7.5	1148.6	8	1169	25	98
114	843	0.12	0.1765	0.0018	1.863	0.023	0.07653	7E-04	1047	10	1067.2	8.3	1107	18	95
115	190.5	0.5	0.199	0.0013	2.167	0.033	0.0788	0.001	1170	6.8	1169	10	1163	27	101

Table C8. Concordant detrital zircon age data obtained from sample GAN2.

Sample GAN2			Isotopic ratios						Ages (Ma)						
Grain #	U [ppm]	Th/U	$^{206}Pb/^{238}U$	±2σ	$^{207}Pb/^{235}U$	±2σ	$^{207}Pb/^{206}Pb$	±2σ	$^{206}Pb/^{238}U$	±2σ	$^{207}Pb/^{235}U$	±2σ	$^{207}Pb/^{206}Pb$	±2σ	% Conc
1	282.9	1.29	0.4927	0.0052	13.1700	0.5100	0.1958	0.0070	2582	23	2683	37	2774	60	93
5	137.6	0.37	0.1699	0.0019	1.7400	0.0430	0.0749	0.0019	1012	10	1021	16	1053	50	96
6	148.8	0.51	0.10218	0.0006	0.8560	0.0180	0.0612	0.0013	627	4	629	10	619	48	101
9	438	0.22	0.16675	0.00086	1.7530	0.0220	0.0766	0.0009	994	5	1027	8	1105	25	90
18	222.7	1.01	0.3278	0.0016	5.2200	0.0590	0.1154	0.0013	1828	8	1855	10	1883	20	97
25	125.2	0.98	0.3432	0.0024	6.1130	0.0960	0.1289	0.0024	1902	11	1989	14	2073	32	92
43	309.4	0.33	0.0898	0.0011	0.7430	0.0310	0.0602	0.0026	555	6	563	18	580	100	96
45	81.89	0.64	0.1728	0.0012	1.7720	0.0400	0.0743	0.0018	1028	6	1032	15	1026	49	100
49	87.6	0.65	0.0929	0.0016	0.7610	0.0420	0.0595	0.0035	573	9	576	26	550	130	104
50	200.6	0.75	0.1642	0.0011	1.6480	0.0310	0.0728	0.0014	980	6	987	12	998	38	98
55	262.4	0.51	0.10345	0.00077	0.8840	0.0190	0.0625	0.0015	635	5	642	10	681	50	93
65	161.4	0.60	0.1764	0.0018	1.7900	0.0500	0.0734	0.0018	1047	10	1040	18	1035	50	101
66	165.4	0.44	0.0892	0.0011	0.7210	0.0270	0.0589	0.0023	551	7	550	16	530	86	104
77	278.8	1.18	0.3381	0.0021	5.3570	0.0840	0.1148	0.0018	1877	10	1877	13	1873	27	100
79	142.9	0.71	0.10667	0.00087	0.9070	0.0220	0.0616	0.0016	653	5	654	12	632	57	103
84	165.5	0.64	0.2447	0.002	3.2410	0.0650	0.0962	0.0021	1411	10	1466	15	1555	44	91
85	157.7	0.49	0.10175	0.0008	0.8460	0.0210	0.0602	0.0016	625	5	621	11	589	58	106
88	225.9	0.65	0.1573	0.0012	1.5540	0.0270	0.0715	0.0012	942	7	951	11	963	36	98
89	181.7	0.33	0.12779	0.00094	1.1580	0.0270	0.0659	0.0016	775	5	779	13	785	51	99
92	242.6	0.32	0.1734	0.0011	1.7930	0.0350	0.0753	0.0016	1031	6	1042	13	1067	42	97
98	573.3	0.56	0.08707	0.00065	0.7040	0.0140	0.0592	0.0012	538	4	542	8	571	40	94
100	114.4	0.45	0.08853	0.00097	0.7180	0.0230	0.0590	0.0021	547	6	547	14	526	76	104

Appendix D: Microfossil processing data

Table D1. Sample maceration and processing log

Samples	Weight	Undissolved (g)	Dissolved (%)	Rock colour	Lithology	Notes about breaking up	#days dissolving in HF	Colour of dissolved material	Added HCl = colour	Time boiling in HCl	Material in test tube	No. of slides
HDM01	51.09	34.34	33	Grey/silver	Laminated shale	Broke into smaller blade/slate pieces ~3cm	s 29/11 - 4/12 (5)	white	Yellow	>1 hr	Low. Suspended in column	3
HDM02	50.07	22.35	55	Grey/green	Laminated shale	Broke into smaller blade/slate pieces ~3cm	s 29/11 - 4/12 (5)	light grey	Yellow	38min	Low. Nothing suspended	3
HDM03	50.15	24.64	51	Grey/green	Laminated shale	large solid pieces after hammering	s 29/11 - 4/12 (5)	dark light grey	Yellow	>1 hr	Low. Suspended content.	3
HDM03 (2)	50.24	20.35	59	Grey/green	Laminated shale	Rock crusher	s 5/12 - 11/12 (6)	dark light grey	Luminescent yellow	20min	Low, grey sediment	3
HDM04	50.41	22.28	56	Dark grey	Laminated shale	No need for hammering, all small pieces	s 29/11 - 4/12 (5)	dark grey (darkest)	Yellow	34min	Very low, grey, nothing suspended	3
HDM05	50.91	24.71	51	Light grey	Laminated shale	Broke into smaller blade/slate pieces ~3cm	s 29/11 - 4/12 (5)	suspended cloud not settling	Yellow	37min	Very low, brown/black particles	3
HDM06	50.72	23.66	53	Light grey	Laminated shale	Broke into smaller blade/slate pieces ~3cm	s 29/11 - 4/12 (5)	light grey	Yellow	40min	Low. Black particles suspended	3
HDM07	50.80	20.46	60	Light grey	Laminated shale	Rock crusher	s 5/12 - 11/12 (6)	dark light grey	Yellow	20min	Very low. Grains visible.	2
HDM08	50.16	24.76	51	Light grey	Laminated shale	Rock crusher	s 5/12 - 11/12 (6)	dark light grey	Yellow	20min	Very low, dark grey particles	2
HDM09	50.13	26.67	47	Light grey	Laminated shale	Rock crusher - solid pieces	s 5/12 - 11/12 (6)	suspended cloud not settling	Yellow	20min	Very low (<1 ml), grey sediment	2
HDM10	50.17	24.46	51	Light grey	Laminated shale	Rock crusher	s 5/12 - 11/12 (6)	light grey	Yellow	20min	Very low (<1 ml), grey sediment	2
HDM11	50.32	25.40	50	Light grey	Laminated shale	Rock crusher	s 5/12 - 11/12 (6)	dark light grey	Yellow	20min	Very low (<1 ml), grey sediment	2
HDM12	50.37	17.34	66	Grey/green	Laminated shale	Rock crusher	s 5/12 - 11/12 (6)	light grey	Yellow	20min	Very low, lumpy grey sediment	2
HDM01X	50.07	13.36	73	Light olive green (very weathered)	Laminated shale	Rock crusher	s 11/12 - 16/12 (5)	grey	Dirty luminescent yellow	20min	Low (<1 ml), grey sediment	2
HDM04X	50.23	20.73	59	Blue/grey (fresher)	Laminated shale	Rock crusher	s 11/12 - 16/12 (5)	grey	Dirty luminescent yellow	20min	Low (<1 ml), grey sediment	1
HDM08X	50.81	28.63	44	Grey hard blocks	Laminated shale	Rock crusher	s 11/12 - 16/12 (5)	dark light grey	Dirty green/yellow	20min	Vey low, grey clays.	2
HDM12X	50.27	27.41	45	Light grey	Laminated shale	Rock crusher	s 11/12 - 16/12 (5)	light brown grey	Dirty green/yellow	20min	Very low, grey fragments.	2
FLM01	50.74	25.63	49	Purple black	Siltstone/fine sand	Rock crusher	s 11/12 - 16/12 (5)	rich rust brown	Very dark brown	20min	Low. Dark minerals and clays.	2
FLM02	50.89	20.98	59	Light purple/grey	Siltstone/fine sand	Rock crusher	s 11/12 - 16/12 (5)	brown but not as dark as 1	Very dark brown	20min	Low. Dark minerals and clays.	2
FLM03	50.98	36.27	29	Purple black	Siltstone/fine sand	Rock crusher	s 11/12 - 16/12 (5)	light purple brown	Very dark brown	20min	Low. Dark minerals and clays.	2
FLM04	50.15	33.53	33	Very dark purple	Siltstone/fine sand	Rock crusher	s 11/12 - 16/12 (5)	light purple grey	Very dark brown	20min	Low. Dark minerals and clays.	1
Ngb	50.59	15.13	70	Light grey/green	Laminated shale	Rock crusher	s 11/12 - 16/12 (5)	Gun metal grey	Dark grey	20min	Very low. Only clays at bottom.	2

Table D2. 40 microscope slide descriptions of the 16 samples processed from the Hoedberg Formation.

Sample and location		Slide	Slide description	Microfossil content
Fig 4.6	HDM01	1	Opaque minerals. sediment/ Floccules of organic matter and clay minerals from 10-100um. Individual grains of apatite (green) 10um. High bi-fringence patterns, needle-like Apatite? Modern contamination present (fibres and plant fragments).	NA
		2	Low organic content. Micas – biotite – laminae and platy minerals. Sediment particles and minor contamination.	NA
		3	Dusty brown floccules of clay, sediment and organic matter. Modern contamination present (fibres).	NA
	HDM02	1	Biotite. Modern contamination present with pervasive cubic salt crystals. Fragments of organic matter with cellular textures.	Colonial cells
		2	Amorphous dark kerogen with occasional spherical shapes, fragmentary or relic envelope structures. Sediment particles (70 - 1130 µm), clay floccules, biotite and modern contamination also present. Pervasive cubic crystals.	Colonial cells
		3	Modern contamination present. Not as much content as 1 and 2. More cellular structures on surface on dark brown fragments. Thin wispy brown fragments also present (20 – 100 µm).	Colonial cells
	HDM03	1	Amorphous dark kerogen (60 - 200 µm). Sediment pieces with floccules of clay minerals (40 – 200 µm), opaque minerals (50 – 120 µm) and modern contamination e.g. filaments.	NA
		2	Organic matter (), sediment particles (600 µm), modern contamination present.	NA
		3	Modern contamination present. Sediment and clay floccules (120 – 400 µm).	Potential SCF (200 µm)
		4	Modern contamination present. Sediment pieces (70 – 1100 µm), clay floccules, and blocky minerals (26 µm).	NA
		5	Semi-translucent to opaque brown fragments of sediment (26 - 360 µm). Blocky insoluble salt pervasive with modern contamination present.	NA
		6	Modern contamination present. 76 - 884µm. Blocky insoluble salt pervasive. Sediment particles and no organic matter present.	NA
	HDM04	1	Barren slide.	NA
		2	Very little material on the slide. Small fragment of biotite (224 µm). Blocky transparent insoluble salt present, structure slightly different with lower relief and rounded edges. Sediment particles: 120 µm	NA
		3	Amorphous, fragmentary kerogen (16 – 129 µm). Opaque minerals (26 – 252 µm), modern contamination noted.	NA
	HDM05	1	Barren – sample ran off the slide.	NA
		2	Clear, transparent amorphous fragment: 0.15mm	NA
		3	Barren. Minor traces of sediment pieces but not noteworthy.	NA
	HDM06	1	High content of amorphous kerogen (400 µm) with cellular structure on the surface: cells in diameter ~ 3 µm. Fragmentary organic matter with possible relict envelopes (60 - 400 µm) and cluster of cells (28 µm). Modern contamination present. Sediment particles (60 – 270 µm). Opaque minerals (60 – 200 µm).	Cluster of cells, possible *Sphaerocongregus variabilis*
		2	Organic matter (170 µm) Modern contamination present. Fragments of light brown/orange kerogen with cellular structure (diameter 2 µm). Blobs with cell structure on surface and cells blobs in larger particles.	Colonial cells with cellular texture.
		3	Modern contamination present organic matter (350 - 800 µm) and opaque minerals (370 µm). Cluster of spheres	NA
	HDM07	1	Very little material present: opaque minerals and transparent, cubic mineral (suspected insoluble salt). Sediment fragments with clay minerals (<2 µm) and organic matter pieces. Minor contamination present in the form of modern fabric fibres.	NA
		2	Very little material on slide and majority of material is transparent blocky mineral.	NA
	HDM08	1	No organic matter. Sediment particles (50 – 400 µm). Blocky minerals. Modern plant contamination – wood fragments.	NA
		2	Barren slide. Wispy brown material.	NA
	HDM09	1	Barren slide. Material obscured by insoluble blocky salt. Biotite fragments (800 - 400 µm).	NA
		2	Barren slide. Material obscured by insoluble blocky salt. Biotite fragments. Minor amounts of sediments (30 – 120 µm)	NA
	HDM10	1	Sparse. Sediment particles and pervasive insoluble salt. Barren slides with minor contamination. Sediment particles and clay floccules (500 µm - 15 cm). Minor organic content (330 µm)	NA
		2	Barren slides with minor contamination. Sediment particles and clay floccules (130 µm – 400 µm).	NA
	HDM11	1	Trace amounts of sediment particles (~ 100 µm).	NA
		2	Barren slide. Trace amounts of sediment particles (~ 100 µm).	NA
	HDM12	1	Brown specimen with spherical shape but too light in colour (200 µm). Particles fragmentary. Contamination.	NA
		2	Barren slide. Contamination with modern wood pieces.	NA
	HDM01X	1	No organic matter. Sediment pieces (20 - 180 µm)	NA
		2	No organic matter. Sediment pieces (40 - 180 µm), barren and fragments light brown/translucent.	NA
	HDM04X	1	Only sediment particles (60 – 270 µm) and clay floccules.	NA
	HDM08X	1	No organic matter. Sediment pieces (60 - 150 µm), barren and fragments light brown/translucent.	NA
		2	No organic matter. Sediment pieces (40 - 180 µm), barren and fragments light brown/translucent.	NA
	HDM12X	1	Barren slide, covered in minerals and grey sediment particles.	NA
		2	Wispy fragments of kerogen.	NA

Table D3. Seven microscope slide descriptions from the four samples processed from the Flaminkberg Formation.

Sample and location		Slide	Slide description	Microfossil content
Fig 4.1	FLM01	1	No organic matter. Micas (~100 µm), orange-rimmed quartz (100 – 250 µm) and iron oxides (75 – 200 µm) present.	NA
		2	No organic matter. Orange-rimmed quartz (110 – 180 µm) and iron oxides (75 – 200 µm) present.	NA
	FLM02	1	No organic matter. Orange-rimmed quartz (90 – 170 µm) and iron oxides (80 – 250 µm) present.	NA
		2	No organic matter. Orange-rimmed quartz (80 – 200 µm) and iron oxides (90 – 240 µm) present.	NA
	FLM03	1	No organic matter. Orange-rimmed quartz (100 – 190 µm) and iron oxides (100 – 150 µm) present.	NA
		2	No organic matter. Orange-rimmed quartz (80 – 190 µm) and iron oxides (100 – 150 µm) present.	NA
	FLM04	1	No organic matter present. Translucent blocky minerals present. Micas – muscovite, orange rimmed quartz and iron oxides present.	NA

Table D4. Two microscope slide descriptions from the one sample processed from the Gannabos Formation.

Sample and location		No. of Slides	Slide description	Microfossil content
Fig 4.8	Ngb	1	No organic matter. Fragmented pieces of sediment (<500 µm) and floccules of clay. Minor contamination in slides.	NA
	Ngb	2	No organic matter. Bits of light brown sediment: 50 – 200 µm. Minor contamination with blocky crystals/insoluble salt.	NA